

TROPICAL INSTABILITY WAVES AND MIXING IN THE
EQUATORIAL PACIFIC OCEAN

A DISSERTATION
SUBMITTED TO THE DEPARTMENT OF EARTH SYSTEM
SCIENCE
AND THE COMMITTEE ON GRADUATE STUDIES
OF STANFORD UNIVERSITY
IN PARTIAL FULFILLMENT OF THE REQUIREMENTS
FOR THE DEGREE OF
DOCTOR OF PHILOSOPHY

Ryan Mahony Holmes

March 2016

© Copyright by Ryan Mahony Holmes 2016
All Rights Reserved

I certify that I have read this dissertation and that, in my opinion, it is fully adequate in scope and quality as a dissertation for the degree of Doctor of Philosophy.

(Leif Thomas) Principal Adviser

I certify that I have read this dissertation and that, in my opinion, it is fully adequate in scope and quality as a dissertation for the degree of Doctor of Philosophy.

(Noah Diffenbaugh)

I certify that I have read this dissertation and that, in my opinion, it is fully adequate in scope and quality as a dissertation for the degree of Doctor of Philosophy.

(Oliver Fringer)

Approved for the University Committee on Graduate Studies

Abstract

The unique dynamics of the equatorial oceans play an important role in the El Niño - Southern Oscillation (ENSO) and the ocean's meridional overturning circulation (MOC), both of which are critical processes that drive global climate variability on a range of time-scales. The character of ENSO depends on the detailed dynamics governing the sea surface temperature (SST) budget and the equatorial waves that help the upper Pacific ocean to adjust to perturbations in atmospheric forcing. Inverse models suggest that the abyssal cell of the MOC is closed through diapycnal upwelling mostly in the tropical oceans and thus depends on abyssal mixing there that has not been well observed. This dissertation makes a number of contributions to our understanding of equatorial ocean dynamics, lateral and vertical mixing at the equator, the behavior of equatorial waves and deep equatorial mixing, with implications for both ENSO and the MOC.

Tropical instability waves (TIWs), the main drivers of lateral eddy mixing in the eastern equatorial Pacific, share a number of dynamical features with submesoscale flows in the mid-latitudes. In particular, their formation depends on the detailed frontal dynamics and sharp vertical gradients around their fringes, with implications for TIW energetics and the accurate representation of TIWs in low-resolution ocean models.

The horizontal strain of a TIW's velocity field can drive modulations in vertical mixing by altering the vertical shear of the Equatorial Undercurrent (EUC) through horizontal vortex stretching. This modulation of the turbulent heat flux can drive a net sea surface cooling over the eastern Pacific cold tongue that may partially offset the warming driven by TIW lateral mixing. The magnitude of the net cooling depends

on the mixing scheme used to parameterize vertical mixing, with implications for the role of TIWs in the mixed-layer heat budget in different ocean models.

Downwelling (upwelling) equatorial Kelvin waves can drive large decreases (increases) in the amplitude of the TIW field in the eastern equatorial Pacific and thus TIW-driven lateral and vertical mixing. The Kelvin waves alter the strength and structure of the background flow from which the TIWs gain energy. However the changes that occur in the TIW energy budget are complex. One major sink of energy, the downward radiation of waves, is strongly altered with implications for deep and abyssal equatorial ocean circulation.

Mixing in the abyssal equatorial Pacific can exhibit a seafloor-intensified vertical structure even over smooth topography. The generation and breaking of lee waves over smooth topography at low latitudes is one possible mechanism that could contribute to this mixing. However, downward-propagating equatorial waves generated at the surface by TIWs or wind events could also supply energy for seafloor-intensified mixing through two possible mechanisms, 1) wave trapping due to the horizontal component of Earth's rotation and 2) inertial instability initiated by wave-driven displacement of fluid away from the equator. These results suggest that more attention should be devoted to measuring and understanding mixing over smooth topography in the abyssal equatorial oceans because of its potential role in the global overturning circulation.

Acknowledgments

There are many people who have contributed to helping me through my degree. Without them I would not have had such a successful time at Stanford. Firstly, I would like to thank my supervisor Leif Thomas. His enthusiasm and positive attitude kept me going through the difficult periods in the research. He was always available for meetings at any time, even when working from completely different time zones. I also greatly appreciate his flexibility in allowing me to spend so much time away from Stanford. I would also like to thank Maggie Hoffman and Dan Whitt for helping me with both coursework and my initial research projects. Discussing classwork, papers and research with them was a very pleasant way to spend a day at work. Nico Grisouard was also a very entertaining group member with whom I always enjoyed discussions.

Jim Moum and Sally Warner from Oregon State University were very enjoyable cruise mates and collaborators during the later part of the degree. I would particularly like to thank Jim for inviting me to participate in an equatorial research cruise and allowing me to take such an active role in cruise planning, data acquisition, data analysis and the publication of results. I would like to thank my committee members. Oliver Fringer for his enjoyable and informative classes and enthusiastic questions during spring review meetings. Sanjiva Lele for teaching me a number of analytical and theoretical techniques in fluid mechanics and for his thoughtful comments on my research. Noah Diffenbaugh for keeping me honest with respect to the scientific method, statistical uncertainty and the big picture. Finally, I would also like to thank Professor Matthew England and the Climate Change Research Centre in Sydney for hosting me while I was living in Australia and helping to expand my research interests

towards larger-scale climate processes.

I would also like to thank Brian Peters, David Koweeek and Matt Fox for being great friends and making their living room available for me to sleep in on many a night while visiting Stanford. My other office mates Matz Haugen and Mike Tsiang for helping to make Stanford such an enjoyable place to work. Daniel Urban for lots of interesting science discussions in the long car trips out to the mountains. And finally my family and my partner Marie for supporting me despite the difficulties of living on another continent.

I would like to thank Robert and Marvel Kirby for providing the funds for my three-year Stanford Graduate Fellowship. Earth System Science departmental funding is also appreciated. Additional funding for conference travel and research was provided by grants awarded to Leif Thomas and Jim Moum by the National Oceanic and Atmospheric Administration and the National Science Foundation. Additional acknowledgments are contained at the end of each chapter.

Copyright Information

Portions of this work have been reproduced from a number of works published elsewhere. Here we include copyright statements consistent with the requirements for reproduction as stated by the copyright holders. The original source of all material obtained elsewhere is clearly indicated throughout the document.

Figure 0.3a (*Jochum and Murtugudde*, 2006), Figure 0.7 (*Lumpkin and Speer*, 2007), sections of Chapter 1 not marked with a star (*Holmes et al.*, 2014) and the entirety of Chapter 2 (*Holmes and Thomas*, 2015) were reproduced from articles published by the American Meteorological Society in the Journal of Physical Oceanography under the following copyright statement.

Copyright 2006, 2007, 2014, 2015 American Meteorological Society (AMS). Permission to use figures, tables, and brief excerpts from this work in scientific and educational works is hereby granted provided that the source is acknowledged. Any use of material in this work that is determined to be fair use under Section 107 of the U.S. Copyright Act September 2010 Page 2 or that satisfies the conditions specified in Section 108 of the U.S. Copyright Act (17 USC 108, as revised by P.L. 94-553) does not require the AMS's permission. Republication, systematic reproduction, posting in electronic form, such as on a web site or in a searchable database, or other uses of this material, except as exempted by the above statement, requires written permission or a license from the AMS. Additional details are provided in the AMS Copyright Policy, available on the AMS Web site located at (<http://www.ametsoc.org/>) or from the AMS at 617-227-2425 or copyrights@ametsoc.org.

Figure 0.5 (*Inoue et al.*, 2012), Figure 0.8 (*Nikurashin and Ferrari*, 2013) and the entirety of Chapter 4 (*Holmes et al.*, 2016) were reproduced with permission from

articles published by the American Geophysical Union.

Figure 0.3b was reproduced from *Moum et al.* (2013) with permission from Macmillan Publishers Ltd.

Figure 0.2 was reproduced from *McPhaden* (2015) with permission from AAAS.

Contents

Abstract	iv
Acknowledgments	vi
Copyright Information	viii
0 Introduction	1
0.1 The ocean as part of the Earth System	1
0.2 Equatorial ocean circulation	3
0.3 The El Niño - Southern Oscillation	5
0.4 Tropical instability waves	7
0.5 Turbulence and vertical mixing in the upper EUC	10
0.6 Equatorial waves	11
0.7 Mixing in the abyssal equatorial oceans	16
1 Tropical Instability Wave Vorticity Dynamics and Fronts	20
1.1 Introduction	21
1.2 Model and general flow description	26
1.2.1 Model setup	26
1.2.2 Properties of model TIVs	27
1.3 Force and torque balances of TIW flow	31
1.3.1 Geostrophic/cyclogeostrophic balance	31
1.3.2 Thermal wind balance/gradient wind balance*	32
1.4 Lagrangian analysis of TIV core water formation	35

1.5	Potential vorticity and vorticity dynamics of TIVs	41
1.6	Frontogenesis	48
1.7	Diabatic processes*	52
1.8	Connection of TIW vorticity and TIW energetics frameworks	54
1.9	Conclusions	55
1.10	Gravity current formation from tropical instability wave fronts* . . .	59
1.10.1	Introduction*	59
1.10.2	Frontogenesis of the TIW fronts*	60
1.10.3	The formation of gravity currents*	63
1.10.4	Gravity current propagation*	65
1.10.5	Dissipation of the gravity current*	66
1.10.6	Summary and potential implications for TIW energetics* . . .	69
2	Tropical Instability Waves and Vertical Mixing	71
2.1	Introduction	72
2.2	Model and general flow description	75
2.2.1	Ocean model setup	75
2.2.2	General flow description and evaluation of model performance	76
2.2.3	Marginal stability	79
2.3	Eulerian TIW modulation of shear and stratification	81
2.4	Lagrangian analysis of energetic vertical mixing patches	84
2.5	A simple mixing model of the EUC: TIW influence	90
2.5.1	Simple 1D mixing model setup	90
2.5.2	The influence of TIWs on the turbulent heat flux	95
2.6	Summary and discussion	102
2.7	Appendix: Marginal stability adjustment algorithm	104
3	Equatorial Kelvin Waves and Tropical Instability Waves	106
3.1	Introduction	107
3.2	Model setup	110
3.3	TIW energetics in the control simulation	112
3.4	The influence of intraseasonal Kelvin waves on TIWKE	117

3.4.1	Kelvin wave ensemble experiments	117
3.4.2	The modified TIWKE budget	122
3.5	Discussion	129
3.5.1	Lateral shear production	129
3.5.2	Downward radiation of TIWKE via pressure fluxes	135
3.5.3	Equatorial heat budget	136
3.6	Summary and implications	138
3.7	Appendix: Kelvin wave eigenfunction in a zonally-uniform background flow	141
4	Equatorial Waves and Deep Equatorial Mixing	144
4.1	Introduction	145
4.2	Data and methods	146
4.3	Results	147
4.4	Discussion: Possible mechanisms driving the observed mixing	151
4.4.1	Near-bottom wave trapping associated with the horizontal component of the Earth's rotation	156
4.4.2	Inertial instability	159
4.5	Conclusion	161
4.6	Appendix 1: CTD χ -pod microstructure measurements	162
4.7	Appendix 2: Yanai waves in the shipboard ADCP	163
4.8	Appendix 3: Linear wave theory including the horizontal component of the Earth's rotation	166
5	Summary and Future Work	169
5.1	Summary of the contributions of this thesis	169
5.2	Future work	171

List of Tables

2.1	Turbulent heat flux averaged over a TIW period from a simple 1D mixing model	101
-----	--	-----

List of Figures

0.1	Annual average circulation in the equatorial Pacific	4
0.2	El Niño and La Niña	5
0.3	Mixed layer heat budget in the eastern Pacific	7
0.4	SST and relative vorticity associated with TIWs in the equatorial Pacific	8
0.5	Observed variations in the turbulent heat flux with TIW phase . . .	12
0.6	SST and subsurface temperature observations of a Kelvin wave and TIWs in late 2014	15
0.7	The global meridional overturning circulation from an inverse model .	17
0.8	Estimated flux of energy converted to internal tides and lee waves in the global ocean	18
1.1	SST and T-S diagrams for Lagrangian particles entering a TIV	27
1.2	The PV, temperature, Rossby number and Richardson number associ- ated with TIV flow	28
1.3	Vertical and baroclinic components of the PV within a TIV	29
1.4	Magnitude of the horizontal buoyancy gradient around a TIV	30
1.5	Errors in geostrophic and cyclogeostrophic balance within a TIV . .	33
1.6	Stream-wise vorticity equation along the trailing edge front entering a TIV	36
1.7	Composite average SST field showing the entrance pathways for fluid entering a TIV	37
1.8	PDFs of temperature, relative vorticity, salinity, latitude, PV and baro- clinic PV for particles entering TIVs	39
1.9	An example group of particles entering a TIV	42

1.10	PV and relative vorticity budgets along Lagrangian trajectories entering a TIV	43
1.11	Net contribution of the different relative vorticity budget terms to changes in vorticity entering TIVs	47
1.12	A schematic illustrating the process of baroclinically-low to vortically-low PV conversion and how it contributes to the formation of anticyclonic vorticity within a TIV	48
1.13	Frontogenesis within a TIV	49
1.14	Evidence for the importance of frontogenesis for driving vortex tilting within the TIW fronts	51
1.15	Horizontal buoyancy gradient budget along Lagrangian trajectories entering a TIV	54
1.16	A sharp front observed in late November 2014 from the R/V Oceanus	60
1.17	Fronts and frontogenesis in the TIW region	61
1.18	Sharpening of a TIW trailing edge front into a propagating gravity current	64
1.19	Propagation speed of the gravity current and comparison to theory	67
1.20	A decaying gravity current	68
1.21	The kinetic energy budget of a gravity current	69
2.1	Stratification and vertical shear along the equator	77
2.2	Vertical shear, stratification and diffusivity within the TIW field	78
2.3	Comparison of simulated vertical shear and stratification to data from the TAO moorings	80
2.4	Adjustment of Richardson-number unstable vertical profiles to marginal stability	81
2.5	Reduced shear squared and Lagrangian trajectories entering a patch of energetic mixing in the upper EUC	85
2.6	Reduced shear squared and zonal shear budgets along Lagrangian trajectories entering an energetic mixing patch	86
2.7	Reduced shear squared and meridional divergence associated with TIWs	88

2.8	Schematic illustrating how TIW strain can drive increases in EUC shear through horizontal vortex stretching	89
2.9	The KPP and P&P parameterizations for interior shear instability . .	93
2.10	Results of a simple 1D mixing model of the EUC forced with periodic TIW strain	95
2.11	Vertical turbulent heat flux averaged over a TIW period	96
2.12	Histograms of zonal shear, diffusivity and vertical heat flux from the simple 1D mixing model	98
2.13	KPP and P&P parametrized diffusivities as a function of zonal shear at constant stratification	99
3.1	Potential influence of equatorial Kelvin waves on TIW phase speed and amplitude in satellite SSH and SST data	109
3.2	Background circulation and EKE in the control simulation	111
3.3	TIWKE budget in the control simulation	115
3.4	Barotropic Rossby waves as a mechanism for TIW energy loss	116
3.5	Linear first-baroclinic-mode Kelvin wave eigenfunctions at -200°E and -140°E	119
3.6	SSH and SST from different ensemble members in the downwelling Kelvin wave experiment	120
3.7	SSH, perturbation 20°C isotherm depth and TIWKE in the forced Kelvin wave experiments	121
3.8	Volume integrated TIWKE budget in the downwelling Kelvin wave experiment	123
3.9	Volume integrated TIWKE budget in the upwelling Kelvin wave experiment	124
3.10	Modifications in the background circulation induced by the presence of Kelvin waves	127
3.11	The components of the lateral shear production term in the downwelling Kelvin wave experiment	131

3.12	The components of the lateral shear production term in the upwelling Kelvin wave experiment	132
3.13	Downwelling Kelvin wave modifications to TIW velocity covariance ellipses in the EUC-SEC shear region	133
3.14	Changes in the meridional eddy heat flux	137
3.15	Time series of upper equatorial heat content	139
4.1	CTD χ -pod microstructure turbulence observations in the abyssal equatorial Pacific.	148
4.2	Histograms of χ and ϵ observations with and without the energetic mixing event	150
4.3	Profiles of velocity, density, shear, stratification, χ and absolute momentum at $1/2^\circ\text{S}$	152
4.4	SADCP observations showing evidence of a downward propagating Yanai wave	154
4.5	Properties of the fitted Yanai wave in the SADCP observations	155
4.6	Time periodic solutions to the $2D$ wave equation including and excluding the horizontal Coriolis term	157
4.7	Time periodic solutions to the $2D$ wave equation with forcing restricted to the Northern Hemisphere	159
4.8	Absolute momentum from solutions to the time periodic $2D$ wave equation	160
4.9	Sensitivity of the observed mixing parameters to noise in the χ -pod instrument	164
4.10	Comparison of observed mixing parameters with different assumed noise levels	165

Chapter 0

Introduction

0.1 The ocean as part of the Earth System

The ocean is an integral part of the Earth System. The ocean's large heat capacity acts to regulate surface temperatures and it provides one third of the equator-to-pole heat transport (*Trenberth and Caron*, 2001), helping to keep many regions of our planet habitable. The ocean also plays a significant role in global biological and geochemical cycles on time scales ranging from geologic to diurnal (*McCreary et al.*, 2001; *Marinov et al.*, 2008; *Landschtzer et al.*, 2015). Past and future climate change both owe much of their character to the ocean. Variations in the strength of the meridional overturning circulation have been implicated in driving glacial-interglacial cycles and rapid climate change in the paleoclimate record (*Alley et al.*, 2003; *McManus et al.*, 2004). More recently, the ocean has absorbed a significant fraction of anthropogenic carbon emissions through the biological and physical carbon pumps, thus reducing the concentration of greenhouse gases in the atmosphere (*Sabine et al.*, 2004). However, changes occurring now in the ocean will have potential implications for the climate for hundreds of years, the inevitable rise of sea level (*Rahmstorf*, 2007) being one example. An understanding of how the surface and interior ocean circulations work, how they are driven and how they respond to changes in forcing is an essential piece of the larger problem of understanding the Earth System and how it responds to anthropogenic perturbations.

The tropical oceans play a particularly important role in global climate and feature a number of unique phenomena not present at higher latitudes. They are a site of strong coupling between the ocean and atmosphere. One notable consequence of this strong coupling is the El Niño - Southern Oscillation (ENSO) in the Pacific Ocean. ENSO is perhaps the most well-known source of interannual variability in the climate system, perturbing regional climates over the entire planet (*McPhaden et al.*, 2006). ENSO events drive a large proportion of the interannual variance in global surface temperature (*Thompson et al.*, 2008; *Banholzer and Donner*, 2014) and are responsible for the largest year-to-year natural variations in the global carbon cycle (*Turk et al.*, 2001). The variability of ENSO is also thought to be linked to mechanisms of decadal variability such as the Pacific Decadal Oscillation (PDO) (*Kleeman et al.*, 1999; *Mantua and Hare*, 2002; *Wittenberg et al.*, 2014), partially responsible for the so-called ‘global warming hiatus’ around the turn of the century (*Kosaka and Xie*, 2013; *Trenberth and Fasullo*, 2013; *England et al.*, 2014). While much progress has been made on developing an understanding of ENSO dynamics (*Wang et al.*, 2012), we still know little about its links with decadal variability, how it may change in the future (*Wang et al.*, 2012; *Cai et al.*, 2015) and how to predict individual events. This last point is made evident by the recently predicted El Niño event that did not eventuate in 2014, and the subsequent ‘super-El Niño’ in 2015 (*Menkes et al.*, 2014; *McPhaden*, 2015). In order to make progress on these problems, we must improve our understanding of the inner-workings of the upper Pacific Ocean. The character of ENSO depends critically on the unique equatorial ocean dynamics that govern the energy, momentum and tracer budgets of the large-scale flow.

The deep tropical oceans also influence the variability of global climate on longer time scales as they play an important role in the global meridional overturning circulation. The meridional overturning circulation of the ocean controls the rate at which the deep ocean inventories of carbon, heat and other tracers are renewed (*Riebesell et al.*, 2009; *Srokosz et al.*, 2012). In the abyssal ocean, tracers are brought back towards the surface primarily through the action of small-scale turbulence (*Munk*, 1966; *Munk and Wunsch*, 1998). Much of this vertical transport is believed to occur

in the tropical oceans (*Lumpkin and Speer*, 2007). Thus the global meridional overturning circulation may also depend on the details of the unique equatorial dynamics that govern small-scale variability in the deep equatorial oceans.

This dissertation describes the research that I have undertaken during my Ph.D. in the Department of Earth System Science at Stanford University. I describe the numerical and observational work that I have completed with the aim of better understanding the dynamics of the equatorial oceans. The main focus is on lateral and vertical mixing and how they influence the energy, momentum and tracers budgets of the large-scale circulation in the equatorial Pacific Ocean. The remainder of this introductory chapter develops the background material on which the subsequent chapters are based, and introduces the fundamental questions addressed.

0.2 Equatorial ocean circulation

Dynamically, the equatorial regions are a unique part of the ocean as a consequence of their location furthest from the axis of Earth's rotation where the angular momentum reaches a maximum. Here, the local vertical component of the rotation of the Earth, or Coriolis parameter $f = 2\Omega \sin \theta$ (Ω is the rotation rate of the Earth and θ is latitude), vanishes. Thus the Earth's rotation, a dominant factor that controls much of mesoscale and basin-scale mid-latitude circulation, exerts less of a constraint on the dynamics. There are a number of consequences of this, including the enhanced role of frictional processes and non-linear dynamics at larger scales (*McPhaden and Taft*, 1988; *Johnson and Luther*, 1994; *Qiao and Weisberg*, 1997), the unique character of equatorial internal waves (*Fedorov and Brown*, 2009; *Farrar*, 2011) and the potential role of the horizontal component of Earth's rotation in the deep ocean (*Maas and Harlander*, 2007; *Stewart and Dellar*, 2011). This thesis discusses many of these features and their consequences.

The vanishing Coriolis parameter at the equator governs the large-scale structure of the buoyancy and momentum fields in the tropics. The lower tropical atmosphere is dominated by predominant easterly trade winds that result in a surface Ekman transport to the north (south) of the wind in the Northern (Southern) Hemisphere.

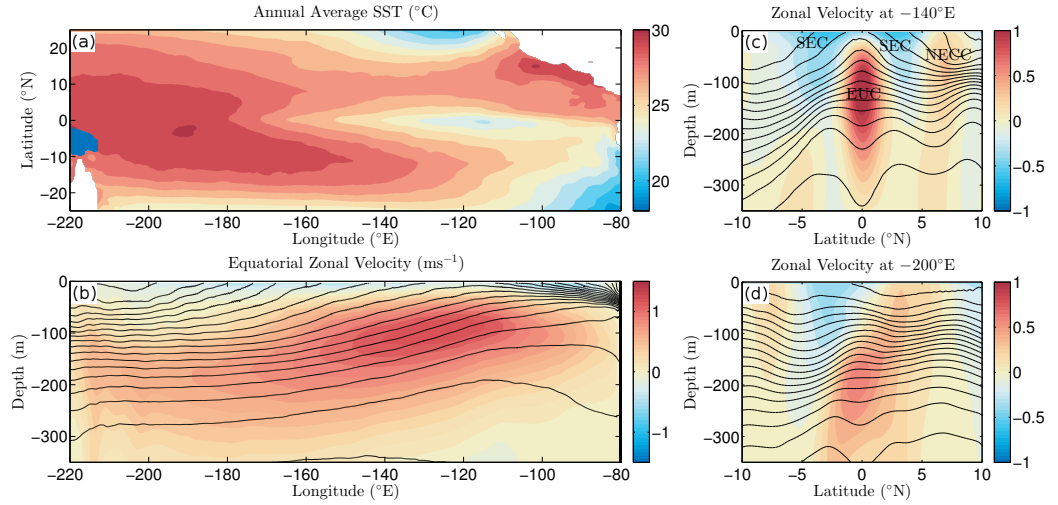


Figure 0.1: Annual average (a) SST, (b) equatorial isopycnals and zonal velocity. Zonal velocity and isopycnals at (c) 140°W and (d) 200°W . The fields are plotted from a realistic Regional Ocean Modeling Systems (ROMS) simulation with climatological forcing that accurately reproduces the observed major circulation features (see Section 1.2 for more details).

Thus the Ekman flow is divergent at the equator and drives upwelling of deeper cold water. In the Pacific Ocean, the easterly trade winds also drive warm surface water to the west within the westward-flowing surface-intensified South Equatorial Current (SEC), resulting in a thermocline that slopes upwards from below the *western warm pool* towards the *eastern cold tongue* (Fig. 0.1). The eastward Equatorial Undercurrent (EUC) driven by the sea surface slope created by the easterly winds shoals along the thermocline (Fig. 0.1b). Off the equator, the north and south equatorial fronts near $\pm 2^{\circ}$ latitude separate the cold tongue from warmer water. To the north of the equator there is also a strong eastward current known as the North Equatorial Counter Current (NECC; Fig. 0.1c). These flow features constitute the background flow of the equatorial Pacific on which interannual, seasonal and intraseasonal variability develops.

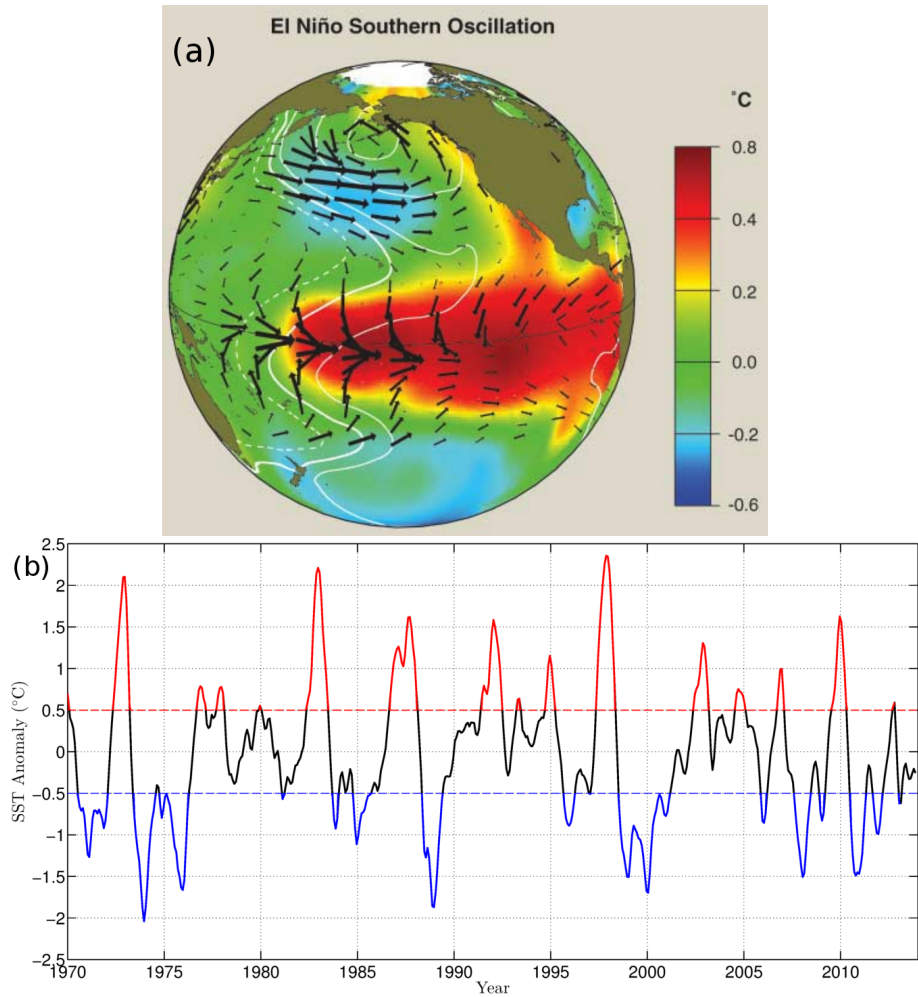


Figure 0.2: (a) The SST and wind stress anomalies associated with El Niño (From McPhaden (2015). Reprinted with permission from AAAS). The La Niña phase has opposite anomalies of SST and wind stress. (b) Time series of the Niño 3.4 index (SST averaged between -120° , -170°E and $\pm 5^{\circ}$ latitude) with El Niño (La Niña) events highlighted in red (blue). The Niño 3.4 time series data were provided by the NOAA/ESRL Physical Sciences Division, Boulder Colorado from their Web site at <http://www.esrl.noaa.gov/psd/>.

0.3 The El Niño - Southern Oscillation

While the easterly trade winds determine the structure of the the sea surface temperature (SST) in the equatorial Pacific, the zonal gradient in SST also influences the trade winds by altering the surface pressure field. This interaction gives rise to

the *Bjerknes feedback*, the central feedback process leading to the growth of ENSO events. The phase of ENSO is usually quantified by the average SST over a region in the eastern equatorial Pacific (the Niño3.4 index; Fig. 0.2b). In a La Niña the trade winds and zonal SST gradient are strong and the Niño3.4 index is anomalously cold, while an El Niño is characterized by anomalously warm eastern Pacific SSTs (Fig. 0.2a). While the linear dynamics associated with the Bjerknes feedback are well understood, the processes that cause the feedback cycle to stop and reverse are not. There are a number of conceptual theories that attempt to describe the ENSO cycle and how transitions between the different phases occur. These include theories that characterize ENSO as a self-sustained oscillation (*Picaut et al.*, 1997; *Jin*, 1997; *Wang*, 2001) and as a stable or damped mode excited by stochastic forcing from both atmosphere and ocean (*Moore and Kleeman*, 1999; *Kessler et al.*, 2003). All of these theories attempt to explain how different processes influence the *heat budget* of the upper equatorial ocean, as this governs the temporal tendency in SST. Equatorial waves in the upper ocean such as Kelvin waves are a particularly important ingredient in many of these theories (*Suarez and Schopf*, 1988; *Wang and Fiedler*, 2006), and will be considered in a later section of this introduction.

In the eastern Pacific, the mixed layer heat budget is dominated by solar radiative heating and balanced by vertical mixing which brings cold water through the base of the mixed layer (Fig. 0.3). *Moum et al.* (2013) showed that the seasonal cycle in SST in the eastern Pacific is a consequence of a seasonal cycle in vertical mixing in the upper EUC (Fig. 0.3b) as the seasonal cycle in solar radiative heating is weak in the tropics. The vertical mixing term and its variations will be discussed in more detail shortly. However, there are several other terms in the mixed layer heat budget that also play an important role. Firstly, the equatorial upwelling of cold water at the equator drives meridional overturning circulations on both sides of the equator known as the *tropical cells* (*Perez and Kessler*, 2009). Poleward flow within the surface Ekman layer is balanced by equatorward flow in the subsurface. The poleward Ekman flow crosses the fronts on either side of the cold tongue and thus drives cooling (which dominates the mean and seasonal heating in Fig. 0.3a). Finally, there are the lateral eddy stirring terms (meridional and zonal eddy heating

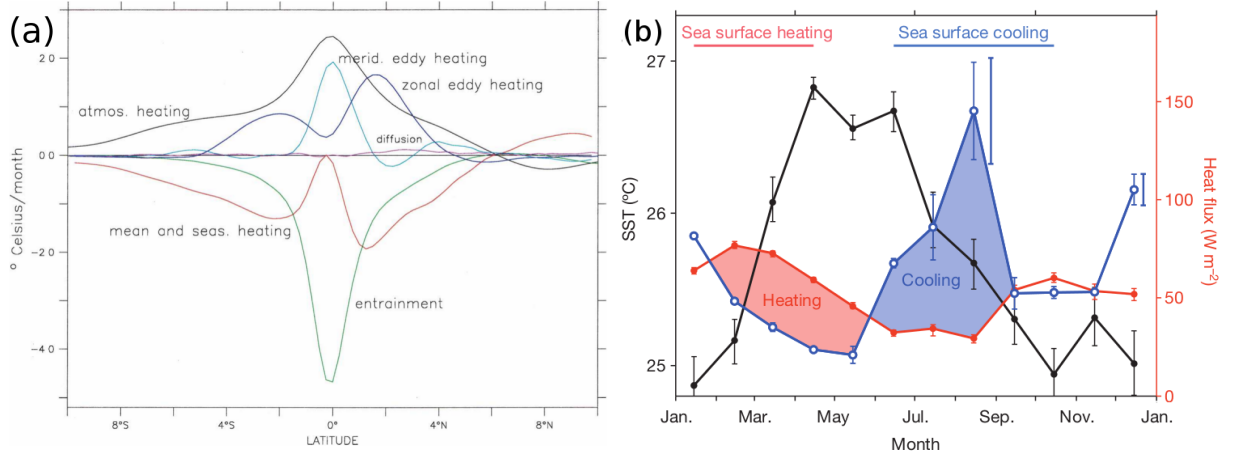


Figure 0.3: (a) Mixed layer heat budget between -145°E and -135°E in the eastern Pacific as a function of latitude from an ocean model (from *Jochum and Murtugudde (2006)* © copyright 2006 AMS). The largest terms are the warming air-sea heat flux term (atmos. heating) and the cooling vertical mixing term (entrainment). (b) Seasonal SST (black), solar radiative heat flux (red) and upper ocean turbulent heat flux (blue) from microstructure turbulence observations at 0°N , -140°E (Reprinted by permission from Macmillan Publishers Ltd: *Nature (Moum et al., 2013)*, © copyright 2013). The seasonal periods of warming and cooling are highlighted and are driven mainly by variations in the turbulent heat flux.

in Fig. 0.3b) that drive warming of the equatorial SST. In the eastern equatorial Pacific these eddy stirring terms are mainly associated with tropical instability waves (TIWs) (*Menkes et al., 2006*).

0.4 Tropical instability waves

Strong lateral and vertical shears exist between the EUC, SEC and NECC in the equatorial region and can act as energy sources for flow instabilities that generate eddies. The potential energy associated with the horizontal buoyancy gradients of the equatorial fronts can also be tapped by instabilities. When the conditions are right, both barotropic and baroclinic instabilities can grow (*Philander, 1976; Cox, 1980*). The dominant form of instability manifests as a series of westward traveling oscillations in the equatorial fronts (Fig. 0.4) with periods of $15 - 30$ days and wavelengths

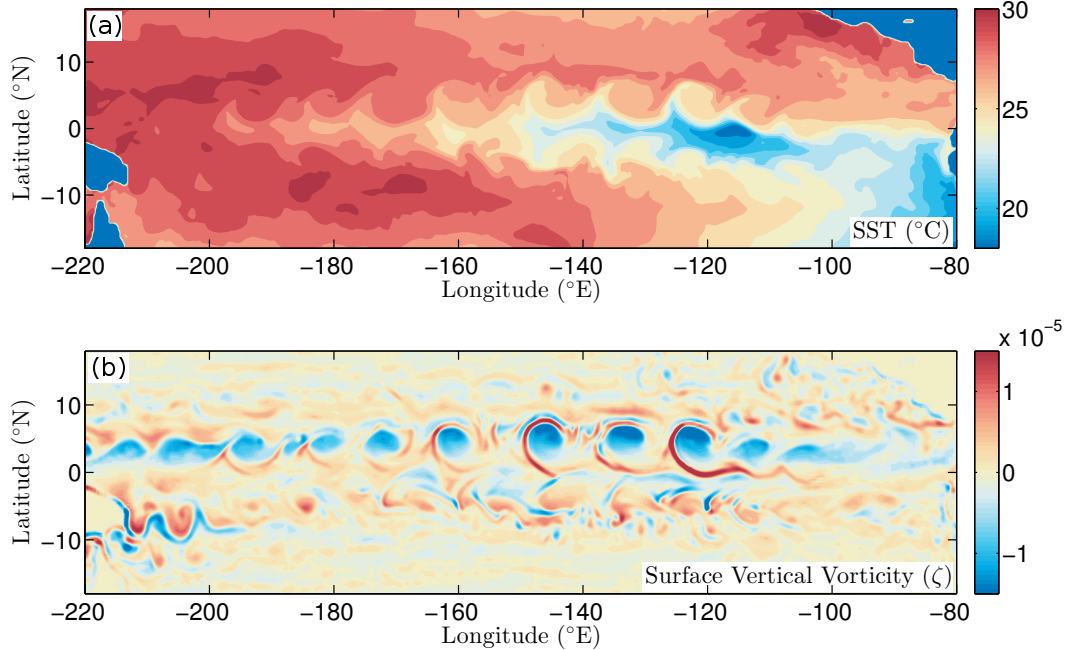


Figure 0.4: (a) SST and (b) surface vorticity $\zeta = \frac{\partial v}{\partial x} - \frac{\partial u}{\partial y}$ on the 10th of October from ROMS simulations of the equatorial Pacific. The cold cusps of westward traveling TIWs are visible along the north and south equatorial fronts and are accompanied by anticyclonic TIVs.

of 1000 – 1500km (*Legeckis, 1977; Qiao and Weisberg, 1995; Willett et al., 2006*). These oscillations are TIWs and they can develop into nonlinear tropical instability vortices (TIVs) (*Flament et al., 1996*) which spin anticyclonically (clockwise in the Northern Hemisphere). The strength of the TIW field is linked to the strength of the trade winds and they exhibit a strong seasonal cycle, developing in May-July and dying off between December and February (*Contreras, 2002*).

The strong vorticity and horizontal circulation of a TIV brings colder upwelled water northwards on its leading (western) side and warmer water southwards on its trailing (eastern) edge. This induces an equatorward eddy heat flux that acts to warm the equatorial region. The TIW lateral heat flux is the dominant process contributing to the lateral eddy heat flux in the Pacific mixed layer heat budget (Fig. 0.3, *Menkes et al. (2006); Jochum et al. (2007)*). In La Niña conditions, where the trade winds,

background circulation and correspondingly the TIWs are strongest, this equatorward heat flux is largest. But in El Niño conditions TIWs are weak and thus do not drive a strong lateral heat flux (*Yu and Liu*, 2003). Thus lateral TIW mixing constitutes a nonlinear negative feedback on the ENSO cycle, and contributes to the observed asymmetry in the ENSO cycle where El Niño's are often stronger and persist for longer than La Niña's (*An and Jin*, 2004; *An*, 2008).

TIWs are typically referred to as mesoscale eddies, in reference to their large lateral scale and apparent similarities with the canonical first-baroclinic-mode mesoscale eddies in the mid-latitudes (gulf stream eddies for example *Kang and Curchitser* (2013)). However, a number of aspects of TIW dynamics suggest that they are somewhat different. By virtue of their location close to the equator where the Coriolis parameter is small, they exhibit **high Rossby number dynamics** with the Rossby number $Ro = \zeta/f$ reaching order 1, where $\zeta = \frac{\partial v}{\partial x} - \frac{\partial u}{\partial y}$ is the vertical component of the relative vorticity, x, u is the zonal direction/velocity and y, v is the meridional direction/velocity. This is in contrast to typical mesoscale eddies in the mid-latitudes which are characterized by Rossby numbers less than 0.1 (*Chelton et al.*, 2011). By virtue of their strong vertical shears TIWs exhibit **low Richardson number dynamics** $Ri = N^2 / |\frac{\partial \mathbf{u}_h}{\partial z}|^2$, where $N^2 = \frac{\partial b}{\partial z} = -\frac{g}{\rho_0} \frac{\partial \rho}{\partial z}$ is the vertical gradient in buoyancy ($b = -\frac{g\rho}{\rho_0}$) or stratification and ρ is the potential density with reference value ρ_0 . In the mid-latitudes, the parameter regime characterized by $Ro \sim 1$, $Ri \sim 1$ is reserved for the submesoscale, with horizontal scales of 100m to 10km (*Thomas et al.*, 2008). Thus the dynamics of TIWs may have more similarities with mid-latitude submesoscale dynamics, despite their large lateral scales that would place them in the mesoscale regime. However, there are also several aspects of TIWs that differ from mid-latitude submesoscale dynamics. Firstly, unlike mid-latitude submesoscale flows geostrophy (the balance between Coriolis and pressure gradient forces, $f\hat{\mathbf{k}} \times \mathbf{u} = -\frac{1}{\rho_0} \nabla P$, where $\hat{\mathbf{k}}$ is the vertical unit vector and P is pressure) may not dominate the dynamics of the background flow on which the submesoscale phenomena develop at the equator. Also, the meridional gradient in the planetary vorticity $\beta = \frac{\partial f}{\partial y}$ is a maximum at the equator and f changes significantly over the meridional extent of the TIW field. This introduces a strong constraint on the vertical vorticity budget of the fluid in the TIW

region that is not present for submesoscale flows in the mid-latitudes. In Chapter 1 we explore the vorticity dynamics of TIWs and investigate the consequences of some of these dynamical constraints for their lateral circulation and behavior.

In addition to their influence on SST, TIWs also affect the distribution of chlorophyll, nutrients and organisms in the upper ocean (*Menkes et al.*, 2002). In energetic seasons, TIWs are thought to have a negative total effect on biological production in the equatorial region as they extract nutrient-rich upwelled water and replace it with nutrient-poor water (*Evans et al.*, 2009). Biological activity is also strongly affected by the sharp fronts in the TIW region due to their convergence and energetic vertical circulation (*Yoder et al.*, 1994). The frontal dynamics associated with these sharp fronts and the processes through which they form are not well understood. It is not clear how the well established theories of frontogenesis in the mid-latitudes (*Hoskins and Bretherton*, 1972; *Hoskins*, 1982) apply to fronts in the equatorial region where the Coriolis parameter is small. In Chapter 1 we explore several new aspects of TIW frontal dynamics including their frontal force and torque balances. We also examine the formation, dynamics and dissipation of very sharp gravity currents that have been observed in the area and are thought to form from TIW fronts.

0.5 Turbulence and vertical mixing in the upper EUC

As discussed above, small-scale vertical mixing in the upper equatorial ocean is a critical component of the mixed layer heat budget (Fig. 0.3). The convergent vertical flow driven by equatorial upwelling drives enhanced vertical gradients in horizontal velocity and buoyancy near the surface in the eastern Pacific. As a consequence, the Richardson number in the upper EUC is low, sitting around the critical value for Kelvin-Helmholtz instability of 1/4 for much of the year (*Smyth and Moum*, 2013). The flow here is in a state of marginal stability induced by the growth of shear instability for $Ri < 1/4$ that acts to reduce the vertical gradients in velocity and buoyancy ultimately raising the Richardson number back above 1/4. As part of this

process heat is fluxed downward resulting in cooling of the mixed layer and SST.

Several recent sets of observations show that the intensity of turbulence and the vertical heat flux in the upper EUC varies greatly with TIW phase (*Lien et al.*, 2008; *Moum et al.*, 2009; *Inoue et al.*, 2012). As the flow is often marginally stable, small variations in shear and stratification can drive large variations in the turbulent heat flux and thus the SST. *Inoue et al.* (2012) observed variations in the turbulent heat flux of several orders of magnitude with TIW phase, associated with variations in shear and stratification (Fig. 0.5). *Moum et al.* (2009) observed turbulent mixing associated with TIWs that drove rapid surface cooling of $1 - 2^{\circ}\text{C/month}$. However, none of these previous studies have been able to establish the fundamental mechanism leading to these variations in detail. Understanding the basic process is critical in order to understand the role of TIWs in the mixed layer heat budget. While TIWs are normally thought to provide an overall warming influence on the budget through their lateral heat flux (Fig. 0.3, *Menkes et al.* (2006)), it is possible that their modifications of the vertical heat flux drive a net cooling that counteracts their lateral warming. In Chapter 2 we investigate which aspects of the TIW flow drive modulation in turbulence and what the net influence is on the turbulent heat flux.

0.6 Equatorial waves

One important process through which the equatorial ocean adjusts to perturbations in wind stress associated with ENSO is through the radiation of equatorial waves (*Picaud et al.*, 1997; *Suarez and Schopf*, 1988; *Wang and Fiedler*, 2006). The mid-latitude Rossby and coastal Kelvin waves have analogous equatorial Rossby and Kelvin waves that propagate only along the equator. These waves play a key role in ENSO events by quickly transmitting energy and heat across the Pacific Ocean providing a non-local influence on the SST budget.

Equatorial waves are trapped within the *equatorial wave guide* near the equator as a consequence of the gradient in the planetary vorticity β . The trapping can be understood by considering the classical dispersion relation for gravity waves in the

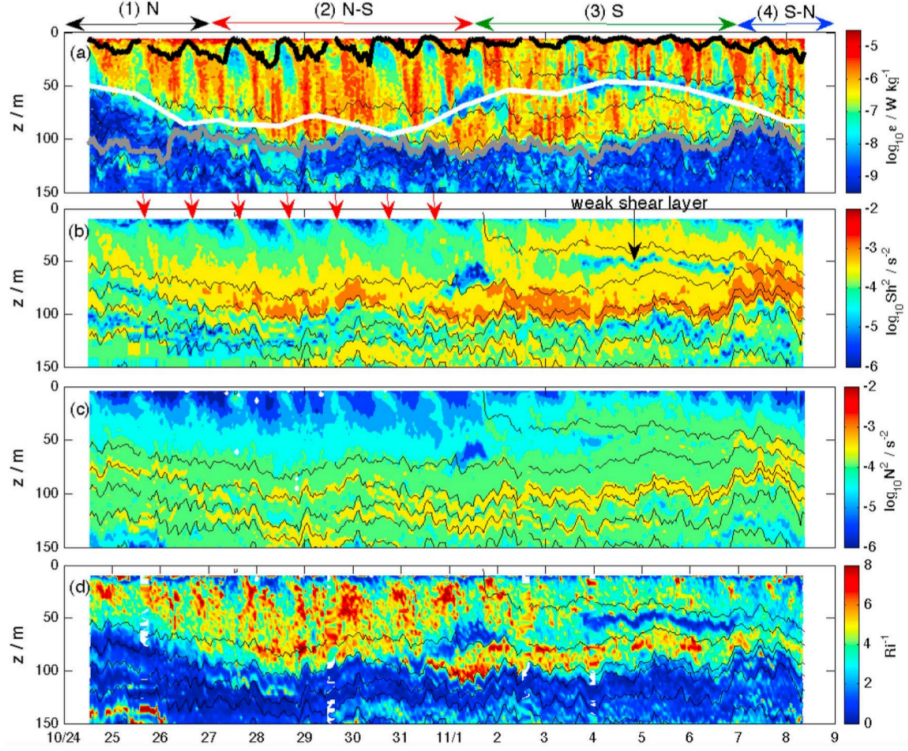


Figure 0.5: Depth-time plot of (a) turbulent kinetic energy dissipation ϵ , (b) total shear squared, (c) stratification and (d) inverse Richardson number from microstructure turbulence observations at 0°N , -140°E (from Inoue et al. (2012), reproduced with permission from the American Geophysical Union)). Order of magnitude variations in turbulence occur with TIW phase (the direction of the TIW meridional velocity is indicated above a), associated with variations in the Richardson number (d).

ocean (e.g. Gill (1982)),

$$\omega^2 = f^2 + N^2 \alpha^2, \quad (0.1)$$

where ω is the wave frequency and $\alpha = l/m$ is the aspect ratio of the wave (l and m are the horizontal and vertical wavenumbers respectively). In the majority of the ocean $N^2 \gg f^2$ and thus the minimum frequency of internal waves is the inertial frequency $\omega = f$. Since f is small at the equator, very long period waves can exist there. However, they cannot exist poleward of their *inertial latitude*, where

$\omega = f$. Low-frequency waves traveling meridionally will reflect from the inertial latitudes back on themselves and ultimately form *meridional modes*, which have a set meridional structure and extent but only propagate zonally. Different flavors of equatorial waves have different meridional modes. The main flavors include the eastward-propagating non-dispersive equatorial Kelvin wave that has zero meridional velocity, the first-meridional-mode Yanai or mixed Rossby-gravity wave that has eastward energy propagation and either eastward or westward phase speed, the high-frequency equatorial gravity waves and both short and long low-frequency equatorial Rossby waves (Gill, 1982).

In the equatorial Pacific, equatorial Kelvin waves are one of the largest sources of intraseasonal variability in subsurface temperature and velocity (McPhaden and Taft, 1988; McPhaden, 2002). Dominant 60 – 90 day frequency downwelling Kelvin waves are typically generated by westerly wind bursts (WWBs) in the western Pacific caused by tropical cyclones, the Madden-Julien Oscillation and/or other sources of atmospheric variability (Hendon *et al.*, 1998; Zhang, 2001). The downwelling Kelvin waves travel eastwards with a typical phase speed of 2.7ms^{-1} (Cravatte *et al.*, 2003) driving the surface zonal velocities eastward and the thermocline downwards. The subduction of the thermocline results in a reduction in the vertical turbulent heat flux as the stratification and vertical gradients in velocity are reduced (Lien *et al.*, 1995). Combined with the anomalous eastward advection of warm SST from the west, this drives in a warming of the SST in the eastern Pacific, initiating changes in the air-sea interaction and potentially the Bjerknes feedback (Bergman *et al.*, 2001). If these feedbacks kick in strongly enough, which typically depends on the background state of the thermocline and winds and the strength of the WWB and Kelvin wave, then this process can initiate an El Niño event. Therefore understanding how equatorial Kelvin waves propagate, their energetics and how they influence the different components of the SST budget in the eastern Pacific is important in order to better understand and predict ENSO events.

Not only do Kelvin waves influence the vertical mixing and mean advection components of the SST budget, they may also influence eddy mixing by altering the TIW

field. A number of previous studies have briefly discussed possible interactions between Kelvin waves and TIWs (*Harrison and Giese*, 1988; *Qiao and Weisberg*, 1998; *Lengaigne et al.*, 2013). First-hand observations of this interaction were obtained during a research cruise on the R/V Oceanus to the eastern Pacific during November and December 2014. During this cruise, we were interested in observing TIW fronts (observations that motivated the gravity current material in Section 1.10) and were using satellite SST data to make predictions for when we would cross fronts. However, these predictions were based on the assumption that the TIWs were traveling with a constant phase speed when they were in fact slowing down. During a 20-day period in late November the TIW field underwent a strong reduction in amplitude and phase speed, as measured by the meridional extent of the fluctuations in the north equatorial front using satellite SST data (Fig. 0.6a-c). This decay in the TIW field occurred as a downwelling Kelvin wave arrived from the western Pacific (Fig. 0.6d). Kelvin waves alter the lateral velocity shear and buoyancy gradients of the background flow, from which the TIWs gain their energy. In Chapter 3 we investigate how both upwelling and downwelling Kelvin waves alter the TIW energy budget, with implications for the lateral mixing term in the SST budget.

The generation of equatorial waves by TIWs themselves may play an important role in the TIW energy budget. TIWs gain energy from both the lateral shear and horizontal buoyancy gradients of the background flow. Their energy saturates when these energy source terms are equal in magnitude to their energy sinks. In Chapter 3 we show that the two main sink terms are associated with (1) small-scale frictional processes and (2) the radiation of energy away from the TIWs as internal waves. The radiation of barotropic Rossby waves away from TIWs in the meridional directions was established in altimetry observations by *Farrar* (2011), and he suggested that they may play a role in connecting the tropical oceans to the subtropics. TIWs are also thought to radiate energy downwards in the form of high-frequency internal waves (*Tanaka et al.*, 2015) and equatorially trapped Yanai and Rossby waves (*Cox*, 1980; *Masina et al.*, 1999). Downward-propagating equatorial Yanai and Rossby waves in particular have been observed in a number of studies below the thermocline in the equatorial oceans (*Harvey and Patzert*, 1976; *Weisberg and Horigan*, 1981;

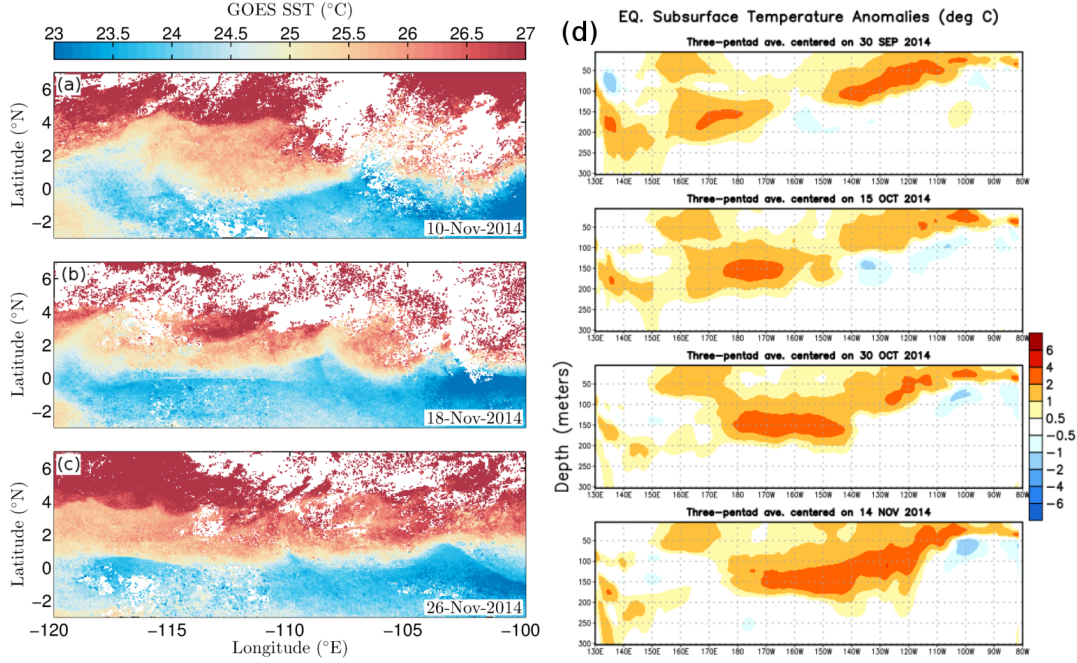


Figure 0.6: Geostationary Operational Environmental Satellites (GOES) SST observations in the eastern equatorial Pacific on the (a) 10th (b) 18th and (c) 26th of November 2014 showing a rapid decrease in the amplitude of the TIW-driven meridional oscillations in the north equatorial front. (d) Upper equatorial heat anomalies between September and November 2014 showing a downwelling equatorial Kelvin wave propagating into the eastern Pacific. The decay of the TIW field corresponds to the arrival of the downwelling Kelvin wave. The image in (d) was provided by the NOAA/NWS Climate Prediction Center, College Park Maryland from their Web site at <http://www.cpc.ncep.noaa.gov/>). The GOES SST data (a-c) was obtained from the JPL Physical Oceanography DAAC (NOAA/NESDIS, 2003).

(*Eriksen and Richman, 1988; Brandt and Eden, 2005; Smyth et al., 2015*). However, the ultimate fate of their energy is not well known. Some studies have suggested that they play a role in generating the deep equatorial jets between 500m and 1000m depth through wave-mean flow interactions (*McCreary, 1984; Ponte, 1988; Ascani et al., 2010*). It is also possible that they propagate to greater depths and generate mixing in the abyssal ocean, thus contributing to the upwelling of deep water as part of the meridional overturning circulation.

0.7 Mixing in the abyssal equatorial oceans

The global overturning circulation consists of two main cells, an upper cell that involves sinking in the North Atlantic and an abyssal cell with sinking next to Antarctica (Fig. 0.7, *Lumpkin and Speer* (2007)). Much of the upwelling in the upper cell is thought to occur adiabatically through Ekman suction in the Southern Ocean (*Marshall and Speer*, 2012). In contrast, the abyssal cell is closed through diapycnal upwelling in the interior (*Nikurashin and Vallis*, 2012). Inverse model calculations suggest that much of this diapycnal upwelling occurs in the tropical regions (*Lumpkin and Speer*, 2007). However, there are very few direct microstructure measurements of mixing in the abyssal tropical oceans (*Waterhouse et al.*, 2014) and thus mixing estimates here rely on parameterizations (*Gregg*, 1989; *Gregg et al.*, 2003; *Kunze et al.*, 2006) that are not necessarily accurate or well tested close to the equator. In Chapter 4 we present new full-depth direct microstructure measurements of mixing on and near the equator in the eastern Pacific that help to address this deficiency in measurement coverage.

The mixing that drives the diabatic upwelling of deep water within the meridional overturning circulation is thought to require $\sim 2\text{TW}$ of energy supplied in roughly equal proportions by the tides and winds (*Munk and Wunsch*, 1998; *Wunsch and Ferrari*, 2004). Much previous work has focused on the generation of internal tides through tidal interactions with rough topography (*St. Laurent and Garrett*, 2002; *Kunze et al.*, 2006; *Garrett and Kunze*, 2007) and their subsequent breaking through a non-linear downscale cascade of internal wave energy (*Gregg*, 1989; *Sun and Kunze*, 1999). The generation of lee waves by geostrophic flow (which is itself driven by the winds) over topographic features, particularly in the Southern Ocean, has also received attention (*Nikurashin and Ferrari*, 2010; *Nikurashin et al.*, 2013). *Nikurashin and Ferrari* (2013) estimated the flux of energy converted to internal tides and lee waves in the global ocean, showing that the largest fluxes occur over rough topography near the mid-ocean ridges and in the Southern Ocean (Fig. 0.8). For the eastern Pacific region near 0°N , -110°E considered in Chapter 4, the generation of internal tides is particularly weak (Fig. 0.8a near 0°N , -110°E , also see *St. Laurent and*

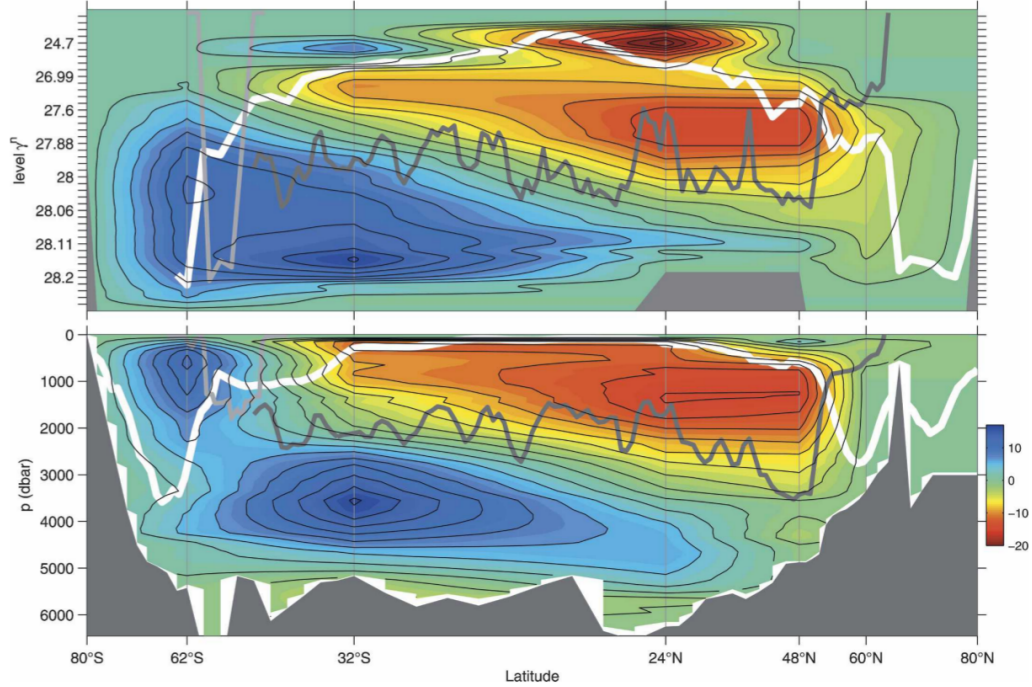


Figure 0.7: The global meridional overturning circulation in (top) density and (bottom) depth space from an inverse model of the ocean circulation (from *Lumpkin and Speer (2007)* © copyright 2007 AMS). The white line indicates typical winter mixed layer depths, the dark gray line the average depth of mid-ocean ridges and the light gray line the depth of Drake Passage.

Garrett (2002)). However, there is some lee wave generation here despite the fact that the topography is relatively smooth (Fig. 0.8b near 0°N , -110°E). Theory suggests that lee waves can be generated over topography with long length scales near the equator because f is small (*Nikurashin and Ferrari, 2011*). Observations in this region are required to confirm this prediction and establish whether lee waves do indeed play a role.

In addition to lee waves, the downward-propagating equatorial waves discussed in the previous section also constitute a potential energy source for mixing the deep equatorial ocean. There are several mechanisms through which these waves could amplify, become unstable and drive mixing. Firstly, the horizontal component of Earth's rotation is known to create internal wave attractors in the deep ocean that

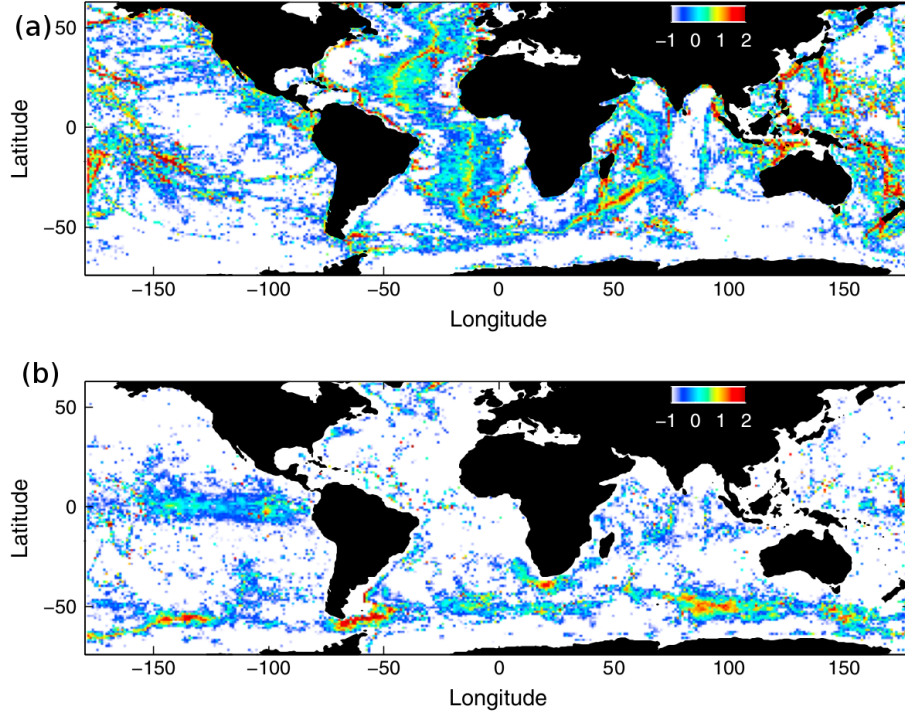


Figure 0.8: Estimates of the flux of energy converted from the (a) barotropic tide to internal tides and from (b) geostrophic flows to lee waves in the global ocean (from *Nikurashin and Ferrari* (2013), reproduced with permission from the American Geophysical Union).

can potentially drive amplification, breaking and mixing (*Gerkema and Shrira*, 2005; *Maas and Harlander*, 2007; *Winters et al.*, 2011). The wave attractors are located close to the seafloor near the internal wave's inertial latitude. Thus low-frequency downward-propagating equatorial waves could drive seafloor-intensified mixing quite close to the equator. A second mechanism is the growth of inertial instability, thought to play a role in mixing the upper equatorial oceans (*Hua et al.*, 1997; *Richards and Edwards*, 2003). As the angular momentum of a motionless fluid is maximum at the equator, it is relatively easy to create a gradient in angular momentum that is the opposite sign to f (the stability condition for inertial instability, *Dunkerton* (1981)) through wave-driven displacements of fluid away from the equator. In Chapter 4 we investigate both of these mechanisms in more detail in an attempt to explain our equatorial deep mixing observations. The downward-propagating equatorial waves

which supply the energy for mixing through these mechanisms are themselves generated at the surface ultimately by the winds. Thus the mechanisms discussed here are one way in which wind energy can drive mixing in the abyssal equatorial ocean and, if found to be important, have implications for our understanding of the global overturning circulation.

Chapter 1

Tropical Instability Wave Vorticity Dynamics and Fronts

RYAN M. HOLMES AND LEIF N. THOMAS

Earth System Science, Stanford University, Stanford, California

LUANNE THOMPSON AND DAVID DARR

School of Oceanography, University of Washington, Seattle, Washington

Tropical instability vortices (TIVs) in the equatorial Pacific exhibit energetic horizontal and vertical circulation characterized by regions of high Rossby number and low Richardson number. Their strong anticyclonic vorticity and vertical shear can influence the broader scale circulation by driving lateral mixing and vertical exchange between the ocean surface and interior. We use a set of nested high-resolution simulations of the equatorial Pacific, with a finest grid size of 3km, to examine the vortex dynamics associated with TIV core water formation. TIV cores are characterized by low values of the Ertel potential vorticity (PV) as the relative vorticity is anticyclonic with magnitude comparable to the local Coriolis parameter. A study of the variation of PV and other scalars along Lagrangian fluid parcel tracks entering the TIVs shows that the low PV water in their

cores is a mix of Equatorial Undercurrent (EUC) water and North Equatorial Counter Current (NECC) water. The EUC water is characterized by strong horizontal vorticity, and thus the baroclinic component of the PV is non-negligible and acts as a source for the anticyclonic vorticity of TIVs. This horizontal vorticity is tilted by an ageostrophic secondary circulation associated with strain induced frontogenesis that tends to form along the path of the EUC water that enters the vortex. Frontogenesis disrupts the cyclogeostrophic balance of the frontal flow and drives differential vertical motions across the front. These results emphasize the role of submesoscale physics in the equatorial region, which are active when both the Rossby and Richardson numbers are $\mathcal{O}(1)$.

The material in the majority of this chapter (Sections 1.1-1.9) has been reproduced from *Holmes et al.* (2014) © copyright 2014 AMS, with the authors and abstract reproduced above. Additional material not in *Holmes et al.* (2014) has been included in Sections 1.3.2 and 1.7 and marked with a star. In addition, Section 1.10 contains a study of the emission of gravity currents by tropical instability waves, material that has not yet been published in the literature.

1.1 Introduction

The mean circulation in the upper equatorial Pacific comprises a series of alternating zonal jets and north and south equatorial temperature fronts on either side of the eastern Pacific cold tongue (*Johnson et al.*, 2001; *De Szoeke et al.*, 2007). The strong lateral and vertical shears between these different flow components can be unstable to barotropic and baroclinic instability (*Philander*, 1976; *Cox*, 1980). The dominant mode of instability manifests as a series of westward traveling meridional oscillations in the equatorial fronts with observed wavelengths of 1000 – 1500km and periods of 15 – 36 days (*Legeckis*, 1977; *Qiao and Weisberg*, 1995; *Willett et al.*, 2006). These tropical instability waves (TIWs) can evolve into nonlinear anticyclonic tropical instability vortices (TIVs) which are only observed routinely to the north of the equator (*Yu et al.*, 1995). The vortices have radii of 500km centered around 4 – 5°N, velocities

stronger than 1ms^{-1} and travel westward at phase speeds of order 0.3ms^{-1} (*Flament et al.*, 1996; *Kennan and Flament*, 2000).

The strong vertical vorticity and associated horizontal circulation of an individual TIW or TIV brings colder upwelled water northwards on its leading (western) side and warmer water southwards on its trailing (eastern) side (*Hansen and Paul*, 1984). This induces an equator-ward eddy heat flux that may influence the heat budget of the equatorial region (*Menkes et al.*, 2006), with implications for the ENSO cycle (*Vialard et al.*, 2001; *Yu and Liu*, 2003). TIWs and TIVs have been found to modulate vertical mixing in the high shear layer above the EUC core (*Lien et al.*, 2008; *Moum et al.*, 2009; *Inoue et al.*, 2012), which also has a strong influence on the equatorial heat budget (*Moum et al.*, 2013).

Much of past research on TIW and TIV dynamics has focused on stability analysis and energetics. Perturbations on a zonally and temporally independent background flow can extract energy from the background meridional shear (barotropic source), background meridional buoyancy gradient (baroclinic source) and background vertical shear (vertical shear production source) (see for example *Proehl* (1996)). Early work concluded that the barotropic source constituted the main energy source for TIWs (*Philander*, 1976, 1978; *Hansen and Paul*, 1984; *Qiao and Weisberg*, 1998). Baroclinic instability associated with the potential energy in the equatorial SST fronts was also thought to contribute (*Cox*, 1980; *Yu et al.*, 1995). More recent work has detailed the spatial distribution and relative importance of these energy source terms (*Luther and Johnson*, 1990; *Masina et al.*, 1999; *Jochum and Malanotte-Rizzoli*, 2004; *Johnson and Proehl*, 2004; *Grodsky et al.*, 2005; *Lyman et al.*, 2007).

In the case of TIVs, these instabilities result in the generation and/or accumulation of anticyclonic vorticity within the vortex core. TIVs exhibit high vorticity Rossby number ($Ro = \zeta/f$, where $\zeta = \frac{\partial v}{\partial x} - \frac{\partial u}{\partial y}$ is the vertical relative vorticity and f is the Coriolis parameter) dynamics with core water characterized by vorticity Rossby numbers reaching -1 (*Kennan and Flament*, 2000), and thus they have close to zero absolute vorticity and anomalously low potential vorticity (PV). The vortex dynamics leading to the generation and accumulation of their strong anticyclonic

relative vorticity has so far received little attention. *Foltz et al.* (2004) used a layer-averaged PV to show that changes in the relative vorticity of water inside Atlantic TIVs were due to advection of relative and planetary vorticity. However, in not using the full Ertel PV defined here as¹

$$q = \boldsymbol{\omega} \cdot \nabla b = \underbrace{(f + \zeta)N^2}_{q_v} + \underbrace{\boldsymbol{\omega}_h \cdot \nabla_h b}_{q_h}, \quad (1.1)$$

they did not consider how horizontal density gradients and vertical shear, encompassed in the baroclinic component q_h , affect the PV and influence the vortex dynamics. The baroclinic component q_h associated with the baroclinicity of the flow can be important relative to the vertical component q_v associated with the absolute vertical vorticity when the Richardson number ($Ri = N^2 / |\frac{\partial \mathbf{u}_h}{\partial z}|^2$, with N^2 the vertical buoyancy gradient or stratification and \mathbf{u}_h the horizontal velocity) of the flow is low. Indeed, *Inoue et al.* (2012) show that TIVs are associated with $\mathcal{O}(1)$ Richardson numbers near the equator in the EUC shear layer, justifying an examination of the vortex dynamics of Pacific TIVs using the full version of the Ertel PV (Eq. (1.1)).

In the mid-latitudes, the $\mathcal{O}(1)$ Rossby and Richardson number regime defines submesoscale flows, with typical horizontal scales 100m-10km (*Thomas et al.*, 2008). Thus, TIVs contain a range of flow features normally associated with mid-latitude submesoscale physics such as strong fronts, vertical velocities, ageostrophic flows and frontogenesis (*Marchesiello et al.*, 2011; *Ubelmann and Fu*, 2011). In particular, they share features in common with submesoscale coherent vortices and intrathermocline eddies (ITEs), i.e. lenticular coherent anticyclonic vortices that are found in the thermocline and that are characterized by water in their cores that has anomalously low PV (*Dugan et al.*, 1982; *McWilliams*, 1985; *Kostianoy and Belkin*, 1989).

The core water in TIVs and fully formed ITEs is characterized by anomalously low values of PV due to near zero absolute vorticity (*Kennan and Flament*, 2000) and low stratification. Following *Thomas* (2008) we refer to this flavor of low PV as

¹In Eq. (1.1), $b = -g\rho/\rho_0$ is the buoyancy, g is acceleration due to gravity, ρ is the density and ρ_0 a reference density. $\boldsymbol{\omega} = f\hat{\mathbf{k}} + \nabla \times \mathbf{u}$ is the absolute vorticity, with vertical component $f + \zeta$ and horizontal component $\boldsymbol{\omega}_h$ and $\hat{\mathbf{k}}$ is the local vertical unit vector.

vortically-low PV. A second flavor of low PV water can occur in the presence of strong horizontal buoyancy gradients at fronts, where the PV can be *baroclinically-low* due to the baroclinicity of the flow. For a 2D front in geostrophic and hydrostatic balance, the thermal wind relation is given by

$$\nabla_h b = f \frac{\partial \mathbf{u}_g}{\partial z} \times \hat{\mathbf{k}} = -f \boldsymbol{\omega}_h. \quad (1.2)$$

The baroclinic PV component associated with this flow is,

$$q_{hg} = \boldsymbol{\omega}_h \cdot \nabla_h b = -\frac{|\nabla_h b|^2}{f}, \quad (1.3)$$

which is negative definite in the Northern Hemisphere, and thus this component always decreases the PV. Baroclinically-low PV water is common at submesoscale fronts in the mid-latitudes where the inverse geostrophic Richardson number, obeying the relation $Ri_g^{-1} = \frac{q_{hg}}{fN^2}$, is $\mathcal{O}(1)$ and thus the baroclinic component q_h is strongly negative and compensates the vertical component q_v .

One proposed generation mechanism for ITEs involves the subduction of parcels of baroclinically-low PV water generated at a submesoscale front (*Thomas*, 2008). The subduction can be driven by the strong vertical velocities associated with frontogenesis (*Spall*, 1995). As these subducting parcels of water with $q \approx 0$ follow sloped isopycnals into the thermocline, their horizontal buoyancy gradient decreases, q_h moves towards zero and thus conservation of total PV implies that q_v must also move towards zero. The parcel of water undergoes baroclinically-low to vortically-low *PV conversion*. The horizontal vorticity of the baroclinic frontal flow acts as a source for the anticyclonic vorticity of the developed ITE through vortex tilting (*Thomas*, 2008).

The low Richardson numbers associated with TIVs near the equator suggests that the baroclinic component of the PV may be substantial and, similar to ITEs and submesoscale flows, may play a roll in the vortex dynamics of TIV core water formation. This is in contrast to mesoscale eddies in the mid-latitudes with similar horizontal scales as TIVs ($\sim 500\text{km}$), where q_h is negligible in comparison to q_v . However, the large meridional scale of a TIV implies that it is influenced by the

gradient in planetary vorticity, and thus TIVs share some characteristics with both submesoscale and mesoscale flows in the mid-latitudes.

The research presented here addresses several outstanding questions relating to the dynamics of TIVs. Firstly, the vortex dynamics leading to the formation of their strong anticyclonic vorticity has not been described in detail. The low PV water forming the TIV core could be sourced through advection from the Southern Hemisphere and equatorial region (*Foltz et al.*, 2004; *Dutrieux et al.*, 2008). Low PV water could also be created locally by non-conservative processes such as friction associated with down-front winds (*Thomas*, 2005), surface cooling or isopycnal mixing. A second outstanding problem is that of the dominant force balance and the frontal dynamics associated with TIVs. The strong rotation of TIVs suggests that centrifugal and other advective effects may be important. For Atlantic TIVs, *Foltz et al.* (2004) found that centrifugal forces were up to 50% as large as geostrophic effects. Analysis of observations from a front on the leading edge of a Pacific TIV suggest that the frontal currents follow a pressure gradient-advection balance rather than geostrophic balance (*Johnson*, 1996). These departures from geostrophic balance could have implications for the detailed frontal dynamics of TIVs, and thus for the formation of their core water.

To address these questions, we use a nested simulation of the equatorial Pacific described in Section 1.2. In this section we also give a general overview of the circulation associated with TIVs. In Section 1.3 we look at the dominant momentum and torque balances of the TIV flow. In Sections 1.4 and 1.5 we examine the physics of TIVs from a new perspective using Lagrangian analysis of the PV and vortex dynamics following the methods of *Thomas* (2008) and *Ubelmann and Fu* (2011). In these sections we describe the entrance pathways and formation mechanisms of TIV core water. Finally, in Section 1.6, we examine the frontogenesis associated with TIVs, with implications for their vortex dynamics and in Section 1.7 we look briefly at the non-conservative processes occurring around these fronts. The main results are discussed and summarized in Sections 1.8 and 1.9.

1.2 Model and general flow description

1.2.1 Model setup

To examine the dynamics of TIVs, a set of 3D nested simulations of the equatorial Pacific at progressively higher resolutions was performed using the Regional Ocean Modeling System (ROMS) (*Shchepetkin and McWilliams*, 2005). A Pacific basin-wide simulation over the region -240°E to -70°E , 30°S to 30°N with 0.25° horizontal resolution, 20 vertical levels and a time step of 10 minutes was performed and spun-up over a 10-year period. Daily climatological surface forcing, initial conditions and boundary conditions were taken from the Common Ocean Reference Experiment Normal Year Forcing field (*Large and Yeager*, 2004). At the meridional boundaries temperature and salinity were nudged to climatological values, while zonal and meridional velocities were nudged to zero. In addition, monthly climatological nudging was used in order to maintain the tropical thermocline. The K-profile parametrization (KPP) vertical mixing scheme was used to parametrize sub-grid scale vertical mixing processes (*Large et al.*, 1994).

In the last year of the basin-wide simulation, a 0.05° mid-resolution simulation was nested inside over the region -145°E to -120°E , 5°S to 10°N . Finally, a 0.025° ($\sim 3\text{km}$) high-resolution simulation was nested inside the mid-resolution simulation with 40 vertical levels ($\sim 9\text{m}$ resolution in the top 100m) and a time step of 1 minute. Both inner nests have horizontal resolutions (6km and 3km respectively) below the 10km reported by *Marchesiello et al.* (2011) as required for numerical convergence as measured by an invariance of the kinetic energy spectrum with resolution. On the inner nests, a combination of nudging and radiation boundary conditions are used, with the exception of a clamped condition on the eastern boundary tracers. Horizontal diffusion of momentum is achieved through a bi-harmonic viscosity with coefficient $1 \times 10^9 \text{m}^4\text{s}^{-1}$ (high-resolution), $1 \times 10^{10} \text{m}^4\text{s}^{-1}$ (mid-resolution) and $1 \times 10^{11} \text{m}^4\text{s}^{-1}$ (basin-wide) and horizontal diffusion of salinity and temperature is achieved through a harmonic diffusion with coefficient $100\text{m}^2\text{s}^{-1}$. ROMS has been successfully used for process studies of TIWs under a similar configuration (*Marchesiello et al.*, 2011).

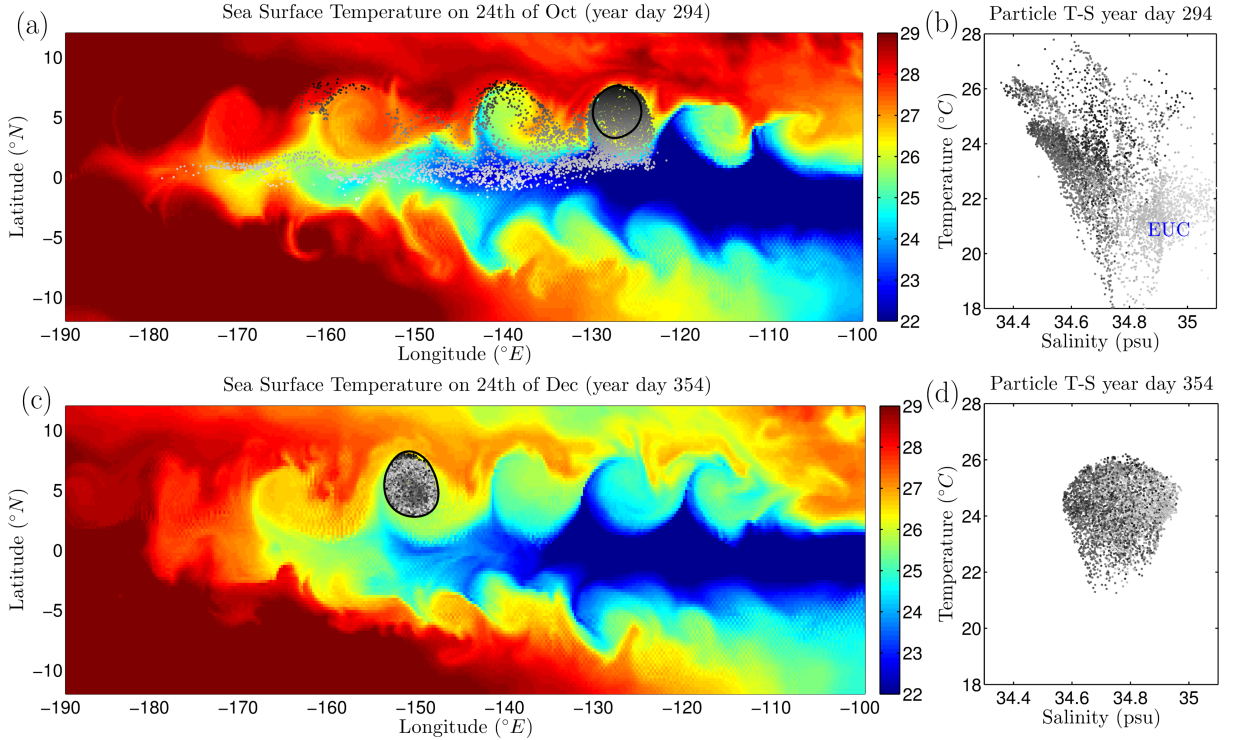


Figure 1.1: Model SST (c) and temperature-salinity diagram (d) for particles inside a TIV on the 24th of December. Model SST (a) and temperature-salinity diagram (b) for the same particles two months earlier on the 24th of October. The particles are shaded according to their latitude on the 24th of October and the TIV streamfunction contour is plotted with the black line. Water from the EUC and the NECC combine and experience significant Lagrangian changes in temperature and salinity (compare b to d) to form TIV core water. The EUC water mass, corresponding to the cold and salty water coming from more southern latitudes is indicated (b).

1.2.2 Properties of model TIVs

The simulations produce TIWs which commence around May and die-off the following January. TIWs are visible as cusps in the SST fields at the north and south equatorial fronts (Fig. 1.1) and are accompanied by anticyclonic vortices (TIVs) in the Northern Hemisphere. The properties of the model TIVs and their fronts compare favorably with the observations of *Flament et al.* (1996), *Kennan and Flament* (2000) and *Johnson* (1996) suggesting that the numerical solutions and the observations are dynamically similar, as discussed below.

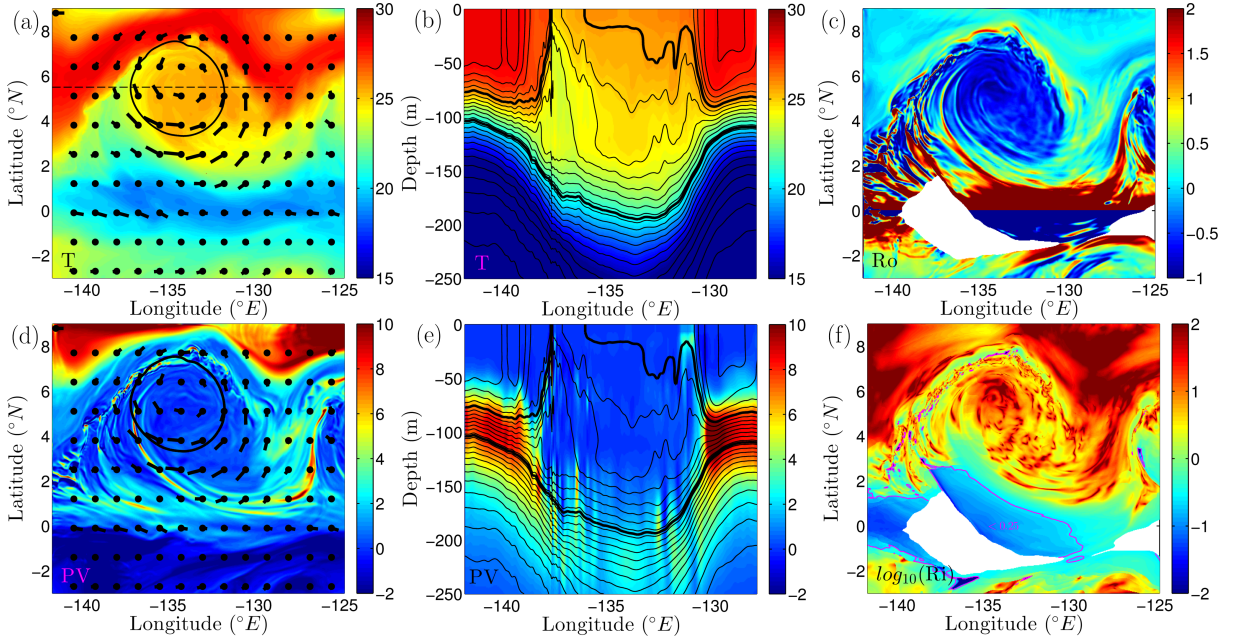


Figure 1.2: Horizontal slices of (a) temperature ($^{\circ}\text{C}$) and (d) PV ($\times 10^{-9}\text{s}^{-3}$) through a TIV at 50 meters depth in the high resolution simulation. Horizontal velocity vectors are shown with the round marker indicating the tail of the vector. For scaling, a 1ms^{-1} velocity vector is shown in the top left hand corner of panels (a) and (d). The stream-function contour enclosing a transport of $\sim 0.23\text{Sv/m}$ is also shown in (a) and (d). Vertical slices of (b) temperature and (e) PV at 5.5°N . The thin black lines represent isopycnals with a spacing of 0.3kgm^{-3} and the bold lines are the 1023 and 1024.6kgm^{-3} isopycnals bounding the TIV control volume. (c) The vorticity Rossby number ($Ro = \zeta/f$) and (f) the log of the Richardson number ($Ri = N^2/|\frac{\partial u}{\partial z}|^2$) averaged over the isopycnal layer bounded by the bold isopycnals. All plots are on the 11th of October (year day 281.2083).

For the purposes of tracking and locating TIVs, and determining whether Lagrangian particles are inside or outside TIVs, we define a control volume that covers the extent of a TIV using a surface stream-function² Ψ condition as in Dutrieux *et al.* (2008). The center of each vortex is identified as being a local minimum in the stream-function. We then define the horizontal extent of the vortex as that

²The stream-function Ψ was calculated by solving the Poisson equation $\nabla^2\Psi = -\zeta_s$, where $\zeta_s = \frac{\partial v_s}{\partial y} - \frac{\partial u_s}{\partial y}$ with (u_s, v_s) the surface velocities in the (x, y) directions, at each time using Dirichlet boundary conditions derived by integrating the conditions $\frac{\partial \Psi}{\partial y} = u_s$, $\frac{\partial \Psi}{\partial x} = -v_s$ around the perimeter of the domain.

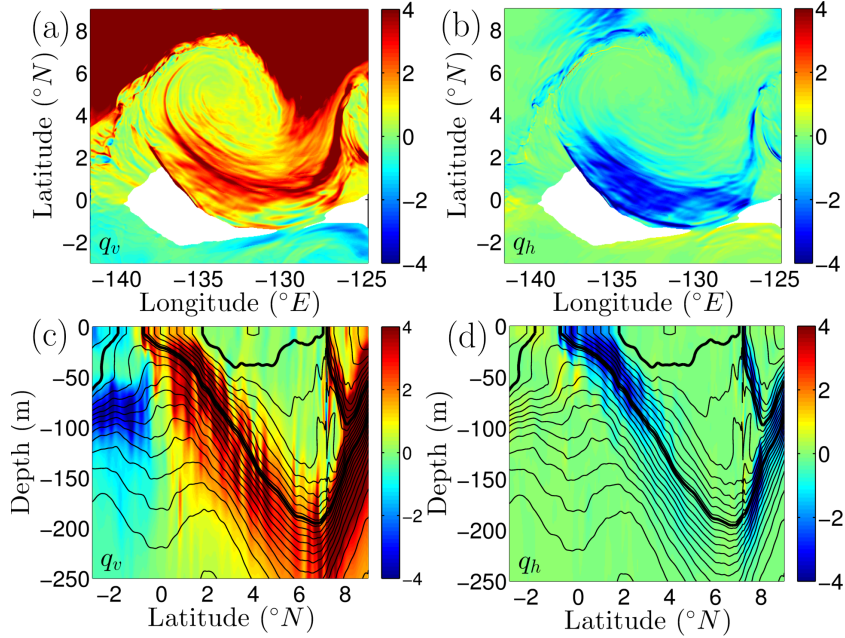


Figure 1.3: The vertical (a and c) and baroclinic (b and d) components of the PV ($\times 10^{-9}\text{s}^{-3}$) in the high-resolution simulation. The thin black lines represent isopycnals with a spacing of 0.3kgm^{-3} and the horizontal slices (a and b) are averaged over the isopycnal layer bounded by the bold 1023 and 1024.6kgm^{-3} isopycnals. The vertical slices (c and d) are at -135°E . All plots are on the 11th of October (year day 281.2083).

Ψ contour enclosing an instantaneous surface closed circulation around the vortex of $\sim 0.23 \times 10^6\text{m}^2\text{s}^{-1}$. This stream-function contour (shown in Figures 1.1a,c and 1.2a,d) is sufficient for the purposes of tracking TIVs. We define the vertical extent of the TIV using the 1023kg m^{-3} and 1024.6kg m^{-3} isopycnal surfaces (Fig. 1.2b,e).

The vortex is characterized by anticyclonic vertical vorticity of magnitude the Coriolis parameter. This is reflected in the vorticity Rossby number of order -1 (Fig. 1.2c) and near zero q_v in the vortex core (Fig. 1.3a). TIVs with vorticities of this magnitude have been observed (i.e. Fig. 15 of *Kennan and Flament (2000)*). The vortex depresses the thermocline and is associated with anomalously low stratification along isopycnal layers that are mid-thermocline to the north, east and west (Figures 1.2b and 1.3c), highlighting its similarity to an ITE (*Thomas, 2008*). The baroclinic

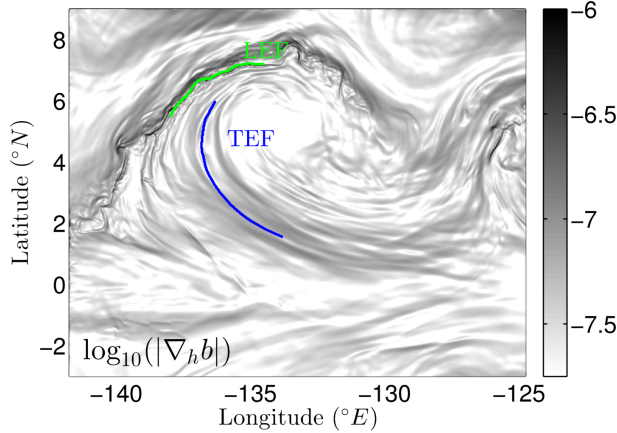


Figure 1.4: The log of the magnitude of the horizontal buoyancy gradient ($\nabla_h b$ (s^{-2})) at 50m depth in the high-resolution simulation on the 11th of October (year day 281.2083). The location of the leading edge front (LEF), defined by the position of a high PV filament at 33m depth, and the trailing edge front (TEF) defined by the outcrop location of the 1022.9kgm^{-3} isopycnal, are shown.

component of the PV q_h (Fig. 1.3b,d), tends to be negative with a magnitude comparable to that of q_v (compare Figures 1.3a to 1.3b and 1.3c to 1.3d) in regions of strong horizontal buoyancy gradients, which here are found on the western leading edge of the vortex and in the EUC shear layer to the south (Fig. 1.4). On the western edge of the vortex, cold water is advected northwards from the upwelling region through the *TIW cold cusp* region (the cusp of cold water with SST between 20 and 25°C in Fig. 1.2a at the leading edge of the vortex). The flow in this region is confluent, with the cold water moving northward and westward faster than the warmer water to its north, driving strong frontogenesis. This confluent flow intensifies the north equatorial front here producing a strong SST front at the leading edge of the cold cusp (marked LEF in Fig. 1.4) where the surface temperature changes by up to 3°C over $\sim 10\text{km}$ and rapid subduction at rates of $\sim 0.5\text{cms}^{-1}$ of the cold equatorial water occurs (consistent with the observations of *Johnson* (1996), who observed subduction rates of up to 0.9cms^{-1}). High gradients in PV and vorticity are visible across the frontal jet (Figures 1.2c,d).

On the east side of the cold cusp, the north equatorial front bends back towards the equator in the south-west corner of the TIV. Here there is a less intense front on

the trailing edge of the TIW cold cusp (marked TEF in Fig. 1.4). Filaments of low PV are entrained into the vortex through this region (Fig. 1.2d), suggesting that this region may provide a source for the water that forms the TIV core. This region is characterized by high vertical shear associated with the EUC shear layer, where the Richardson number is frequently below the critical value for vertical shear instability of 1/4 (Fig. 1.2f). The shear and Richardson number above the EUC are modulated by the presence of the TIV, in agreement with the observations of *Lien et al.* (2008). The westward surface flow induced by the southern part of the vortex over the EUC core increases the vertical shear, and thus a decrease in the Richardson number occurs at longitudes coincident with the span of the vortex (Fig. 1.2f). The vertical shear has an associated southward pointing horizontal vorticity which, when coupled with the buoyancy gradient associated with the north equatorial front, results in a large negative q_h (Fig. 1.3b), of the same order of magnitude as q_v . The importance of this store of baroclinically-low PV is discussed further in Section 31.5.

1.3 Force and torque balances of TIW flow

1.3.1 Geostrophic/cyclogeostrophic balance

The question of whether geostrophic balance and thermal wind balance are dynamical constraints at the equator is important for the frontogenesis mechanism discussed in Section 1.6. Here we calculate the percentage error in the geostrophic and cyclogeostrophic balances using the model output diagnostics. The geostrophic (GB) and cyclogeostrophic (CGB) force balances are expressed as,

$$GB : -\frac{1}{\rho_0} \nabla_h P - f \hat{\mathbf{k}} \times \mathbf{u} = 0, \quad (1.4)$$

$$CGB : -\frac{1}{\rho_0} \nabla_h P - f \hat{\mathbf{k}} \times \mathbf{u} - \text{Proj}_{\hat{\mathbf{k}} \times \mathbf{u}} (\mathbf{u} \cdot \nabla \mathbf{u}) = 0, \quad (1.5)$$

where the first term is the pressure gradient force, the second term is the Coriolis force and the third term in Eq. (1.5) is the centrifugal force, being the portion of horizontal momentum advection perpendicular to the horizontal velocity. The

projection operator is defined as $\text{Proj}_{\hat{\mathbf{b}}}(\mathbf{a}) = (\mathbf{a} \cdot \hat{\mathbf{b}}) \hat{\mathbf{b}}$, where $\hat{\mathbf{b}} = \frac{\mathbf{b}}{|\mathbf{b}|}$. The percentage error in the departure from these balances is expressed as (following a method similar to *Capet et al. (2008)*),

$$\gamma_{GB} = \frac{\left| \frac{1}{\rho_0} \nabla_h P + f \hat{\mathbf{k}} \times \mathbf{u} \right|}{\left| \frac{1}{\rho_0} \nabla_h P \right| + \left| f \hat{\mathbf{k}} \times \mathbf{u} \right|} \times 100, \quad (1.6)$$

and

$$\gamma_{CGB} = \frac{\left| \frac{1}{\rho_0} \nabla_h P + f \hat{\mathbf{k}} \times \mathbf{u} + \text{Proj}_{\hat{\mathbf{k}} \times \mathbf{u}}(\mathbf{u} \cdot \nabla \mathbf{u}) \right|}{\left| \frac{1}{\rho_0} \nabla_h P \right| + \left| f \hat{\mathbf{k}} \times \mathbf{u} \right| + \left| \text{Proj}_{\hat{\mathbf{k}} \times \mathbf{u}}(\mathbf{u} \cdot \nabla \mathbf{u}) \right|} \times 100, \quad (1.7)$$

so a 0% error indicates a perfectly balanced flow.

Geostrophic balance appears to hold throughout much of the domain at 33m depth, with percentage error mostly less than 30% for latitudes greater than $\pm 2^\circ$ (Fig. 1.5a). A notable exception to this is within the vortex, where larger errors are seen, in particular in the northern part of the vortex. The curvature throughout the vortex is high, and thus the centrifugal term becomes important. The vortex is closely in cyclogeostrophic balance (Fig. 1.5b), with only the zero-velocity center of the vortex appearing to be out of balance (an artifact of the near zero local pressure gradient force and velocity). In particular, where the flow of the vortex penetrates close to the equator, the cyclogeostrophic balance holds while the geostrophic balance breaks down (compare Figures 1.5a and 1.5b). This indicates that the strong curvature and rotation of the vortex acts to constrain the flow and provide a diagnostic force balance that would not otherwise exist at the equator. The vortex is thus responsible for the balance asymmetry around the equator, where the region between $0^\circ - 2^\circ S$ appears out of cyclogeostrophic balance while that between $0^\circ - 2^\circ N$ is more closely in cyclogeostrophic balance.

1.3.2 Thermal wind balance/gradient wind balance*

In Section 1.3.1 we examined the force balance of the TIV flow. In this section we examine the horizontal torque balance of the TIV flow and assess how well the thermal

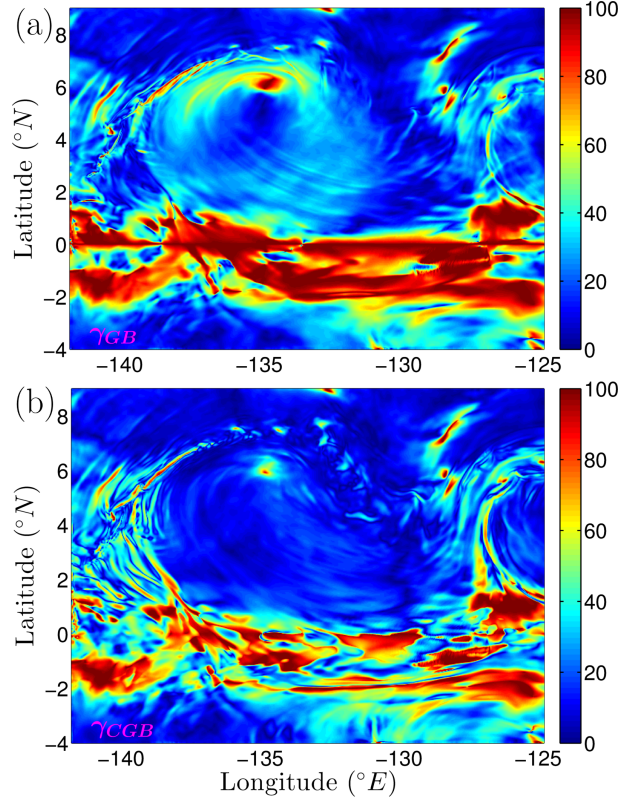


Figure 1.5: Plots of the percentage error in the geostrophic (a) and cyclogeostrophic (b) force balances at 33m depth from equations (1.6) and (1.7). The flow is closely in geostrophic balance in most regions, even within a few degrees of the equator. The regions of the flow with high curvature inside the vortex, and the region where the vortex flow penetrates over the equator are characterized by currents that are more accurately described by the cyclogeostrophic balance. The fields are evaluated on 12th October (year day 282.7917).

wind balance holds by evaluating terms in the equation,

$$\frac{\partial \omega_{\tilde{y}}}{\partial t} = -\frac{\partial b}{\partial \tilde{x}} + \frac{\partial F_{\tilde{x}}}{\partial z} + f \frac{\partial \tilde{v}}{\partial z} - \frac{\partial}{\partial z} (\mathbf{u} \cdot \nabla \tilde{u}), \quad (1.8)$$

for the stream-wise component of the vorticity $\omega_{\tilde{y}} = \frac{\partial \tilde{u}}{\partial z}$, where \tilde{y} and \tilde{v} (\tilde{x} and \tilde{u}) are the coordinate and velocity in the stream-wise (transverse) direction. If the thermal wind balance were to hold then the first and third term on the right-hand side of Eq. (1.8) would cancel and the other terms involving the frictional force in

the transverse direction ($F_{\tilde{x}}$), tilting, stretching, and advection of relative vorticity (which are encompassed in the last term in Eq. (1.8)), and the time rate of change of vorticity ($\frac{\partial \omega_{\tilde{y}}}{\partial t}$) would be negligible.

The terms in Eq. (1.8) were evaluated in the western portion of the vortex along the trailing edge front on a line defined by the outcrop of the 1022.9kgm^{-3} isopycnal (marked TEF in Fig. 1.4) as a function of latitude. A *buoyancy gradient weighted average* of Eq. (1.8) was performed, defined by the operation

$$\langle X \rangle_{BG} = \frac{1}{\int_V |\nabla_h b| dV} \int_V X |\nabla_h b| dV, \quad (1.9)$$

where X represents a term in Eq. (1.8). The volume integral was performed over segments 50km long and 50km wide along the TEF over the upper 80m of the ocean defining the volume V centered at each latitude. The stream-wise direction was defined as parallel to the horizontal velocity averaged over each segment. This gives terms,

$$TTD = \left\langle \frac{\partial \omega_{\tilde{y}}}{\partial t} \right\rangle_{BG} \quad (1.10)$$

$$BTOR = \left\langle -\frac{\partial b}{\partial \tilde{x}} \right\rangle_{BG} \quad (1.11)$$

$$FRC = \left\langle \frac{\partial F_{\tilde{x}}}{\partial z} \right\rangle_{BG} \quad (1.12)$$

$$PTLT = \left\langle f \frac{\partial \tilde{v}}{\partial z} \right\rangle_{BG} \quad (1.13)$$

$$ADV = \left\langle -\frac{\partial}{\partial z} (\mathbf{u} \cdot \nabla \tilde{u}) \right\rangle_{BG} \quad (1.14)$$

$$SCF = \left\langle \frac{\partial C_{\tilde{x}}}{\partial z} \right\rangle_{BG} \quad (1.15)$$

Where additionally SCF represents the shear in the centrifugal force,

$$\mathbf{C} = -\text{Proj}_{\hat{\mathbf{k}} \times \mathbf{u}} (\mathbf{u} \cdot \nabla \mathbf{u}) = (C_{\tilde{x}}, C_{\tilde{y}}). \quad (1.16)$$

We also split the tilting of planetary vorticity ($PTLT$) into geostrophic $PTLT_g \equiv -BTOR$ and ageostrophic $PTLT_{ag} \equiv PTLT - PTLT_g$ parts. Each of these terms

was averaged over a time period of 40 hours following the movement of the TEF to give a picture of the robust features in the stream-wise horizontal vorticity balance within the vortex (Fig. 1.6). The largest terms are the shear in the centrifugal force SCF and the tilting of planetary vorticity $PTLT$, showing that thermal wind balance is not dominant within the vortex.

If the *gradient-wind balance* were to hold, then the residual of the sum of the centrifugal force SCF , the tilting of planetary vorticity $PTLT$ and the baroclinic torque $BTOR$ would be zero. This residual ($GWR = SCF - PTLT_{ag}$ in Fig. 1.6) is around 25% of the centrifugal force and results in a small negative rate of change in vorticity TTD , with friction (FRC) accounting for the small difference between the residual and the time tendency term (compare GWR and TTD in Fig. 1.6). This rate of change of vorticity can be explained simply by the zonal propagation of the vortex and its interior features. Such a translation would give a time tendency in $\omega_{\tilde{y}}$ of $\frac{\partial \omega_{\tilde{y}}}{\partial t} = -u_s \frac{\partial \omega_{\tilde{y}}}{\partial x}$, where u_s is the zonal phase speed of the feature and x is the zonal direction. The average zonal phase speed of each vortex center (defined using the stream-function minimum) in the mid-resolution simulation is $u_s = -0.51\text{ms}^{-1}$, giving an estimate for the time tendency in vorticity ($ZPR = \langle -u_s \frac{\partial \omega_{\tilde{y}}}{\partial x} \rangle_{BG}$ in Fig. 1.6). This quantity matches the gradient-wind residual closely (compare ZPR and GWR in Fig. 1.6), showing that the gradient-wind balance holds in the translating reference frame of the TIV.

1.4 Lagrangian analysis of TIV core water formation

In order to investigate the source of the low PV core water we performed Lagrangian particle track calculations. The TIV cores in the basin-wide and mid-resolution simulations were seeded throughout the season with Lagrangian particles with 5m vertical spacing and grid-resolution horizontal spacing. The particles were then advected offline backwards in time for several hundred days in the basin-wide simulation and two months in the mid-resolution simulation to determine their source regions. The

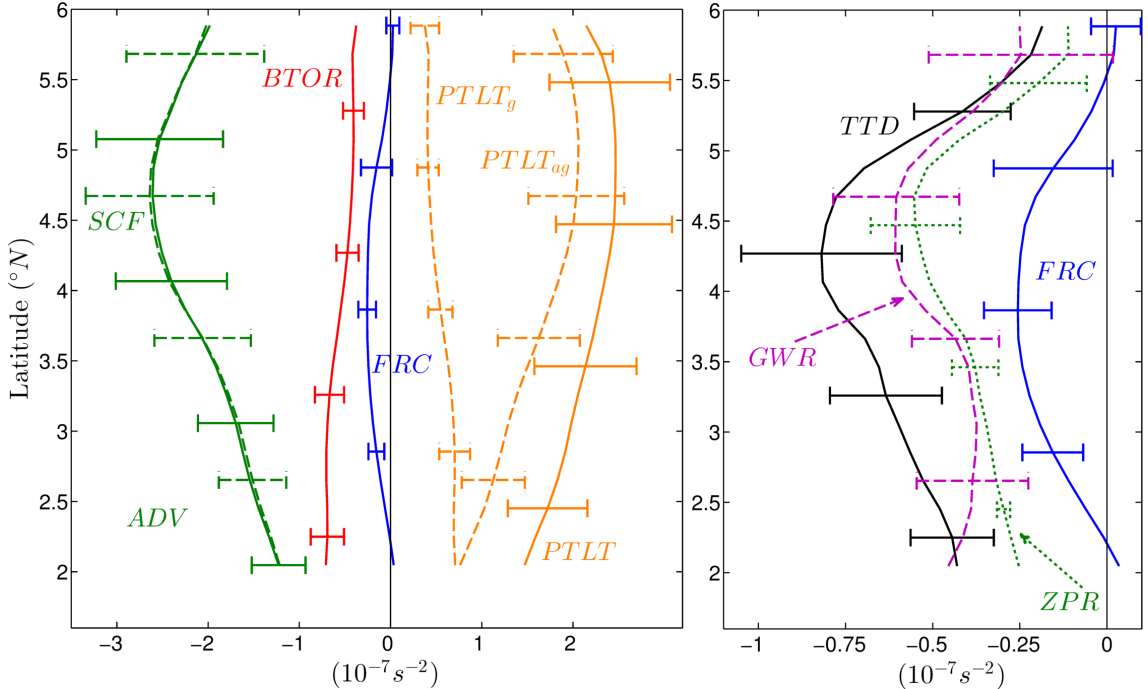


Figure 1.6: Terms in the stream-wise vorticity equation (Eq. (1.8)) as a function of latitude along the trailing edge front (TEF in Fig. 1.4). Each term is buoyancy gradient weighted averaged (according to Eq. (1.9)) over a volume $50\text{km} \times 50\text{km} \times 80\text{m}$ centered on the TEF. A time composite average is also performed over a period of 40 hours following the movement of the TEF, with the error bars representing the ± 1 standard deviation over this time period. The terms are from Eq. (1.10) where $BTOR$ represents the baroclinic torque, TTD the time tendency in stream-wise vorticity, ADV the combined effects of the advective terms, FRC the frictional torque, SCF the shear in the centrifugal force, $PTLT$ the tilting of planetary vorticity split into geostrophic $PTLT_g$ and ageostrophic $PTLT_{ag}$ parts, $GWR = PTLT_{ag} + SCF$ the residual of the gradient wind balance and ZPR the apparent advective acceleration resulting from zonal propagation of the feature at a speed $u_s = -0.51\text{ms}^{-1}$. The results are split into two plots for clarity with smaller terms on the right and FRC shown on both for scale.

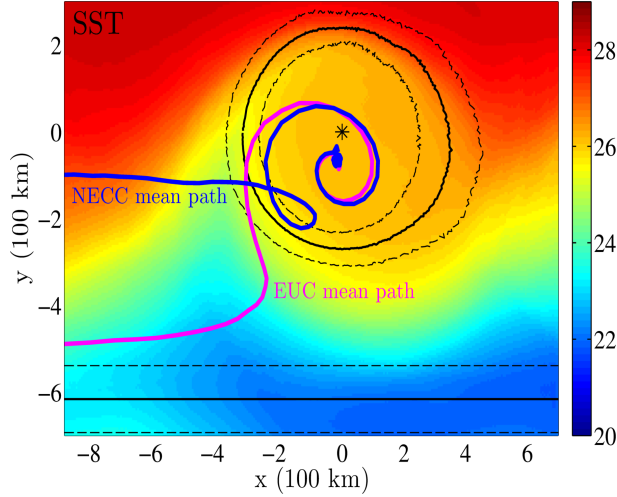


Figure 1.7: Composite average SST field ($^{\circ}\text{C}$) calculated by averaging the SST fields for each vortex at each day in the mid-resolution simulation around their center point, identified by the minimum in the surface stream-function. This center point is shown by the black star, with the solid and dashed lines indicating the mean and ± 2 standard deviation radial position of the TIV control volume stream-function contour. The mean and ± 2 standard deviation positions of the equator are also shown. The tracks shown are the center of mass tracks for particles coming from the EUC and particles coming from the NECC. We classified particles as NECC particles vs. EUC particles if they passed above the latitude of 5°N between 2 months and 15 days before entering the TIV (i.e. they passed north of the center of the next TIV to the west).

output time frequency used for the backward integration was once per day.

Many of the particles in an example trajectory calculation in the basin-wide simulation remain in the same TIV for two months as it translates westwards (compare particle positions in Fig. 1.1c on December 24th and in Fig. 1.1a two months earlier), indicating that TIVs do transport a considerable amount of water zonally. At the same time, many particles enter the TIV from the west, mostly through the EUC and some through a more northern pathway encompassing the NECC to the north, and TIVs to the west (consistent with the findings of Dutrieux *et al.* (2008) for TIVs in the Atlantic). Average or center of mass tracks can be calculated using the mid-resolution particles for these two entrance pathways (Fig. 1.7), confirming that most particles enter from the west through the south-west corner of the TIV.

Considerable changes in temperature and salinity occur along the Lagrangian fluid tracks entering the TIVs, with a predominant tendency for homogenization (compare Figures 1.1b and 1.1d). This indicates that non-conservative processes may be important in forming the properties of the core water of TIVs. To investigate these changes, the evolution in time of PDFs for various tracers can be calculated over the Lagrangian particles (Fig. 1.8). For each particle, a shifted time axis is defined with day 0 as that time when the particle *first* enters the control volume of the TIV it was seeded in. The differences between the tracer PDFs at day 0 (black curve in Figures 1.8a,c,e), and for earlier times (at 5 day intervals up to 150 days before TIV entrance, colored curves in Figures 1.8a,c,e) confirm that considerable Lagrangian changes occur.

The PDFs for temperature and latitude (Figures 1.8a and 1.8d) are consistent with the idea that TIV core water is sourced from the EUC and NECC. The temperature PDF describes mixing between water masses of two different temperature ranges, one with a narrow temperature distribution around 28°C (consistent with NECC water) and the other with a broad temperature distribution between 12°C to 22°C (consistent with EUC water). The latitude PDFs at early times (blue curves in Fig. 1.8d) show two distinct peaks around 1°N and around 6.5°N. The 1°N EUC peak is large, indicating that this is the dominant water source. In particular, this PDF shows that very little of the TIV core water is sourced recently from the Southern Hemisphere, in contrast to the results of *Foltz et al.* (2004), who found that TIVs in the western Atlantic were sourced partially from Southern Hemisphere water. The peak of the latitude PDF around 2.5°N at -5 days (darkest red curve in Fig. 1.8d), and its subsequent movement north indicate that the majority of particles enter TIVs from the south beginning in their south-west corner. This is consistent with the center of mass tracks (Fig. 1.7) where the dominant entrance pathway for TIV water is from the south-west. Averaged over the particles, the dominant sign of the radial buoyancy gradient (measured relative to TIV centers) is negative at the entrance time (not shown), indicating that most particles enter through the weaker frontal region (the TEF in Fig. 1.4) on the east side of the cold cusp. The evolution of the PDF of particle depths (not shown), shows that the particles are closest to the surface in this

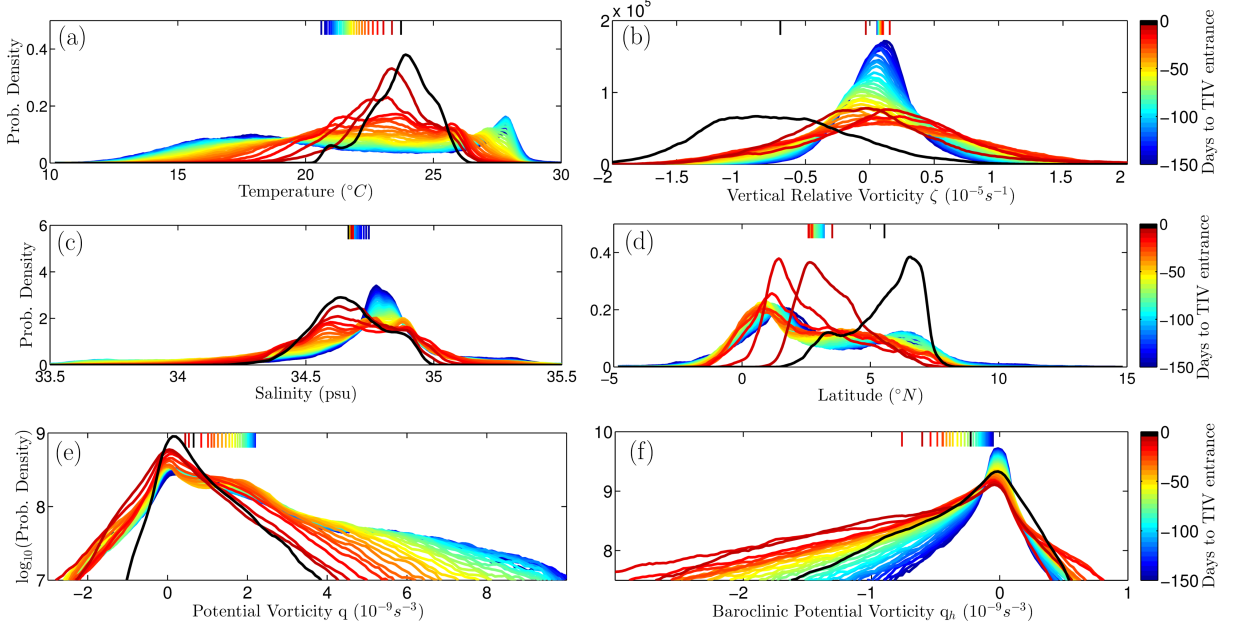


Figure 1.8: Particle PDFs for temperature (a), vertical relative vorticity (b), salinity (c), latitude (d), PV (e) and baroclinic PV (f) in the basin-wide simulation on a shifted time axis relative to the time at which each particle enters the TIV it was seeded in. The black curve in each plot represents the PDF over the particles at the time at which each particle enters the TIV (day 0), which corresponds to a different calendar day for each particle. The colored curves represent the distribution over the particles of each tracer at 5 day intervals up to 150 days (dark blue curve) before the TIV entrance. Over 480,000 particles were used to calculate each PDF, and the number of particles in each PDF is the same. The PDFs are compilations over particles that enter the TIVs in the months September–December over the longitude range (-160°E to -110°E). The distribution means are represented as straight ticks at the top of the plots.

TEF region and subduct around the time that they enter the TIV control volume.

The salinity PDF (Fig. 1.8c) describes a general freshening as the particles begin in the saltier western Pacific and move towards the fresher eastern Pacific before entering the TIVs. The distribution means show a gradual increase in temperature and a gradual decrease in salinity (Figures 1.8a,c). This implies that the particles' density decreases and suggests that external surface forcing and/or mixing is acting. A composite average of the surface buoyancy flux (calculated as for Fig. 1.7, not shown) suggests that heating of EUC water close to the surface in the TIW cold cusp may

be responsible for the increase in mean temperature. Mixing with water masses not tagged with particles could also explain both the salinity and temperature changes. The changes in distribution shapes are most rapid at times around when the particles enter the TIVs (Fig. 1.8). This indicates that mixing between the water masses that were tagged with the particles is occurring leading up to the TIV entrance time, emphasizing the fact that TIVs homogenize tracers. These non-conservative effects are the subject of current research, with some results discussed briefly in Section 1.7.

The vertical relative vorticity distribution is skewed slightly towards cyclonic values at early times (Fig. 1.8b), consistent with the northern portion of the EUC. However, in the last five days before particles enter the TIVs they acquire considerable anticyclonic vorticity. The development of this strong anticyclonic vorticity will be examined in the next section.

The distribution for the PV (Fig. 1.8e, plotted on a log scale) describes a systematic decrease as PV is lowered (the high PV tail disappears) to the values present in the TIV core. The mean has a steady decrease, indicating that diabatic and/or frictional processes may be occurring. Similar to the other tracers, these changes appear to be most rapid just before the particles enter the TIVs, when the particles are in the vicinity of the cold cusp and close to the frontal regions in this area. This suggests that frontal processes may play a role in controlling the change of properties along Lagrangian tracks and influence the key process of PV lowering.

The importance of frontal processes and stores of baroclinically-low PV are quantified in the PDF of q_h (Fig. 1.8f, plotted on a log scale). This PDF is skewed towards negative values, suggesting that the horizontal vorticity is most often pointing in the opposite direction to the horizontal buoyancy gradient. This is expected given that the geostrophic and thermal wind balance (giving a negative definite q_h as in Eq. (1.3)) holds in much of the domain (Fig. 1.5a). However, positive values do make a considerable contribution indicating that ageostrophic shears are present. The q_h distribution mean is initially of small magnitude (blue curves in Fig. 1.8f) and becomes more strongly negative as the frontal regions around the TIVs and the north equatorial front are approached. Finally, between day -5 and day 0 (darkest red and black curves in Fig. 1.8f), a rapid decrease in magnitude of q_h occurs, where much of the

negative tail in the distribution disappears. This, along with the rapid development of anticyclonic vertical vorticity (Fig. 1.8b), may indicate that the baroclinically-low PV is being converted to vortically-low PV as the particles enter the TIVs. We quantify this in the next section using diagnostics of the PV and vertical vorticity.

1.5 Potential vorticity and vorticity dynamics of TIVs

We consider an example set of 56 particles entering a TIV that were advected online in the high-resolution simulation (Fig. 1.9). These particles follow a path similar to the EUC center of mass entrance pathway (Fig. 1.7), moving into the vortex south-west corner while descending in the vertical (Fig. 1.9c). We perform a Lagrangian analysis of various properties along the particle tracks (Fig. 1.10). Prior to interpolation onto the particle tracks, fields were spatially filtered with a 14km/5 grid point horizontal filter followed by a 3 grid point vertical filter. An ensemble average was then performed over the 56 particles in order to average over the high spatial variability in the underlying fields (this spatial variability is represented by the error bars in Fig. 1.10).

A Lagrangian analysis of the various components of the Ertel PV (Eq. (1.1)) shows that the 56 particles have low PV throughout their path (Fig. 1.10a). However, at the initial time (year day 283.4), their low PV is due to near cancellation between the baroclinic (q_h in Fig. 1.10a) and vertical (q_v in Fig. 1.10a) components. At this time, the particles are at the northern end of the EUC shear layer and their baroclinically-low PV comes from the strong vertical shear in this region (e.g. Fig. 1.2f). This baroclinically-low PV is surface intensified (Fig. 1.9c) and over the time period from year day 283.5 to 284.5, the particles subduct (Fig. 1.9c) and move to the northern side of the vortex (Fig. 1.9a) out of the baroclinically-low PV region. At late times (after year day 284.5), the PV is still low, as required by the near-conservation of PV, but now both the vertical and baroclinic components are near zero (Fig. 1.10a). The terms fN^2 and ζN^2 nearly cancel and the PV is vortically-low due to a near zero

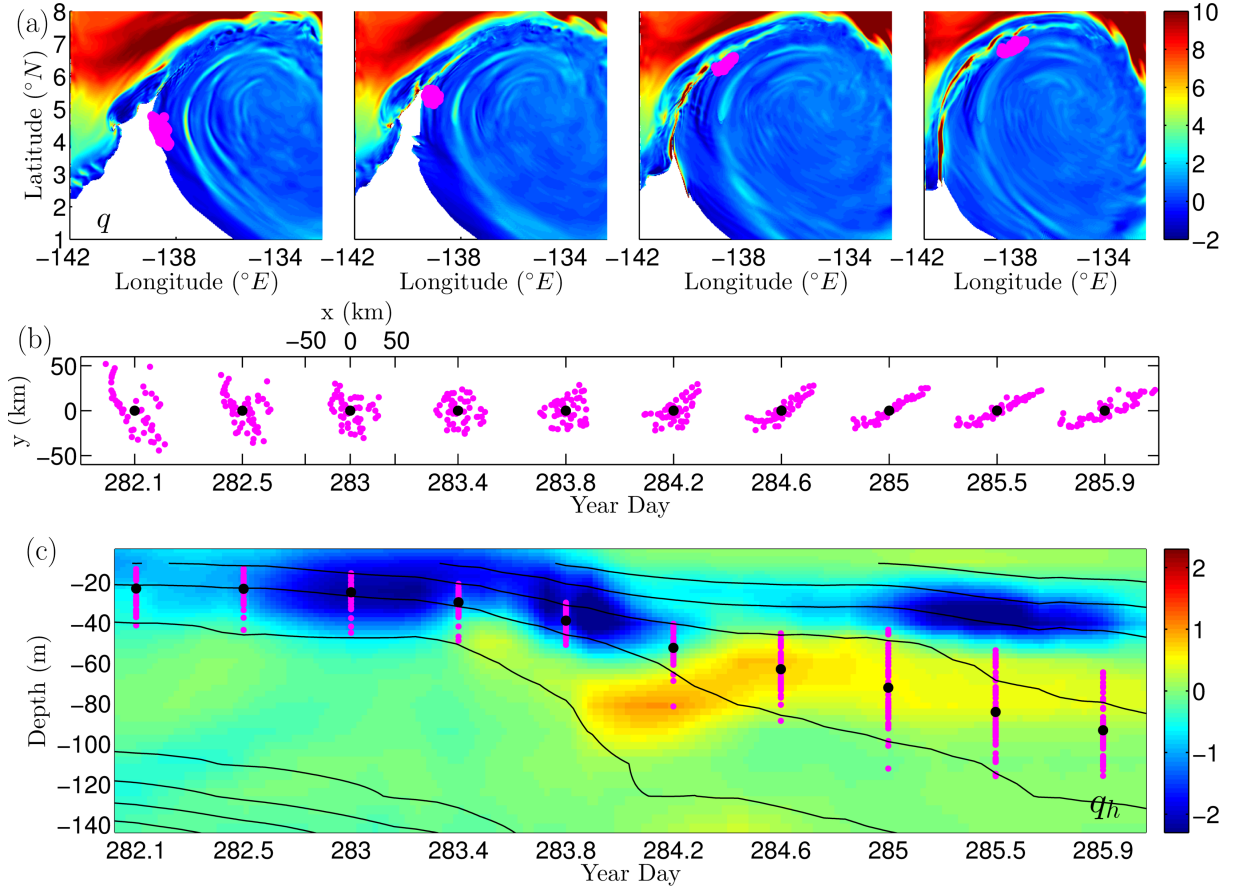


Figure 1.9: (a) Positions of 56 particles at year days 282, $283\frac{1}{3}$, $284\frac{2}{3}$ and 286 lying close to the $1023.67 \text{ kg m}^{-3}$ isopycnal surface in the high-resolution simulation. The field plotted on the isopycnal is PV ($\times 10^{-9} \text{ s}^{-3}$), with the isopycnal outcrop on the edge of the blank regions. (b) Horizontal distribution of particle positions relative to the particles center of mass as a function of time. (c) Depth-time slice of q_h ($\times 10^{-9} \text{ s}^{-3}$) along the particle center of mass track. The thin black lines represent isopycnals with a spacing of 0.2 kg m^{-3} . The vertical positions of the particles are shown at times corresponding to those in (b).

absolute vertical vorticity. The particles have obtained strong anticyclonic vorticity with values approaching $-f$ typical of the flow in the TIV core.

To understand this creation of negative vertical relative vorticity ζ , we examine

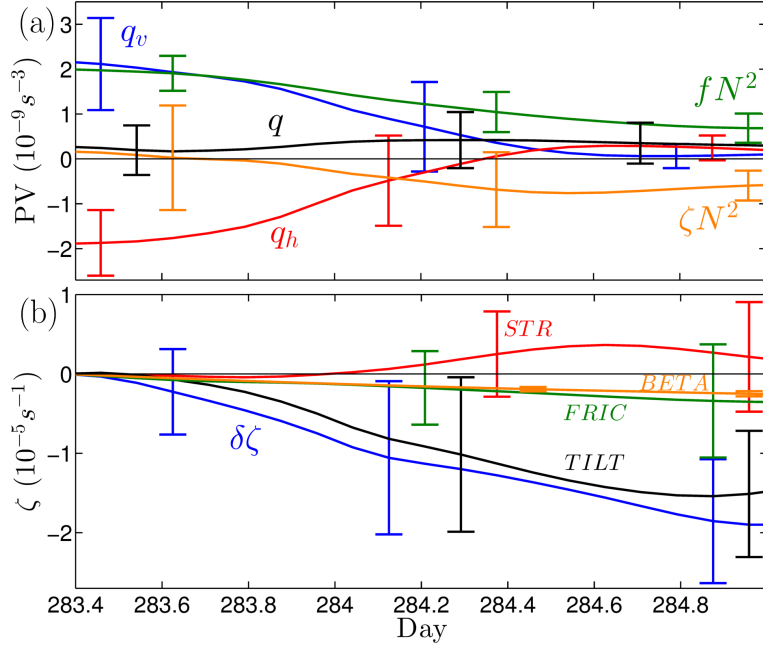


Figure 1.10: Ensemble-average Lagrangian time series of the different terms in the Ertel PV (Eq. (1.1)) (a) and in the time-integrated vertical relative vorticity Eq. (1.17) (b) made following the 56 particles shown in Fig. 1.9. In (a), q is the total PV split into vertical q_v and baroclinic q_h parts. The vertical term is further split into planetary fN^2 and relative ζN^2 vorticity components. In (b), $\delta\zeta$ is the change in relative vorticity, $TILT$ represents changes in ζ driven by vortex tilting, STR by vortex stretching/squashing, $FRIC$ by frictional torques and $BETA$ by advection of planetary vorticity (see Eq. (1.18)). The error bars represent the ± 1 standard deviation spread over the particle ensemble caused by spatial variability in the underlying fields over the span of the floats.

the Lagrangian evolution equation for the vertical relative vorticity,

$$\frac{D\zeta}{Dt} = -v \frac{df}{dy} + (f + \zeta) \frac{\partial w}{\partial z} + \frac{\partial u}{\partial z} \frac{\partial w}{\partial y} - \frac{\partial v}{\partial z} \frac{\partial w}{\partial x} + (\nabla \times \mathbf{F}) \cdot \hat{\mathbf{k}}, \quad (1.17)$$

where \mathbf{F} denotes the frictional force in the momentum equations, parametrized using the KPP mixing scheme and a horizontal bi-harmonic viscosity in ROMS. We have not included the negligible solenoidal term (*Ubelmann and Fu, 2011*). Performing an ensemble average over the particles (denoted by $\langle \cdot \rangle$) and a Lagrangian time integral along the particle tracks (denoted $\int_{\mathcal{L}} \cdot dt$) allows the total change in vorticity $\delta\zeta =$

$\int_{\mathcal{L}} \frac{D\zeta}{Dt} dt$ to be attributed to terms on the right-hand side of Eq. (1.17),

$$\begin{aligned} BETA &= \int_{\mathcal{L}} \left\langle -v \frac{df}{dy} \right\rangle dt \\ STR &= \int_{\mathcal{L}} \left\langle (f + \zeta) \frac{\partial w}{\partial z} \right\rangle dt \\ TILT &= \int_{\mathcal{L}} \left\langle \frac{\partial u}{\partial z} \frac{\partial w}{\partial y} - \frac{\partial v}{\partial z} \frac{\partial w}{\partial x} \right\rangle dt \\ FRIC &= \int_{\mathcal{L}} \left\langle (\nabla \times \mathbf{F}) \cdot \hat{\mathbf{k}} \right\rangle dt. \end{aligned} \quad (1.18)$$

Thus changes in the vertical relative vorticity can occur through meridional advection of planetary vorticity (*BETA*), stretching of vertical vorticity (*STR*), tilting of horizontal vorticity into vertical vorticity (*TILT*) and frictional torques (*FRIC*). In the analysis shown below, we calculate the tilting term as a residual of the other terms

$$TILT = \delta\zeta - STR - BETA - FRIC, \quad (1.19)$$

to minimize the error due to finite difference truncation, which is worse for the tilting term than the other terms as it contains the horizontal derivative of the vertical velocity. However, calculation of the direct tilting term from Eq. (1.18) (not shown) gives a qualitatively similar result and does not change the conclusions below.

A Lagrangian analysis of these terms along the particle tracks (Fig. 1.10b) shows that the decrease in relative vorticity $\delta\zeta$ comes primarily from vortex tilting (*TILT* in Fig. 1.10b), where the horizontal vorticity associated with the EUC shear layer (and associated with q_h in Fig. 1.10a) is tilted downwards to form anticyclonic vertical vorticity. This term dominates the change in ζ (Fig. 1.10) as the particles subduct and leave the surface frontal region between year days 283.5 and 285 (Fig. 1.9c). There are also contributions from frictional effects (*FRIC* in Fig. 1.10b) and from advection of planetary vorticity (*BETA* in Fig. 1.10b), although they are not sufficient to explain the development of strong anticyclonic vorticity without vortex tilting. The vortex stretching term is positive (*STR* in Fig. 1.10b), but is dominated by the other terms. This positive stretching is associated with a reduction in stratification of the source

water to levels appropriate for the TIV core.

The process of baroclinically-low to vortically-low PV conversion demonstrated above can provide a source for the anticyclonic rotation of the TIV by purely conservative processes. This source is conservative because the increase in q_h is compensated by a reduction in ζ such that the total PV (Eq. (1.1)) remains constant (Fig. 1.10a). Other possible conservative sources for ζ could be changes in stratification N^2 through vortex stretching and changes in f along the fluid tracks through advection of planetary vorticity. However, non-conservative changes in the total PV q could also give rise to changes in vorticity as well.

To quantify the relative importance of these different sources of anticyclonic vorticity to TIVs, we calculated the amount of vertical relative vorticity ζ that would be acquired given the observed change in q_h , q , f and N^2 on particles run off-line in the mid-resolution simulation. The following calculation includes particles that enter three TIVs in the mid-resolution simulation from any source, including both the EUC and NECC, and thus is a global calculation over all TIV core water sources in contrast to the specific calculation in figures 1.9 and 1.10 used to demonstrate the PV conversion mechanism associated with q_h .

Rearranging the equation for the PV (Eq. (1.1)) and normalizing by a mean $\overline{N^2} = 1.6 \times 10^{-4} \text{s}^{-2}$ and mean $\overline{f} = 1.27 \times 10^{-5} \text{s}^{-1}$ appropriate for the vortex center at 5°N gives,

$$\frac{\Delta\zeta}{\overline{f}} = \underbrace{\frac{\Delta q}{\overline{f} \overline{N^2}}}_{\delta_q} - \underbrace{\frac{\Delta f}{\overline{f}}}_{\delta_{-f}} - \underbrace{\frac{\Delta q_h}{\overline{f} \overline{N^2}}}_{\delta_{-q_h}} - \underbrace{\frac{(\overline{f} + \overline{\zeta})\Delta N^2}{\overline{f} \overline{N^2}}}_{\delta_{N^2}}, \quad (1.20)$$

We choose Δ to represent a net change for each particle from four days before it enters the TIV control volume to one day afterward, as this is when most of the change in ζ occurs. The mean $\overline{\zeta}$ was defined as the average ζ over this same period for each particle. For each particle that experiences a decrease in ζ of at least $-0.5 \times 10^{-5} \text{s}^{-1}$ over this period, we calculate δ_q , δ_{-f} , δ_{-q_h} and δ_{N^2} , where we use the same spatial filtering as for Fig. 1.10.

For $\sim 100,000$ particles in the mid-resolution simulation that satisfy the ζ decrease condition, a PDF was calculated of each term in Eq. (1.20) (Fig. 1.11). The

major contributor to the decrease in ζ for particles entering the TIVs is the advection of planetary vorticity, δ_{-f} . This distribution has a mean of -0.58 , suggesting that northward advection of planetary vorticity results in reduction of ζ of order half a vorticity Rossby number. The contribution of non-conservative processes (δ_q in Fig. 1.11), has a PDF that is nearly symmetrically distributed around zero, apart from a slight negative tail associated with a preference for PV reduction. The contribution from changes in stratification (δ_{N^2} in Fig. 1.11) is minor and generally acts to increase ζ through vortex stretching as the stratification reduces entering the vortices. The baroclinic term (δ_{-q_h} in Fig. 1.11) provides a significant contribution in this global calculation (mean -0.36) that is systematically negative. Thus the horizontal vorticity of TIV source water cannot be neglected as it generates considerable anticyclonic vorticity for TIVs.

The Lagrangian analysis above focuses on changes in relative vorticity, and by its nature does not take into account advection of the initial relative vorticity distribution. The evolution of vorticity along the particle paths (Fig. 1.8b) shows that the vorticity distribution of particles is initially skewed towards cyclonic values and changes considerably on entering the TIV. There is only minor overlap between the vorticity distributions at early times with the distribution as the particles enter the TIVs. The TIVs will go on to homogenize absolute vorticity within their cores (not shown in Fig. 1.8b), and thus the relative vorticity distribution has little memory of its initial distribution and advection of relative vorticity has a minor influence.

The process of baroclinically-low to vortically-low PV conversion generates some of the anticyclonic rotation of TIV core water. This process can be understood schematically by assuming for simplicity that the PV remains zero throughout the conversion process (Fig. 1.12). A water parcel in the EUC shear layer can have zero PV because of cancellation between the projection of the horizontal vorticity and that of the vertical vorticity onto the total buoyancy gradient vector (baroclinically-low PV in Fig. 1.12). If this water parcel is then moved into the core of the TIV, where there is non-zero stratification and no horizontal buoyancy gradient, it must obtain anticyclonic vorticity of $-f$ in order to conserve PV (vortically-low PV in Fig. 1.12). The ingredients required for this process are not only the source of baroclinically-low

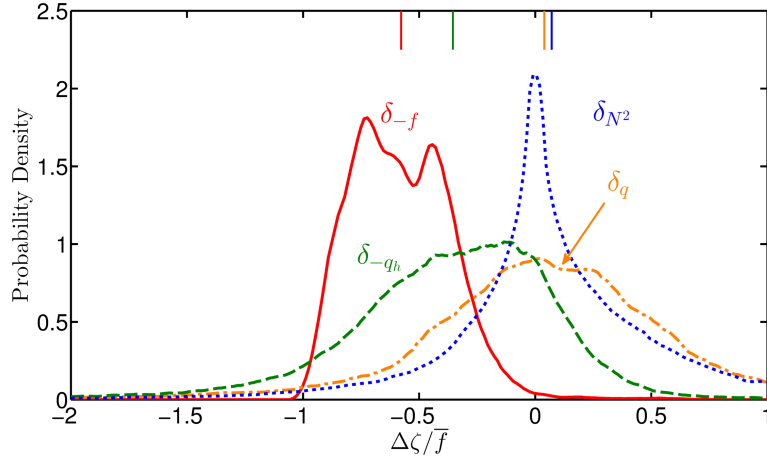


Figure 1.11: PDFs of the contribution to reductions in vertical vorticity $\Delta\zeta$ driven by the different terms in the PV given in Eq. (1.20). This is a global calculation over all TIV core water sources that considers $\sim 100,000$ particles that enter three TIVs in the mid-resolution simulation. The vorticity is normalized by $\bar{f} = 1.27 \times 10^{-5} s^{-1}$, a value of the planetary vorticity representative of the vortex center at $5^\circ N$. The change in vorticity is calculated over a 5 day period starting 4 days before the particles enter the TIV and ending one day after they enter, with only decreases in ζ of more than $-0.5 \times 10^{-5} s^{-1}$ considered. The fields are filtered in space (5 grid points in the horizontal, 3 points in the vertical as in Fig. 1.10) before interpolation on to particle tracks. δ_f represents the change in ζ due to advection of planetary vorticity, δ_{N^2} due to changes in stratification (vortex squashing/stretching), δ_{qh} due to changes in the baroclinic PV (vortex tilting) and δ_q to non-conservative changes in PV (all from Eq. (1.20)).

PV in the EUC shear layer, but also a differential vertical circulation ($\frac{\partial w}{\partial y}$ and $\frac{\partial w}{\partial x}$ in Eq. (1.17)) that drives the vortex tilting. The western portion of the vortex in which this conversion process occurs is characterized by strong strain, as indicated by the straining of the example particle positions into a thin line between year days 283.4 and 285 (Fig. 1.9b), the same time period over which PV conversion and vortex tilting occurs (Fig. 1.10). Horizontal strain occurring in the presence of a horizontal buoyancy gradient can give rise to frontogenesis and a secondary circulation that provides the differential vertical motions required for the vortex tilting.

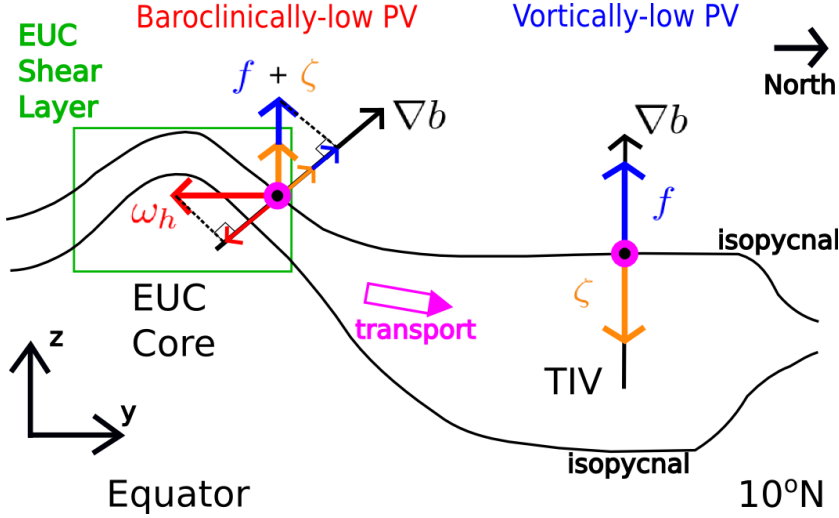


Figure 1.12: A schematic showing the process of baroclinically-low to vortically-low PV conversion acting to form the strong anticyclonic rotation of a TIV. A parcel of water in the EUC shear layer (left pink circle) has baroclinically-low PV as the projection of the horizontal vorticity onto the total buoyancy gradient vector compensates the projection of the vertical vorticity onto the total buoyancy gradient vector. If the parcel of water is moved into the TIV core (right pink circle), where the horizontal buoyancy gradient is small, then it must obtain strong anticyclonic rotation in order to conserve PV.

1.6 Frontogenesis

The particles considered in the previous section enter the vortex along a path that runs through the frontal regions in the western portion of the vortex. Both the trailing edge and leading edge fronts (Fig. 1.4) form as a result of frontogenesis. The equation governing the Lagrangian evolution of the horizontal buoyancy gradient in the absence of diabatic processes is,

$$\frac{D|\nabla_h b|^2}{Dt} = \underbrace{-2\nabla_h b \cdot \left(\frac{\partial \mathbf{u}_h}{\partial x} \cdot \nabla_h b, \frac{\partial \mathbf{u}_h}{\partial y} \cdot \nabla_h b \right)}_{HCL} - \underbrace{2\nabla_h b \cdot (N^2 \nabla_h w)}_{DVADV}. \quad (1.21)$$

The horizontal buoyancy gradient can change due to horizontal strain and shearing (*HCL* in Eq. (1.21)), differential vertical advection in a stratified fluid (*DVADV* in Eq. (1.21)) and diabatic processes which have been neglected. The western portion

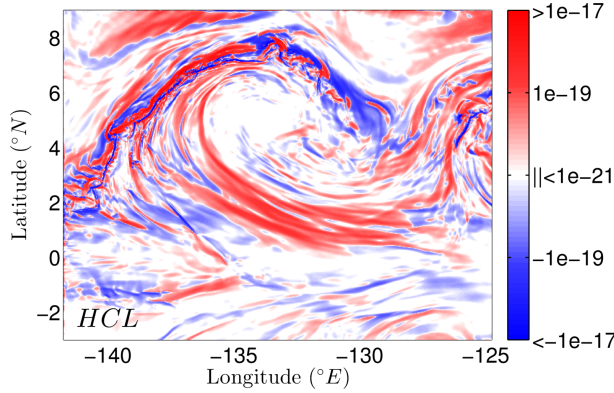


Figure 1.13: The log of the horizontal strain and shearing term ($HCL (s^{-5})$) in the equation for the Lagrangian change in horizontal buoyancy gradient magnitude (Eq. (1.21)) at 50m depth in the high-resolution simulation on the 11th of October (year day 281.2083). Note that the color scale has been adjusted in order to show both frontogenetic and frontolytic values on a log scale.

of the vortex around the LEF and TEF is characterized by strong positive HCL indicating that the horizontal velocity field is increasing the horizontal buoyancy gradient here (Fig. 1.13). HCL reaches $\sim 10^{-17}s^{-5}$, which is enough to increase $|\nabla_h b|$ by up to $\sim 10^{-6}s^{-2}$ in 1 day.

According to the classical frontogenesis theories of *Hoskins and Bretherton* (1972) and *Hoskins* (1982), a front undergoing strain and shearing that acts to increase the horizontal buoyancy gradient will acquire an ageostrophic secondary circulation in the across-front plane in the sense to restore thermal wind balance by increasing the vertical shear in the geostrophic flow, reducing the horizontal buoyancy gradient and re-stratifying the front. These theories assume that thermal wind balance is a dominant constraint on the flow, which is part of the force balance along the TEF (Fig. 1.5). Thus we may expect such a secondary circulation to be associated with the horizontal confluence/shearing in the western portion of the vortex.

The ageostrophic secondary circulation associated with frontogenesis is thermally-direct in the sense that the buoyancy flux $w'b'$, where $'$ denotes a deviation from an across front average, is positive and acts to reduce the horizontal buoyancy gradient. Such a circulation will act to tilt the horizontal vorticity downwards, providing that horizontal vorticity is ‘anticyclonic’ (*Molemaker et al.*, 2005), i.e. it results in a

negative value of the baroclinic PV, which is always the case for a flow in thermal wind balance. Therefore the signature of an ageostrophic secondary circulation driven by frontogenesis is a frontal region with correlations between positive HCL , positive buoyancy flux $w'b'$ and negative vortex tilting $\omega_h \cdot \nabla_h w$ (the third and fourth terms on the right-hand side of Eq. (1.17)).

The area of interest is along the TIV core water entrance pathway through the TIW cold cusp on the western side of the TIV. Here, the cold cusp is experiencing strong strain and shearing as the LEF and TEF fronts are squeezed together (Figures 1.4 and 1.13) in a process resemblant of the filament intensification of *McWilliams et al.* (2009). A feature of this cold cusp is a near-surface filament of high PV associated with the cyclonic side of the LEF (marked with the green LEF line in Figures 1.14c and 1.4). As a consequence of PV conservation, this near-surface high PV filament acts as a barrier to surface cross flow, and therefore separates the surface water to its north-west, outside the vortex, from surface water to its south-east, inside the vortex. Using this near-surface high PV filament as a reference frame, we have calculated across-front slices of PV, vertical velocity, vortex tilting, buoyancy flux $w'b'$ and HCL (Figures 1.14a,b,d,e,f respectively) averaged over the region indicated in Fig. 1.14c. The slices are calculated by performing an along-front average within this region (magenta box in Fig. 1.14c) and a time composite average over a time period of 72 hours (36 separate times) in order to show only the robust features.

The results show that the water surrounding the LEF moves downwards as it moves rapidly north-east, with vertical velocities reaching up to 50m/day (Fig. 1.14b). The strong positive HCL at the surface responsible for the formation and maintenance of the LEF is accompanied by strong negative HCL at mid-depths (Fig. 1.14f). This region of negative HCL is surrounded on either side by positive HCL . The across front position of the maximum density at each depth, marking the peak of the TIW cold cusp, moves from 0 to -50km toward the center of the vortex with depth (marked with the magenta line in figures 1.14a,b,d,e,f). It is through this cold filament that cold EUC water is entering the vortex. In particular, the set of 56 particles considered in the Lagrangian analysis (figures 1.9 and 1.10) move through this cold filament (their average position is indicated by the magenta cross in figures

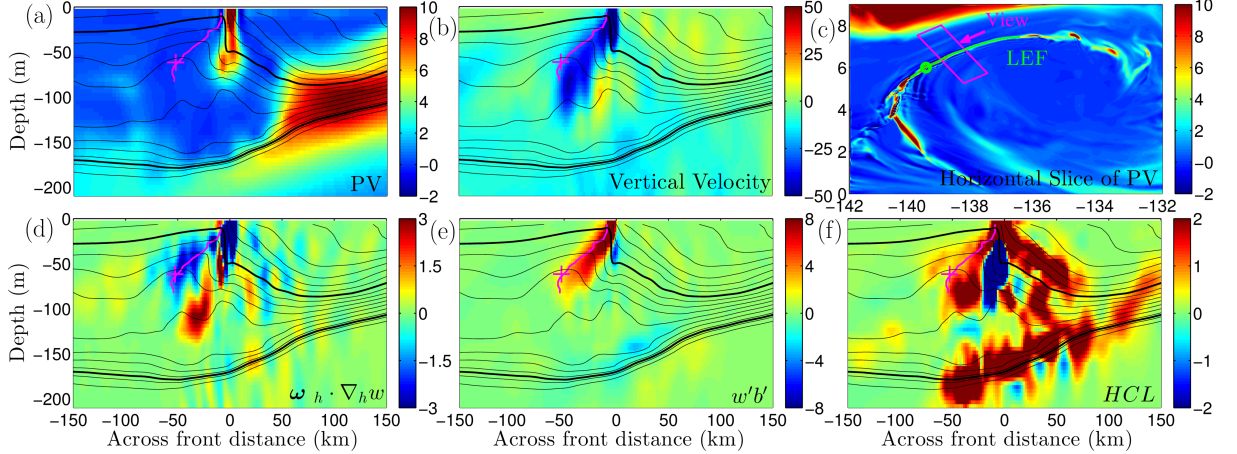


Figure 1.14: Composite average across front slices of PV ($\times 10^{-9} \text{ s}^{-3}$) (a), vertical velocity (m/day) (b), vortex tilting $\omega_h \cdot \nabla_h w$ ($\times 10^{-10} \text{ s}^{-2}$) (d), buoyancy flux $w'b'$ ($\times 10^{-7} \text{ m}^2 \text{ s}^{-3}$) (e) and HCL ($\times 10^{-19} \text{ s}^{-5}$) (f) over 72 hours from year day 282.79 to year day 285.63 (36 separate times) in the high-resolution simulation. The region location is shown by the magenta box in (c) over a horizontal slice of the PV ($\times 10^{-9} \text{ s}^{-3}$) at 17m depth half way through the composite average time period (year day 284.21). The reference point used for the time composite average is the intersection point of the near-surface high PV filament (green line marked LEF) with the 6° latitude line (shown with a green circle in c). The composite average is performed by moving the region in time in order to keep its center point a constant zonal distance from this reference point. The angle of the region is maintained perpendicular to the LEF. The prime in the calculation of the buoyancy flux $w'b'$ (e) is defined as the difference from a 75km box-car across-front filter at each depth. The result is robust for filter sizes between 25km and 125km. HCL denotes changes in the horizontal buoyancy gradient driven by horizontal strain/shear (Eq. (1.21)). The across front position of the cold filament is marked by the magenta line, being the maximum in density at each depth. The average position of the 56 particles considered in the Lagrangian analysis in figures 1.9 and 1.10 relative to the LEF is shown by the magenta plus symbol. The thin black lines represent isopycnals with a spacing of 0.2 kg m^{-3} down to 1025.4 kg m^{-3} and the bold lines are the 1023 and 1024.6 kg m^{-3} isopycnals bounding the TIV control volume.

1.14a,b,d,e,f). This cold filament is characterized by positive HCL below depths of 25m (Fig. 1.14f around magenta line). The buoyancy flux $w'b'$ around the cold filament is positive (Fig. 1.14e around magenta line), indicating that the cold filament is experiencing a thermally direct circulation coincident with the positive HCL. Finally,

this cold filament is also characterized by negative vortex tilting (Fig. 1.14d around magenta line) and thus there is strong evidence that the water in this cold filament is subject to a thermally-direct secondary circulation associated with frontogenesis that acts to tilt horizontal vorticity downwards. The composite average vortex tilting reaches magnitudes of $-2 \times 10^{-10}\text{s}^{-2}$ (Fig. 1.14d), which is enough to reduce the relative vorticity by $-1.7 \times 10^{-5}\text{s}^{-1}$ in one day, on the same order as that observed in the Lagrangian analysis (Fig. 1.10b).

1.7 Diabatic processes*

In Sections 1.5 and 1.6 we examined the vortex tilting that leads to TIV core water formation and the frontogenesis that drives it. It was evident that the frontogenesis and vortex tilting is a spatially and temporally intermittent process, occurring around thin filaments and buoyancy fronts that are entrained into the TIVs through the TEF region. This intermittency results in large differences between the behavior of water parcels that are within close proximity of one another, and results in the large spreads in properties observed in the Lagrangian analysis (Fig. 1.10). Around such sharp features, it may be expected that diabatic and frictional processes may play a role in the dynamics, and influence the evolution of the horizontal buoyancy gradient. Here we examine the diabatic terms in Eq. (1.21).

Performing an ensemble average and a Lagrangian time integral of Eq. (1.21) as for the vertical relative vorticity equation (in obtaining Eq. (1.18) from Eq. (1.17)) gives terms,

$$\begin{aligned} DIAB &= \int_{\mathcal{L}} \langle 2\nabla_h \mathcal{H} \cdot \nabla_h b \rangle dt \\ DIAB_v &= \int_{\mathcal{L}} \langle 2\nabla_h \mathcal{H}_v \cdot \nabla_h b \rangle dt \\ DIAB_h &= \int_{\mathcal{L}} \langle 2\nabla_h \mathcal{H}_h \cdot \nabla_h b \rangle dt \\ DYN &= \int_{\mathcal{L}} \langle -2\mathbf{Q} \cdot \nabla_h b \rangle dt, \end{aligned} \tag{1.22}$$

where $DIAB$, $DIAB_v$ and $DIAB_h$ indicate the total change in horizontal buoyancy

gradient attributable to total, vertical and horizontal diabatic processes respectively, and DYN indicates the combined influence of HCL and $DVADV$ in Eq. (1.21).

The ensemble mean of $|\nabla_h b|^2$ (Fig. 1.15) shows that frontogenesis occurs between days 283.5 and 285, and that it is driven by the dynamical terms (DYN in Fig. 1.15), consistent with figures 1.9b and 1.14. However, $|\nabla_h b|^2$ also reduces considerably at later times (Fig. 1.15), a reduction that is required to form the vortically-low PV water in the TIV core with zero horizontal buoyancy gradient through the simplified picture of baroclinically-low to vortically-low PV conversion (Fig. 1.12). This reduction in the horizontal buoyancy gradient is driven by diabatic processes ($DIAB$ in Fig. 1.15) that become significant as the spatial variability and gradients increase around day 283.5.

Splitting the diabatic term into parts due to vertical diffusion of buoyancy ($DIAB_v$ in Fig. 1.15) and horizontal diffusion of buoyancy ($DIAB_h$ in Fig. 1.15) suggests that both of these processes contribute. Horizontal diffusion of temperature and salinity in the model is achieved through a harmonic diffusion that acts on sharp gradients in the tracer fields. Thus it is not surprising that $DIAB_h$ becomes significant along this track (Fig. 1.15) as the strain acts to increase horizontal gradients.

Vertical diffusion is parametrized in the ROMS model using the Richardson number based KPP mixing scheme (Large *et al.*, 1994). The baroclinically-low PV water entering the vortex through the TEF region is characterized by low Richardson numbers (Fig. 1.2f). Therefore this water experiences vertical mixing driven by the KPP parametrization, and this mixing is correlated with the buoyancy field in such a way as to reduce the horizontal buoyancy gradient (as $DIAB_v$ is negative in Fig. 1.15). This may indicate that vertical mixing, focused on the baroclinically-low PV water mass moving from the EUC, mixes in warmer water from the surface mixed layer and thus reduces the temperature difference to the nearby TIV core water with high Richardson number (Fig. 1.2f). Further analysis of the non-conservative processes beyond the scope of this thesis are required to confirm this.

The competition between dynamical frontogenesis and diabatic diffusion of buoyancy (Fig. 1.15) is one example that highlights the importance of these small-scale non-conservative processes to the larger circulation.

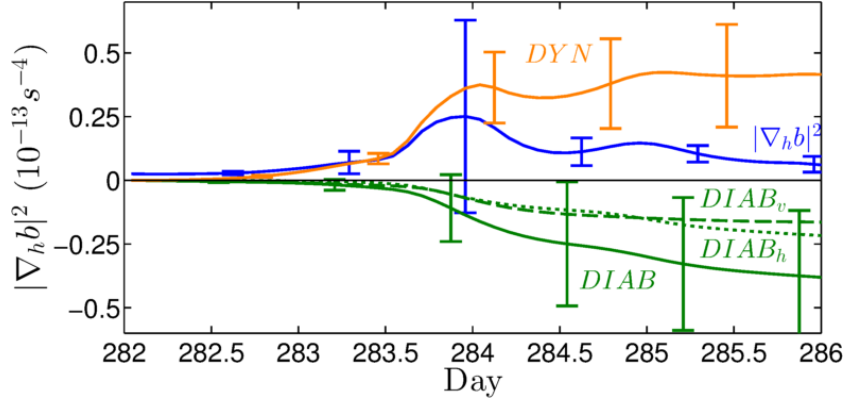


Figure 1.15: Lagrangian time series of the magnitude of the horizontal buoyancy gradient (blue line) calculated as in Fig. 1.10. Also shown are the time integrated and ensemble averaged effect of the diabatic terms $DIAB$, $DIAB_v$, $DIAB_h$ and advection based terms DYN from Eq. (1.22).

1.8 Connection of TIW vorticity and TIW energetics frameworks

This work has focused on the vortex dynamics of fully developed TIVs, in contrast to many previous studies which considered the energetics of tropical instabilities. While these two different approaches generally tackle different questions, it is possible to make some broad connections between them. As described by Proehl (1996), tropical instabilities on a time-independent zonal flow can gain kinetic energy through lateral shear production (BT), vertical shear production (VS) and from background potential energy sources (BC),

$$BT = -\overline{u'v'} \frac{\partial \bar{u}}{\partial y} \quad (1.23)$$

$$VS = -\overline{u'w'} \frac{\partial \bar{u}}{\partial z} \quad (1.24)$$

$$BC = \overline{w'b'}, \quad (1.25)$$

where $'$ denotes a perturbation from a zonal average (indicated by the over-bar). Using simple scaling arguments it can be shown that the relative importance of the

vertical to lateral shear production VS/BT is dependent on the relative size of the baroclinic term in the PV. To do this, we make a simple scaling assumption about the momentum fluxes associated with the tropical instabilities, namely that the vertical momentum flux $\overline{u'w'}$ is an order one constant times the horizontal momentum flux $\overline{u'v'}$ times the isopycnal slope of the background flow,

$$\overline{u'w'} \sim -\frac{\partial \bar{b}/\partial y}{\bar{N}^2} \overline{u'v'}, \quad (1.26)$$

i.e. we assume that the flow runs mostly along isopycnals. This scaling law was found to be qualitatively accurate in the TIV region by calculating perturbations from a zonal mean in the basin-wide simulation. Under this scaling assumption we find that the ratio of the vertical shear production to lateral shear production energy source terms for perturbation kinetic energy is controlled by the ratio of terms in the background PV,

$$\frac{VS}{BT} \sim \frac{q_h}{\zeta N^2}. \quad (1.27)$$

Thus the large relative magnitude of the baroclinic PV component in the region above the EUC shear layer (Fig. 1.3) implies that vertical shear production may make a significant contribution to the kinetic energy of the tropical instabilities, and hence to the vorticity of TIVs. Previous studies have concluded that this term is negligible (*Weisberg and Weingartner, 1988; Masina et al., 1999; Grodsky et al., 2005*) or makes a small contribution (*Cox, 1980; Qiao and Weisberg, 1998*). It should be mentioned that the relative magnitude and sign of the different energy sources vary significantly with season and location (*Luther and Johnson, 1990; Masina et al., 1999*) and with the level of lateral mixing included in the model (*Pezzi and Richards, 2003*).

1.9 Conclusions

Using a set of nested high-resolution simulations of the equatorial Pacific we have studied the vortex dynamics of TIVs making extensive use of the Ertel PV. This approach has yielded insights into TIV dynamics and revealed analogies between TIVs

and submesoscale processes in the mid-latitudes. The $\mathcal{O}(1)$ Richardson numbers associated with the high vertical shear in the EUC shear layer (Fig. 1.2f) indicates that the baroclinic component of the PV is of comparable magnitude to the vertical component (Fig. 1.3). This baroclinic component acts as a source of anticyclonic vorticity for developed TIVs (Fig. 1.11) through the mechanism of baroclinically-low to vortically-low PV conversion (Fig. 1.12), a mechanism that is also involved in the formation of submesoscale intrathermocline eddies in the mid-latitudes (Thomas, 2008). However, in contrast to submesoscale flows at mid-latitudes, the gradient in planetary vorticity plays an important role in the dynamics of TIVs. Specifically, a large fraction of the change in vertical relative vorticity experienced by water parcels entering a TIV is associated with a change in planetary vorticity. It is important to note however that our analysis of Lagrangian trajectories of TIV core water showed that very little of this low PV water is sourced from the Southern Hemisphere (Fig. 1.8d). This is contrary to the results of Foltz *et al.* (2004), who found that some northward cross-hemisphere exchange occurred in the western Atlantic. Our simulations suggest that there is little evidence for significant northward cross-hemisphere exchange associated with TIVs in the central and eastern equatorial Pacific.

We have shown that vortex tilting of horizontal vorticity associated with the EUC shear layer provides a significant source for the anticyclonic rotation of the vortex (contributing around -0.4 of a Rossby number, Fig. 1.11). This vortex tilting is consistent with a frontogenetic secondary circulation driven by the strain induced by the velocity field of the TIV itself. This work has highlighted the importance of frontal dynamics to the larger scale circulation in the equatorial Pacific. These frontal dynamics are influenced by the curvature in TIV streamlines. The frontal region on the western side of TIVs was found to be in cyclogeostrophic balance with the centrifugal force playing an important role (Fig. 1.5). Indeed a study of the horizontal vorticity balance along the TEF (not shown) indicates that the gradient-wind balance holds closely in the moving frame of the TIV, with the shear in the centrifugal force being the dominant term. Despite the large curvature, the sign of the baroclinic PV component was in most cases negative indicating that the horizontal vorticity associated

with these fronts was consistent with thermal wind balance (Fig. 1.3b). This indicates that a thermally-direct secondary circulation driven by frontogenesis will tilt vorticity downwards as observed (Fig. 1.14d). However, the details of frontogenesis and the associated secondary circulation in a flow with such high curvature are as yet unknown and will be the subject of further research.

Capturing the frontal dynamics and the process of baroclinically-low to vertically-low PV conversion in an ocean model requires accurate simulation of the EUC shear layer and the associated horizontal buoyancy gradient. The details of the flow in this region may depend on the horizontal resolution, vertical resolution and vertical mixing parametrization included in the model. For example, the relative importance of the baroclinic contribution to vertical vorticity reduces going from our mid-resolution to our low-resolution simulation, i.e. the ratio of the mean δ_{q_h} to mean δ_f in Fig. 1.11 reduces from 0.62 to 0.56 for an equivalent calculation on the same TIVs in the low-resolution simulation. While this is not a large numeric difference, this effect is expected to be systematic with reducing resolution as the grid aspect ratio reduces. This suggests that the PV conversion mechanism and submesoscale physics may be difficult to resolve in low-resolution simulations and the vortex dynamics may be altered. Indeed, *Marchesiello et al.* (2011) showed using a test for numerical convergence as measured by an invariance of the kinetic energy spectrum with resolution, that horizontal grid spacings of less than 10km are required to capture the submesoscale physics of TIVs well. Thus global circulation models with $\sim 1^\circ$ horizontal resolution may not simulate TIV dynamics correctly, which may have implications for TIV driven lateral stirring and vertical mixing and thus for the heat budget of the equatorial region.

This work has suggested that non-conservative processes associated with friction and diabatic changes in buoyancy may play an important role in the dynamics of TIVs. For example, the role of the diabatic terms in the Lagrangian evolution of the horizontal buoyancy gradient (Fig. 1.15), and the mixing and homogenization of temperature and salinity and lowering of PV that occurs in the process of TIV core water formation (Fig. 1.8a,c,e). A net lowering of PV can be driven by surface cooling or frictional processes associated with wind stress. Surface cooling is unlikely

at these low latitudes, suggesting that in this case frictional processes are responsible. In the case of ITEs in the mid-latitudes, the source of baroclinically-low PV can be an upwards surface PV flux through wind driven destruction of PV (*Thomas, 2008*). Frictional reduction of PV by the easterly trade winds that blow down-front along the north equatorial front and drive equatorial upwelling may be a process of importance for TIV dynamics, and may be the only explanation for net lowering of PV. Quantifying the role of non-conservative processes in the dynamics of the PV and other tracers is the subject of future research.

This work was supported by the National Oceanic and Atmospheric Administration grant NA06OAR4310058. The offline particle calculations were performed using ROMS offline floats written by X. Capet.

1.10 Gravity current formation from tropical instability wave fronts*

RYAN M. HOLMES AND LEIF N. THOMAS

Earth System Science, Stanford University, Stanford, California

1.10.1 Introduction*

We have seen how important the frontal regions around the TIW cold cusps are for the dynamics of the TIWs themselves (e.g. Section 1.6). These fronts can become very sharp and are known to shape the biological geography of the equatorial region (Yoder *et al.*, 1994). Due to their small lateral and vertical scales they are also a hot spot for frictional and diabatic processes (as discussed in Section 1.7), and may play an important role in the downscale transfer of energy and dissipation of the TIWs.

During a research cruise on the R/V Oceanus in late November 2014 a sharp front was observed near the trailing edge of a TIW cusp at -109.5°E , 0.75°N (Fig. 1.16). The front was characterized by a warm mass of water of approximately 30m depth moving south-westwards and overriding cooler water (Fig. 1.16a). The frontal gradient in temperature was sharp, with a 0.5°C change in temperature over less than 20m observed using the ships instruments (not shown). Large changes in the surface zonal and meridional velocity also occurred as the front passed (Fig. 1.16c,d). The warm side of the front was characterized by vigorous turbulence with the turbulent kinetic energy dissipation rate as measured using a shear microstructure instrument reaching 10^{-5}Wkg^{-1} (Fig. 1.16b).

This and previous (*McHugh*, 2013) observations of sharp fronts in the TIW cold cusp region open a number of important questions. 1) How do these sharp fronts form? 2) What are their dynamics? 3) How do they dissipate? 4) How important are they for the energetics of the TIW field? In order to address these questions, we analyze the results of a high-resolution ROMS simulation of the equatorial Pacific similar to those discussed in the earlier portions of this chapter (the model setup was described

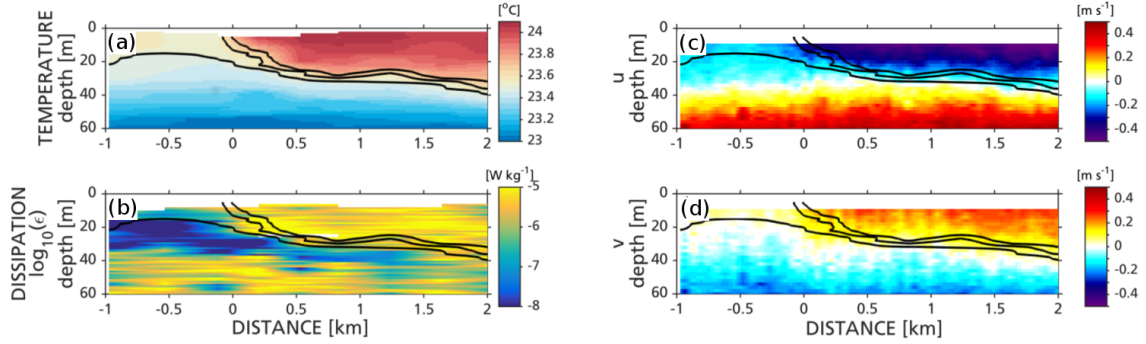


Figure 1.16: (a) Temperature, (b) turbulent kinetic energy dissipation rate ϵ , (c) zonal velocity and (d) meridional velocity measured along a ship track crossing a sharp front at -109.5°E , 0.75°N in November 2014. Figure provided by S. Warner and J. Moum from Oregon State University.

in Section 1.2.1). The simulation has 0.05° ($\sim 6\text{km}$) horizontal resolution and 50 vertical levels nested over the TIW region inside a Pacific basin-wide simulation with 0.25° horizontal resolution. In Section 1.10.2 we briefly describe the formation of the large-scale fronts in the TIW region. In Section 1.10.3 we describe how these fronts can sharpen to the point where their dynamics change and they become similar to an unbalanced gravity current. In Section 1.10.4 we examine whether these features do indeed propagate like gravity currents. In Section 1.10.5 we examine how the features dissipate. Section 1.10.6 summarizes and discusses the potential implications for TIW energetics.

1.10.2 Frontogenesis of the TIW fronts*

The North Equatorial Front (NEF), along the northern edge of the cold tongue, typically strengthens in boreal summer and fall due to a number of processes *De Szoeke et al.* (2007). At some point the background flow goes unstable and TIWs grow (*Philander*, 1976; *Cox*, 1980). The TIWs exert strain on the NEF driving frontogenesis and frontolysis, as quantified using the frontogenesis function HCL (Eq. (1.21)). At the large-scale, this process is similar to the straining of fronts by a mesoscale eddy field (i.e. *Hoskins and Bretherton* (1972)). Once the TIWs have fully developed there

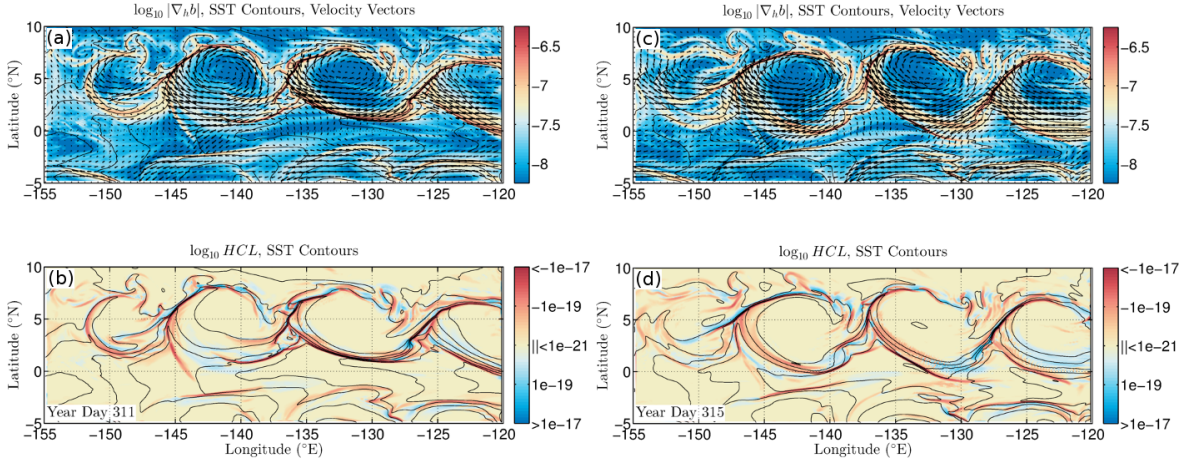


Figure 1.17: (a,c) The magnitude of the horizontal buoyancy gradient, SST contours and surface velocity vectors and (b,d) the frontogenesis function HCL (see Eq. (1.21)) from a 0.05° resolution simulation of the equatorial Pacific. Fields are shown on the 11th (a,b) and 16th (c,d) of November.

are a number of frontogenetic and frontolytic regions (Fig. 1.17). The strongest frontogenesis occurs along the leading northern and western edge of the TIW cold cusps where the SEC curves northwards into the NECC (e.g. near 6°N , -144°E , -136°E and -126°E in Fig. 1.17a,b). These leading edge fronts experience the strongest frontogenesis due to high lateral strain and have received much attention in the literature (Yoder *et al.*, 1994; Johnson, 1996). However, there are also strong fronts and frontogenesis along more southern trailing edge fronts on the eastern edge of the TIW cold cusps (e.g. near 2°N , -132°E in Fig. 1.17a,b). North-east of these fronts the westward flow of the northern SEC branch is strengthened in the southern part of the TIVs and strains the front against the relatively weak northward flow to the west of the front (velocity vectors in Fig. 1.17a,c).

The frontogenetic strain acting on the trailing edge front could be driven by a number of different processes:

1. TIW strain: The balanced component of TIW flow can drive confluence along the front. If barotropic instability contributes to the TIW instability process then the strain can be particularly large as temperature acts as a strained passive tracer. Also, the TIW flow can be across SST contours if the velocity

field becomes unbalanced as it approaches the equator. In Section 1.3.1 we showed that the centrifugal force plays a large role in the force balance of flow within a TIV, potentially driving flow across SST contours.

2. Convergence of zonal flow driven by vertical mixing: The SEC is strongest east of the trailing edge front because the stratification is high limiting momentum exchange with the EUC below. Within the cold cusp to the west of the front the stratification is low and the eastward momentum of the EUC penetrates to the surface.
3. Geostrophic Stress/Vertical Mixing: Strong vertical mixing within a front can drive time-dependence of the frontal flow and frontogenesis. Vertical mixing weakens the geostrophic shear allowing the pressure gradient force to accelerate flow towards the cold side of the front. For a non-uniform front, the resulting sheared cross-front flow varies across the front with the geostrophic shear and thus can drive convergence and frontogenesis. This can be thought of in terms of the convergence of an across-front Ekman transport associated with a *geostrophic stress* applied at the surface by the surface shear of the geostrophic flow (*Thompson*, 2000; *Cronin and Kessler*, 2009; *Wenegrat and McPhaden*, 2015). This process may be particularly important near the equator because the geostrophic stress is inversely proportional to f , and the resultant Ekman transport and convergence is inversely proportional to f^2 . In addition, the anticyclonic rotation of a TIV further lowers the effective f .
4. Air-sea feedbacks: The SST is warm east of the front destabilizing the atmospheric boundary layer and resulting in a stronger westward wind stress. On the cold western side of the front the boundary layer is more stable and thus the westward wind stress is weaker. This results in a convergent wind stress, but is likely to be minor for sharp fronts.

It is difficult to determine which process is acting at any particular time without further study outside the scope of this work. However, it is likely that TIW strain is the dominant process at the larger scales as it does not depend on small-scale

frictional processes.

Along the trailing edge front, frontogenesis is often sporadic with frontolysis and frontogenesis alternating in time and space. On a number of occasions in these simulations, the trailing edge front strengthens, propagates towards the equator and dissipates (e.g. compare Figures 1.17a,b with 1.17c,d near -134°E). In the following section we examine the frontal dynamics of the trailing edge front during an example of this process.

1.10.3 The formation of gravity currents*

Here we examine the behavior of a strong trailing edge front in the southern portion of a TIV. Initially (Fig. 1.18a-d) the front is characterized by strong along-front velocities with a change in along-front velocity $> 1\text{ms}^{-1}$ (Fig. 1.18c) across the frontal outcrop. Convergence in the across-front velocity at the surface, accompanied by downwards vertical velocity, drives frontogenesis (Fig. 1.18c). This front is similar to a submesoscale mid-latitude front, with stronger downward vertical velocity on the cold side of the front than upward vertical velocity on the warm side (*Shcherbina et al.*, 2013). The cold side is also characterized by strong cyclonic vorticity (not shown). As time progresses, the front moves towards the equator (Fig. 1.18e) and turns to orient NW-SE. The across-front velocities strengthen and the along-front velocities weaken (compare Figures 1.18c and 1.18g). By year day 314 the front looks like an gravity current, with the warm side flowing towards the front. The buoyancy gradient is focused at the frontal outcrop followed by a warm surface layer of $\sim 50\text{m}$ depth (Fig. 1.18f). The change in surface temperature across the front is 2°C in 15km.

To examine the dynamics acting as the front moves towards the equator, we consider the following across-front force balance:

$$\underbrace{\frac{\partial u}{\partial t}}_{ACC} = \underbrace{-u \frac{\partial u}{\partial x}}_{UADV} - \underbrace{v \frac{\partial u}{\partial y}}_{VADV} - \underbrace{w \frac{\partial u}{\partial z}}_{WADV} - \underbrace{\frac{1}{\rho_0} \frac{\partial P}{\partial x}}_{PGD} + \underbrace{fv}_{COR} + \underbrace{\frac{\partial}{\partial z} \left(\nu_{KPP} \frac{\partial u}{\partial z} \right)}_{VIS} + \nu_h \nabla_h^2 u \quad (1.28)$$

where u is the across front velocity, defined to be positive towards the warm side of

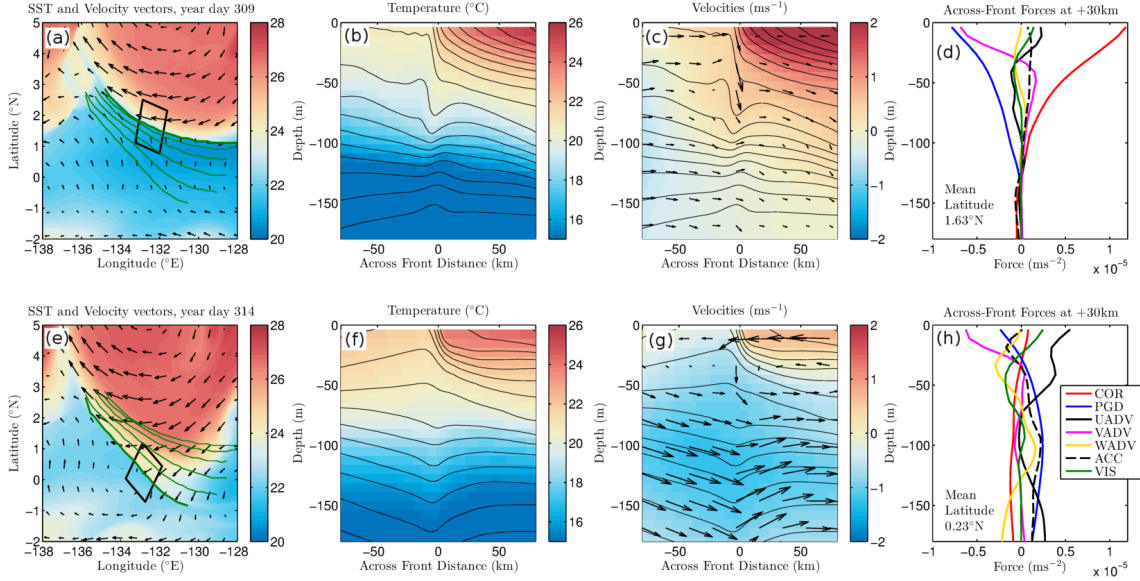


Figure 1.18: (a,e) SST and surface velocity vectors. Marked in green is the location of the trailing edge front on year days 309 – 314. The black box indicates the region over which along-front averages are taken. (b,f) Along-front average temperature with 0.2 kg m^{-3} isopycnals. (c,g) Along-front velocity and across-front + vertical velocity vectors. (d,h) Profiles of the across-front force balance at 30km on the warm side. The terms are from Eq. 1.28 and are described in the text. (a-d) are on year day 309 and show a TIW front at 1.63°N in a cyclogeostrophic balance between *COR*, *PGD* and *VADV*. (e-h) show the front on year day 314 where it has moved closer to the equator to 0.23°N and where the across-front advective force *UADV* has become important suggesting that the front has become a gravity current.

the front (positive x) and v is the along front velocity flowing with warm water on the right. The force balance is evaluated in the frame of the moving front, with the time derivative $\frac{\partial}{\partial t}$ calculated as a difference of subsequent across-front slices.

On day 309, the front is in a cyclogeostrophic balance between the pressure gradient force, the Coriolis force and the centrifugal force (blue, red and magenta lines in Fig. 1.18d), as was found in Section 1.3.1. As the front moves towards the equator (from a mean latitude of 1.63°N on day 309 to 0.23°N on day 314) f reduces and the Coriolis force weakens, breaking the cyclogeostrophic balance. The centrifugal and pressure gradient forces then drive the front to accelerate forwards. By year day 314 the Coriolis force is close to zero (red line in Fig. 1.18h). The barotropic component

of the pressure gradient force is also much weaker (compare the depth average of the blue line in Figures 1.18d and 1.18h) as a result of sea surface height changes (not shown). However, the baroclinic component is still strong. Most importantly, the along-front advective force $u \frac{\partial u}{\partial x}$ is now a dominant component of the force balance, indicating that the front is unbalanced with dynamics consistent with a gravity current.

1.10.4 Gravity current propagation*

In the previous section we saw evidence of the formation of a gravity current as the force $u \frac{\partial u}{\partial x}$ became important approaching the equator. In this section we compare the frontal propagation speed to two simple gravity current models. The gravity current models are discussed in *McHugh* (2013). The first model is based on a simple two-layer system,

$$c_{GCS} = \sqrt{g' h_0} \quad (1.29)$$

$$g' = g(\rho_a - \rho_c)/\rho_a, \quad (1.30)$$

where c_{GCS} is the predicted propagation speed, ρ_a is the density of ambient fluid in the lower layer and ρ_c is the density of the gravity current or upper layer that has depth h_0 . The ocean model we are using has continuous stratification and thus in order to make a comparison we must estimate some representative h_0 that approximates the depth of the current. We take $h_0 = 60\text{m}$ as by this depth the frontal temperature gradient in the model changes sign (Figures 1.18b,f). We take ρ_a and ρ_c as the average surface densities on the cold and warm sides of the front respectively out to distances between 15km and 80km from the frontal outcrop, with the spread in results between these used to estimate the uncertainty.

The second model is based on assuming that the front obeys an advection - pressure gradient force balance, which leads to the expression (*McHugh*, 2013),

$$c_{FB} = \sqrt{\frac{-2}{h_0 \rho_a} \int_{-h_0}^0 P(z) dz} \quad (1.31)$$

where c_{FB} is the predicted propagation speed from this model, and $P(z)$ is the vertical pressure profile evaluated within the current on the warm side. We evaluate $P(z)$ at distances between 15km and 80km to the warm side of the front and use the spread in values as an estimate of the uncertainty, as for the two-layer model above.

We compare these two gravity current model propagation speeds to the measured speed of the front discussed in the previous section (Fig. 1.19). The front speed is measured in the simulations by comparing the position of the maximum in the horizontal buoyancy gradient between subsequent times and taking the component of the velocity perpendicular to the frontal line. The background flow speed, defined as the average across-front velocity $\pm 80\text{km}$ on either side of the front over the depth of the current h_0 (dotted line with stars in Fig. 1.19), is subtracted from the translation speed of the front to extract the self-translation of the frontal feature (solid line with circles in Fig. 1.19). The resultant speed shows an acceleration of the front between year days 309 and 313, consistent with the loss-of-balance discussed in the previous section. After this acceleration, the frontal propagation speed compares well with the two gravity current models, suggesting that the front has indeed become a gravity current.

1.10.5 Dissipation of the gravity current*

In this section we examine how the gravity current-like features dissipate after leaving the main TIW front. The feature considered in the previous section dissipates as a result of a wind event that deepens the boundary layer through mixing, removing the velocity shear and stratification of the current (not shown). However, this wind event is fortuitous and not likely to be general mechanism for the dissipation of these features.

To establish the likely dissipation mechanism, we examine the energy budget of a decaying feature traveling westward along the equator after detaching from a TIW trailing edge front (Fig. 1.20). The feature is characterized by strongly sheared southwestward flow in the upper 50m overlying the easterly flowing EUC. The across-front anomalies in temperature and velocity associated with the feature decay over a 8-day

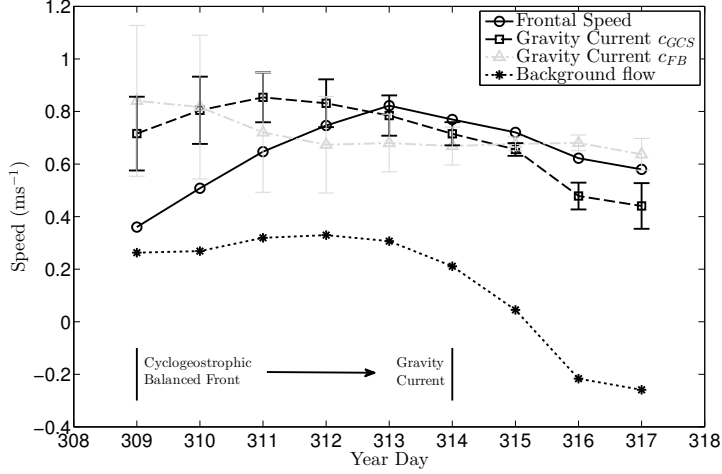


Figure 1.19: Propagation speed of the front considered in Fig. 1.18 with time (solid line). The background flow speed (dotted line) has been subtracted to obtain the self-translation speed of the frontal feature. Also shown are the predictions of two gravity current speed models (dashed black and gray lines) from equations (1.30) and (1.31). The error bars represent the $\pm 2\sigma$ spread over speeds calculated using lateral current scales of 15km to 80km as discussed in the text.

period between year days 250 and 258 (compare Figures 1.20a,d with 1.20c,f). No strong wind events occur in the vicinity of the feature over its lifetime.

To establish why the feature dissipates, we examine the kinetic energy budget of the feature (in the along-front averaged framework) by using the deviation from an across-front average $\mathbf{u}' = \mathbf{u} - \bar{\mathbf{u}}$ to define the feature,

$$\frac{\partial K_{GC}}{\partial t} = \underbrace{\rho_0 \int_{-W}^W \int_{-H}^0 \mathbf{u}' \cdot \mathbf{F}'_V dx dz}_{\mathcal{F}_V} + \underbrace{\rho_0 \int_{-W}^W \int_{-H}^0 \mathbf{w}' b' dx dz}_{\mathcal{P}} + \underbrace{\text{other terms}}_{\mathcal{R}}, \quad (1.32)$$

where the across-front average is defined by $\overline{\alpha(x, z)} \equiv \frac{1}{2W} \int_{-W}^W \alpha(x, z) dx$, where α is any along-front averaged variable, x is the across-front direction and W is the across-front width defining the feature over which the average is taken. $K_{GC} = \frac{1}{2} \rho_0 \int_{-W}^W \int_{-H}^0 (u'^2 + v'^2) dx dz$ is the kinetic energy of the feature, $\frac{\partial}{\partial t}$ represents the tendency following the feature. \mathcal{F}_V represents changes in kinetic energy due to the frictional force resulting from vertical viscosity \mathbf{F}_V (parameterized using KPP) and

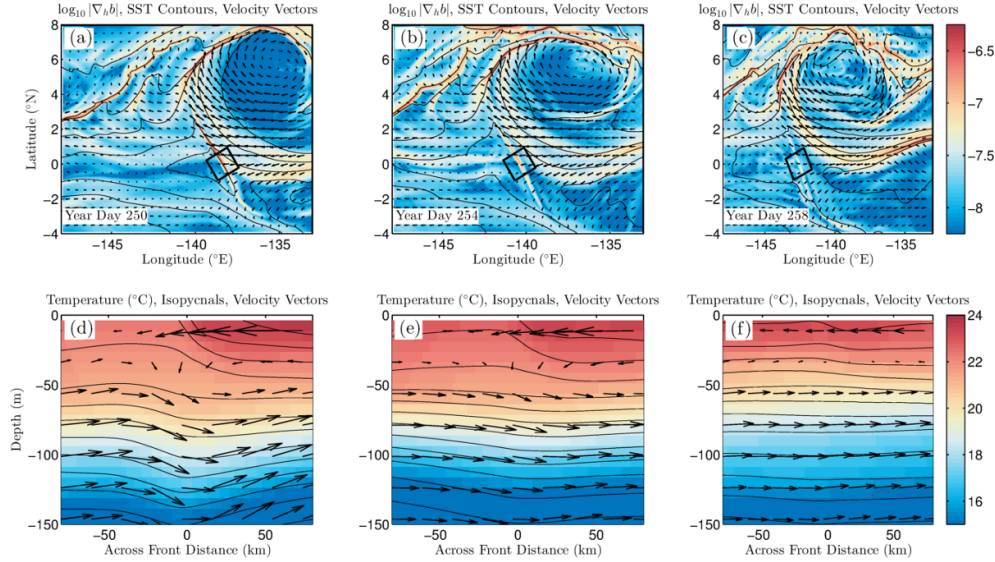


Figure 1.20: (a-c) Magnitude of the surface horizontal buoyancy gradient, with SST contours and surface velocity vectors and (d-f) across-front slices averaged along the front within the black boxes shown in (a-c). Plots are shown on 3 different days separated by 4 days. The gravity current-like feature decays as it propagates away from a trailing edge front.

\mathcal{P} represents conversion to potential energy accomplished through the buoyancy flux $w'b'$. We have lumped other terms such as horizontal friction, advective and pressure fluxes and kinetic energy exchanges with the mean flow into the residual \mathcal{R} . Time integrating this equation beginning at year day $t_0 = 250$ (i.e. Fig. 1.20d) gives,

$$K_{GC}(t) = \int_{t_0}^t \mathcal{F}_V dt + \int_{t_0}^t \mathcal{P} dt + \int_{t_0}^t \mathcal{R} dt + K_{GC}(t_0) \quad (1.33)$$

We calculate this time-integrated budget for the feature shown in Fig. 1.20 using an across-front width $W = 50\text{km}$ over the upper 150m (Fig. 1.21). The available potential energy (APE) is also calculated in the across-front frame using a resorting of the density field. However, the APE of the feature is much smaller than its kinetic energy as the frontal length scale is much smaller than the Rossby radius of deformation (Gill, 1982). Both the kinetic energy (solid line in Fig. 1.21) and APE (gray line in Fig. 1.21) of the feature decay as it travels westwards between year days

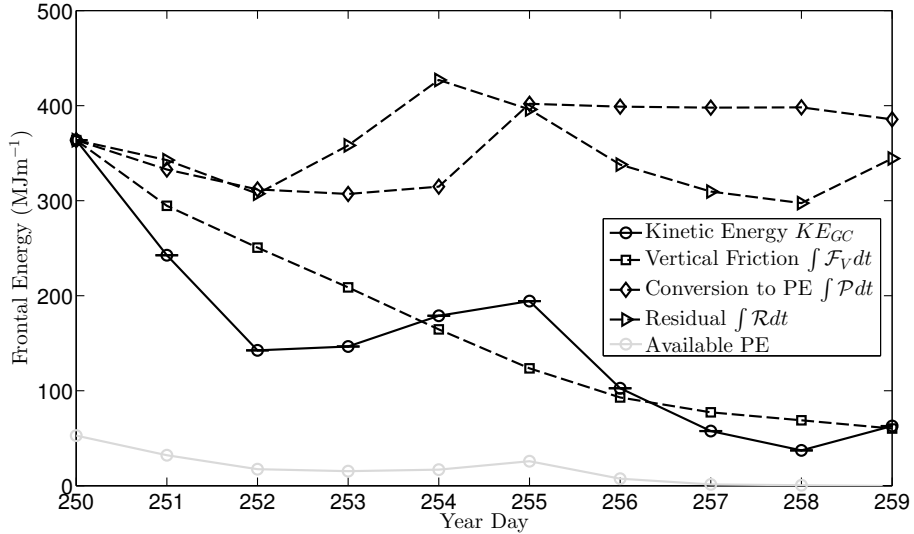


Figure 1.21: Energy budget per unit length along the gravity current feature shown in Fig. 1.20. The solid black line represents the kinetic energy of the feature and the solid gray line the available potential energy of the feature, both of which decay over this time period. The dashed lines represent the vertical friction (squares), conversion to potential energy (diamonds) and residual (triangles) terms in the time-integrated kinetic energy budget (Eq. (1.33)). The initial kinetic energy has been added to these terms. The vertical friction term drives a rapid decay in the kinetic energy of the feature.

250 and 259. The main cause for the decay in kinetic energy is the vertical friction term (dashed line with squares in Fig. 1.21). Neither the conversion to potential energy term (dashed line with diamonds in Fig. 1.21) nor the residual term (dashed line with triangles in Fig. 1.21) make sustained contributions to the kinetic energy tendency. We conclude that the main dissipation mechanism is the vertical mixing of momentum driven by high vertical shear as the feature translates westwards over the eastwards flowing EUC.

1.10.6 Summary and potential implications for TIW energetics*

Motivated by a number of recent observations of very sharp fronts near the trailing edge of TIW cold cusps, we have examined the formation of similar features in a

high-resolution model of the equatorial Pacific. In the simulations, the features are formed from TIW trailing edge fronts that are initially in cyclogeostrophic balance (Fig. 1.18d). As the front propagates towards the equator, f reduces allowing the centrifugal and pressure gradient forces to accelerate the across-front flow and front propagation speed. The across-front advective force $u \frac{\partial u}{\partial x}$ becomes important in the force balance (Fig. 1.18h), suggesting that the feature has become a gravity current. The propagation speed of the feature agrees closely with theoretical estimates for the propagation speed of a gravity current (Fig. 1.19), adding further support to this hypothesis. Finally, the features appear to dissipate in general through the action of vertical friction as they override the EUC (Fig. 1.21).

The gravity current features are formed from TIW trailing edge fronts, suggesting that they ultimately extract energy from the large-scale TIW field. In order to quantify this energy loss mechanism for the TIWs, we perform a simple scaling calculation. Over the 60-day time period of the simulations, 4 strong gravity current emission events were identified by eye over the TIW region. The energy budget calculation (Fig. 1.21) suggests that the features contain $\sim 400 \text{ MJm}^{-1}$ of energy. The length of a feature is $\sim 500 \text{ km}$ (e.g. Fig. 1.20a). Combining these rough estimates suggests that the emission of the gravity current-like features constitutes an energy drain of 0.15 GW for the total TIW field. This is around two orders of magnitude smaller than the main PE conversion and lateral shear production energy sources for the TIW field (see Chapter 3 Fig. 3.3 and *Tanaka et al. (2015)*), suggesting that these features do not play an important role in the overall energetics of the TIWs. However, the estimate is rough and may change depending on model resolution and other factors. More research and observations are required to more thoroughly answer the question as to whether these gravity currents play an important role in TIW energetics. In addition, these features constitute an interesting case study for frontal dynamics in a unique parameter regime, and their influences on biological processes also warrant further study.

Chapter 2

Tropical Instability Waves and Vertical Mixing

RYAN M. HOLMES AND LEIF N. THOMAS

Earth System Science, Stanford University, Stanford, California

Small-scale turbulent mixing in the upper Equatorial Undercurrent (EUC) of the eastern Pacific cold tongue is a critical component of the SST budget that drives variations in SST on a range of time-scales. Recent observations have shown that turbulent mixing within the EUC is modulated by Tropical Instability Waves (TIWs). A regional ocean model is used to investigate the mechanisms through which large-scale TIW circulation modulates the small-scale shear, stratification and shear-driven turbulence in the EUC. Eulerian analyses of time series taken from both the model and the Tropical Atmosphere Ocean (TAO) array suggest that increases in the zonal shear of the EUC drive increased mixing on the leading edge of the TIW warm phase. A Lagrangian vorticity analysis attributes this increased zonal shear to horizontal vortex stretching driven by the strain in the TIW horizontal velocity field acting on the existing EUC shear. To investigate the impact of horizontal vortex stretching on the turbulent heat flux averaged over a TIW period the effects of periodic TIW strain are

included as forcing in a simple 1D mixing model of the EUC. Model runs with TIW forcing show turbulent heat fluxes up to 30% larger than runs without TIW forcing, with the magnitude of the increase being sensitive to the vertical mixing scheme used in the model. These results emphasize the importance of coupling between the large-scale circulation and small-scale turbulence in the equatorial regions, with implications for the SST budget of the equatorial Pacific.

The material in this chapter has been reproduced from *Holmes and Thomas* (2015) © copyright 2015 AMS, with the authors and abstract reproduced above.

2.1 Introduction

Small-scale turbulent mixing of heat in the tropical Pacific is an important component of the Sea Surface Temperature (SST) budget and contributes to changes in SST over a range of time-scales. Variations in diapycnal turbulent transport play a role in the seasonal cycle of SST (*Moum et al.*, 2013) and the diurnal cycle in SST (*Bernie et al.*, 2005; *Danabasoglu et al.*, 2006). Modulations in turbulence at time-scales of weeks to months associated with intraseasonal Kelvin waves (*Lien et al.*, 1995; *McPhaden*, 2002), the Madden-Julian Oscillation (*Chi et al.*, 2014) and Tropical Instability Waves (TIWs) (*Menkes et al.*, 2006; *Moum et al.*, 2009; *Inoue et al.*, 2012) may have an important impact on the mean state of the Pacific Ocean and thus on global climate.

Generated in the eastern tropical Pacific and Atlantic Oceans, TIWs propagate westwards with wavelengths of 700-1600km and periods of 15-40 days (*Qiao and Weisberg*, 1995; *Kennan and Flament*, 2000; *Willett et al.*, 2006; *Lyman et al.*, 2007). TIWs are generated through barotropic and baroclinic instability of the mean equatorial current system (*Philander*, 1976; *Cox*, 1980; *Masina et al.*, 1999; *Lyman et al.*, 2005), and vary seasonally and interannually, obtaining peak amplitudes in boreal fall and winter and in La Niña conditions (*Contreras*, 2002; *An*, 2008). Near the Equator, TIW meridional advection of the equatorial fronts results in several °C variations in SST, organized into alternating warm and cold phases. TIWs and their associated vortices (TIVs) drive lateral heat fluxes that warm the cold tongue by $\sim 1^{\circ}\text{C}/\text{month}$

(Menkes *et al.*, 2006; Jochum *et al.*, 2007; Graham, 2014), potentially contributing to the asymmetry of the ENSO cycle (An, 2008; Imada and Kimoto, 2012). Jochum and Murtugudde (2006) suggested that TIWs warm the cold tongue not through typical eddy mixing, but instead through modifications of the air-sea fluxes and vertical entrainment. The modifications of air-sea fluxes by TIWs have received considerable attention (Thum *et al.*, 2002; Seo *et al.*, 2007; Small *et al.*, 2009), while the modifications of vertical entrainment by TIWs have been observed only recently.

These observations have shown that TIWs modulate vertical mixing in the upper EUC (Lien *et al.*, 2008; Moum *et al.*, 2009; Inoue *et al.*, 2012). Here, the gradient Richardson number (Ri) of the flow is preconditioned to drop below the critical value for shear instability of 1/4, where

$$Ri = N^2 / \left(\left(\frac{\partial u}{\partial z} \right)^2 + \left(\frac{\partial v}{\partial z} \right)^2 \right), \quad (2.1)$$

$N^2 = \frac{\partial b}{\partial z}$ is the buoyancy frequency squared, $b = -g\rho/\rho_0$ is the buoyancy, g is the acceleration due to gravity, ρ is the potential density, ρ_0 is a reference density and u, v are the zonal and meridional velocities respectively. A telltale signature that shear instabilities have been active is for a flow to be in a state of marginal stability, where the Richardson number is close to 1/4 and the reduced shear squared,

$$Sh_{red}^2 \equiv \left(\frac{\partial u}{\partial z} \right)^2 + \left(\frac{\partial v}{\partial z} \right)^2 - 4N^2, \quad (2.2)$$

is near zero. Indeed, observations show that for three quarters of the year, the upper EUC is in this state (Smyth and Moum, 2013). Using a Lagrangian float, Lien *et al.* (2008) observed that the vertical entrainment flux at the base of the mixed layer varied with TIW phase along the Equator, with the highest values occurring leading into the TIW warm phase. They attributed this increase in entrainment flux to an increase in the Sh_{red}^2 , and pointed out that it could not be explained by variations in wind-driven mixing. More recently, Inoue *et al.* (2012) observed modifications of deep-cycle turbulence (a layer of strong turbulence below the mixed layer which shows a distinct diurnal cycle), mixed layer depth and the turbulent heat flux with TIW

phase using a two-week time series of micro-structure profiles at -140°E , 0°N . Their measurements show that the highest values of Sh_{red}^2 , dissipation, and turbulent heat flux occur at the leading edge of the TIW warm phase when the meridional velocity switches from northward to southward, consistent with the observations of *Lien et al.* (2008).

The mechanism through which TIWs modulate small-scale turbulent mixing is not known. *Moum et al.* (2009) hypothesized that the extra meridional shear added by TIWs can push the marginally stable reduced shear squared above the EUC core over the threshold for shear instability producing stronger turbulence. However, the meridional shear associated with TIWs is significantly weaker than the zonal shear in this region (see Fig. 4 of *Inoue et al.* (2012)). TIWs also influence both zonal velocities and the density field near the Equator (*Lyman et al.*, 2007; *Jochum et al.*, 2007; *Inoue et al.*, 2012), suggesting that other processes may be at play. It is also unclear if TIW-induced variations in mixing lead to a net cooling or warming of equatorial SSTs. *Moum et al.* (2009) observed turbulent mixing associated with TIWs that drove surface cooling of $1 - 2^{\circ}\text{C/month}$. In contrast, the modeling study of *Menkes et al.* (2006) found that variations in the vertical turbulent entrainment flux on TIW time scales had a rectified warming influence of $0.37^{\circ}\text{C/month}$. In this article we identify the mechanism responsible for the modulation of mixing by TIWs in a regional ocean model of the equatorial Pacific with a highly resolved TIW field. These simulations are combined with a one-dimensional (1D) vertical mixing model to quantify the net turbulent heat fluxes associated with TIWs and assess their sensitivity to the vertical mixing parameterization scheme.

The article is organized as follows. Section 2.2 describes the ocean model and evaluates its performance in the upper EUC in comparison to observations from the Tropical Atmosphere Ocean (TAO) mooring array (*McPhaden et al.*, 1998). Section 2.3 examines the factors influencing mixing on TIW time scales in the upper EUC, using both the model and TAO data. Section 2.4 examines the dynamics behind the modulation of mixing by TIWs using a Lagrangian analysis. Section 2.5 examines the total influence of TIWs on the turbulent heat flux using a simple 1D mixing model of the EUC and Section 2.6 discusses and summarizes the results.

2.2 Model and general flow description

This section describes the ocean model setup (Section 2.2.1) and its main features, evaluates its performance in comparison to observations (Section 2.2.2) and discusses a feature of the observations not well represented in the model, that of marginal stability (Section 2.2.3).

2.2.1 Ocean model setup

In this article we analyze results from a set of 3D nested simulations of the equatorial Pacific performed with the Regional Ocean Modeling System (ROMS) (*Shchepetkin and McWilliams*, 2005). The outer nest is a Pacific basin-wide simulation over the region -240°E to -70°E , 30°S to 30°N with 0.25° horizontal resolution, 50 vertical levels and a time step of 10 minutes. It was spun-up for 5 years, initialized from a previous 10 year spin-up run (*Holmes et al.*, 2014). Daily climatological surface forcing, initial conditions and boundary conditions were taken from the Common Ocean Reference Experiment Normal Year Forcing field (*Large and Yeager*, 2004). In addition, a diurnal cycle in shortwave radiation was imposed, as we found this was necessary to produce the appropriate shear and stratification in and near the mixed layer (not shown), consistent with the studies of *Kawai and Wada* (2007) and *Bernie et al.* (2007). At the meridional boundaries temperature and salinity were nudged to climatological values, while zonal and meridional velocities were nudged to zero. Monthly climatological nudging was used in the western Pacific warm pool in order to maintain the tropical pycnocline. The K-profile parameterization (KPP) vertical mixing scheme was used to parameterize sub-grid scale vertical mixing processes (*Large et al.*, 1994). Its role is discussed further in Sections 2.2.3 and 2.5.

In order to perform Lagrangian particle advection and analyze Lagrangian shear and stratification budgets (Section 2.4), a high-resolution simulation was nested offline inside the last year of the basin-wide simulation over the region -155°E to -120°E , 5°S to 10°N . This nest has a horizontal resolution ($1/20^{\circ}$, $\sim 6\text{km}$) below the 10km reported by *Marchesiello et al.* (2011) as required for numerical convergence as measured by an invariance of the kinetic energy spectrum with resolution. In the

high-resolution simulation, a combination of nudging and radiation boundary conditions were used, with the exception of a clamped condition on the eastern boundary for tracers. These boundary conditions were taken from the outer nest at daily resolution. Horizontal diffusion of momentum was achieved with a bi-harmonic viscosity with coefficient $1 \times 10^{10} \text{m}^4\text{s}^{-1}$ (high-resolution) and $1 \times 10^{11} \text{m}^4\text{s}^{-1}$ (basin-wide) and harmonic horizontal diffusion of salinity and temperature was included with coefficient $100 \text{m}^2\text{s}^{-1}$. ROMS has been successfully used for process studies of TIWs under similar configurations (*Marchesiello et al.*, 2011; *Holmes et al.*, 2014). In the next subsection we discuss the general features of the model near the Equator and evaluate the model performance by comparison to observations from the TAO array.

2.2.2 General flow description and evaluation of model performance

The model produces vigorous TIWs with meridional velocities reaching 0.5ms^{-1} on the Equator (Fig. 2.1b) that advect the north equatorial front across the Equator inducing SST variations of order 2°C (Figures 2.1a and 2.2), consistent with the findings of *Qiao and Weisberg* (1995) and *Inoue et al.* (2012). North of the Equator, Tropical Instability Vortices (TIVs) centered around 4°N are characterized by an anticyclonic circulation with vorticity close to $-f$ (f is the Coriolis parameter), that induces variations in zonal velocity and stratification (*Holmes et al.* (2014) and Fig. 2.2). These features and the spatial structure of the TIWs and TIVs are consistent with the observations of *Qiao and Weisberg* (1995) and *Kennan and Flament* (2000).

In this article we focus on the upper EUC shear layer between the EUC core and the mixed layer, where the shear, stratification and Sh_{red}^2 are largest (Figures 2.1c-e,g and 2.2a-c). This layer contains the turbulent deep-cycle and upper-core layers observed by *Inoue et al.* (2012). These are manifest in the model as an enhancement of the daily-averaged vertical diffusivity, which reaches values $> 10^{-3} \text{m}^2\text{s}^{-1}$ at these depths (Fig. 2.2d). The model contains variations in a number of properties, including the Sh_{red}^2 , with TIW phase. These modulations are discussed in Section 2.3.

Profiles of model vertical shear and stratification averaged over the TIW season

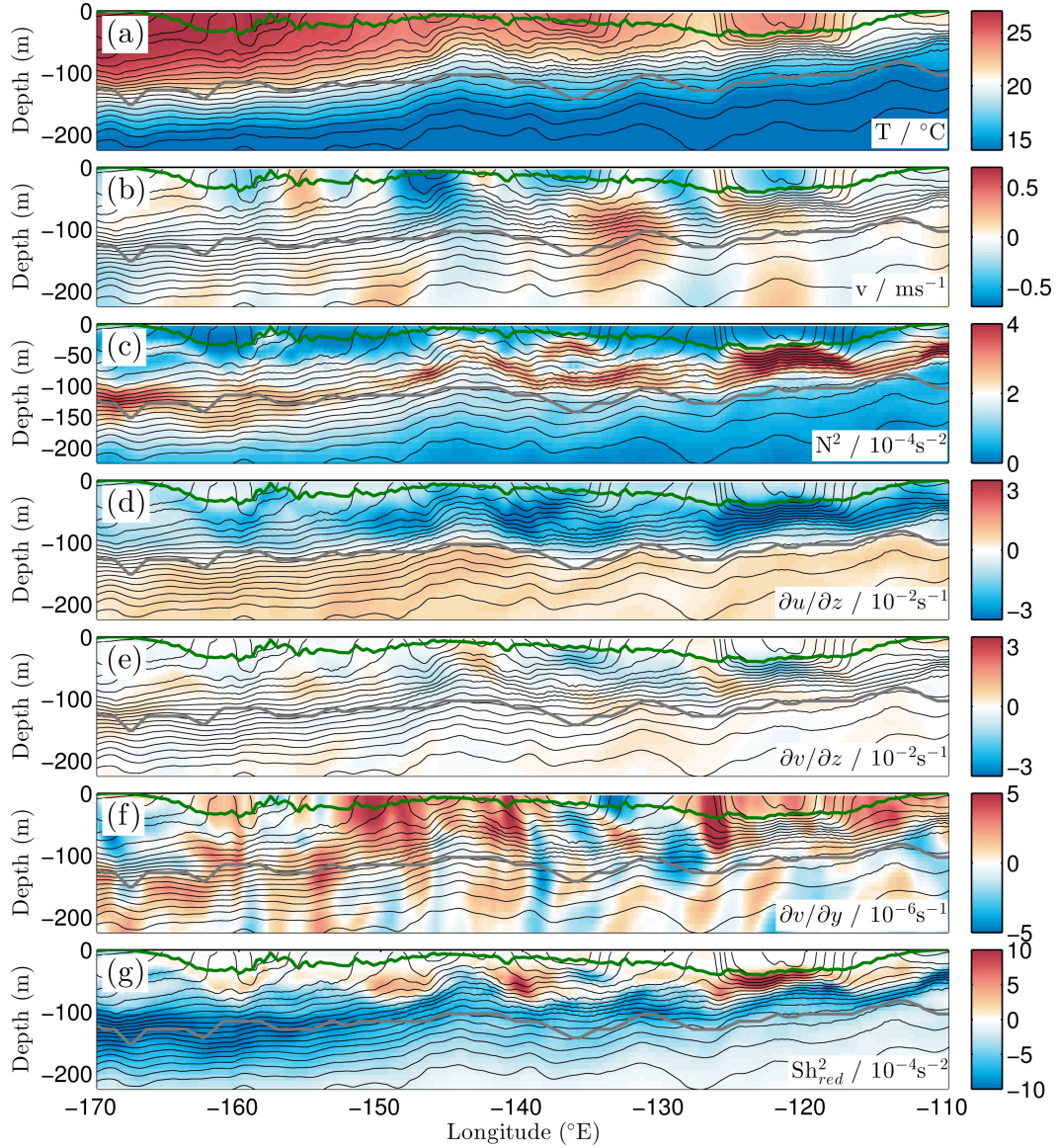


Figure 2.1: Daily-averaged (a) temperature, (b) meridional velocity, (c) stratification, (d) zonal shear, (e) meridional shear, (f) meridional difffluence and (g) reduced shear squared along the Equator on year day 262.5 of the basin-wide ROMS simulation. The dark green lines indicate the depth of the KPP mixed layer, the gray lines indicate the depth of the EUC core and the black contours are isopycnals at 0.2 kg m^{-3} spacing. High Sh_{red}^2 generally occurs at the leading edge of a TIW warm phase and is accompanied by high zonal shear and preceded by meridional difffluence.

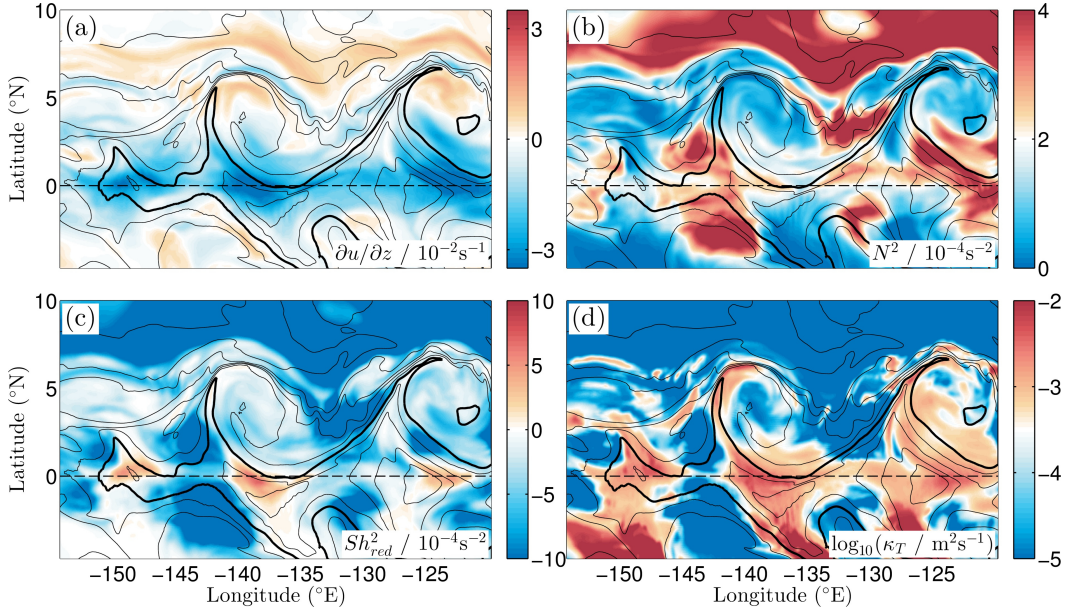


Figure 2.2: Daily-averaged (a) zonal shear, (b) stratification, (c) reduced shear squared and (d) vertical diffusivity at 72m depth on year day 262.5 of the high-resolution ROMS simulation. Also shown are contours of SST at 0.75 $^{\circ}$ C intervals, with the 25° isotherm highlighted in bold. The dashed line indicates the Equator. In (c), three patches of high Sh_{red}^2 are visible at the leading edge of TIW warm phases.

(Sep-Dec) of the last year of the basin-wide simulation compare favorably with data taken from the TAO array mooring at -140° E, 0° N (Fig. 2.3). The TAO data is averaged over the neutral-ENSO years 1996, 2001, 2003 and 2005. The zonal shear in the model compares well with the TAO data in the upper EUC shear layer (compare red dashed line with black line in Fig. 2.3a), but the shear below the EUC core is too weak. The average EUC core depth is 10m too deep in the model (134m in ROMS vs. 122.5m in the TAO observations). The stratification is stronger in the surface layer and the pycnocline is slightly weaker in the model (compare red dashed line with black line in Fig. 2.3b). However, the stratification due to salinity is not included in the observations and the profile of stratification due to salinity from the model (green dashed line in Fig. 2.3b) suggests that the comparison may be improved if salinity data from the TAO mooring was available. The model Sh_{red}^2 compares well with the observations throughout the upper 150m where data is available. Above 80m

the mean Sh_{red}^2 is close to zero in both the observations and the model, in agreement with the observations of *Smyth and Moum* (2013). However, the daily-averaged Sh_{red}^2 does reach positive values on some occasions, as discussed in the next section.

2.2.3 Marginal stability

In the model, the daily-averaged Sh_{red}^2 occasionally reaches positive values well above the criteria for K-H instability (Figures 2.1g and 2.2c). *Smyth and Moum* (2013) showed that six-hourly averaged profiles of the Richardson number in the upper EUC remain in a state of marginal stability, a characteristic not reproduced by the model. In these regions the KPP vertical diffusivity (Fig. 2.2d) approaches its maximum interior value of $K_0 = 2 \times 10^{-3} \text{ m}^2 \text{s}^{-1}$ (see Section 2.5). This suggests that the mixing scheme is not able to provide enough mixing at high Sh_{red}^2 in order to restrict the Sh_{red}^2 to negative or near zero daily-averaged values.

To evaluate the influence of this issue on our results, we constructed an algorithm to enforce marginal stability offline for all regions in the simulations where $Sh_{red}^2 > 0$. The algorithm is similar to the *Price et al.* (1986) mixing scheme and iteratively applies vertical fluxes of temperature, salinity and momentum in a Prandtl number one ratio until regions of $Sh_{red}^2 > 0$ are removed, subject to the constraints of conservation of heat, salt and momentum (see Section 2.7 for a description of the algorithm). The resulting profiles have regions of marginal stability (Fig. 2.4 between 100m and the surface) bordered by thin regions with strong momentum and buoyancy gradients (Fig. 2.4 near 100m), in agreement with theories of eddy-driven mixing (*Holzer and Siggia*, 1994). This algorithm will be used in Sections 2.3 and 2.4 to evaluate the impact of not enforcing marginal stability on our results. The KPP interior mixing parameterization for shear instability and its relation to marginal stability are examined in more detail in Section 2.5.

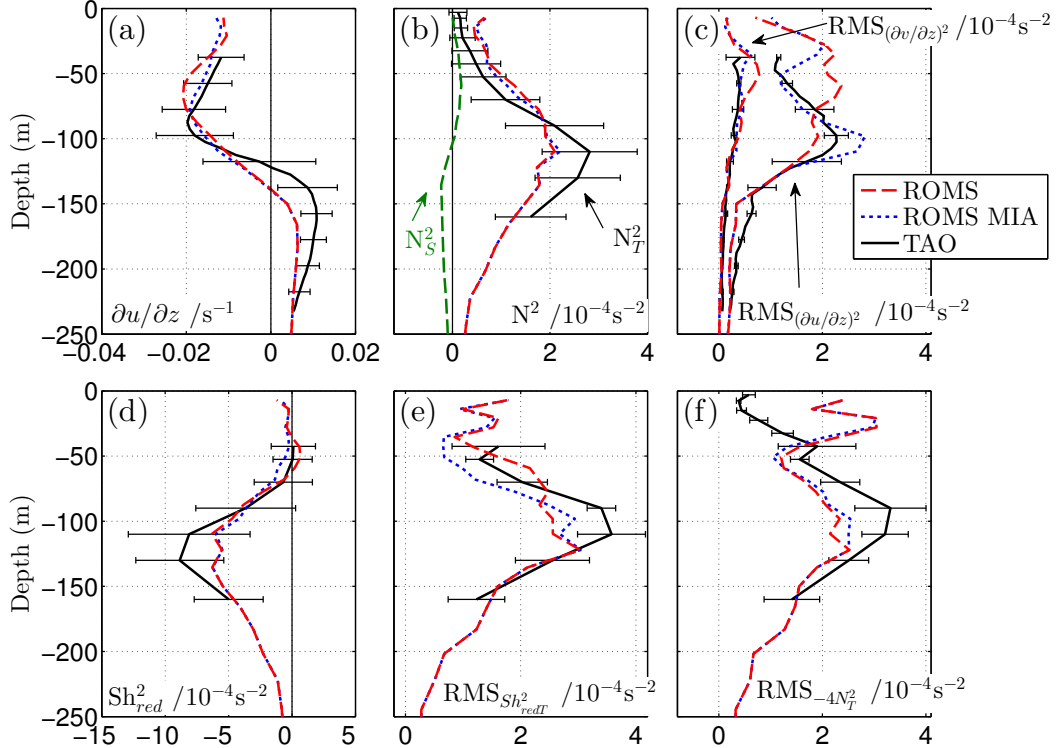


Figure 2.3: Comparison of mean profiles at -140°E , 0°N from the TAO array mooring (black lines) with the basin-wide ROMS simulation without and with adjustment to marginal stability (red dashed and blue dotted lines respectively). The profiles are averaged over the September-December period. The TAO data is averaged over the neutral-ENSO years 1996, 2001, 2003 and 2005. (a) Mean zonal velocity shear and (b) mean stratification, where the green dotted N_S^2 line indicates the buoyancy gradient due only to salinity in ROMS. The TAO data N_T^2 is calculated only with temperature. (d) Mean reduced shear squared. Root mean square (RMS) temporal variations in the (c) zonal and meridional shear squared, (e) reduced shear squared using only temperature stratification and (f) temperature stratification. The RMS values are obtained by taking the square root of the total power between the frequencies $1/50 \text{ day}^{-1}$ and $1/5 \text{ day}^{-1}$ calculated from the power spectrum of the respective variables in the months September-December. The error bars represent the $\pm 2\sigma$ standard error spread over the four neutral-ENSO years included in the TAO calculation.

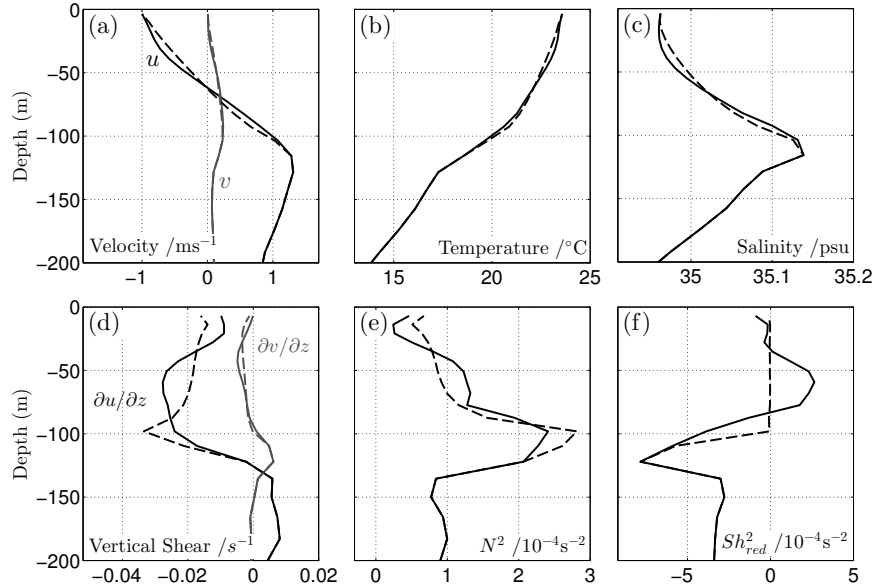


Figure 2.4: Vertical profiles of (a) velocity, (b) temperature, (c) salinity, (d) vertical shear, (e) stratification and (f) reduced shear squared at -140°E , 0°N on year day 268.5 from the model. The solid lines show the original profiles and the dashed lines show the profiles after adjustment to marginal stability ($Sh_{red}^2 = 0$) for unstable regions ($Sh_{red}^2 > 0$) using the algorithm described in Section 2.7. Note the reduction in shear and stratification in the unstable region between 40m and 80m depth, and the consequent accumulation of shear and stratification on the edges of this region.

2.3 Eulerian TIW modulation of shear and stratification

This section examines the variations in shear, stratification and mixing on TIW time and length scales. Temperature, velocity, vertical shear and stratification all vary around their mean state along the Equator as a function of TIW phase (Figures 2.1 and 2.2). The highest Sh_{red}^2 , where the most mixing is expected, occurs on the leading edge of TIW induced warm perturbations (Fig. 2.2c), highlighted by near-surface bowl-shaped isopycnals (Fig. 2.1a,g near -159°E , -149°E , -141°E and -125°E). This is in agreement with the observations of *Lien et al.* (2008). This phase of the TIW generally corresponds to a change in meridional velocity from northwards to southwards (Fig. 2.1b), in agreement with the observations of *Inoue et al.* (2012).

Each component of the Sh_{red}^2 , the stratification, zonal shear and meridional shear (Fig. 2.1c-e), varies at TIW length scales along the Equator. While the variations in meridional shear (Fig. 2.1e) are the clearest, they are weaker in magnitude than the variations in zonal shear and stratification, and are not clearly correlated with the Sh_{red}^2 (compare Figures 2.1e and 2.1g near patches of high Sh_{red}^2). While the stratification shows large variations relative to its mean, it appears to be stronger in patches of high Sh_{red}^2 (compare Figures 2.1c and 2.1g). The zonal shear also shows large variations relative to its mean, with strongly negative zonal shear patches closely correlated with high Sh_{red}^2 patches (compare Figures 2.1d with 2.1g and 2.2a with 2.2c). This suggests that increases in zonal shear are responsible for the patches of high Sh_{red}^2 .

To quantitatively analyze temporal variations in the shears, stratification and mixing due to TIWs, we calculated their RMS variation over the TIW frequency band by taking the square root of the total power between periods of 5 and 50 days from the power spectrum of time series at each depth at -140°E , 0°N (Figures 2.3c,e,f). Average RMS values were also obtained from the TAO observations by calculating individual spectra for Sep-Dec of each year. The shape of the profiles and the comparative results were found to be insensitive to the frequency window used. The vertical motion of the EUC core did not influence the results discussed below, as tested by calculating the RMS values in EUC core relative depth coordinates (not shown).

There are strong temporal variations in Sh_{red}^2 at TIW frequencies (Fig. 2.3e), with the RMS value approaching the magnitude of the mean Sh_{red}^2 (compare Figures 2.3e and 2.3d). As for the variations with longitude (Fig. 2.1), the temporal variations in Sh_{red}^2 at -140°E , 0°N are due to variations in zonal shear squared ($RMS_{(\partial u/\partial z)^2}$ in Fig. 2.3c) and stratification (Fig. 2.3f). The variations in meridional shear squared ($RMS_{(\partial v/\partial z)^2}$ in Fig. 2.3c) at TIW frequencies are much weaker than the other components in both model and observations. This suggests that TIW meridional shear is not directly responsible for the modulation of vertical mixing, contrary to the hypothesis of *Moum et al.* (2009). *Jing et al.* (2014) also noted that temporal variations in the amplitude of 2hr-8day oscillations in the upper EUC, potentially linked to higher

frequency motions and turbulence, were more correlated with variations in the EUC zonal shear than with the meridional shear of TIWs.

The model and observed RMS values agree well below the surface layer (compare red dashed lines and black lines in Figures 2.3c,e,f). The temporal variation in stratification (Fig. 2.3f) is weaker in the model than the observations, which may be a result of the weaker thermocline in the model (Fig. 2.3b). The largest discrepancy between model and observations is in the temporal variations in zonal shear squared in the upper EUC between 120m and 40m (compare red dashed and black lines in Fig. 2.3c). The vertical structure is different, with the model zonal shear varying too much in the upper half of this region and too little in the lower half. These differences were traced to the failure of the KPP interior mixing scheme to enforce marginal stability.

RMS profiles calculated using the marginal stability adjustment algorithm (see Section 2.7) are more similar to the observations (blue dotted lines in Fig. 2.3). The mean quantities show only small improvements, with a reduction in the mean zonal shear, stratification and Sh_{red}^2 between 75m and 40m as a result of the additional mixing (compare blue dotted to red dashed lines in Figures 2.3a,b,d). However, the RMS variation in zonal shear squared shows large changes, with a reduction between 85m and 40m and an increase around 100m (compare blue dotted line and red-dashed line in Fig. 2.3c), consistent with the mixing and expulsion of gradients from regions with $Sh_{red}^2 > 0$. Corresponding to the changes in zonal shear squared variations there are changes to variations in Sh_{red}^2 (Fig. 2.3e), with only minimal changes to variations in stratification (Fig. 2.3f).

Temporal variations in zonal shear squared and stratification are similar in magnitude (compare Figures 2.3c and 2.3f), suggesting that they are equally important in driving modulations in the Sh_{red}^2 . However, the patches of high Sh_{red}^2 , and thus high mixing, are generally associated with high shear magnitudes and relatively high stratification (e.g. compare Figures 2.1c,d,g and Figures 2.2a,b,c near patches of high Sh_{red}^2), as opposed to anomalies of low stratification and low shear. This suggests that the patches of high mixing are driven by increases in shear, as opposed to decreases in stratification. This hypothesis is supported by the Lagrangian diagnostic analyses

performed in the next section.

2.4 Lagrangian analysis of energetic vertical mixing patches

In this section, we examine the dynamical processes responsible for the increase in Sh_{red}^2 on the leading edge of the TIW warm phase. We analyze a set of Lagrangian particles that entered a patch of high Sh_{red}^2 located at -139°E on year day 262.5 (Fig. 2.5). The particles were chosen by first advecting particles seeded within the patch of high Sh_{red}^2 backwards in time to identify the source regions of the high Sh_{red}^2 , and then evenly seeding particles across these regions for a forwards in time Lagrangian calculation. A subset of these particles were then chosen that had $Sh_{red}^2 > 2 \times 10^{-4}\text{s}^{-2}$ and that were located in the upper EUC shear layer between depths of 120m and 30m on year day 262.5. The particles satisfying these conditions were sourced from two different water masses. 88% of the particles entered the region of high Sh_{red}^2 from the west through the EUC (black EUC particles in Fig. 2.5). The other 12% of particles entered the region of high Sh_{red}^2 from the east from a nearby TIV (white TIV particles in Fig. 2.5). The TIV particles entered higher in the water column, reflecting the negative vertical shear in zonal velocity in the upper EUC, the westward flow of the southern portion of the TIV, and the warmth and lighter density of the TIV water mass in comparison to the equatorial water.

The Sh_{red}^2 following this set of particles (green line in Fig. 2.6a) increases rapidly in time to values above zero, and thus the presence of high Sh_{red}^2 in the high mixing patch is not a result of advection. This increase in Sh_{red}^2 is due to a rapid increase in zonal shear squared (black line in Fig. 2.6a) as the stratification stays relatively constant (blue line in Fig. 2.6a), and the meridional shear squared is small (red line in Fig. 2.6a). This is consistent with the Eulerian analysis in the previous section.

To determine the cause of the increase in zonal shear, we perform a Lagrangian

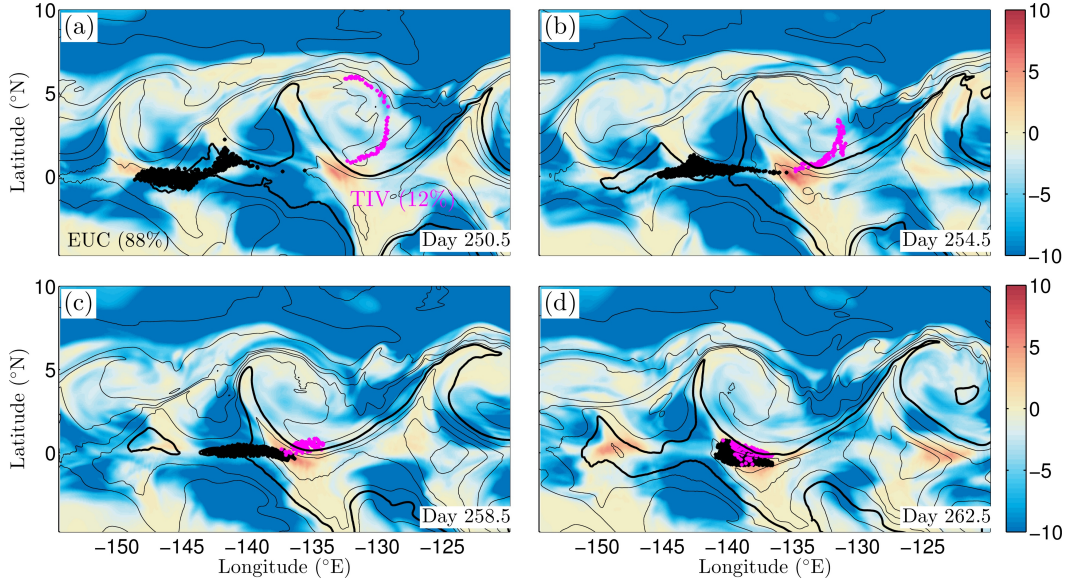


Figure 2.5: Daily-averaged $Sh_{red}^2 / 10^{-4} \text{ s}^{-2}$ in the upper EUC at 72m depth at four different times separated by 4 days from the high-resolution simulation. The contours are SST at 0.75°C intervals, with the 25°C isotherm in bold. Shown are the positions of Lagrangian particles that enter the patch of high Sh_{red}^2 at -140°E , 0°N on day 262.5 (d). These Lagrangian particles are identified either as EUC particles (893 particles comprising 88% of the total), if they enter the region from the west through the EUC, or TIV particles (123 particles comprising 12% of the total), if they enter the region from the east.

budget of zonal shear along the particle tracks. The zonal shear satisfies,

$$\frac{D}{Dt} \left(\frac{\partial u}{\partial z} \right) = \frac{\partial u}{\partial z} \frac{\partial v}{\partial y} + \left(f - \frac{\partial u}{\partial y} \right) \frac{\partial v}{\partial z} - \frac{\partial b}{\partial x} + \frac{\partial F_x}{\partial z}, \quad (2.3)$$

which is equivalent to the equation for the north-south component of the vorticity for the primitive equations, where F_x is the frictional force in the zonal direction.

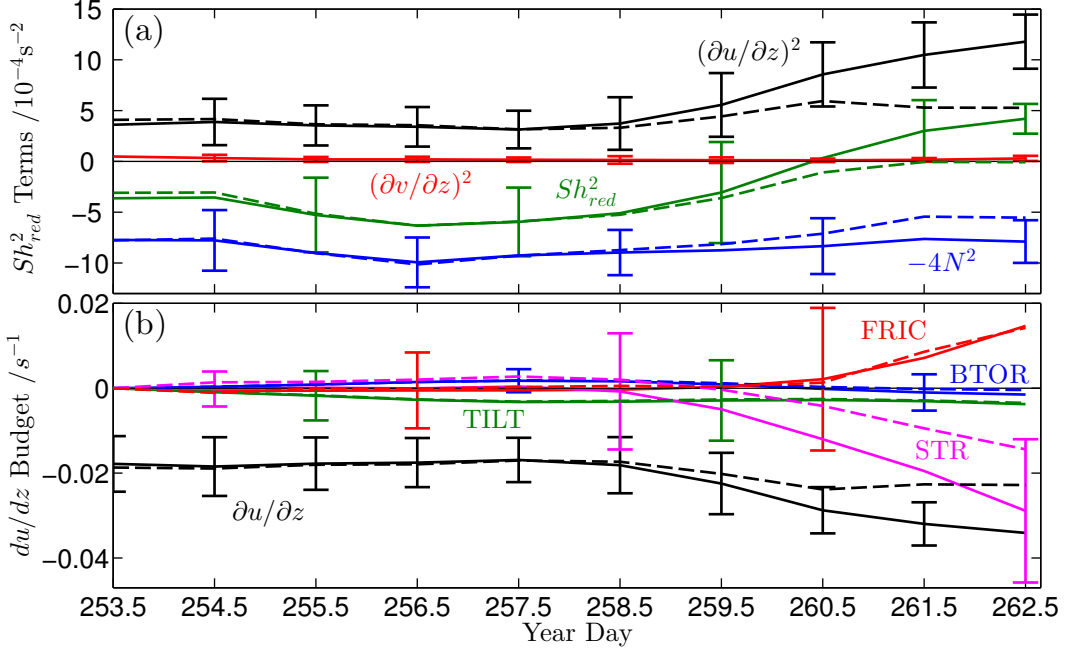


Figure 2.6: (a) The evolution of the reduced shear squared Sh_{red}^2 and its components; the zonal shear squared $((\partial u / \partial z)^2)$, meridional shear squared $((\partial v / \partial z)^2)$ and -4 times the stratification $(-4N^2)$ following the particles shown in Fig. 2.5. (b) An analysis of diagnostics in the zonal shear $(\partial u / \partial z)$ budget (Eq. (2.4)) following the particles shown in Fig. 2.5. *TILT* denotes vortex tilting, *STR* denotes horizontal vortex stretching, *FRIC* denotes the frictional torque and *BTOR* denotes the baroclinic torque. The error bars represent the $\pm 1\sigma$ spread over the particle ensemble, representing the spatial variability in the underlying fields over the span of the particles. The dashed lines in (a) and (b) are the equivalent curves obtained by first sorting every vertical profile in the simulations using the marginal stability adjustment algorithm described in Section 2.7 and then taking finite difference derivatives according to Eq. (2.4). The marginal stability adjusted *FRIC* (red dashed curve in (b)) is calculated as a residual.

Integrating along a particle path from a time t_0 to t gives,

$$\begin{aligned} \frac{\partial u}{\partial z}(t) - \frac{\partial u}{\partial z}(t_0) &= \underbrace{\int_{t_0}^t \frac{\partial u}{\partial z} \frac{\partial v}{\partial y} d\tau}_{STR} + \underbrace{\int_{t_0}^t \left(f - \frac{\partial u}{\partial y} \right) \frac{\partial v}{\partial z} d\tau}_{TILT} \\ &\quad - \underbrace{\int_{t_0}^t \frac{\partial b}{\partial x} d\tau}_{BTOR} + \underbrace{\int_{t_0}^t \frac{\partial F_x}{\partial z} d\tau}_{FRIC}. \end{aligned} \quad (2.4)$$

Thus a change in zonal shear following a particle can be attributed to horizontal vortex stretching (*STR*), vortex tilting (*TILT*), the baroclinic torque (*BTOR*) or frictional torques (*FRIC*). We analyze these terms along the particle tracks shown in Fig. 2.5, where we choose t_0 as day 253.5. The terms are calculated by taking the vertical derivative of the zonal momentum equation diagnostics output of ROMS. The numerical accuracy of these calculations were checked by comparing each quantity against the same quantities calculated directly using finite difference derivatives of the velocity and buoyancy, which gave closely consistent results (not shown).

The dominant process driving an increase in the magnitude of the zonal shear as the particles enter the high mixing patch is horizontal vortex stretching (*STR* in Fig. 2.6b). Vortex tilting and the baroclinic torque are negligible (*TILT* and *BTOR* in Fig. 2.6b). The increase in Sh_{red}^2 drives an increase in vertical mixing that acts to decrease the magnitude of the shear, as shown by the positive frictional torque (*FRIC* in Fig. 2.6b). However, the KPP mixing scheme does not provide enough mixing to enforce marginal stability against the horizontal vortex stretching. Equivalent Lagrangian curves calculated by taking finite difference derivatives of the model variables adjusted for marginal stability (using the algorithm described in Section 2.7) show that the additional mixing provided by this algorithm drives a decrease in stratification and limits the increase in zonal shear (dashed curves in Fig. 2.6a,b). The strength of horizontal vortex stretching also decreases, because it depends on the shear itself (dashed magenta curve in Fig. 2.6b). However, horizontal vortex stretching remains the driver behind the increase in mixing, which now manifests itself as a low stratification anomaly. Further Lagrangian analyses of other patches of high mixing confirm the ubiquity of this mechanism (not shown).

Horizontal vortex stretching here relies on meridional difffluence $\frac{\partial v}{\partial y} > 0$ (see *STR* in Eq. (2.4)) away from the Equator that acts on the existing shear of the EUC to increase it. Positive meridional difffluence driven by the horizontal flow of TIWs is present at the leading edge of the TIW warm phase (Fig. 2.1f, also see Fig. 3 of Perez *et al.* (2010)), in the same phase as the high Sh_{red}^2 (compare Figures 2.1f and 2.1g near the patches of high Sh_{red}^2). The correlation between $\frac{\partial v}{\partial y}$ and $\frac{\partial u}{\partial z}$ in the upper EUC shear layer at -140°E , 0°N reaches a maximum at a lag of 2 days

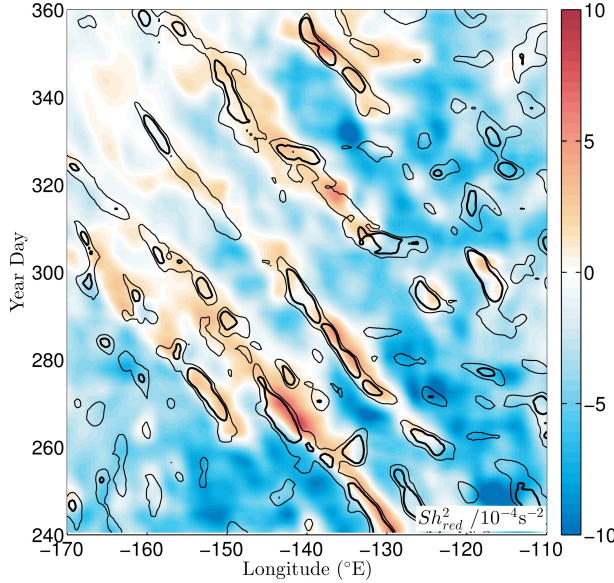


Figure 2.7: Longitude-time plot of the reduced shear squared (color) and meridional divergence ($\frac{\partial v}{\partial y}$, contours) at 72m depth on the Equator from the basin-wide ROMS simulation. The x -axis is longitude and the y -axis is time in year days for the months September-December. The thin (thick) contours denote where $\frac{\partial v}{\partial y} = 1 \times 10^{-6} \text{ s}^{-1}$ ($2 \times 10^{-6} \text{ s}^{-1}$). Note that positive meridional diffluence is often collocated or leads high Sh_{red}^2 patches, consistent with horizontal vortex stretching.

of -0.25 (significant at 95%), showing that maximum meridional diffluence leads minimum (maximum magnitude) zonal shear at 2 days. This is consistent with the pathway of Lagrangian fluid parcels in the EUC and the time integrated nature of the vortex stretching term in Eq. (2.4), where meridional diffluence must act over time to increase the zonal shear. This is further illustrated with a Hovmoeller diagram of the Sh_{red}^2 and meridional diffluence, which highlights the strong correspondence between the two variables, with most patches of high mixing preceded by meridional diffluence in longitude and time (Fig. 2.7).

Modulation of vertical mixing through horizontal vortex stretching does not require the horizontal circulation of TIWs to be divergent. While TIWs are associated with large-scale vertical motions (as discussed in *Jochum and Murtugudde (2006)* and *Perez et al. (2010)*), in our simulations most of the horizontal vortex stretching is a result of the component of the TIW velocity field that is horizontally non-divergent

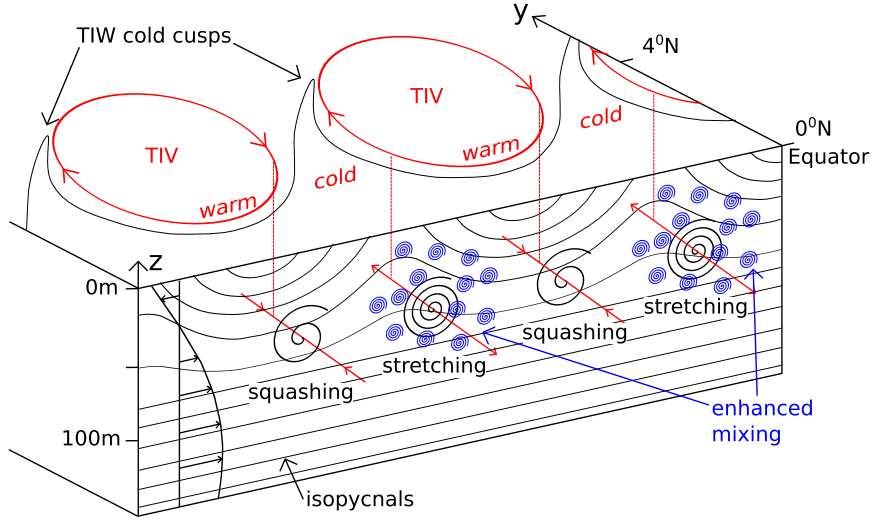


Figure 2.8: A schematic showing how periodic strain driven by the TIW velocity field (red lines) acts on the horizontal vorticity of the EUC (indicated by the large black spirals) to increase or decrease the shear leading to patches of high (small blue spirals) and low turbulent mixing along the Equator.

$(\frac{\partial u}{\partial x} + \frac{\partial v}{\partial y} \approx 0)$. The physics of the mechanism are summarized in Fig. 2.8.

On the trailing edge of the TIW warm phase, TIW horizontal strain drives meridional confluence ($\frac{\partial v}{\partial y} < 0$) and thus horizontal vortex squashing. Because of the dependence of the vortex stretching on the zonal shear itself (STR in Eq. (2.4)), meridional confluence does not drive strong reductions in shear. While not the focus of this study, Lagrangian analyses show that patches of low Sh_{red}^2 , and thus low turbulent mixing, can be partially attributed to restratification driven by TIW meridional shear acting on the north equatorial front (not shown). This TIW driven periodic stratification, combined with the variations in mixing itself, may contribute to the variations in stratification at TIW frequencies seen in the Eulerian analysis (Fig. 2.3f). Furthermore, this emphasizes that the meridional shear of TIWs, while having a limited direct contribution to the Sh_{red}^2 , plays a role in driving variations in stratification that influence mixing.

The non-linear nature of horizontal vortex stretching, whereby vortex stretching drives large increases in shear while squashing drives lesser decreases in shear, suggests that TIWs may increase the average levels of turbulence in the upper EUC. This is

examined in the following section.

2.5 A simple mixing model of the EUC: TIW influence

This section discusses the total influence of the TIW modulation of the shear on the turbulent heat flux in the context of a simple 1D mixing model of the EUC forced by periodic TIW horizontal strain with alternating periods of meridional diffluence and confluence. We quantify this influence by comparing these 1D mixing model runs with and without TIW strain forcing.

2.5.1 Simple 1D mixing model setup

We split the zonal flow at -140°E , 0°N into two parts associated with the EUC and the TIWs respectively,

$$u = \underbrace{\tilde{u}(z, t)}_{EUC} + \underbrace{u'(x, y, z, t)}_{TIW}, \quad (2.5)$$

where we assume that the TIW part is horizontally non-divergent and follows a simple 15-day sinusoidal oscillation,

$$\frac{\partial v'}{\partial y} = -\frac{\partial u'}{\partial x} = \alpha(z, t) = A(z) \sin\left(\frac{2\pi t}{15 \text{ days}} + \phi_0\right), \quad (2.6)$$

where ϕ_0 represents the initial phase. The vertical shape function,

$$A(z) / s^{-1} = 2.8 \times 10^{-6} + 5.2 \times 10^{-9}z, \quad (2.7)$$

was chosen by fitting the *RMS* variations in $\partial v/\partial y$ in the TIW frequency band (calculated from the 3D ROMS model in a similar fashion to the profiles in Fig. 2.3) to a linear function in z . Although we do not have direct observations of $\partial v/\partial y$ to compare to Eq. (2.7), we would expect this fitted amplitude to be similar to observations, given that the 3D model TIW meridional velocity amplitude and $\partial v/\partial z$

amplitude (Fig. 2.3c) compare favorably with observations, and the lateral structure of the 3D model TIWs is comparable to observations (*Qiao and Weisberg, 1995; Kennan and Flament, 2000*).

With the idealized TIWs, the zonal momentum equation for the EUC portion of the velocity field becomes

$$\frac{\partial \tilde{u}}{\partial t} = -\frac{\partial u'}{\partial x} \tilde{u} + \{\text{other advection terms}\} - \frac{1}{\rho_0} \frac{\partial \tilde{P}}{\partial x} + F_x, \quad (2.8)$$

where F_x represents a frictional force associated with vertical mixing and surface forcing and \tilde{P} is the pressure associated with the EUC portion of the flow. We assume that the advection terms in the curly brackets can be treated as external forcing in this 1D framework, and can be included as part of a large-scale forcing term PA . This term represents the pressure gradient and advective processes that maintain the EUC against vertical mixing and was chosen to balance the wind stress over the total water column. It has a cubic Gaussian shape

$$PA = -\frac{\tau_x}{\rho_0} e^{(z/d)^3} \left(\int_{-\infty}^0 e^{(z'/d)^3} dz' \right)^{-1}, \quad (2.9)$$

with decay scale $d = 120\text{m}$, chosen as it matched the form of the 3D model pressure gradient well.

Dropping the $\tilde{\cdot}$, the above approximations result in a simple 1D diffusion equation model for the EUC velocity $u(z, t)$, where we also include equations for the temperature $T(z, t)$ and salinity $S(z, t)$,

$$\frac{\partial u}{\partial t} = \underbrace{\alpha(z, t)u}_{\text{TIW Strain}} + \underbrace{PA}_{\text{Pressure/Adv.}} - \underbrace{\frac{\partial}{\partial z} \left(-\kappa_v \frac{\partial u}{\partial z} \right)}_{\text{Diffusion}}, \quad (2.10)$$

$$\frac{\partial \{T, S\}}{\partial t} = \underbrace{-\frac{1}{r_T} \{T - T_0, S - S_0\}}_{\text{Restoring}} - \underbrace{\frac{\partial}{\partial z} \left(-\kappa_T \frac{\partial \{T, S\}}{\partial z} \right)}_{\text{Diffusion}}. \quad (2.11)$$

The Newtonian restoring added to the temperature and salinity equations represents the pressures that maintain the stratification against vertical mixing. The main

results are not very sensitive to values of the restoring time scale between 1 and 15 days (not shown), and thus $r_T = 5$ days was chosen. We solve these equations on the same 50 level vertical grid as the 3D ROMS model.

The surface forcing at -140°E , 0°N averaged over the TIW season (Sep-Dec) from the 3D ROMS model was used to force the 1D model, including a $\tau_x = -0.08\text{Nm}^{-2}$ zonal wind stress, a free-slip bottom boundary condition, a downward shortwave radiative heat flux of 275Wm^{-2} and a combined sensible plus latent heat flux of -180Wm^{-2} . We found that including a diurnal cycle of shortwave radiation did not significantly change the results discussed here, and thus for simplicity we discuss only model runs without a diurnal cycle.

We compare the results of simulations using two parameterizations for the diffusion terms in Equations (2.10) and (2.11). The diffusivity and viscosity in both schemes are split into components above and below the boundary layer depth (H_{BL}),

$$\kappa = \begin{cases} \kappa_{BL} & , \quad z > -H_{BL}, \\ \kappa_{int} & , \quad z \leq -H_{BL}, \end{cases} \quad (2.12)$$

where the boundary layer depth and boundary layer diffusivity/viscosity κ_{BL} are determined in both schemes by the KPP boundary layer model of *Large et al.* (1994). However, the schemes differ in the interior parameterization for the diffusivity/viscosity κ_{int} , with the first scheme (the KPP scheme) using the KPP interior form used in the 3D ROMS model (*Large et al.*, 1994),

$$\kappa_v = K_0 \left(1 - \left(\frac{Ri}{Ri_0} \right)^2 \right)^3 + \kappa_{vB}, \quad (2.13)$$

$$\kappa_T = K_0 \left(1 - \left(\frac{Ri}{Ri_0} \right)^2 \right)^3 + \kappa_{TB}, \quad (2.14)$$

where κ_v is the viscosity, κ_T is the diffusivity for scalars, $K_0 = 2 \times 10^{-3}\text{m}^2\text{s}^{-1}$, $Ri_0 = 0.7$ and the background diffusivities are $\kappa_{TB} = 1 \times 10^{-5}\text{m}^2\text{s}^{-1}$ and $\kappa_{vB} = 1 \times 10^{-4}\text{m}^2\text{s}^{-1}$ (Fig. 2.9). These parameters are consistent with previous parameter

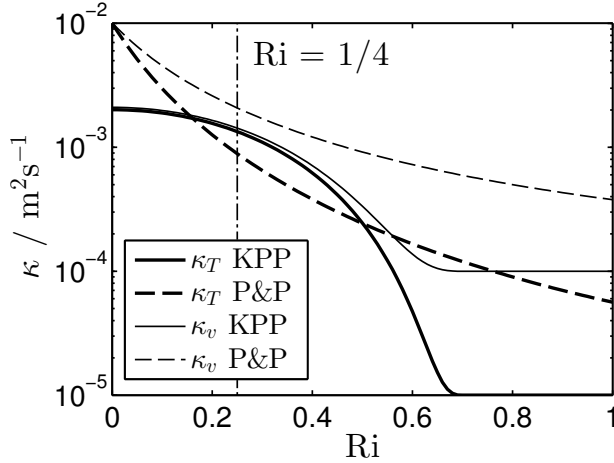


Figure 2.9: The interior diffusivities (κ_T) and viscosities (κ_v) assigned by the KPP (Large *et al.*, 1994) and P&P (Pacanowski and Philander, 1981) interior mixing schemes for shear instability as a function of the gradient Richardson number (as in Equations (2.14) and (2.15)).

choices for this scheme (Large *et al.*, 1994; Large and Gent, 1999; Zaron and Moum, 2009). The K_0 parameter is smaller than values used elsewhere, and was chosen as it gave the most appropriate mean EUC depth in the 3D ROMS model as determined by a sensitivity study (not shown).

The second scheme replaces κ_{int} with the form of Pacanowski and Philander (1981) (we refer to this scheme as the P&P scheme),

$$\begin{aligned}\kappa_v^{PP} &= K_0^{PP} \left(1 + \frac{\text{Ri}}{\text{Ri}_0^{PP}} \right)^{-2} + \kappa_{vB}, \\ \kappa_T^{PP} &= \kappa_v^{PP} \left(1 + \frac{\text{Ri}}{\text{Ri}_0^{PP}} \right)^{-1} + \kappa_{sB},\end{aligned}\quad (2.15)$$

where $K_0^{PP} = 0.01 \text{ m}^2 \text{s}^{-1}$ and $\text{Ri}_0^{PP} = 0.2$. These parameters are consistent with previously cited values (e.g. Pacanowski and Philander (1981); Blanke and Delecluse (1993) and Li *et al.* (2001)). The P&P parameterization should be more successful at enforcing marginal stability than the KPP parameterization, as it has a steeper increase in diffusivity as the Richardson number passes $1/4$ and thus can provide relatively more mixing at low Richardson numbers (Fig. 2.9). At low Richardson numbers

the P&P scheme has a Prandtl number greater than 1 unlike KPP, and thus preferentially mixes momentum over buoyancy to more efficiently increase the Richardson number. At high Richardson numbers both schemes have Prandtl numbers greater than 1.

The simple 1D mixing model runs were initialized with the 3D ROMS model profiles at -140°E , 0°N averaged over the TIW season (Sep-Dec), and run for 200 days. We choose the 10th TIW period between days 135–150 for our analysis because by this time the results are not sensitive to the initial phase, ϕ_0 , of the strain α .

The simple 1D model shows similar qualitative results to the 3D ROMS model. During periods when $\alpha(z, t) > 0$ (Figures 2.10a,b), the zonal shear increases, peaking in magnitude 3-4 days after the maximum strain (Figures 2.10c,d). High zonal shear is accompanied by low Richardson numbers (Figures 2.10g,h) resulting in large diffusivities (Figures 2.10i,j) that mix out the stratification (Figures 2.10e,f) through the divergence of the turbulent heat flux (Figures 2.10k,l),

$$J_q = -C_p \rho_0 \kappa_T \frac{\partial T}{\partial z}, \quad (2.16)$$

where C_p is the specific heat of seawater. As the TIW strain switches sign to become negative ($\alpha < 0$ in Figures 2.10a,b), the shear is reduced both through vortex squashing and as a result of the mixing itself. The T-S restoring and the surface heat fluxes then act to restore the stratification profile before the TIW strain switches sign and a new phase of increased mixing begins.

In these simple 1D mixing model simulations, the P&P scheme does a better job at enforcing marginal stability than KPP, restricting the Richardson number to larger values (compare Figures 2.10g and 2.10h). The P&P diffusivity is able to reach higher values when the Richardson number is low (compare Figures 2.10i and 2.10j), and preferentially mixes momentum over buoyancy as the Prandtl number is greater than 1. This results in lower maximum turbulent heat fluxes for P&P compared to KPP (compare Figures 2.10k to 2.10l). The turbulent heat fluxes averaged over a TIW period (Fig. 2.11) are also lower for P&P compared to KPP (compare black and blue lines in Fig. 2.11a) for model runs both with periodic TIW strain ($\alpha(z, t)$) as in Eq.

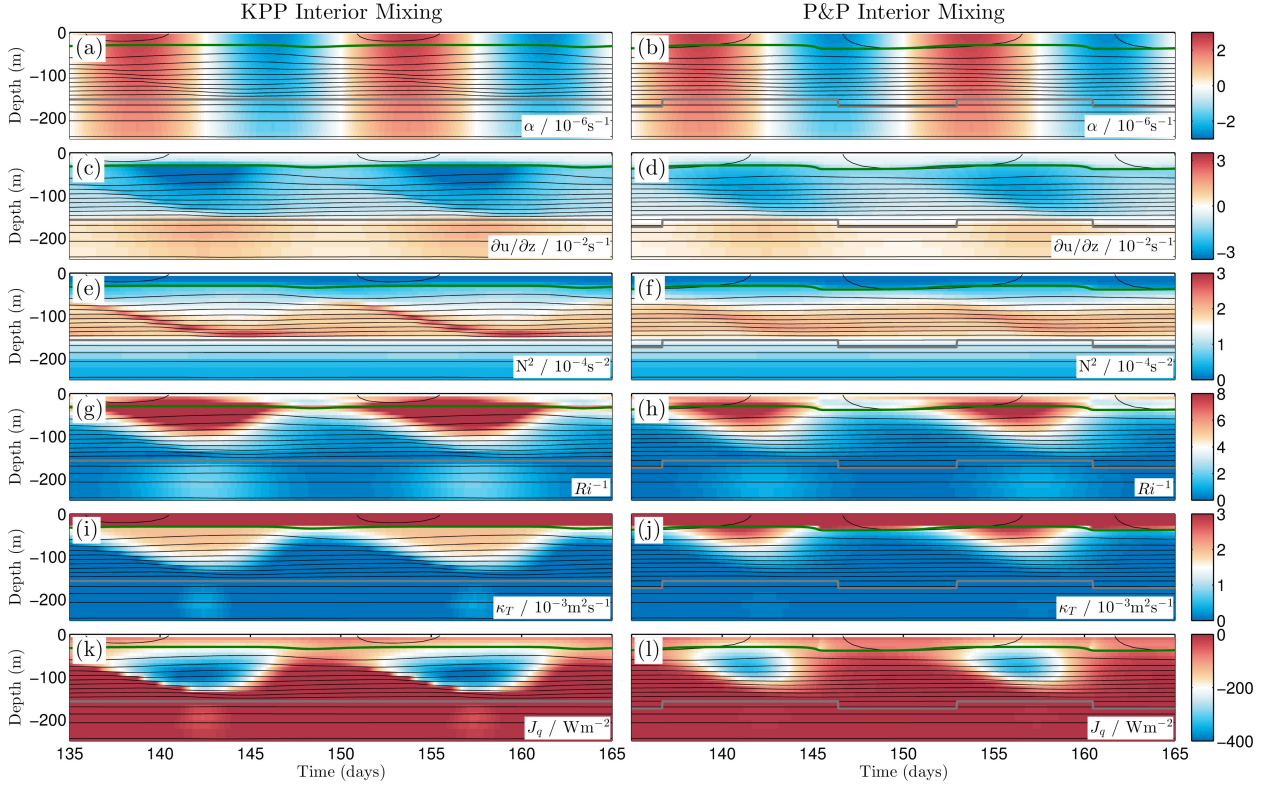


Figure 2.10: Time-depth plots of simple 1D mixing model runs using KPP (left) and P&P (right) over days 135-165. The imposed TIW periodic strain (a,b), zonal shear (c,d), stratification (e,f), inverse Richardson number (g,h), diffusivity (i,j) and vertical turbulent heat flux (k,l). The dark green lines indicate the depth of the KPP mixed layer, the gray lines indicate the depth of the EUC core and the black contours are isopycnals at 0.2 kg m^{-3} spacing.

(2.6), solid lines in Fig. 2.11a) and runs without TIW periodic strain ($\alpha(z, t)$ set to zero, dashed lines in Fig. 2.11a).

2.5.2 The influence of TIWs on the turbulent heat flux

Inclusion of TIW periodic strain results in an increase in the magnitude of the turbulent heat flux averaged over a TIW period (Fig. 2.11a). The increase is restricted to depths below 75m for the KPP simulation (compare black solid and dashed curves in Fig. 2.11a), while for P&P, the heat flux increases at all depths (compare blue solid and dashed curves in Fig. 2.11a). The rectified change in turbulent heat flux R at a

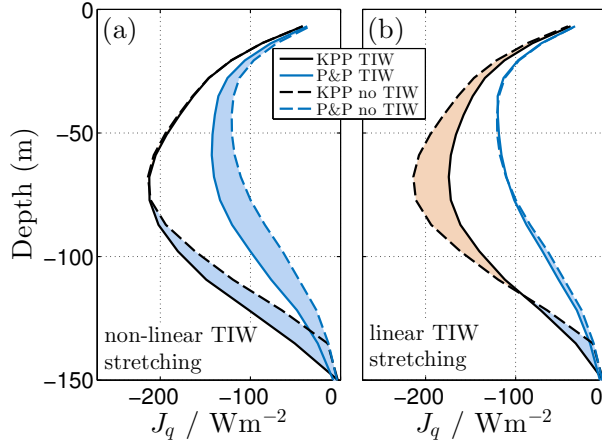


Figure 2.11: The vertical turbulent heat flux (J_q , Eq. (2.16)) averaged over days 135 – 150 for simple mixing model runs with ($\alpha(z, t)$ as in Eq. (2.6), solid lines) and without ($\alpha(z, t) = 0$, dashed lines) TIWs. Shown are runs with non-linear TIW stretching (a), where the TIW body force depends on the velocity itself $\alpha(z, t)u(z, t)$ and linear TIW stretching (b), where the TIW body force depends on a mean velocity $\alpha(z, t)\bar{u}(z)$. Areas are shaded according to whether adding TIWs increases (blue) or decreases (orange) the turbulent heat flux averaged over a TIW period. Adding non-linear TIW stretching increases the turbulent heat flux in all cases with the magnitude of the increase depending on the parameterization for shear instability used.

given depth is defined as,

$$\begin{aligned} R &\equiv \overline{J_q(t)} - \overline{J_q}^n \\ &= -\rho_0 c_p \left[\kappa(Ri) \frac{\partial \overline{T}}{\partial z} - \kappa(\overline{Ri}^n) \frac{\partial \overline{T}^n}{\partial z} \right], \end{aligned} \quad (2.17)$$

where $\overline{\quad}$ represents an average over a TIW period and $\overline{\quad}^n$ represents an equivalent average in the run without TIWs. There are a number of non-linearities in the system that are potentially responsible for rectification $R \neq 0$:

1. The influence of variations in stratification, both through the dependence of the Richardson number on stratification ($Ri = N^2/(\partial u/\partial z)^2$), and the dependence of the heat flux on the product of the diffusivity and the vertical temperature gradient ($\kappa \partial \overline{T}/\partial z \neq \kappa \overline{\partial T}/\partial z$).

2. The non-linear dependence of the diffusivity on the Richardson number and through it on the shear, which differs between the two mixing schemes ($\overline{\kappa(Ri)} \neq \kappa(\overline{Ri})$).
3. The influence of mixing on the underlying shear distribution. Even if the diffusivity depends linearly on the shear (i.e. removing non-linearity 2), the mixing acts preferentially at high shears and thus can result in rectification ($\overline{\partial u/\partial z} \neq \overline{\partial u/\partial z}^n$).
4. The non-linear influence of vortex stretching on the shear ($\overline{\partial u/\partial z} \neq \overline{\partial u/\partial z}^n$).

The influence of temporal variations in stratification and the temperature gradient on the heat flux (non-linearity 1) is minimal. While the vertical gradient in stratification is large, its temporal variations are weaker than the corresponding variations in shear (compare Figures 2.10e,f with 2.10c,d), and thus do not have a strong influence on the temporal variations in Richardson number (compare Figures 2.10e,f with 2.10g,h). In addition, dT/dz averaged over a TIW period is similar to dT/dz from the no TIW runs (not shown), and the distribution over a TIW period of the turbulent heat flux at a fixed depth matches the distribution of diffusivity closely (compare blue distributions in Figures 2.12e,f to 2.12c,d), implying minimal influence by variations in dT/dz .

The non-linear dependence of the KPP and P&P diffusivity on the Richardson number and shear (non-linearity 2) has a strong influence on the turbulent heat flux averaged over a TIW period, and is responsible for the differences between the two mixing schemes. Given that variations in stratification are minimal, this non-linearity is well captured by considering the dependence of the diffusivity on the shear at an average value of the stratification for each mixing scheme (Fig. 2.13). Using a Taylor series expansion of the functional dependence of the diffusivity on the shear, $G = \kappa(\partial u/\partial z)$, about the shear averaged over a TIW period $\overline{\partial u/\partial z}$, it can be shown

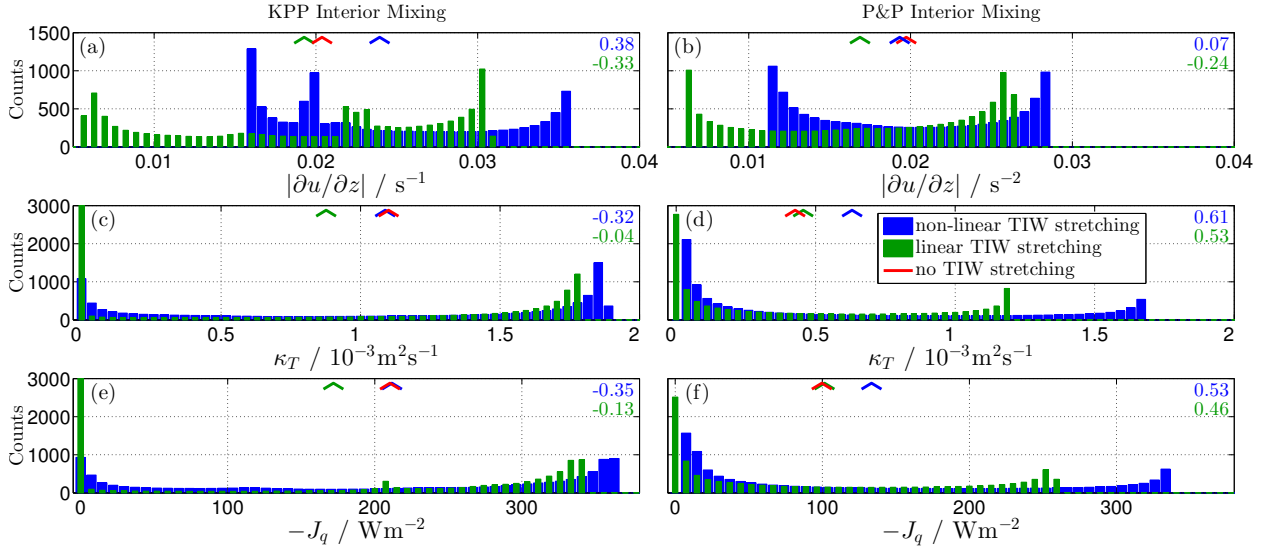


Figure 2.12: Histograms of the magnitude of the zonal shear (a,b), diffusivity (c,d) and turbulent heat flux (e,f) over a TIW period at 75m depth for simple 1D mixing model runs with the KPP (a,c,e) and P&P (b,d,f) mixing schemes. The blue (green) histograms show the results of runs with non-linear (linear) TIW stretching. The distribution means are indicated with arrows at the top of the figures, including the mean for runs without TIWs (red arrows). The skew of each distribution is indicated in the upper right of each panel. The distribution of negative turbulent heat flux is plotted to facilitate comparison with the diffusivity distributions.

that to first order in the shear oscillation variance $\text{var}(\partial u / \partial z)$,

$$\begin{aligned} R_\kappa &\equiv \overline{G} - G\left(\frac{\partial u}{\partial z}\right) \\ &\approx \frac{1}{2}G''\text{var}\left(\frac{\partial u}{\partial z}\right), \end{aligned} \quad (2.18)$$

where R_κ is the rectification effect of this non-linearity and G'' is the curvature of G . Thus, as a consequence of the positive curvature of the P&P curve (Fig. 2.13), the distribution of P&P diffusivity over a TIW period at an example depth is positively skewed (0.61 at 75m, blue distribution in Fig. 2.12d), resulting in a positive rectification effect $R_\kappa > 0$ (compare no TIW to non-linear TIW means in Fig. 2.12d). On the other hand, the negative curvature of the KPP curve (Fig. 2.13) results in a negatively skewed KPP diffusivity distribution over a TIW period (-0.32 at 75m,

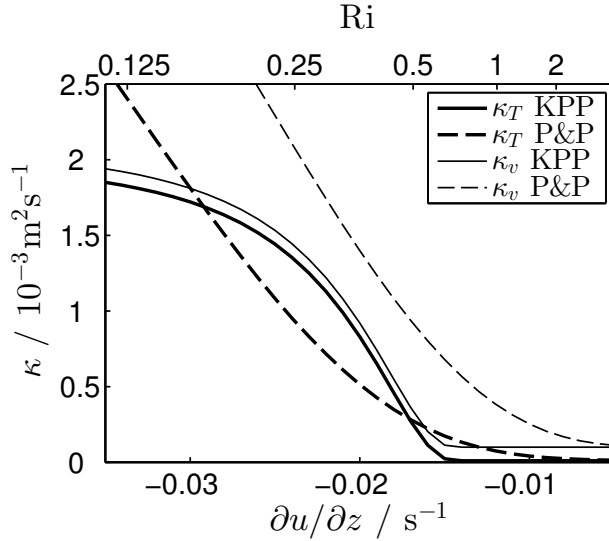


Figure 2.13: The KPP and P&P interior diffusivities (κ_T) and viscosities (κ_v) as a function of the shear $\partial u / \partial z$ for a stratification of $N^2 = 1.42 \times 10^{-4} \text{ s}^{-2}$, close to the stratification at 75m averaged over the period shown in Fig. 2.5 for both the KPP ($N^2 = 1.37 \times 10^{-4} \text{ s}^{-2}$) and P&P ($N^2 = 1.47 \times 10^{-4} \text{ s}^{-2}$) runs. The corresponding values of the Richardson number are shown on the top axis. A linear diffusivity scale is used to highlight the different curvatures of the two schemes.

blue distribution in Fig. 2.12c) and would tend to result in a negative rectification effect. However, the total rectification R is also influenced by the other two non-linearities, the influence of the mixing on the shear distribution (non-linearity 3) and the non-linearity in vortex stretching (non-linearity 4), that can cause differences between the shear averaged over a TIW period and the shear for the no TIW run ($\overline{\partial u / \partial z} \neq \overline{\partial u / \partial z}^n$), and influence the oscillation amplitude ($\text{var}(\partial u / \partial z)$).

Non-linearities 3 and 4 have counteracting influences on the shear distribution. The mixing preferentially acts at high shear (for both mixing schemes), tending to negatively skew the shear magnitude distribution and result in a rectified decrease in the shear magnitude averaged over a TIW period compared to runs without TIWs. The non-linearity of vortex stretching induces stronger vortex stretching at high shears, positively skewing the shear magnitude distribution and resulting in a rectified increase in the shear magnitude averaged over a TIW period compared to runs without TIWs. For P&P, the skew of the shear magnitude distribution is small (0.07, blue

distribution in Fig. 2.12b) and so is the rectified change in mean shear magnitude (compare no TIW to non-linear TIW means in Fig. 2.12b), suggesting that mixing and vortex stretching compensate. While for KPP, the skew of the shear magnitude distribution is positive (0.38, blue distribution in Fig. 2.12a), and the rectified change in mean shear magnitude is positive (compare no TIW to non-linear TIW means in Fig. 2.12a) suggesting that the vortex stretching non-linearity overpowers the mixing non-linearity for KPP. However, interpreting the impact of non-linearities 3 and 4 on the heat fluxes based solely on these qualitative arguments is potentially misleading as they can interact with each other and with non-linearity 2 associated with the curvature in G .

To quantitatively evaluate the importance of the vortex stretching non-linearity compared to the other non-linearities 1-3, we replace the regular non-linear TIW stretching ($\alpha(z, t)u(z, t)$ in Eq. (2.10)) with linear TIW stretching ($\alpha(z, t)\bar{u}(z)$, where $\bar{u}(z)$ was the mean velocity profile between days 135 – 150 from the simulations with non-linear TIW stretching). In simulations performed with linear TIW stretching, the TIW body force no longer depends on the magnitude of the instantaneous velocity, and thus without mixing, a simple symmetric sinusoidal oscillation in shear at each depth would result. Indeed, in these linear runs, the skew of the shear magnitude distributions becomes negative as a result of the mixing non-linearity 3 (compare the skews of the blue and green distributions in Figures 2.12a and 2.12b). These changes result in modifications to the distributions of the diffusivity and the turbulent heat flux (compare blue and green distributions in Figures 2.12c-f). In particular, the turbulent heat flux averaged over a TIW period in simulations with linear TIW stretching is now reduced in comparison to the non-linear TIW stretching runs (compare Figures 2.11a and 2.11b). For KPP, linear TIW stretching results in a rectified decrease in the heat flux, as a consequence of both the negative curvature of the KPP G curve (Fig. 2.13) and the mixing non-linearities. For P&P the linear TIW stretching results in no change in the average turbulent heat flux compared to simulations without TIWs, likely as a result of cancellation between the mixing non-linearity and the non-linearity associated with the positive curvature of the P&P G curve (Fig. 2.13). These results emphasize that the dependence of horizontal vortex stretching

Table 2.1: Turbulent heat flux J_q (Wm^{-2}) averaged over days 135 – 165 between 50m and 100m from the simple 1D mixing model runs.

Scheme	$K_0 / \text{m}^2\text{s}^{-1}$	Ri_0	$K_0^{PP} / \text{m}^2\text{s}^{-1}$	J_q no TIWs	J_q TIWs	% increase
KPP	2×10^{-3}	0.7	-	-197	-201	2
KPP	4×10^{-3}	0.7	-	-231	-248	7
KPP	2×10^{-3}	0.8	-	-206	-210	2
P&P	-	-	1×10^{-2}	-98	-129	32
P&P	-	-	5×10^{-3}	-100	-127	27
Peters 88	-	-	-	-71	-100	41

on the shear itself is the critical non-linearity that gives rise to the rectified increase in turbulent heat flux $R > 0$ when TIWs are added.

In the context of this simple 1D mixing model for the EUC, TIWs increase the turbulent heat flux averaged over a TIW period through horizontal vortex stretching. Averages of J_q between 50 and 100m (Table 2.1), indicative of the total change in heat content induced by turbulent mixing between this depth layer and the surface, show that TIWs cool the upper ocean in both parameterizations examined here. However, the magnitude of the cooling varies between parameterizations. Using the P&P parameterization, which more realistically enforces marginal stability, TIWs increase the turbulent heat flux averaged between 50 – 100m by 30%. Runs conducted using the $\kappa(Ri)$ curves of Peters *et al.* (1988), which have very rapid increases in diffusivity as the Richardson number decreases below 1/4, show a further enhancement of the turbulent heat flux by TIWs to 40% (Table 2.1). This suggests that the rectified TIW influence is larger for parameterizations that are more successful at enforcing marginal stability and whose diffusivity formulas are more consistent with observations.

While the details of the simple 1D mixing runs are sensitive to the parameters in the mixing schemes, the influence of TIWs on the heat flux is not sensitive to these parameters, only to the shape and curvature of the $\kappa(Ri)$ curve. Sensitivity studies where the KPP maximum diffusivity K_0 was doubled to $4 \times 10^{-3}\text{m}^2\text{s}^{-1}$ (as in Large and Gent (1999)), the KPP critical Richardson number Ri_0 was changed to 0.8 (as in Large and Gent (1999)) and the P&P maximum diffusivity K_0^{PP} was halved to

$5 \times 10^{-3} \text{m}^2 \text{s}^{-1}$ (as in *Ma et al.* (1994)) show only small changes to the influence of TIWs on the turbulent heat flux (Table 2.1).

2.6 Summary and discussion

Recent observations (*Lien et al.*, 2008; *Moum et al.*, 2009; *Inoue et al.*, 2012) have shown that TIWs modulate vertical mixing in the upper EUC, with potential implications for the role of TIWs in the equatorial SST budget. Using a regional ocean model, we have examined the mechanisms through which TIWs modulate the Sh_{red}^2 , a proxy for mixing. Contrary to previous hypotheses, our results suggest that the varying TIW meridional shear plays a minor direct role in modulations of mixing (Fig. 2.3c). Instead, we find that TIW horizontal strain modifies the zonal shear of the upper EUC through horizontal vortex stretching (Fig. 2.8), acting to increase vertical mixing leading into the TIW warm phase. By including the effects of TIW horizontal strain in a simple 1D mixing model of the EUC, we further showed that adding TIWs can result in a rectified increase in the turbulent heat flux and thus sea surface cooling in this simple context. The amount of sea surface cooling induced by TIWs is larger for parameterizations that are more successful at enforcing the observed (*Smyth and Moum*, 2013) physical constraint of marginal stability. This result has potential implications for the SST budget in ocean models using Richardson number based mixing parameterizations, such as many of the CMIP5 ocean models (*Huang et al.*, 2014).

Horizontal vortex stretching here relies on TIW horizontal strain interacting with the vertical shear in the upper EUC. This coupling of vertical and horizontal processes is a signature of submesoscale physics, which have been found previously to play a role in the dynamics of TIWs and TIVs (*Holmes et al.*, 2014). *MacDonald and Chen* (2012) found that a similar mechanism involving lateral spreading at a river outlet was important in enhancing stratified-shear turbulence in a coastal scale flow. The meridional diffluence that drives vortex stretching acts frontolytically on the equatorial fronts to decrease the horizontal buoyancy gradient. However, the constraint

of thermal wind balance is weakened near the equator where the Coriolis parameter is weak. The tilting of planetary and relative vorticity that would normally act (in the mid-latitudes) to decrease the shear and maintain thermal wind balance in response to the decreasing horizontal buoyancy gradient does not act strongly here. Thus this process is distinctly different to the frontogenetic intensification of shear and turbulence discussed by *Skyllingstad and Samelson* (2012).

In the context of a simple 1D mixing model of the EUC, TIWs increased the turbulent heat flux by $\sim 30\text{Wm}^{-2}$ (Fig. 2.11a and Table 2.1), which is of similar magnitude to the TIW lateral heat fluxes estimated in *Jochum and Murtugudde* (2006). For a 30m deep mixed layer, this additional heat flux drives an additional cooling of -0.6°C/month , a significant fraction of the $1 - 2^\circ\text{C/month}$ cooling implied by the turbulent heat flux observations of *Moum et al.* (2009) and comparable to the $\mathcal{O}(1^\circ\text{C/month})$ TIW lateral heating rate (*Menkes et al.*, 2006; *Jochum et al.*, 2007). Thus the additional mixing induced cooling effect of TIWs could potentially compensate for TIW lateral heating. However, this result must be considered with caution given the simplified nature of the 1D mixing model and the parameterized mixing.

We have not considered here any rectified influence of TIWs on the surface heat fluxes. The studies of *Thum et al.* (2002) and *Seo et al.* (2007) found variations in the latent heat flux of $\sim 50\text{Wm}^{-2}$ per $^\circ\text{C}$ of TIW induced SST change, with the sensible heat flux changes being significantly smaller. *Seo et al.* (2007) showed that the rectified influence of these changes averaged over a TIW period was negligible ($< 1\text{Wm}^{-2}$), and thus we expect the increase in turbulent heat flux due to TIWs to dominate any TIW induced changes in air-sea fluxes.

Our results, combined with the study of *Zaron and Moum* (2009), suggest that there are several improvements that could be made to the interior KPP mixing parameterization scheme to better model the equatorial oceans and the influence of TIWs on vertical mixing. The inclusion of the KPP boundary layer scheme has been shown to significantly improve simulations of the tropical Pacific compared to the original *Pacanowski and Philander* (1981) scheme (*Li et al.*, 2001). Our modeling work and observations of $\kappa(Ri)$ curves (i.e. Fig. 1 of *Zaron and Moum* (2009)) suggest that using the interior schemes of *Pacanowski and Philander* (1981) or *Peters et al.* (1988)

combined with the KPP boundary layer model (*Large et al.*, 1994) may perform better than the original KPP scheme with respect to enforcing marginal stability and thus modeling the influence of TIWs on vertical mixing. This type of scheme has been used in the HadCM3 climate model (*Gordon et al.*, 2000), although the authors did not discuss the reasons for this choice. However, in any future vertical mixing sensitivity study it must be noted that the strength of TIWs themselves is influenced by vertical mixing, rendering the interpretation of results difficult (*Chen et al.*, 1994).

We thank J. Moum for useful discussions. The computations were performed at the Stanford Center for Computational Earth and Environmental Science. We thank the TAO Project Office of NOAA/PMEI for providing the TAO data. R. Holmes was supported by a Stanford Graduate Fellowship while undertaking this study.

2.7 Appendix: Marginal stability adjustment algorithm

The algorithm described here is similar to the *Price et al.* (1986) mixing scheme, but acts offline as a diagnostic tool. Given some initial profiles of velocities $u^I(z)$, $v^I(z)$, potential temperature $T^I(z)$, salinity $S^I(z)$ and buoyancy $b^I(z)$ we wish to find sorted profiles $u(z)$, $v(z)$, $T(z)$, $S(z)$, $b(z)$ that are stable or marginally stable throughout the water column ($Sh_{red}^2 \leq 0$), subject to conservation of momentum, heat and salt. In order to satisfy these conditions, we construct an algorithm that induces down-gradient fluxes of momentum, heat and salt iteratively at each unstable vertical grid point ($Sh_{red}^2 > 0$) in the profile until that point is marginally stable ($Sh_{red}^2 = 0$). At each iteration the fluxes are imposed at a Prandtl number one ratio, and the flux formulation conserves momentum, heat and salt by construction. For each vertical profile, the algorithm proceeds as follows;

1. Homogenize regions with negative stratification:
while($N^2(z) < 0$ at some z)
 - (a) Find block of grid-points with $N^2(z) < 0$

- (b) Homogenize $u(z)$, $v(z)$, $T(z)$ and $S(z)$ within this block conserving total momentum, heat and salt within block.
 - (c) Recalculate $N^2(z)$ everywhere
2. Enforce marginal stability at unstable grid-points:
while($Sh_{red}^2 > 0$ at some z)
- (a) Find the grid-point k with maximum Sh_{red}^2
 - (b) Apply down-gradient fluxes of momentum, heat and salt at this grid point, with the same effective diffusivity $\kappa_v = \kappa_T = \kappa_S$, until $Sh_{red}^2(k) = 0$
 - (c) Recalculate Sh_{red}^2 everywhere

An example calculation is shown in Fig. 2.4. In the second while loop, the applied fluxes result in reduced stratification and shear at the grid point of interest, but increased shear and stratification at the neighboring grid points. As the algorithm continues, these high gradients are expelled from the unstable region. The resulting profiles have lower shear and stratification in the now marginally stable region (Fig. 2.4d,e,f between 80m and 40m) and increased shear and stratification on the edges of the marginally stable region (Fig. 2.4d,e,f between 110m and 80m, and above 40m).

Chapter 3

Equatorial Kelvin Waves and Tropical Instability Waves

RYAN M. HOLMES AND LEIF N. THOMAS

Earth System Science, Stanford University, Stanford, California

Tropical instability waves (TIWs) and equatorial Kelvin waves are dominant sources of intraseasonal variability in the equatorial Pacific ocean, and both play important roles in the heat and momentum budgets of the large-scale flow. While individually they have been well studied, little is known about how these two features interact. Here we examine the influence of Kelvin waves on TIW kinetic energy (TIWKE) using an ensemble set of $1/4^\circ$ ocean model simulations of the equatorial Pacific Ocean. The results suggest that TIWKE can be significantly modified by 60-day Kelvin waves. Downwelling Kelvin waves induce a decay in TIWKE and upwelling Kelvin waves induce growth in TIWKE through modifications of the background circulation from which TIWs extract energy. However, the manner in which the TIWKE budget adjusts to these changes in background circulation is complex. Changes driven by a number of minor terms are amplified by lateral shear production associated with the meridional shear in zonal velocity, $-\rho_0 \overline{u'v'} \frac{\partial U}{\partial y}$, which itself depends on TIWKE

through the TIW momentum flux $\overline{u'v'}$. The transfer of TIWKE from the surface to deep ocean through pressure work also plays a major role as a negative feedback. These results have implications for the strength and temporal evolution of SST anomalies in the eastern equatorial Pacific in response to variations in atmospheric forcing.

The material in this chapter is being prepared for submission to *J. Phys. Oceanogr.* in March 2016.

3.1 Introduction

Equatorial Kelvin waves in the Pacific ocean play an important role in the El Niño - Southern Oscillation (ENSO) as they facilitate the adjustment of the upper ocean to perturbations in atmospheric forcing across the basin (*Picaut et al.*, 1997; *Suarez and Schopf*, 1988; *Wang and Fiedler*, 2006). Kelvin waves are typically generated in the western Pacific by wind stress anomalies associated with tropical cyclones, the Madden-Julien Oscillation and other sources of atmospheric variability (*Hendon et al.*, 1998; *Zhang*, 2001). The dominant intraseasonal first-baroclinic-mode Kelvin waves propagate eastward with typical speeds of 2.7ms^{-1} (*Cravatte et al.*, 2003), although their propagation and structure are also influenced by the state of the background equatorial circulation (*McPhaden et al.*, 1986; *Giese and Harrison*, 1990; *Johnson and McPhaden*, 1993a,b). The Kelvin waves modify the background circulation in the central and eastern Pacific, including the thermocline depth, zonal currents, sea surface temperature (SST) and thus the air-sea interactions critical for ENSO (*McPhaden and Taft*, 1988; *Lien et al.*, 1995; *Bergman et al.*, 2001; *McPhaden*, 2002). However, the influence of Kelvin waves on the smaller-scale variability in the eastern Pacific is not as well studied.

Tropical instability waves (TIWs) are a second major source of intraseasonal variability in the eastern Pacific that were first observed as meridional oscillations in the equatorial fronts (*Legeckis*, 1977; *Malard et al.*, 1987; *Willett et al.*, 2006; *Jiang et al.*, 2009). Generated through barotropic and baroclinic instability, they travel westward with wavelengths of 700-1600km and periods of 15-40 days (*Philander*, 1976; *Cox*,

1980; *Qiao and Weisberg*, 1995; *Masina et al.*, 1999; *Kennan and Flament*, 2000; *Lyman et al.*, 2007). Their strength varies both interannually with the ENSO cycle (*An*, 2008) and seasonally, where they obtain peak amplitude in boreal fall and winter (*Contreras*, 2002), the same period over which Kelvin wave variability peaks (*Kessler et al.*, 1995). TIWs drive strong lateral eddy stirring and influence small-scale turbulent mixing, and thus play an important role in the mixed-layer heat budget (*Menkes et al.*, 2006; *Jochum et al.*, 2007; *Moum et al.*, 2009; *Graham*, 2014; *Holmes and Thomas*, 2015).

Several studies have highlighted the potential for interactions between TIWs and Kelvin waves. *Harrison and Giese* (1988) and *Giese and Harrison* (1991) saw modulations in TIW amplitude in a numerical model in response to the presence of Kelvin waves, and inferred changes in the TIW-driven meridional heat flux. In the observations of *Qiao and Weisberg* (1998), the end of the TIW season coincided with the arrival of a strong intraseasonal Kelvin wave from the western Pacific, which they suggest may have decreased the background current shear $\frac{\partial U}{\partial y}$, resulting in a decay in TIW amplitude. Finally, a number of studies have discussed the potential link between the intraseasonal wind variability that generates Kelvin waves, Rossby waves reflected from the eastern boundary, and the strength and phasing of TIWs (*Allen et al.*, 1995; *Lawrence et al.*, 1998; *Lawrence and Angell*, 2000; *Benestad et al.*, 2001). All of these studies hint at the potential importance of interactions between free equatorial waves and TIWs for setting the magnitude and temporal evolution of SST anomalies in the eastern equatorial Pacific in response to variations in atmospheric forcing. However, no study has yet explored the details of how Kelvin waves influence the TIW kinetic energy (TIWKE) budget.

Analysis of satellite sea surface height (SSH) and SST data in the equatorial Pacific suggests that Kelvin waves may alter both the phase speed and amplitude of TIWs (Fig. 3.1). In late 2013 and early 2014, several downwelling (positive perturbation SSH) and upwelling (negative perturbation SSH) Kelvin waves propagated across the Pacific (Fig. 3.1a), encountering an energetic set of westward propagating TIWs (Fig. 3.1b). The TIWs appear to propagate faster during the upwelling phases and slower during the downwelling phases (magenta phase lines in Fig. 3.1b), as might

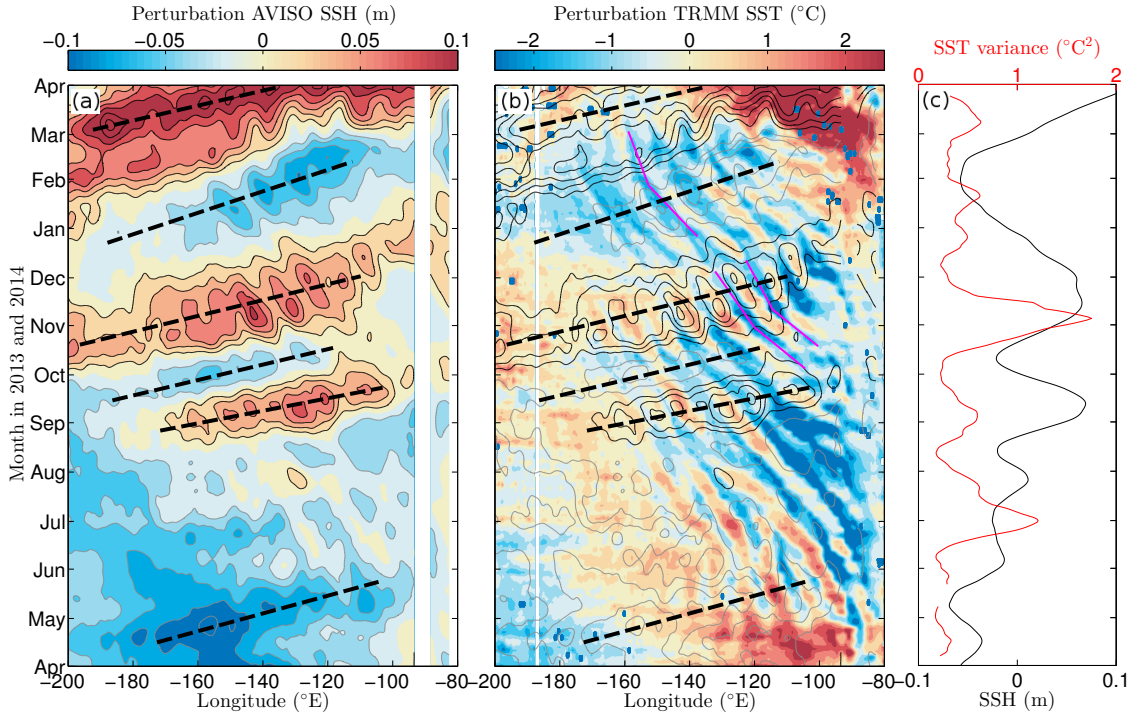


Figure 3.1: (a) Perturbation SSH from AVISO altimetry data averaged between $\pm 2^\circ$ latitude in 2013 and 2014. Raw SSH anomalies are filtered with a 3.75° moving average in longitude and 15-day moving average in time. Black (gray) contours show positive (negative) perturbation SSH in both (a) and (b). (b) Perturbation TMI TRMM microwave satellite SST data (*Wentz et al.*, 2015) averaged between 1°N and 2°N . 3-day average SST anomalies are filtered with a 0.75° moving average in longitude and 3-day moving average in time. Downwelling and upwelling Kelvin wave phases are marked with black dashed lines. Several TIW phases are marked with magenta lines in (b). (c) SST variance (red) and SSH anomalies between -140°E and -120°E .

be expected from Doppler shifting associated with the Kelvin wave zonal velocity. In addition, the strength of the SST anomalies associated with the TIWs, a proxy for the TIW amplitude, appears to vary with the Kelvin wave phase. Stronger SST anomalies occur following upwelling phases and weaker anomalies occur after downwelling phases (e.g. October–December 2013 between -140°E and -110°E in Fig. 3.1). The final strong downwelling phase initiated in February and March 2014 is accompanied by a complete disappearance of the TIW SST anomalies.

Motivated by these observations and previous studies we address the question;

How do intraseasonal Kelvin waves influence the properties of TIWs in the equatorial Pacific? We use a set of $1/4^\circ$ ocean model simulations described in section 3.2 forced with first-baroclinic-mode Kelvin waves in the western Pacific. In section 3.3 we analyze the energetics of TIWs in the control simulation that does not include Kelvin waves. In section 3.4 we examine the changes in the TIWKE budget induced when both downwelling and upwelling Kelvin waves propagate through the eastern Pacific. In section 3.5 we discuss some of the processes governing the complex behavior of the TIWKE budget and briefly discuss the TIW-driven meridional heat flux. Finally, in section 3.6 we summarize our findings and discuss their implications.

3.2 Model setup

We will examine the interaction between equatorial Kelvin waves and TIWs in a set of Regional Ocean Modeling System (ROMS; *Shchepetkin and McWilliams* (2005)) simulations. The simulations span the Pacific ocean over the region -240°E to -70°E , 30°S to 30°N with 0.25° horizontal resolution, 50 vertical levels and a time step of 10 minutes. They are spun up from rest over a 10-year period using initial conditions, forcing and boundary conditions taken from the Common Ocean Reference Experiment Normal Year Forcing (CORENYF) fields (*Large and Yeager*, 2004). Analysis shown here is from the final year of the spin-up period (hereafter the ‘control simulation’). The K-profile parameterization was used to parameterize sub-grid scale vertical mixing processes (*Large et al.*, 1994). Horizontal diffusion of momentum was achieved with a bi-harmonic viscosity with coefficient $1 \times 10^{11} \text{m}^4\text{s}^{-1}$ and harmonic horizontal diffusion of salinity and temperature was included with coefficient $100 \text{m}^2\text{s}^{-1}$. ROMS has been successfully used for process studies of TIWs under similar configurations (*Marchesiello et al.*, 2011; *Holmes et al.*, 2014; *Holmes and Thomas*, 2015).

To simplify the analysis and interpretation, we remove the seasonal cycle by using temporally constant atmospheric forcing. Surface forcing, initial conditions and boundary conditions are taken from six-month July–December averages of the CORENYF bulk forcing fields. This season has strong trade winds and produces energetic TIWs, ideal for this process study. The interaction of Kelvin waves with

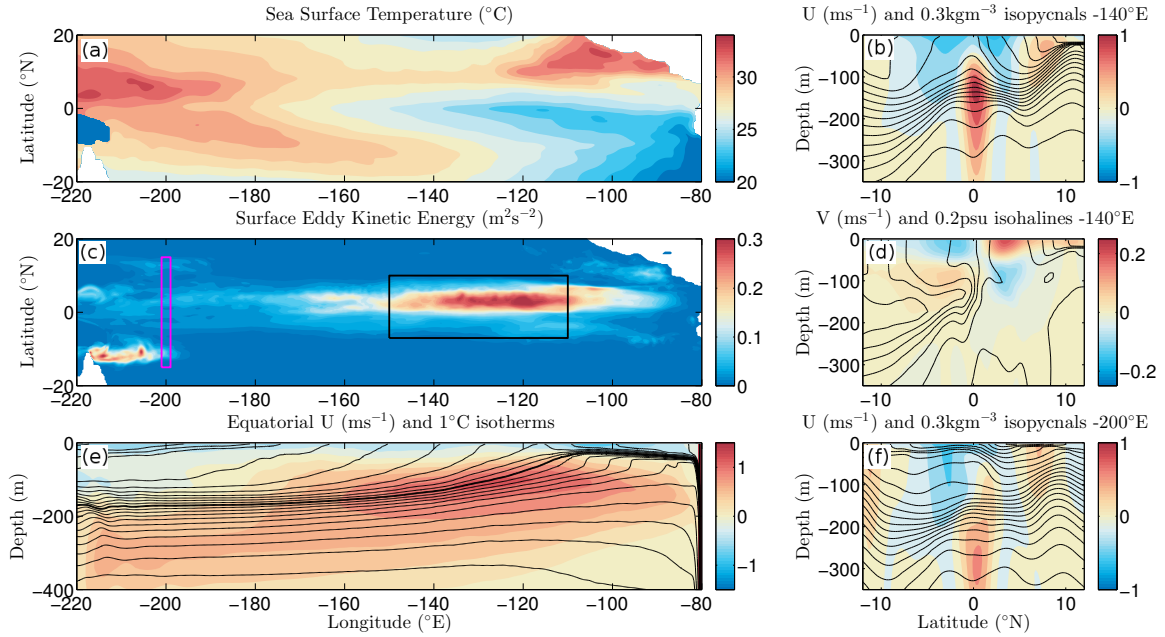


Figure 3.2: (a) SST and (c) surface eddy kinetic energy taken from the control simulation. (b) Zonal velocity and isopycnals and (d) meridional velocity and salinity contours at -140°E . (e) Equatorial zonal velocity and isotherms. (f) Zonal velocity and isopycnals at -200°E . The black box in (c) indicates the control volume used for the TIWKE budget and the magenta box indicates the Kelvin wave forcing region.

the seasonally-varying TIW field is outside the scope of this article.

The simulations produce a general circulation with similar features to observations (Fig. 3.2). A sloped thermocline leans upward toward the eastern Pacific cold tongue that is bounded by warmer water to the north (Fig. 3.2a,e). The SSTs are warmer than observed in the far western Pacific and in the Costa Rica dome region as there is no wind stress variability (Fig. 3.2a). The cold tongue SST is 1-2°C cooler than observed annual mean values, and the Equatorial Undercurrent (EUC) is slightly stronger than annual mean observations, reaching 1.1ms^{-1} (Fig. 3.2b). The simulations produce a statistically-steady TIW field with surface eddy kinetic energy exceeding $0.2\text{m}^2\text{s}^{-2}$ (comparable to peak observed EKE values, *Flament et al. (1996)*) over an extensive area reaching from -150°E to -100°E (Fig. 3.2c). The TIWs have a dominant period near 34 days (not shown).

3.3 TIW energetics in the control simulation

In this section we examine the TIWKE budget in the statistically-steady control simulation that does not contain Kelvin waves. The ocean model solves the hydrostatic primitive equations, which can be written in terms of buoyancy as,

$$\frac{D\mathbf{u}_h}{Dt} + f\hat{\mathbf{k}} \times \mathbf{u} = -\frac{1}{\rho_0} \nabla_h P + \mathbf{F}_h, \quad (3.1)$$

$$0 = -\frac{1}{\rho_0} \frac{\partial P}{\partial z} + b, \quad (3.2)$$

$$\nabla \cdot \mathbf{u} = 0, \quad (3.3)$$

$$\frac{Db}{Dt} = \mathcal{H}, \quad (3.4)$$

where $\mathbf{u} = (u, v, w)$ is the three-dimensional velocity, \mathbf{u}_h is the horizontal velocity, $f = 2\Omega \sin \theta$ is the Coriolis parameter, Ω is the rotation rate of the Earth, θ is latitude, $\hat{\mathbf{k}}$ is the unit vector in the local vertical, ρ_0 is a reference density, P is pressure, $\mathbf{F} = (F_x, F_y, 0)$ is the frictional force, $b = -g\rho/\rho_0$ is buoyancy, ρ is potential density, g is the acceleration due to gravity and \mathcal{H} represents diabatic processes. We now perform a Reynolds decomposition of the flow field into background and TIW components, $\mathbf{u} = \bar{\mathbf{u}} + \mathbf{u}' = \mathbf{U} + \mathbf{u}'$. In the control simulation the over-line denotes a time average over the whole year and the time varying flow components are the TIWs. For the Kelvin wave simulations considered in the next section, the over-line will denote an ensemble average and both background and TIW flow components will vary in time.

Using the standard procedure (for example see *Masina et al. (1999)*) an equation for the evolution of the TIWKE,

$$\mathcal{K} = \frac{1}{2} \rho_0 (\overline{u' u'} + \overline{v' v'}), \quad (3.5)$$

can be derived from the equations of motion (3.1)-(3.4),

$$\begin{aligned} \frac{\partial \mathcal{K}}{\partial t} = & -\nabla \cdot \left(\mathcal{K}\mathbf{U} + \overline{\mathbf{u}'P'} + \frac{1}{2}\rho_0 \overline{\mathbf{u}'(u'u' + v'v')} \right) + \rho_0 \overline{w'b'} \\ & + \rho_0 \overline{\mathbf{u}'_h \cdot \mathbf{F}'_H} - \rho_0 \overline{\mathbf{u}'u'} \cdot \nabla U - \rho_0 \overline{\mathbf{u}'v'} \cdot \nabla V. \end{aligned} \quad (3.6)$$

The time tendency term on the left-hand side is zero for the control simulation but non-zero for the ensemble simulations considered in the next section. The terms on the right-hand side are the convergence of the mean, pressure and TIW fluxes of TIWKE, the potential energy (PE) conversion term, the frictional term and the shear production terms of which there are six associated with each of the spatial derivatives of the background zonal U and meridional V velocities. These terms are evaluated from the daily-averaged model output. The frictional and pressure flux divergence terms are calculated by taking the dot product of the velocity with the model diagnostic frictional and pressure gradient forces. Thus we calculate the divergence of the pressure fluxes directly and not the individual flux components.

The TIWKE budget in the control simulation is dominated by production of TIWKE by lateral shear production acting on the meridional shear in zonal velocity,

$$LSP = -\rho_0 \overline{u'v'} \frac{\partial U}{\partial y} \quad (3.7)$$

(Figures 3.3b,e), conversion of mean *PE* to TIWKE (Figures 3.3c,f), the transport of TIWKE by pressure fluxes (Fig. 3.3i) and the removal by friction (Fig. 3.3h). Integrating the budget over a control volume bounding the TIW region spanning the top 244m, -150°E to -110°E and 7°S to 10°N shows that *PE* conversion is the largest net source ($17.6 \pm 1.0\text{GW}$) followed by *LSP* ($12.6 \pm 1.5\text{GW}$)¹. The *LSP* has two source regions, one associated with the cyclonic shear between the EUC and

¹ The uncertainty on these volume integrated values was estimated by calculating the spread between 10 sets constructed by rejecting a random 10% of the 360 days in the control simulation for each set. 10 sets were chosen for consistency with the ensemble simulations described in the next section and for computational reasons. To account for temporal auto-correlation (which is not a problem for the ensemble simulations considered in the next section) the degrees of freedom were reduced by $34/3$ as 34 days was the TIW period and we assume that the TIWs are perfect sinusoids that require 3 sampling points to constrain.

South Equatorial Current (SEC) near 1.5°N at 70m depth and one associated with the anticyclonic shear between the SEC and North Equatorial Counter Current (NECC) near the surface at 4°N (compare Figures 3.3b,e and 3.2b). There is also a sink region on the southern side of the EUC. The conversion from mean PE has a peak further north near 5°N (Fig. 3.3f) and a source region in the Southern Hemisphere east of -140°E (Fig. 3.3c). These TIWKE source terms are broadly consistent with previous literature, although the exact mix of source regions and strengths varies with season and model (*Luther and Johnson*, 1990; *Masina et al.*, 1999; *Pezzi and Richards*, 2003). The other shear production terms make small contributions which overall are not large sources or sinks of TIWKE (Figures 3.3g,j,k, $\frac{\partial V}{\partial x}$ production not shown).

Friction is a large sink of TIWKE in the control volume ($-13.6 \pm 0.6\text{GW}$, Fig. 3.3h), mostly in the upper EUC and SEC region where TIWs are known to drive strong variations in vertical mixing (*Moum et al.*, 2009; *Holmes and Thomas*, 2015). The divergence of the pressure flux suggests that energy is radiated away from the regions in which it is generated by *LSP* and PE conversion (compare Fig. 3.3i to Figures 3.3e and 3.3f). Some energy is deposited in surrounding regions at the surface near the equator and between 100m and 150m at 5°N (Fig. 3.3i), helping to expand the spatial extent of the TIWKE (compare Fig. 3.3i to Fig. 3.3d). However, TIWKE energy radiation out of the control volume via pressure fluxes is also the largest mechanism of TIWKE loss, accounting for $-15.1 \pm 1.7\text{GW}$. $6.4 \pm 0.5\text{GW}$ of this outward pressure flux is dissipated in the model layer near the seafloor, where the TIWKE budget is dominated by a balance between pressure flux convergence and friction due to quadratic bottom drag (not shown). Of the remaining $8.7 \pm 2.2\text{GW}$ leaving the control volume, $6 \pm 0.6\text{GW}$ is lost through the lateral boundaries at all depths (as calculated by integrating the pressure flux divergence over the full water column), leaving $2.7 \pm 2.8\text{GW}$ to be lost to friction and other processes within the deep water column below 244m depth but above the bottom model layer.

The loss of $6 \pm 0.6\text{GW}$ through lateral radiation is partially accounted for by meridionally-propagating barotropic Rossby waves generated by the TIWs. These were discussed by *Farrar* (2011) in the context of altimetry observations. Barotropic

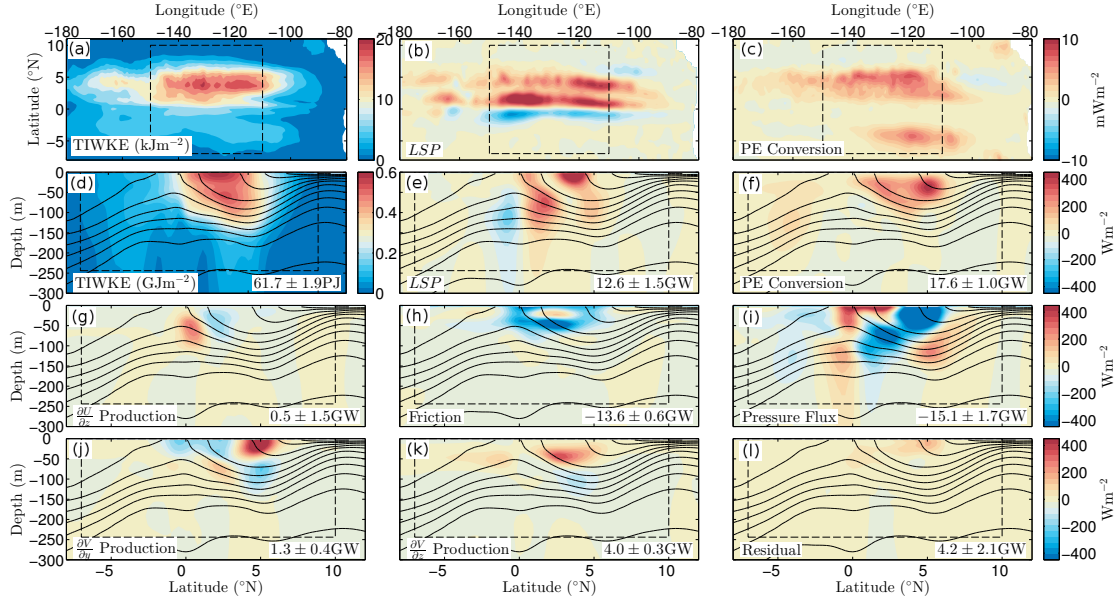


Figure 3.3: Longitude-latitude plots of (a) TIWKE, (b) LSP (see Eq. (3.7)), and (c) conversion of mean PE into TIWKE from the control simulation integrated over the top 244m. Latitude-depth plots of (d) TIWKE and (e-l) TIWKE energy budget terms (see Eq. (3.6)) integrated between the longitudes of -150°E and -110°E . The dashed lines show the control volume (7°S to 10°N , -150°E to -110°E , top 244m) over which each term is integrated, with the totals shown in the bottom right of each panel. The contours are isopycnals at 0.5kgm^{-3} spacing. The net TIWKE budget is dominated by creation of TIWKE through LSP (b,e) and PE conversion (c,f), removal of TIWKE by friction (h) and radiation of TIWKE out of the control volume by the pressure fluxes (i). The residual (l) has a lower magnitude than these four main terms. The uncertainty on the totals is calculated using a sub-sampling technique accounting for auto-correlation as described in footnote 1.

waves are evident in the model SSH (Fig. 3.4a) and barotropic velocity (Fig. 3.4b) fields, with wave crests oriented NW-SE in the Northern Hemisphere and SW-NE in the Southern Hemisphere. Using estimates of the zonal wavelength (1300km; Fig. 3.4d), period (34 days; Fig. 3.4e) and the dispersion relation for barotropic Rossby waves (see *Farrar (2011)*),

$$\omega = \frac{-\beta k}{k^2 + l^2}, \quad (3.8)$$

where ω is the frequency, $\beta = \partial f / \partial y$ and k and l are the zonal and meridional wavenumbers respectively, gives a good prediction for the orientation of wave crests

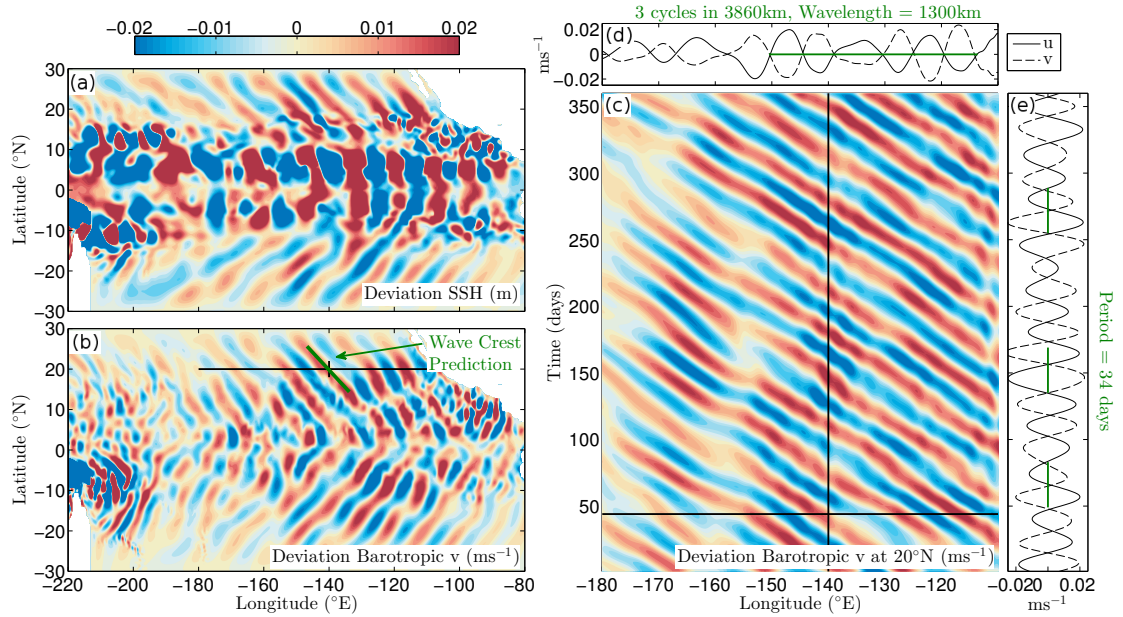


Figure 3.4: Deviation (a) SSH and (b) barotropic meridional velocity on day 44 of the control simulation. (c) Longitude-time plot of the deviation barotropic meridional velocity at 20°N. (d) Barotropic velocities on day 44 as a function of longitude at 20°N. (e) Time series of barotropic velocities at -140°E , 20°N . The green lines in (d) and (e) indicate estimates of the wavelength (1300km) and period (34 days) of the wavelike features. Using these estimates and the dispersion relation for barotropic Rossby waves (Eq. (3.8)) gives a good prediction for the orientation of wave crests (green line in b).

at 20°N in the model (green line in Fig. 3.4b), suggesting that these waves are indeed barotropic Rossby waves. In addition, using estimates of the velocity amplitude $u_a = v_a = 0.02\text{ms}^{-1}$ (Fig. 3.4b-e) and SSH amplitude $\zeta_a = 0.02\text{m}$ (Fig. 3.4a) we can obtain an estimate of the net meridional energy flux associated with these waves $F = L\bar{E}c_g$, where $L = 4400\text{km}$ is the zonal length of the control volume between -150°E and -110°E and the wave-period-averaged energy density \bar{E} and meridional

group velocity c_g are given by,

$$\overline{E} = \frac{1}{2} \left(\frac{1}{2} \rho_0 H (u_a^2 + v_a^2) + \frac{1}{2} \rho_0 g \zeta_a^2 \right), \quad (3.9)$$

$$c_g = \frac{2\beta kl}{(k^2 + l^2)^2}. \quad (3.10)$$

Using the above parameters we obtain an estimated northward flux of 1.7GW, and thus if there is an equivalent southward flux in the Southern Hemisphere then the total flux of energy lost through barotropic Rossby wave radiation accounts for over half of the 6 ± 0.6 GW of energy lost from the TIWKE budget through lateral pressure flux radiation. Thus barotropic Rossby wave radiation appears to play an important role in the TIWKE budget.

3.4 The influence of intraseasonal Kelvin waves on TIWKE

In this section we examine the changes in the TIWKE and TIWKE budget induced by the passage of intraseasonal Kelvin waves along the equator.

3.4.1 Kelvin wave ensemble experiments

In order to study the interaction of the statistically-steady TIW field with a Kelvin wave, we nudge the model horizontal velocity in the western Pacific to force first-baroclinic-mode Kelvin waves with known properties. We force the Kelvin waves between the longitudes of -201°E and -199°E , where TIWKE is minimal (magenta box in Fig. 3.2c). There is a non-zero background flow and meridional variations in stratification at this location (Fig. 3.2f), which influence the spatial structure of the Kelvin-wave mode. To take this into account, we solve for the structure of a linear Kelvin wave in the control simulation background flow at this location assuming that this background flow is zonally-uniform. The calculation is described in the Appendix and is similar to that described by *McPhaden et al.* (1986). The assumption of zonal

uniformity is expected to work well in the forcing region in the western Pacific where zonal variations are weak (Fig. 3.2e). The first-baroclinic mode obtained from this calculation at -200°E has a wave speed of $c = 2.80\text{ms}^{-1}$ and an altered spatial structure relative to the structure without a background flow (compare Figures 3.5a and 3.5c). At -140°E the linear first-baroclinic-mode Kelvin wave has a different spatial structure with a stronger amplitude around the EUC core because the EUC is stronger at -140°E than at -200°E (compare Figures 3.5f and 3.5c). The phase speed of 2.68ms^{-1} at -140°E is also slightly slower than that at -200°E . These phase speeds are consistent with that measured in the equatorial Pacific (Cravatte *et al.*, 2003). In order to force the Kelvin wave, the zonal flow between -201°E and -199°E is nudged to the background flow (Fig. 3.2f) plus the spatial structure in Fig. 3.5c multiplied by a half-sine temporal factor with given frequency ω . The temporal factor represents either a downwelling half-sine Kelvin wave pulse or an upwelling half-sine Kelvin wave pulse, which differ by a phase shift of π (illustrated in Fig. 3.5g). The nudging time scale used is $1/3$ day.

When constructing an energy budget for the TIWs it is necessary to separate the flow into TIW and background flow components. For the control simulation this was done using a simple time average. However, when introducing temporal variability in the background flow in the form of a propagating Kelvin wave with a time scale not necessarily well separated from the TIW time scale, this method no longer works. Another possibility is to use a longitude filter, but again the zonal scale of the TIWs and Kelvin waves are not necessarily well separated. To avoid these problems we perform an ensemble of 10 simulations for both the downwelling and upwelling cases. Each ensemble member consists of a single Kelvin wave pulse forced for 30 days in the western Pacific followed by a spin-down period of 120 days (Fig. 3.5g). The Kelvin wave forcing is initialized from different times in the control simulation for each ensemble member and thus the phasing of the TIWs is different in each member (3 example ensemble members are shown in Fig. 3.6 for the downwelling experiment). An average over the ensembles (the over-line in Eq. (3.6)) thus separates the TIW field while retaining the time and longitude dependence in both TIW and background flow fields. The initialization times were distributed evenly over the last 4×34 days

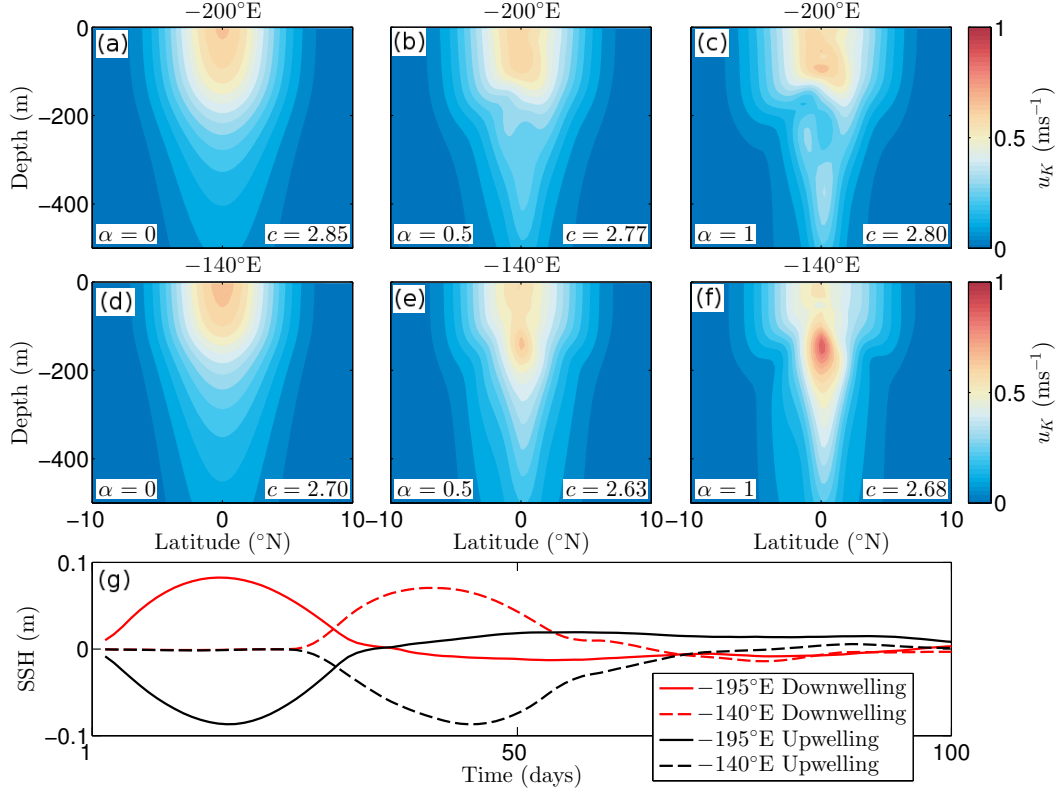


Figure 3.5: (a-f) The zonal velocity of the first-baroclinic-mode Kelvin wave as a function of the mean flow strength α , where $\alpha = 0$ indicates no mean flow and $\alpha = 1$ indicates the full mean flow (see Eq. (3.36)). For (a)-(c) the mean flow and stratification used is that at -200°E (Fig. 3.2f) and for (d)-(f) the mean flow used is that at -140°E (Fig. 3.2b) from the control simulation. The corresponding wave speeds are indicated in the subplot titles. As the mean flow is introduced the mode acquires some small-scale structure, but the large-scale pattern remains the same. (g) Time series of ensemble average SSH from downwelling (red) and upwelling (black) experiments at -195°E (solid) and -140°E (dashed).

of the control simulation as 34 days was the dominant TIW period.

Due to the necessity of performing an ensemble of simulations, it was not possible to test more than one set of Kelvin wave parameters. We choose to examine intraseasonal Kelvin waves with a 60-day period, a dominant peak in the observed Kelvin wave spectrum (*McPhaden and Taft, 1988; Kessler et al., 1995; Cravatte et al.,*

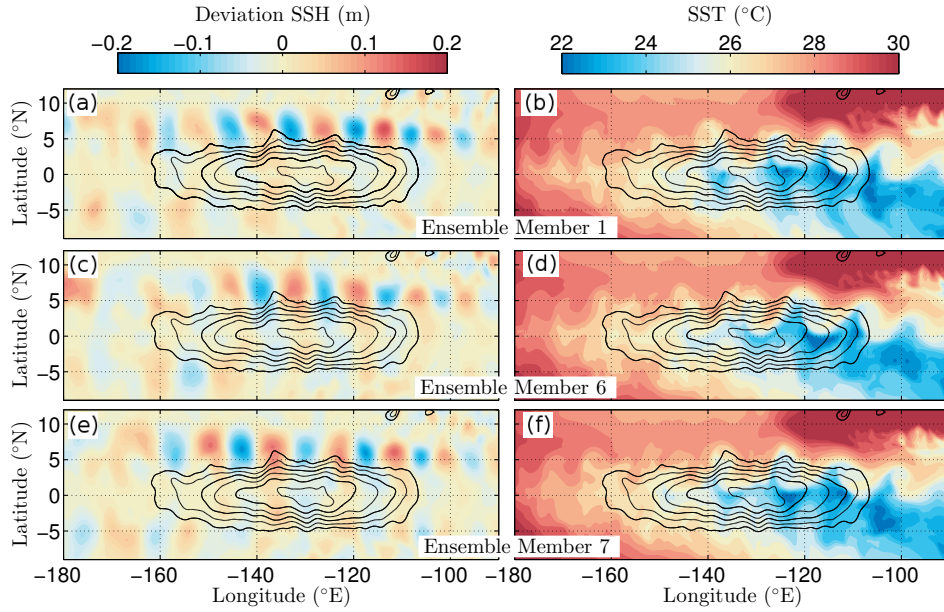


Figure 3.6: (a,c,e) SSH deviation from the ensemble mean and (b,d,f) SST for 3 ensemble members of the downwelling Kelvin wave experiment at day 45. 0.01m contours of the ensemble mean SSH anomaly (only contours $\geq 0.02\text{m}$ are shown) on every panel indicate the positive SSH anomaly of the downwelling Kelvin wave at this time. The different ensemble members differ in the phasing of the TIW field. Thus the TIW and background flow components can be separated using an average over all 10 ensemble members.

2003). The amplitude of the forcing was tuned using a trial-and-error method to produce Kelvin waves with $\pm 0.08\text{m}$ variations in SSH, $\pm 15\text{m}$ variations in 20°C isotherm depth (Fig. 3.7a) and a maximum of $\pm 1.5^\circ\text{C}$ variations in subsurface temperature at -140°E . These values represent a strong but realistic Kelvin wave in comparison to observations (*Johnson and McPhaden, 1993b,a; Kessler et al., 1995; Cravatte et al., 2003; Jiang et al., 2009*).

The propagation of the Kelvin waves across the basin is clearly visible in SSH and the depth of the 20°C isotherm (Fig. 3.7a-d). The ensemble average does a good job of removing the TIW variability (compare Figures 3.7a,b with Figures 3.7c,d). The wave signal begins at -200°E and is visible there over the forcing period of 30 days. The phase speed appears to be relatively constant across the basin, with only a small slowing from 2.8ms^{-1} at -200°E to 2.68ms^{-1} at -140°E predicted for an ideal Kelvin

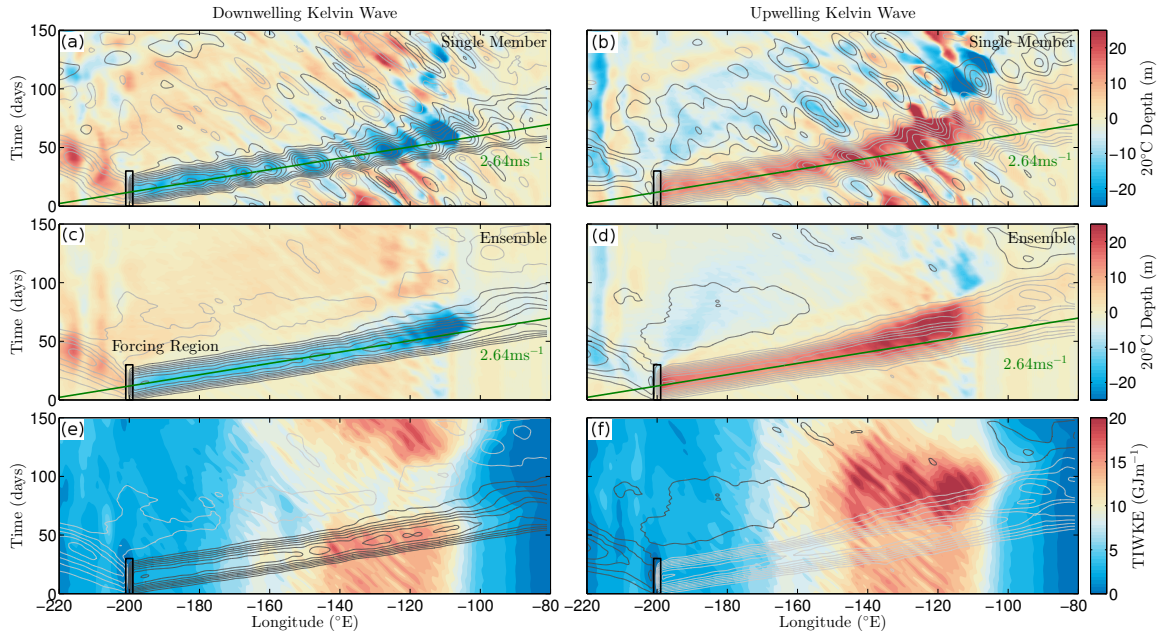


Figure 3.7: Time-longitude plots of the perturbation depth of the 20°C isotherm on the equator for a single (a) downwelling and (b) upwelling ensemble member and for the ensemble average (c) downwelling and (d) upwelling experiments. Time-longitude plot of the TIWKE integrated over the top 244m and between 7°S and 10°N for (e) downwelling and (f) upwelling experiments. Also shown are 0.01m contours of deviation SSH, with dark gray contours indicating positive values and light gray contours indicating negative values. The forcing region and time period is shown with the black box. The green line in (a-d) indicates a phase speed of 2.64ms⁻¹.

mode (see Fig. 3.5). The perturbations in the 20°C isotherm are largest near -120°E (Fig. 3.7c-d) where this isotherm approaches the surface (Fig. 3.2e). However, the signal in the 20°C isotherm is not visible east of -100°E because this isotherm is restricted close to the surface there. From the SSH signals, there does not appear to be significant changes in the downwelling (upwelling) wave amplitude until -105°E (-120°E), although given the change in stratification across the basin an energy flux calculation outside the scope of this article would be necessary to establish this. Amplitude and phase speed changes in the far eastern Pacific east of -120°E may be associated with the conversion of energy from the first-baroclinic to the second-baroclinic mode (Gill and King, 1985; Cravatte *et al.*, 2003). The forcing applied in the western Pacific also forces a westward propagating Rossby wave signal visible in

both SSH and 20°C isotherm depth (Fig. 3.7c,d west of -200°E). In addition, there is evidence of Rossby waves reflected from the eastern boundary as a result of the incident Kelvin wave (not shown), which may have an additional impact on the TIWs at later times (*Allen et al.*, 1995; *Lawrence et al.*, 1998; *Lawrence and Angell*, 2000; *Benestad et al.*, 2001).

The Kelvin waves drive large variations in the latitude and depth integrated TIWKE (Fig. 3.7e,f). TIWKE is suppressed by the downwelling wave and enhanced by the upwelling wave, in agreement with observations (Fig. 3.1, *Qiao and Weisberg* (1998)). These changes occur uniformly with longitude in the region of TIW activity. The peak/trough in TIWKE occurs 20 – 30 days after the peak in the Kelvin wave pulse passes by. The TIWKE is then restored toward its original strength ~ 50 days after the waves have completely passed. There is some evidence of advection of TIWKE by the Kelvin wave in the far eastern Pacific (the colored contours between -100°E and -80°E in Fig. 3.7b), but the large changes in TIWKE are clearly not due to Kelvin wave advection.

As discussed in the previous section, the TIWs gain energy from both the *LSP* and conversion of mean PE to TIWKE. The Kelvin waves alters the background zonal velocity U and density structure, and thus may alter the balance of the TIWKE budget resulting in growth and decay of TIWKE.

3.4.2 The modified TIWKE budget

We now examine the Kelvin wave induced modifications to the TIWKE budget. Firstly, the TIWKE budget from the 10-member ensemble average at the initial time (not shown), well before the Kelvin wave arrives in the eastern Pacific, agrees well with the budget in the control simulation (Fig. 3.3). To describe how the budget is altered by the Kelvin waves, we examine time series of the TIWKE budget integrated over the control volume (as for Fig. 3.3) 7°S to 10°N , -150°E to -110°E over the top 244m (Figures 3.8 and 3.9). The zonal length of this control volume is less than a third of the 15,000km zonal wavelength of the Kelvin wave (see Fig. 3.6).

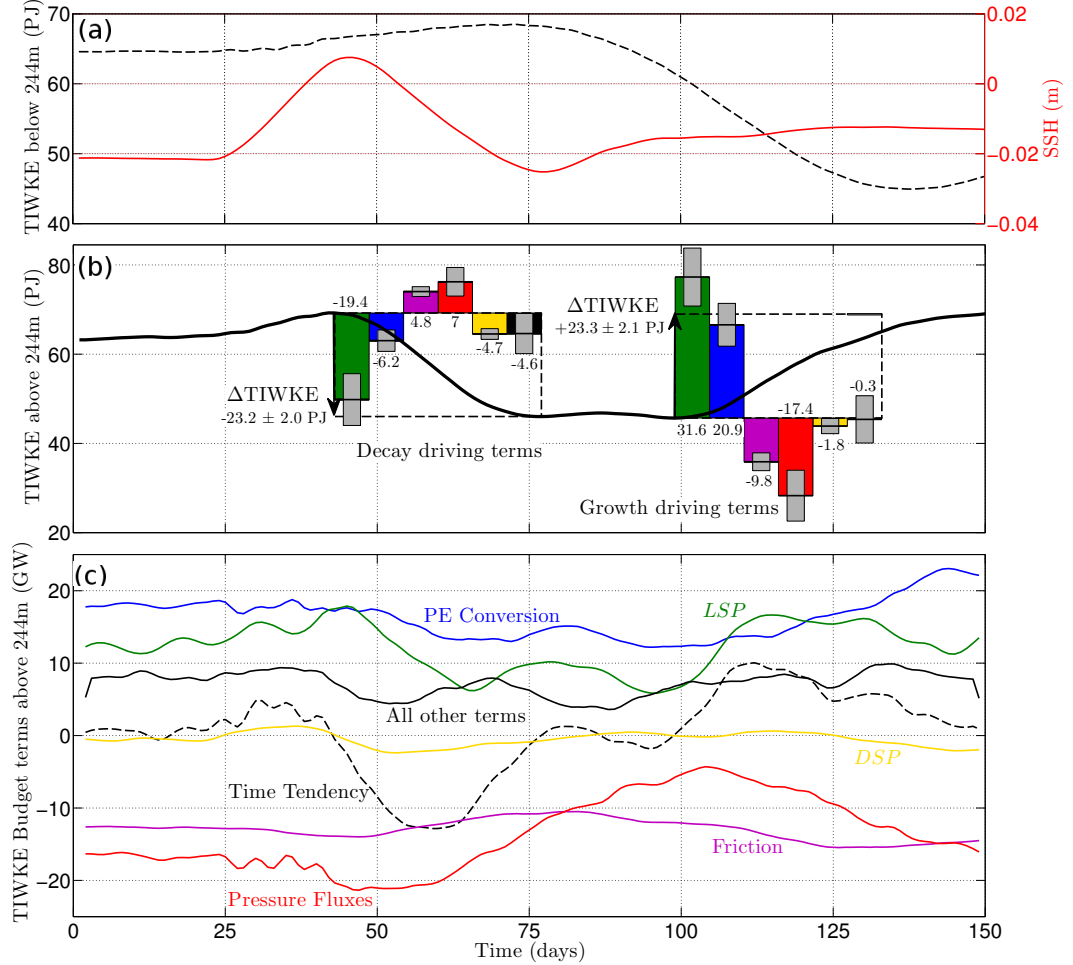


Figure 3.8: TIWKE and TIWKE budget terms as a function of time integrated over the control volume bounded by longitudes -150°E and -110°E and latitudes 7°S and 10°N for the downwelling Kelvin wave experiment. (a) TIWKE below 244m (black dashed, left axis) and SSH (red, right axis). (b) TIWKE above 244m (black line). (c) TIWKE budget terms including PE conversion (blue), LSP (Eq. (3.7); green), friction (purple), pressure flux divergence (red), time tendency (dashed black), DSP (Eq. (3.11); yellow) and all other terms including residual (solid black). In (b) each colored bar corresponds to the time integral of the corresponding colored term in (c) over the TIWKE decay (days 43 to 77) and growth (days 99 to 149) periods according to Eq. (3.12), indicating how much each term contributes to the net change in TIWKE (in PJ) over these periods. The gray regions correspond to the $\pm 2\sigma$ spread over 10 sets of 9 ensemble members constructed using the jackknife method (see footnote 2).

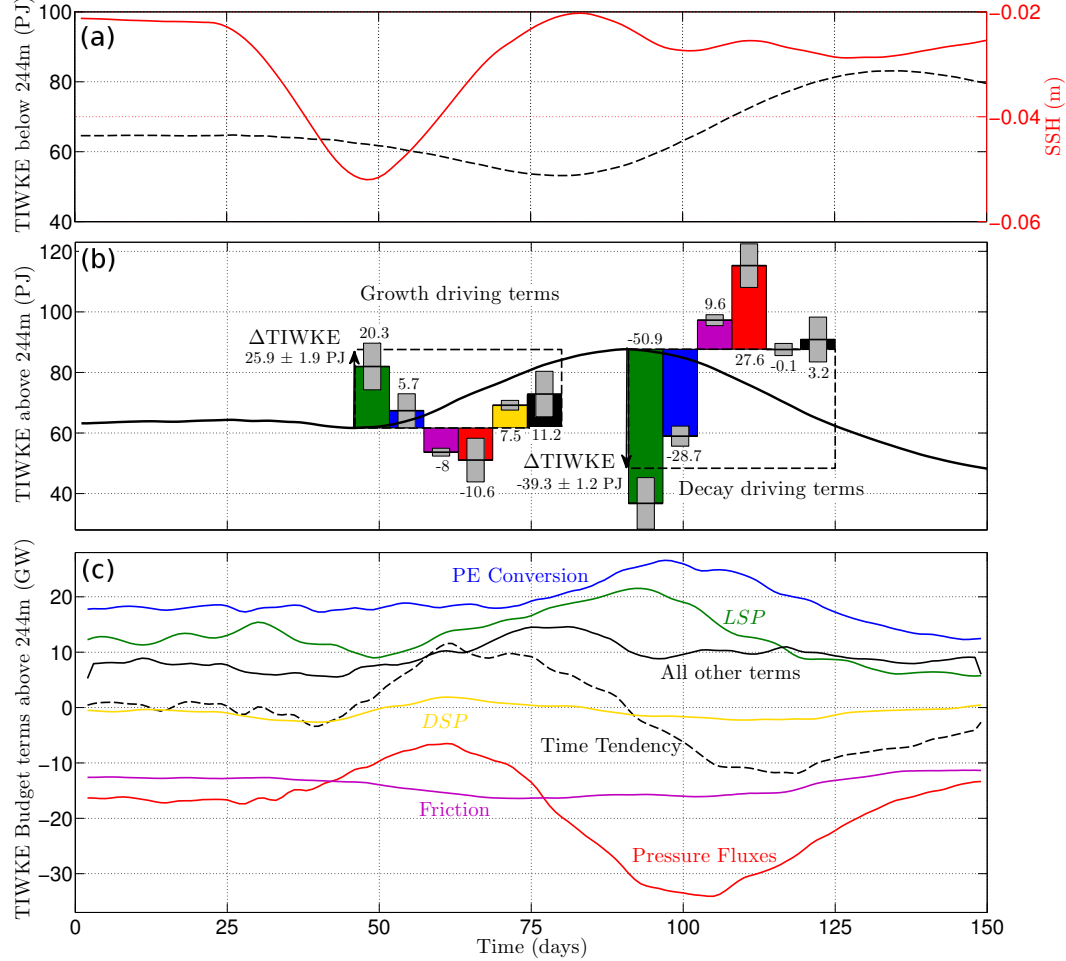


Figure 3.9: As for Fig. 3.8 but for the upwelling Kelvin wave experiment. The TIWKE growth period in (b) is between days 46 and 91, and the decay period is between days 91 and 149.

Downwelling Kelvin wave

For the downwelling experiment, there is a small period of TIWKE growth followed by a decay of $23.2 \pm 2.0 \text{PJ}$ ² (or 38% of the control $61.7 \pm 1.9 \text{PJ}$) between days 43 and 77 beginning as the SSH signal of the Kelvin wave within the control volume

² The estimated uncertainty of $\pm 2.0 \text{PJ}$, and all subsequent uncertainty estimates on volume and time integrated quantities from the ensemble experiments, was calculated using the jackknife method (*Efron and Stein, 1981*) as the $\pm 2\sigma$ spread in the given quantity over 10 ensemble sets of 9 members constructed by leaving one member out for each set.

peaks (compare black line in Fig. 3.8b with red line in Fig. 3.8a). Once the Kelvin wave has passed, the TIWKE is then restored to its control strength between day 99 and the end of the experiment. The small period of growth up to day 43 is partially driven by the convergent $\frac{\partial U}{\partial x} < 0$ at the leading edge of the downwelling Kelvin wave through the $\frac{\partial U}{\partial x}$ shear production term,

$$DSP = -\rho_0 \overline{u' u'} \frac{\partial U}{\partial x}, \quad (3.11)$$

(compare yellow line and black dashed line in Fig. 3.8c). DSP shows a clear phase relationship with the Kelvin wave SSH field (compare yellow line in Fig. 3.8c to red line in Fig. 3.8a) and a simple latitude-depth spatial structure similar to the Kelvin wave velocity field (not shown). The negative DSP associated with the divergent $\frac{\partial U}{\partial x} > 0$ on the trailing edge of the Kelvin wave pulse also helps to initiate the decay in TIWKE after day 43 (yellow line in Fig. 3.8c soon after day 43), along with the pressure flux radiation term (red line in Fig. 3.8c soon after day 43) and several other small terms in the budget (solid black line in Fig. 3.8c soon after day 43) including $\frac{\partial V}{\partial y}$ production and mean advection (not shown). Once the decay in TIWKE is initiated the LSP drops sharply driving a strong negative time tendency in TIWKE (compare black dashed and green line in Fig. 3.8c between days 48 and 70). The subsequent growth in TIWKE after day 99 once the Kelvin wave has passed is also accompanied by a large change in LSP .

To establish which terms are responsible for the net changes in TIWKE we time integrate the TIWKE budget terms over the decay (between days 43 and 77) and growth (between days 99 and 149) periods, subtracting off the initial budget. For example, the total contribution of changes in LSP to changes in volume integrated TIWKE over a period between days t_1 and t_2 is

$$\int_{t_1}^{t_2} \int_V LSP(x, y, z, t) - LSP(x, y, z, t_1) dV dt, \quad (3.12)$$

where $\int_V dV$ indicates an integral over the control volume and the budget should be roughly balanced at time t_1 to minimize the residual. Changes in LSP are the largest

driver of changes in TIWKE, being responsible for 19.4 ± 5.8 PJ of the reduction in TIWKE over the decay period and 31.6 ± 6.5 PJ of the increase in TIWKE over the growth period (green bars in Fig. 3.8b). Other terms make small contributions including the PE conversion (blue bars in Fig. 3.8b), *DSP* (yellow bars in Fig. 3.8b) and other terms (black bars in Fig. 3.8b). The frictional term generally opposes the changes in TIWKE with reduced (increased) friction during weak (strong) TIWKE periods (purple bars in Fig. 3.8b).

The rate at which TIWKE is radiated out of the control volume via pressure fluxes changes as a consequence of the changes in TIWKE (solid red line in Fig. 3.8c). Neither bottom-drag or the loss of energy through radiation out of the lateral boundaries change significantly during the passage of the Kelvin wave (not shown), and thus the changes in pressure flux divergence are associated with changes in the transfer of energy between the upper (above 244m) and deep (below 244m) ocean. The reduction in TIWKE in the surface ocean is followed by a decrease in the rate at which TIWKE is radiated to depths below 244m, which acts as a negative feedback on the surface TIWKE changes contributing 7.0 ± 3.2 PJ of TIWKE during the decay period (first red bar in Fig. 3.8b). Subsequently, a decay of the TIWKE below 244m occurs (black dashed line in Fig. 3.8a) where the variations in the TIWKE budget are dominated by a balance between time tendency and pressure flux divergence (not shown). Near the end of the time series the surface TIWKE is restored, followed by an increase in the downward radiation rate which begins to restore the deep TIWKE (compare red line in Fig. 3.8c with black dashed line in Fig. 3.8a after day 110).

Upwelling Kelvin Wave

For the upwelling experiment, the TIWKE undergoes changes roughly the reverse of those occurring in the downwelling experiment. There is a short period of decay followed by a growth of 25.9 ± 1.9 PJ (or 42% of the background 61.7PJ) between days 46 and 91 beginning as the peak SSH signal of the Kelvin wave passes through the control volume (compare black line in Fig. 3.9b with red line in Fig. 3.9a). Once the Kelvin wave has passed by, the TIWKE then decays to values below its original strength by the end of the experiment. Once again, the *LSP* drives most

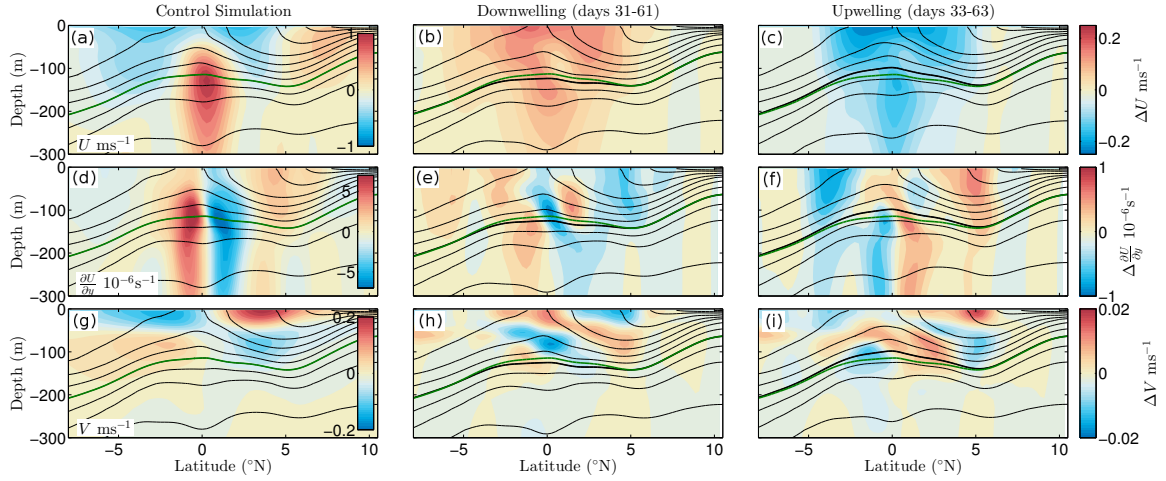


Figure 3.10: (a) Zonal velocity U , (d) $\frac{\partial U}{\partial y}$, and (g) meridional velocity V from the control simulation averaged between the longitudes of -150°E and -110°E . Deviations in these variables from the control simulation averaged over the (b,e,h) downwelling and (c,f,i) upwelling wave peaks between days 31 – 61 and 33 – 63 respectively. The contours indicate 0.3kgm^{-3} isopycnals and the 1025.1kgm^{-3} isopycnal is highlighted using a thicker line. The green contour indicates the 1025.1kgm^{-3} isopycnal from the control simulation on every panel. The downwelling (upwelling) wave results in a general weakening (strengthening) of the circulation except near the EUC core and below.

of the changes in TIWKE (green bars in Fig. 3.9b). The *DSP* appears to play an important role in the initial weakening of TIWKE and then helps initiate the growth around day 50 (compare black dashed and yellow lines in Fig. 3.9c). The rate at which TIWKE is radiated downward via pressure fluxes again acts as a negative feedback, driving an increase in the TIWKE below 244m well after the increase in surface TIWKE (compare red line in Fig. 3.9c with black dashed line in Fig. 3.9a). For the upwelling experiment, there is also a large reduction in pressure flux radiation as the Kelvin wave passes. This is discussed further in section 3.5.2.

Changes in the background circulation

The growth and decay in TIWKE is a result of modifications to the background circulation by the Kelvin waves. The downwelling Kelvin wave alters the background flow by reducing the magnitude of the SEC and increasing the magnitude of the

EUC by a smaller amount (compare Figures 3.10b and 3.10a). This differs from the predicted changes due to a linear Kelvin wave which show a stronger perturbation near the EUC core and weaker variations near the surface (Fig. 3.5f). The differences are due to other processes that are not taken into account in the linear calculation, such as friction, non-linearities and the influence of the TIWs on the background circulation. For example, the enhanced relative amplitude near the surface may be due to alterations of the boundary layer depth, H , by the Kelvin wave pulses, which alter how wind-driven momentum penetrates the surface ocean. To estimate the potential influence of this process on the zonal velocity response, we assume that the frictional force within the boundary layer, F_B , is driven by a wind stress τ such that $F_B(H) = \tau/H/\rho_0$. Equating an anomaly in this force to an anomalous acceleration $\frac{\partial u}{\partial t} = \frac{\Delta u}{\Delta T} = F_B(H + \Delta H) - F_B(H)$ implies that variations in the boundary layer depth ΔH can drive a velocity anomaly Δu of,

$$\Delta u = -F_B(H) \frac{\Delta H}{H + \Delta H} \Delta T. \quad (3.13)$$

At -140°E , the boundary layer depth reached 24m (19m) in the downwelling (upwelling) ensemble Kelvin wave experiments and thus we estimate $\Delta H = \pm 2.5\text{m}$. We estimate $F_B(H) = -4 \times 10^{-7}\text{ms}^{-2}$ from an average of the control simulation model diagnostic zonal frictional force over the boundary layer depth of $H = 21.5\text{m}$. Using these values and the Kelvin wave pulse time scale of $\Delta T = 30$ days results in velocity variations of $\Delta u = \pm 0.12\text{ms}^{-1}$. Thus Kelvin wave-induced variations in the boundary layer depth could potentially explain some of the enhanced response in zonal velocity near the surface (compare to velocity scale in Figures 3.10b and 3.10c).

The net influence of the downwelling Kelvin wave is a weakening in the lateral shear $\frac{\partial U}{\partial y}$ in most locations except near the EUC core and below (compare Figures 3.10e and 3.10d). In particular, the shear regions between the SEC and NECC (near the surface near 5°N in Fig. 3.10e) and between the upper EUC and SEC (50m depth near 1°N in Fig. 3.10e) weaken. In contrast, the upwelling wave results in a strengthened SEC (compare Figures 3.10c and 3.10a) and strengthened lateral shear in most regions except on either side of the EUC core and below (compare Figures

3.10f and 3.10d).

The Kelvin wave modifications to the buoyancy field appear to be relatively minor, with the only noticeable change occurring in the region near the EUC core (compare thick green and thick black isopycnals in Figures 3.10a-c). Changes also occur to the background meridional circulation, with the tropical cells weakening slightly in the downwelling experiment and strengthening in the upwelling experiment (compare Figures 3.10g-i). Overall, the downwelling Kelvin wave appears to drive a weakening of the background circulation consistent with the subsequent reduction in TIWKE. In contrast, the upwelling wave drives an overall strengthening of the circulation and thus an intensification of the TIWKE. However, the actual changes in the TIWKE budget presented above (Figures 3.8 and 3.9) are complex, as we discuss in the next section.

3.5 Discussion

Here we discuss some of the processes that play a role in the complex behavior of the TIWKE budget (sections 3.5.1 and 3.5.2) presented in the previous section. We also briefly discuss the resulting changes in the TIW meridional heat flux and their influence on the upper equatorial heat content (section 3.5.3).

3.5.1 Lateral shear production

The main net driver of the changes in TIWKE in the surface ocean is the *LSP* (green bars in Figures 3.8b and 3.9b). However, *LSP* depends on the TIWKE itself through the momentum flux $\overline{u'v'}$ (Eq. (3.7)), and thus much of the change in *LSP* may be due to changes in the TIWKE itself, as opposed to changes in the background shear $\frac{\partial U}{\partial y}$. The relationship between *LSP* and the TIWKE provides the system with its sensitive nature, where strong growth or decay in the TIWKE can be initiated by small changes to other terms in the TIWKE budget. The downwelling Kelvin wave causes a net negative perturbation to a number of terms in the TIWKE budget (as discussed in the previous section) that unbalances the TIWKE budget such that the

net sink terms (friction and pressure flux radiation) dominate the source terms as the wave peak passes (day 43 in Fig. 3.8c). This results in a rapid decay in TIWKE which continues until the negative feedback associated with changes in the downward radiation of TIWKE via pressure fluxes reverses the trend by day 77 (red line in Fig. 3.8c). The situation is reversed for the upwelling wave.

To look at this process in more detail, we decompose the LSP term into its dependence on the TIWKE, the background shear and the normalized momentum flux,

$$LSP(x, y, z, t) = -\rho_0 \overline{u'v'} \frac{\partial U}{\partial y} = -\mathcal{K} C_{uv} \frac{\partial U}{\partial y}, \quad (3.14)$$

where $C_{uv} = \frac{\overline{u'v'}}{\frac{1}{2}(\overline{u'u'} + \overline{v'v'})}$ is the normalized momentum flux. Now a further decomposition can be performed into terms involving the time-independent control simulation fields (denoted B , see Fig. 3.3) and the varying fields (denoted D),

$$\begin{aligned} LSP(x, y, z, t) = & \underbrace{-\mathcal{K}^B C_{uv}^B \frac{\partial U^B}{\partial y}}_{LSP^{BBB}(x, y, z)} - \underbrace{\mathcal{K}^B C_{uv}^B \frac{\partial U^D}{\partial y}}_{LSP^{BBD}(x, y, z, t)} \\ & - \underbrace{\mathcal{K}^B C_{uv}^D \frac{\partial U^B}{\partial y}}_{LSP^{BDB}(x, y, z, t)} - \underbrace{\mathcal{K}^D C_{uv}^B \frac{\partial U^B}{\partial y}}_{LSP^{DBB}(x, y, z, t)} + \underbrace{\text{Higher Order}}_{LSP^{HO}(x, y, z, t)}, \end{aligned} \quad (3.15)$$

where LSP^{BBB} denotes the shear production term from the control simulation, LSP^{BBD} denotes the varying part associated with the varying component of the background shear $\frac{\partial U^D}{\partial y}(x, y, z, t) = \frac{\partial U}{\partial y}(x, y, z, t) - \frac{\partial U^B}{\partial y}(x, y, z)$. LSP^{BDB} denotes the varying part associated with changes in the relationship between u' and v' through C_{uv} , LSP^{DBB} denotes the varying part associated with changes in the TIWKE \mathcal{K} and LSP^{HO} denotes the remaining terms that are higher order in the varying parts.

Time series of the terms in Eq. (3.15) for both downwelling (Fig. 3.11) and upwelling (Fig. 3.12) experiments show that the higher-order terms (yellow LSP^{HO} in Figures 3.11b and 3.12b) are small relative to the other terms. The term associated with the varying background shear shows a clear relationship with the Kelvin wave (compare red dashed line in Figures 3.11a and 3.12a with blue LSP^{BBD} in Figures

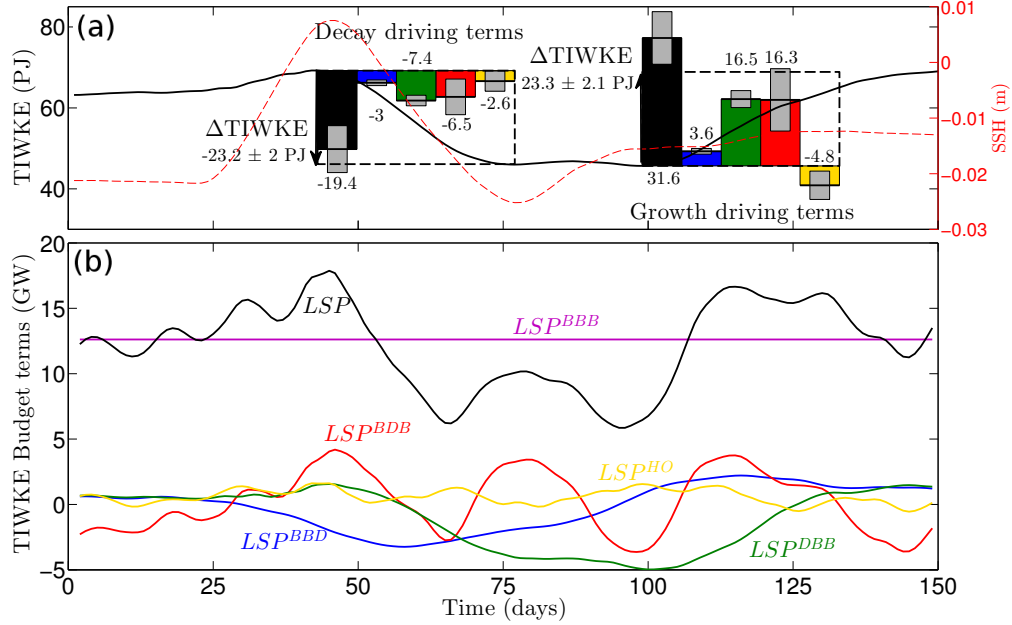


Figure 3.11: (a) TIWKE (black line) and SSH (red dashed line) from the downwelling experiment as for Fig. 3.8a,b. (b) Component terms of the LSP (black line, identical to green line in Fig. 3.8c) according to Eq. (3.15). LSP^{BBB} denotes the value from the control simulation, LSP^{BBD} denotes the varying part associated with changes in the background shear $\frac{\partial U}{\partial y}$, LSP^{DBD} denotes the varying part associated with changes in the relationship between u' and v' , LSP^{DBB} denotes the varying part associated with changes in TIWKE and LSP^{HO} denotes higher-order terms. The bars in (a) show the time-integrated contributions of each term in (b) calculated as for the bars in Fig. 3.8b.

3.11b and 3.12b). For the downwelling experiment LSP^{BBD} shows a negative perturbation that peaks soon after the peak of the wave passes, consistent with an overall weakening of the background lateral shear $\frac{\partial U}{\partial y}$ driven by the downwelling Kelvin wave (Fig. 3.10e). This supports the hypothesis of *Qiao and Weisberg* (1998) and refutes the suggestions of *Harrison and Giese* (1988) and *Giese and Harrison* (1991) that downwelling Kelvin waves increase TIWKE by increasing the magnitude of $\frac{\partial U}{\partial y}$ on either side of the EUC. Our results suggest that this is not the case because the TIWKE (Fig. 3.3d) and momentum flux $\overline{u'v'}$ are weaker on either side of the EUC and below (where the lateral shear is increased, Fig. 3.10e) than closer to the surface

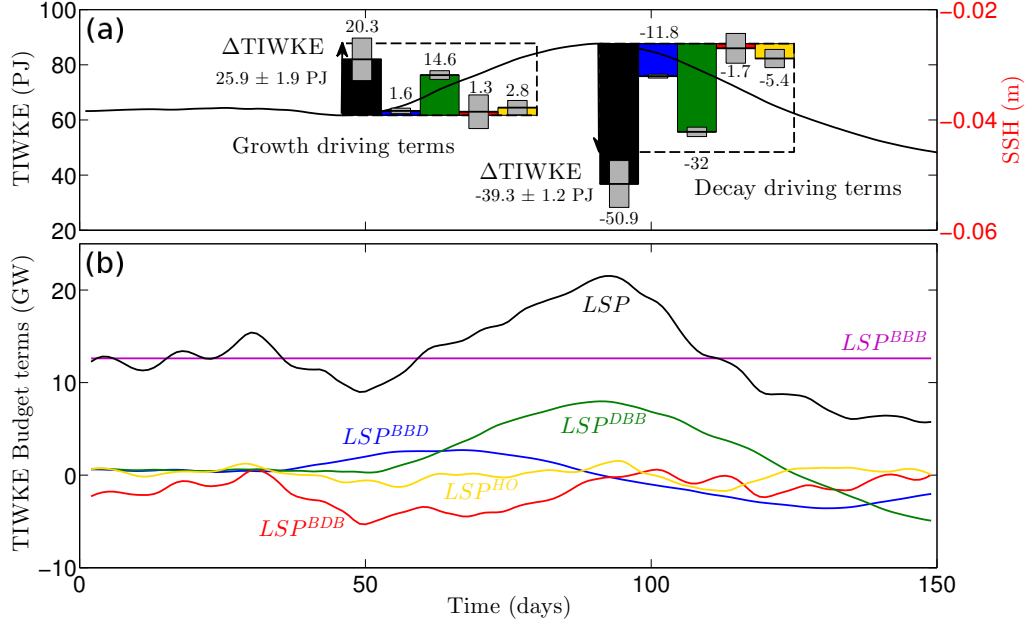


Figure 3.12: As for Fig. 3.11 except for the upwelling experiment.

in the EUC-SEC and SEC-NECC shear regions (where the lateral shear is decreased, Fig. 3.10e).

While the changes in background shear through the LSP^{BBD} term do drive a decrease (increase) in TIWKE in the downwelling (upwelling) experiment, these changes are only a small proportion of the total TIWKE change driven by LSP (compare blue and black bars in Figures 3.11a and 3.12a). In both upwelling and downwelling experiments, the term associated with varying TIWKE, LSP^{DBB} , is the largest contributor over both decay and growth periods (green bars in Figures 3.11a and 3.12a). LSP^{DBB} encapsulates the sensitive nature of the TIWKE budget. A small initial imbalance in the budget can cause runaway changes in TIWKE driven by LSP^{DBB} and any other terms that depend on the amplitude of the TIWs, for example the PE conversion term.

Finally, variations in the relationship between u' and v' , through the term LSP^{BDB} , also play a role in driving variations in LSP (red line in Figures 3.11b and 3.12b and red bars in Figures 3.11a and 3.12a). In the downwelling experiment, the sharp drop in LSP^{BDB} between days 45 and 65 (contributing $-6.5 \pm 4.4 \text{ PJ}$ to the drop in volume

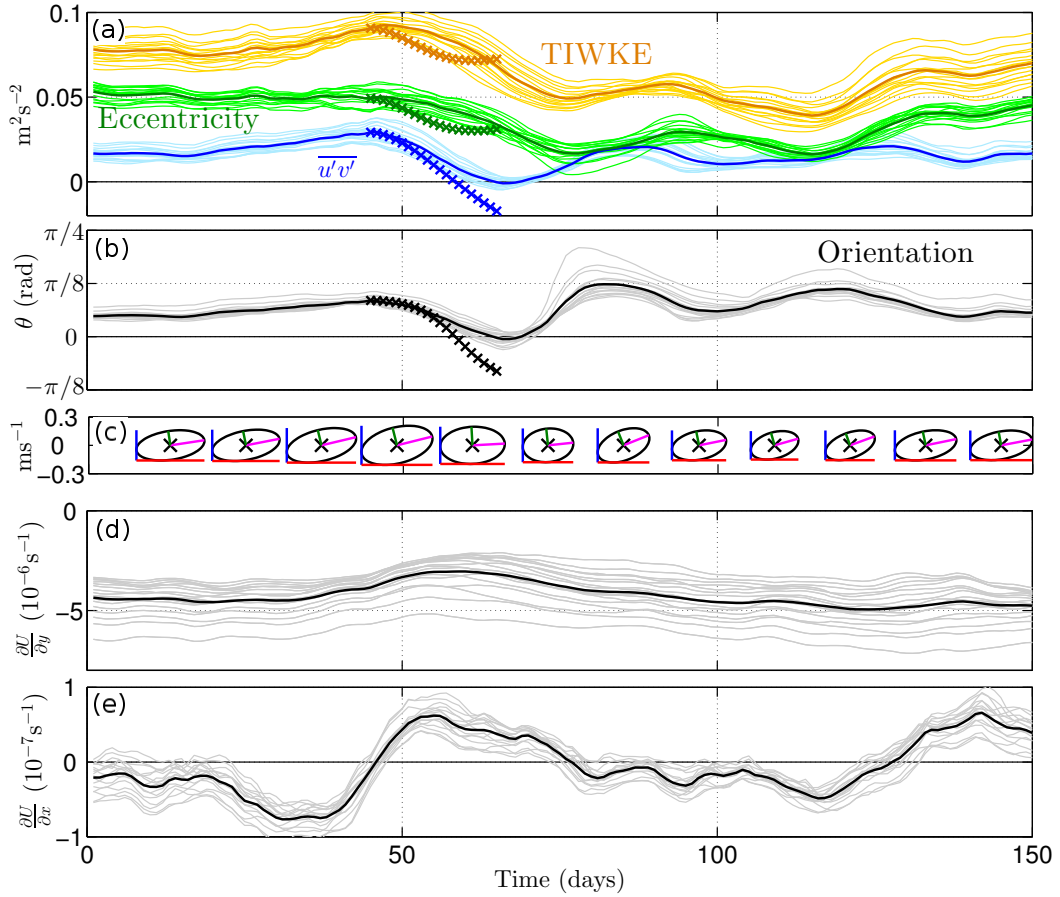


Figure 3.13: (a) TIWKE, $\bar{u}'\bar{v}'$ covariance momentum flux, and ellipse eccentricity $L = \frac{1}{2} (\bar{u}'\bar{u}' - \bar{v}'\bar{v}')$ averaged between $-150^\circ E$ and $-110^\circ E$ in the region $1^\circ N$ to $1.75^\circ N$, 92m to 63m depth from the downwelling experiment. The thin lines denote each latitude-depth grid point within this region and the thick lines their average. (c) TIW velocity covariance ellipses and their (b) orientation θ corresponding to the momentum fluxes in (a) (see Equations (3.16)-(3.18) and *Waterman and Hoskins (2013)*). In (c) the magenta line is the major axis a (Eq. (3.16)) and the green line is the minor axis b (Eq. (3.17)) in ms^{-1} . Background (d) $\frac{\partial U}{\partial y}$ and (e) $\frac{\partial U}{\partial x}$ at the same locations as (a). The crosses in (a) and (b) show estimated changes in the corresponding properties driven by the changes in background shear (d,e) between days 45 and 65 (see Eq. (3.19))

integrated TIWKE, red bar in Fig. 3.11a) is mostly a consequence of changes in the EUC-SEC shear region near 80m depth at $1.5^\circ N$. In this region $\bar{u}'\bar{v}'$ drops almost to

zero, despite much smaller changes in the TIWKE (compare blue lines to brown lines in Fig. 3.13a). This can be understood by considering TIW eddy covariance ellipses in this region, whose properties can be derived from the momentum fluxes,

$$a^2 = \overline{u'u'} \cos^2 \theta + \overline{u'v'} \sin 2\theta + \overline{v'v'} \sin^2 \theta, \quad (3.16)$$

$$b^2 = \overline{u'u'} \cos^2 \left(\theta + \frac{\pi}{2} \right) + \overline{u'v'} \sin 2 \left(\theta + \frac{\pi}{2} \right) + \overline{v'v'} \sin^2 \left(\theta + \frac{\pi}{2} \right), \quad (3.17)$$

$$\theta = \frac{1}{2} \tan^{-1} \left(\frac{\overline{u'v'}}{L} \right), \quad (3.18)$$

where a and b are the major and minor ellipse axis lengths, $L = \frac{1}{2} (\overline{u'u'} - \overline{v'v'})$ is the ellipse eccentricity and θ is the ellipse orientation (*Waterman and Hoskins*, 2013). The covariance momentum flux $\overline{u'v'}$ is only non-zero for eccentric $L \neq 0$ ellipses oriented off the coordinate axes $\theta \neq \frac{n\pi}{2}$, where n is an integer. As for the TIWKE budget calculations above, the momentum fluxes are calculated from the ensemble deviation velocities at each location and then averaged between -150°E and -110°E . Between days 45 and 65 the TIW eddy covariance ellipses (Fig. 3.13c) undergo a rotation such that the ellipse orientation θ aligns closely with the zonal direction (Fig. 3.13b) and the ellipticity reduces (green lines in Fig. 3.13a), both of which result in a reduction in $\overline{u'v'}$ without necessarily changing the TIWKE (see Eq. (3.18)).

Kelvin wave induced changes in the background shears $\frac{\partial U}{\partial y}$ (Fig. 3.13d) and $\frac{\partial U}{\partial x}$ (Fig. 3.13e) can potentially drive these changes in orientation and ellipticity through advective deformation of the TIW covariance ellipses. We consider the influence of these two shear components by examining evolution equations for the momentum fluxes,

$$\begin{aligned} \frac{\partial \overline{u'u'}}{\partial t} &= -2\overline{u'u'} \frac{\partial U}{\partial x} - 2\overline{u'v'} \frac{\partial U}{\partial y} + \text{other terms}, \\ \frac{\partial \overline{u'v'}}{\partial t} &= -\overline{v'v'} \frac{\partial U}{\partial y} - \overline{u'v'} \frac{\partial U}{\partial x} + \text{other terms}, \end{aligned} \quad (3.19)$$

where we neglect the other terms such as friction, advection of the perturbation flow by itself, and the Coriolis force. We also neglect changes driven by the shears in meridional velocity $\frac{\partial V}{\partial x}$ and $\frac{\partial V}{\partial y}$ (and thus the momentum flux $\overline{v'v'}$) as they are small at

this location (Fig. 3.10g-i). Time evolving these equations beginning at time $t_i = 45$ using the measured initial momentum fluxes $\overline{u'v'}(t_i)$ and $\overline{u'u'}(t_i)$ and the measured deviation shears $\frac{\partial U}{\partial y}(t) - \frac{\partial U}{\partial y}(t_i)$ and $\frac{\partial U}{\partial x}(t) - \frac{\partial U}{\partial x}(t_i)$ gives a good prediction for the decay in $\overline{u'v'}$ (blue crosses in Fig. 3.13a). This reduction in $\overline{u'v'}$ is due not only to a reduction in the TIWKE (brown crosses in Fig. 3.13a) associated with LSP^{DBB} , but also because the Kelvin wave modifications in background shear reduce the ellipticity (green crosses in Fig. 3.13a) and rotate the ellipse orientation toward the east (black crosses in Fig. 3.13b), thus altering the phase relationship between u' and v' and driving a reduction in the LSP through LSP^{DBB} in Eq. (3.15).

3.5.2 Downward radiation of TIWKE via pressure fluxes

The loss of TIWKE through its radiation via pressure fluxes to the deep ocean below 244m is one of the most important processes that influences the temporal evolution of the surface and deep TIWKE (red lines in Figures 3.8c and 3.9c). In particular, pressure flux radiation plays an important role as a negative feedback by helping to stabilize the TIWKE changes driven by the sensitive LSP . However, the rate at which energy is lost via pressure fluxes also appears to change before significant changes in TIWKE occur, particularly for the upwelling experiment (red line in Fig. 3.9c around day 60). These changes may be due to the influence of the vertical velocity of the Kelvin wave on the vertical group velocity of the waves that facilitate the downward energy transfer across 244m. The vertical velocity field of the Kelvin wave can alter both the background stratification, N^2 , and the vertical wavenumber, m , of any vertically-propagating wave by stretching and squeezing both isopycnals and phase lines through advection,

$$\frac{\partial N^2}{\partial t} = -\frac{\partial w}{\partial z}(t)N^2, \quad (3.20)$$

with the vertical wavenumber m obeying a similar equation. A divergent (convergent) vertical velocity field $\frac{\partial w}{\partial z} > 0$ ($\frac{\partial w}{\partial z} < 0$) leads to a decrease (increase) in the magnitudes of both N^2 and m . To evaluate how this influences the vertical group velocity, we consider the possibility that the downward-propagating waves that facilitate the

downward energy transfer across 244m are either classical internal-gravity waves or long-wave limit equatorially-trapped Kelvin, Rossby or Yanai waves. All of these flavors of waves have a vertical group velocity magnitude, $|c_{gz}|$, that depends on N^2 and $|m|$ in the ratio (*Gill*, 1982; *Kessler and McCreary*, 1993; *Smyth et al.*, 2015),

$$|c_{gz}| \sim \frac{N^2}{|m|^3}, \quad (3.21)$$

Therefore a stretching of phase lines and isopycnals under a divergent vertical velocity field $\frac{\partial w}{\partial z} > 0$ leads ultimately to an increase in c_{gz} (the cubic dependence on $|m|$ dominates), while a convergent vertical velocity field leads to a decrease in c_{gz} . At the leading edge of the downwelling Kelvin wave the vertical velocity field is divergent at 244m (the maximum in w for the linear Kelvin wave mode equivalent to Fig. 3.5f is at ~ 1000 m depth), leading to an increase in the downward group velocity that may explain the increase in the magnitude of the pressure flux divergence occurring as the downwelling Kelvin wave pulse peaks (red line near day 49 in Fig. 3.8c). In contrast, at the leading edge of the upwelling Kelvin wave the vertical velocity field is convergent at 244m, potentially explaining the decrease in the magnitude of the pressure flux divergence occurring after the upwelling Kelvin wave pulse passes (red line near day 50 in Fig. 3.9c). Why this process is asymmetric, with the pressure flux term showing a larger magnitude change in the upwelling experiment (compare red lines in Figures 3.8c and 3.9c around day 50), requires further study.

3.5.3 Equatorial heat budget

The growth and decay in TIWKE induced by the Kelvin waves results in changes in the TIW-driven meridional heat flux. The mean temperature balance is,

$$\frac{\partial \bar{T}}{\partial t} = \bar{\mathcal{H}} - \nabla \cdot (\bar{\mathbf{u}}\bar{T} + \bar{\mathbf{u'}}\bar{T'}), \quad (3.22)$$

where \mathcal{H} represents non-conservative terms such as parameterized turbulent diffusion and penetrative solar radiation and the other terms on the right hand side are the

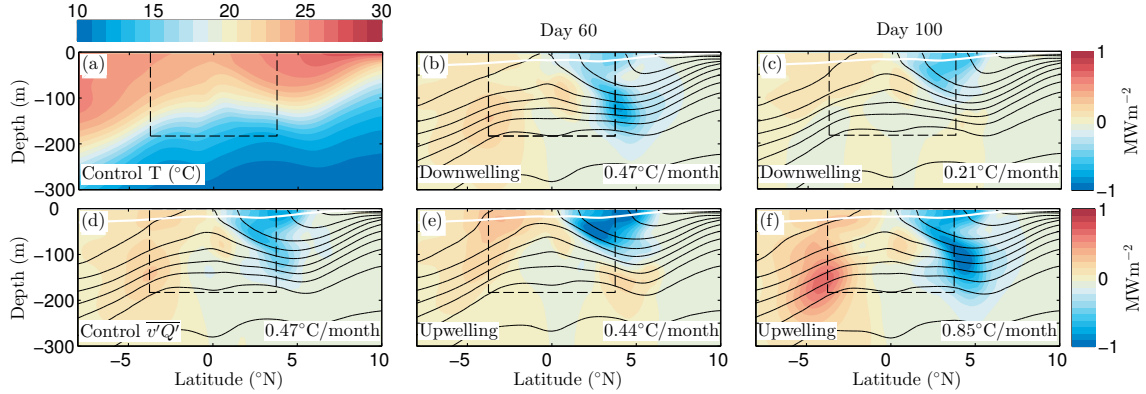


Figure 3.14: (a) Temperature and (b-f) meridional eddy heat flux $\overline{v'Q'} = C_p\rho_0\overline{v'T'}$, where C_p is the specific heat and ρ_0 a reference density, averaged between -150°E and -110°E from the control simulation (a,d), on day 60 for the downwelling (b) and upwelling (e) experiments and on day 100 for the downwelling (c) and upwelling (f) experiments. In the bottom right corner the average value of the induced heating over the control volume above -183m and between $\pm 3.75^\circ$ latitude (indicated with the dashed box) is shown. The white line indicates the boundary layer depth. On day 60, shortly following the Kelvin wave peak, the eddy fluxes are shifted vertically with no change in the magnitude of the heating they produce. Later, on day 100, the eddy heat fluxes have reduced (increased) in the downwelling (upwelling) experiment due to the changes in TIWKE.

convergence of mean and eddy fluxes. The overline is defined as for the TIWKE budget (see section 3.3). In the control simulation, the TIWs transport heat southward across 3.75°N in the upper 200m (Fig. 3.14d). There is also a weaker and deeper northward transport across 3.75°S . The net convergence of these fluxes acts to warm the upper equatorial region above 183m by 0.47°C/month .

The Kelvin waves alter the TIW-driven meridional heat transport through modifications in background gradients and TIWKE. As the Kelvin waves pass, the meridional eddy heat flux patterns shift vertically without changing significantly in magnitude (Figures 3.14b,e on day 60). Later (day 100) the meridional eddy heat fluxes are weakened in the downwelling experiment (eddy heating reduces to 0.21°C/month , Fig. 3.14c) and strengthened in the upwelling experiment (eddy heating increases to 0.85°C/month , Fig. 3.14f). These changes begin once the TIWKE is maximally perturbed after day 75 and last until the TIWKE is restored to near its original values

after day 125 (compare Fig. 3.15d with Figures 3.8b and 3.9b).

The changes in the meridional eddy heat fluxes play an important role in the heat budget of the upper equatorial ocean. The heat content of the upper equatorial ocean (expressed as an average temperature) in the control volume -150°E to -110°E , $\pm 3.75^{\circ}$ latitude, upper 183m, undergoes a $\sim 0.7^{\circ}\text{C}$ increase due to the downwelling Kelvin wave (solid line in Fig. 3.15a) and a $\sim 0.7^{\circ}\text{C}$ decrease due to the upwelling Kelvin wave (solid line in Fig. 3.15b). This is driven by zonal advection of the background zonal temperature gradient and vertical advection of the thermocline, which are both components of the mean heat convergence, $-\nabla \cdot (\bar{\mathbf{u}}\bar{T})$ (Fig. 3.15c). The time integral of the mean heat convergence starting as the Kelvin waves arrive on day 21 describes the increase and subsequent decrease in heat content as the Kelvin wave peak passes through the control volume well (dashed lines in Figures 3.15a and 3.15b). While the Kelvin wave induced vertical advection is reversible, the zonal advection of a single Kelvin wave pulse is single signed and thus drives a net increase (decrease) in the heat content for the downwelling (upwelling) wave (as shown by the dashed lines in Figures 3.15a and 3.15b which do not return to their initial values). However, this net change in heat content is counteracted by the changes in meridional eddy heat flux convergence (Fig. 3.15d and time integrated dotted lines in Figures 3.15a and 3.15b), which restores the heat content to its initial value.

3.6 Summary and implications

Motivated by observations of the potential influence of intraseasonal Kelvin waves on TIWs in the eastern equatorial Pacific (Fig. 3.1, *Qiao and Weisberg (1998)*), we have examined the TIWKE budget in a set of $1/4^{\circ}$ resolution ocean model simulations. In a control simulation with a statistically-steady TIW field the TIWKE budget is dominated by the creation of TIWKE through conversion from mean PE and lateral shear production acting on the meridional shear in zonal velocity $\frac{\partial U}{\partial y}$ (*LSP*), and removal of TIWKE through friction and radiation via pressure fluxes (Fig. 3.3). Intraseasonal Kelvin waves propagating through the eastern Pacific change this budget by altering the background current shears and density structure that act as sources

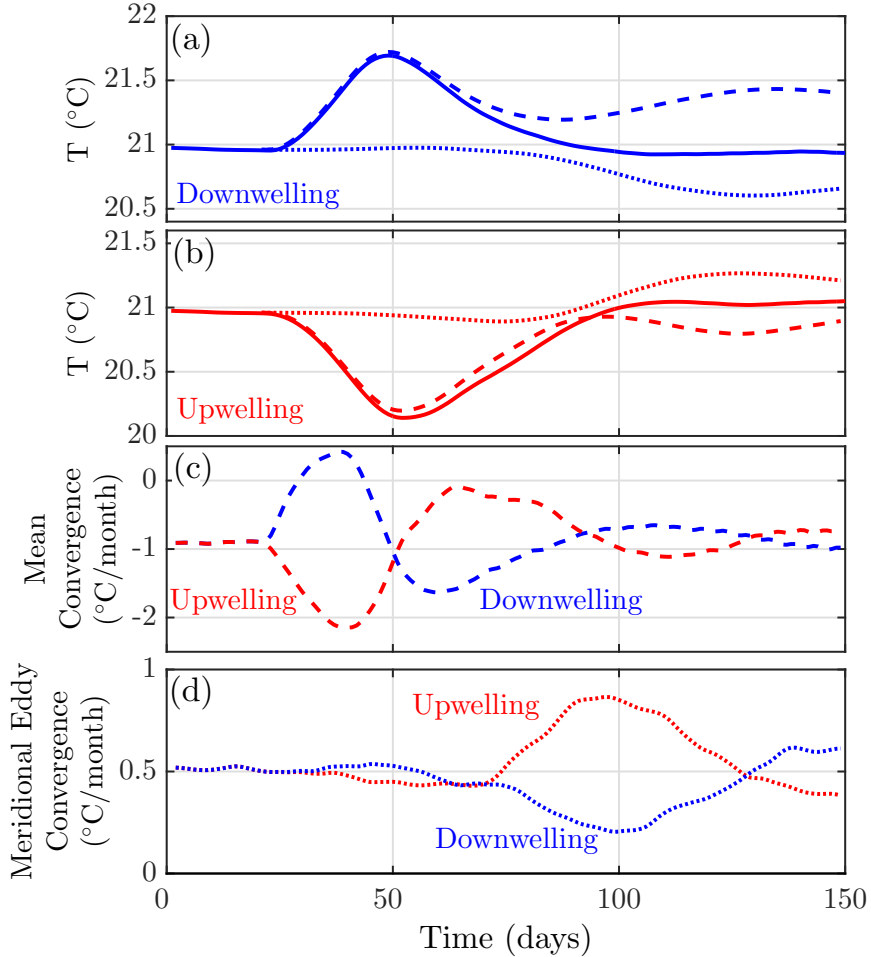


Figure 3.15: Time series of terms in the heat budget (expressed in terms of an average temperature) of the upper equatorial ocean above -183m between -150°E and -110°E , $\pm 3.75^{\circ}$ latitude. Average temperature in (a) downwelling and (b) upwelling experiments (solid lines). (c) Convergence of mean heat fluxes, $-\nabla \cdot (\bar{\mathbf{u}}T)$, and (d) convergence of meridional eddy heat fluxes, $-\frac{\partial}{\partial y}(\bar{v'}T')$, for both downwelling (blue) and upwelling (red) experiments. Also shown in (a) and (b) are the time integrated mean convergence (dashed) and meridional eddy convergence (dotted) terms starting at day 21 just before the Kelvin waves arrive. The large initial changes in heat content are driven by the mean heat convergence through Kelvin wave zonal and vertical advection. Kelvin wave zonal advection drives a net change in heat content (compare dashed lines in (a) and (b) before and after the Kelvin wave passes) which is compensated for by changes in the meridional eddy convergence (dotted lines in (a) and (b) after the Kelvin wave passes).

of energy for the TIWs (Fig. 3.10). Strong downwelling Kelvin waves weaken the background circulation and can reduce the volume integrated TIWKE by 38%. Upwelling Kelvin waves strengthen the background circulation and can intensify the volume integrated TIWKE by 42%. *LSP* is the main driver of the growth and decay of TIWKE due to its dependence on the TIWKE itself (green lines in Figures 3.8c, 3.9c, 3.11b and 3.12b). However, the modifications to the TIWKE budget that initiate this growth and decay are complex, with a number of processes contributing. Among these are changes in the background shear $\frac{\partial U}{\partial y}$ near the surface between the SEC and both the EUC and NECC (LSP^{BBB} in Figures 3.11a and 3.12a), and zonal convergence/divergence of the zonal flow $\frac{\partial U}{\partial x}$ on the leading and trailing edge of the Kelvin wave pulses (*DSP* in Figures 3.8b and 3.9b). The changes in background shear also alter the correlation between u' and v' in the upper EUC, thus impacting the momentum flux $\overline{u'v'}$ independent of changes in TIWKE (Fig. 3.13). Second-order adjustments in the background meridional-vertical circulation of the tropical cells are more subtle and deserve further study.

In response to the modifications in TIWKE in the upper ocean, the rate at which energy is radiated away from the TIW region via pressure fluxes also changes. Weakened (strengthened) radiative loss in the downwelling (upwelling) experiment acts as a negative feedback to stabilize the growth and decay of upper ocean TIWKE (red lines in Figures 3.8c and 3.9c). These changes are mostly associated with adjustments in the rate at which TIWKE is radiated downward out of the surface ocean to the mid-depth and deep ocean below 244m, with potential implications for the radiation of waves into the deep ocean, the intraseasonal variability of the deep ocean, and abyssal mixing (*Tanaka et al.*, 2015; *Holmes et al.*, 2016).

Changes in TIWKE induced by propagating Kelvin waves have implications for SST variability in the eastern Pacific as TIWs play an important role in the mixed-layer heat budget (*Menkes et al.*, 2006; *Jochum et al.*, 2007; *Holmes and Thomas*, 2015). An initial investigation showed that the TIW-driven meridional heat flux undergoes significant changes in response to the changes in TIWKE, impacting the heat content in the upper 200m (Fig. 3.15). However, changes in the mixed-layer heat budget were significantly more complex (not shown) and deserve to be studied

further. One drawback of the current setup is that SST variability is damped by the assigned bulk flux forcing and fixed wind stress. Air-sea feedbacks play an important role not only in allowing the upper ocean to adjust to perturbations in TIWKE and upper ocean structure, but also by influencing the propagation of the Kelvin waves themselves (*Hendon et al.*, 1998; *Roundy and Kiladis*, 2006; *Shinoda et al.*, 2008). How the interaction between Kelvin waves and TIWs influences the evolution of SST anomalies in the eastern equatorial Pacific remains an important question to be addressed by future research.

The computations were performed at the Stanford Center for Computational Earth and Environmental Science. R. Holmes was supported by a Robert and Marvel Kirby Stanford Graduate Fellowship while undertaking this study. The altimeter products (Fig. 3.1a) were produced and distributed by the Copernicus Marine and Environment Monitoring Service (CMEMS) (<http://www.marine.copernicus.eu>). TMI data (Fig. 3.1b) are produced by Remote Sensing Systems and sponsored by the NASA Earth Sciences Program. Data are available at www.remss.com.

3.7 Appendix: Kelvin wave eigenfunction in a zonally-uniform background flow

The derivation here is similar to that in *McPhaden et al.* (1986) except that the background buoyancy field is not assumed to be in geostrophic balance with the zonal velocity. We start with the hydrostatic, traditional equations of motion linearized about a zonally-uniform background flow with zonal velocity $U(y, z)$ and buoyancy field $B(y, z)$ into which we substitute an assumed wave form in the zonal direction

and time, $\{u, v, w, b, \phi\}(y, z)e^{i(kx - \omega t)}$,

$$-ik(c - U)u + vU_y + wU_z - fv = -ik\phi,$$

$$fu = -\phi_y,$$

$$-b = -\phi_z,$$

$$iku + v_y + w_z = 0,$$

$$-ik(c - U)b + vB_y + wN^2 = 0,$$

where the subscripts denote differentiation, $N^2 = B_z$, $c = \omega/k$ and $f = \beta y$. These equations can be combined into a single equation for the pressure perturbation ϕ :

$$A\phi_{yy} + B\phi_{yz} + C\phi_{zz} + D\phi_y + E\phi_z - \frac{1}{c - U}(F\phi_z + G\phi) = 0, \quad (3.23)$$

where,

$$A = 1, \quad (3.24)$$

$$B = \frac{1}{N^2} (fU_z - B_y), \quad (3.25)$$

$$C = \frac{f}{N^2} (f - U_y), \quad (3.26)$$

$$D = -\frac{2}{y} - \frac{S_y}{S} - \frac{B_{yz}}{N^2} - B_y \left(\frac{1}{N^2} \right)_z + \frac{B_y S_z}{N^2 S}, \quad (3.27)$$

$$\begin{aligned} E = f \left(\frac{U_z}{N^2} \right)_y + \frac{U_z f}{N^2} & \left(\frac{B_y S_z}{N^2 S} - \frac{1}{y} - \frac{S_y}{S} - \frac{B_{yz}}{N^2} \right) \\ & + \left(f^2 S - \frac{2fU_z B_y}{N^2} \right) \left(\frac{1}{N^2} \right)_z - \frac{f B_y U_{zz}}{N^4}, \end{aligned} \quad (3.28)$$

$$F = \frac{f}{N^2} (fU_z + B_y), \quad (3.29)$$

$$G = \beta + \frac{f S_y}{S} + \frac{f B_{yz}}{N^2} + f B_y \left(\frac{1}{N^2} \right)_z - \frac{f B_y S_z}{N^2 S}, \quad (3.30)$$

$$S = 1 - \frac{U_y}{f} + \frac{B_y U_z}{N^2 f}. \quad (3.31)$$

Eq. (3.23) becomes identical to Eq. (4) of *McPhaden et al.* (1986) when assuming that the background flow is in thermal wind balance $B_y = -fU_z$. Once ϕ is obtained, the other variables can be obtained through the polarization relations:

$$u = -\frac{1}{f}\phi_y, \quad (3.32)$$

$$b = \phi_z, \quad (3.33)$$

$$w = \frac{ik}{N^2} (c - U)\phi_z - v\frac{B_y}{N^2}, \quad (3.34)$$

$$v = \frac{ik}{fS} \left(\phi + \frac{U_z}{N^2} (c - U)\phi_z - (c - U)u \right). \quad (3.35)$$

Eq. (3.23) is solved using MatLab's *eigs* routine (where c is the eigenvalue) using second-order finite differences. The boundary conditions used on ϕ are that $\frac{\partial\phi}{\partial z} = 0$ at $z = 0, -H$ and $\phi = 0$ at $y = \pm L$, where L is taken as 15° latitude.

In order to ensure that the first-baroclinic-mode Kelvin wave is correctly identified, a number of solutions are obtained at different values of the parameter α between 0 and 1, where the background flow U and B above are given by,

$$\begin{aligned} U &= \alpha U_R, \\ B &= \frac{1}{2L} \int_{-L}^L B_R dy + \alpha \left(B_R - \frac{1}{2L} \int_{-L}^L B_R dy \right), \end{aligned} \quad (3.36)$$

where U_R and B_R are the zonal velocity and buoyancy fields averaged over the control simulation and over the forcing longitudes between -201° E and -199° E. For $\alpha = 0$, there is no background flow and the background buoyancy field is meridionally uniform. In this case standard zero-mean-flow wave theory gives wave modes that are separable into baroclinic (stretched cosines/sines under the WKB approximation) and meridional modes (cylindrical functions). As the mean flow is introduced by increasing α from 0 toward 1, the first-baroclinic-mode Kelvin wave acquires significant small-scale structure (Fig. 3.5a-c). However, the large-scale structure remains similar and the mode is easily identified among the other modes with large wave speeds (not shown).

Chapter 4

Equatorial Waves and Deep Equatorial Mixing

RYAN M. HOLMES AND LEIF N. THOMAS

Earth System Science, Stanford University, Stanford, California

JAMES N. MOUM

College of Earth, Ocean, and Atmospheric Sciences, Oregon State University, Corvallis, Oregon

Little is known about mixing in the abyssal equatorial oceans in spite of its inferred importance for upwelling dense water. Here we present full-depth microstructure turbulence profiles obtained in the equatorial Pacific that show evidence for intense wind-generated abyssal mixing. Mixing was intensified over the bottom 700m where the diffusivity reached $10^{-3} m^2 s^{-1}$, of similar intensity to mixing driven by tidal flow over rough topography. However, here the mixing was found over smooth topography. We suggest that the intense mixing could have been driven by surface-generated equatorial waves through two possible mechanisms 1) near-bottom wave trapping as a result of the horizontal component of the Earth's rotation and 2) inertial instability. The generation of lee waves over smooth topography at low latitudes and their subsequent breaking is another viable mechanism for the mixing.

The material in this chapter has been reproduced from *Holmes et al.* (2016) (with permission from the American Geophysical Union), with the authors and abstract reproduced above.

4.1 Introduction

Turbulence-enhanced mixing in the abyssal ocean controls the vertical structure of the ocean interior and thus quantifying its sources of energy and spatial structure is crucial for understanding the abyssal ocean circulation (*Ito and Marshall*, 2008; *Ferrari*, 2014). *Munk and Wunsch* (1998) suggested that an energy flux of $\sim 2\text{TW}$ is required to drive abyssal mixing, provided in roughly equal portions by tides and winds (*Wunsch and Ferrari*, 2004). Much work has focused on the generation of internal tides (*St. Laurent and Garrett*, 2002; *Kunze et al.*, 2006; *Garrett and Kunze*, 2007) and lee waves (*Nikurashin and Ferrari*, 2010, 2013) by tidal and geostrophic flow over rough topography and their subsequent breaking through a non-linear downscale cascade of internal wave energy (*Gregg*, 1989; *Sun and Kunze*, 1999). These processes generate seafloor-intensified profiles of mixing over topographic features (*Ledwell et al.*, 2000; *Waterhouse et al.*, 2014) which are consistent with the current understanding of the abyssal circulation (*Ferrari*, 2014) and account for an estimated $1.2 - 1.4\text{TW}$ of energy input to mixing (*Wunsch and Ferrari*, 2004; *Nikurashin and Ferrari*, 2013). However, less is known about the remaining $0.6 - 0.8\text{TW}$, a significant proportion of which is thought to be provided by internal waves generated by winds at the surface.

In addition to the energy sources driving mixing, the spatial distribution of mixing is not well known. The data obtained so far is sparse and suggests that spatial variability is large (*Whalen et al.*, 2012; *Waterhouse et al.*, 2014), indicating that uncertainties in global mean values are still large (*Ivey et al.*, 2008). Much recent work has focused on mid- and high-latitude regions such as the Southern Ocean (*Garcia et al.*, 2004; *Sheen et al.*, 2014). However, inverse models of the ocean's mass budget predict that much of the zonally-integrated diapycnal flow closing the abyssal meridional overturning cell occurs in the tropical Indian and Pacific Oceans (*Lumpkin and Speer*, 2007). These regions are poorly sampled, particularly the near-equatorial

oceans. *Nikurashin and Ferrari* (2013) suggested that the equatorial region was a hot spot for deep mixing using an empirical parameterization of tidal and lee wave driven interior mixing. In particular, their parameterization predicted enhanced lee wave driven mixing near the equator even in regions with relatively smooth topography. However, global estimates of abyssal mixing rates obtained using fine-scale parameterizations for internal wave mixing suggest that mixing at the equator is weak (*Kunze et al.*, 2006). Some observational work has focused on the upper 1000m and shown high levels of mixing in the vicinity of the deep-equatorial jets (*Dengler and Quadfasel*, 2002; *Whalen et al.*, 2012). However, our focus here is on abyssal mixing that could contribute to closure of the abyssal overturning cell.

In this article we present observations of energetic seafloor-intensified mixing below 3000m near 110°W in the eastern equatorial Pacific. These observations were obtained in a region of smooth topography suggesting that the tides do not energize the mixing, although topographic lee waves remain a possible explanation. However, our observations suggest that this mixing could also have been energized by a low-frequency equatorially trapped wave generated by winds at the surface. The article is organized as follows. In Section 4.2 we describe the data and data processing. In Section 4.3 we describe the main features of the mixing data. In Section 4.4 we discuss the potential mechanisms driving the observed mixing. Section 4.5 concludes. The appendices provide a description of the microstructure turbulence measurement techniques (Section 4.6), analysis of the Shipboard Acoustic Doppler Current Profiler (SADCP) data (Section 4.7) and a description of the linear wave theory used in Section 4.4.1 (Section 4.8).

4.2 Data and methods

The CTD χ -pod microstructure turbulence instrument (*Moum and Nash*, 2009) used in this study measures temperature gradients at high resolution using fast-response thermistors mounted on a CTD cage. To avoid the influence of the wake of the CTD cage on the measurements, thermistors are mounted extending from the top and bottom of the CTD package and data is only used providing the CTD package is moving

vertically faster than 0.4ms^{-1} . Measurements of small-scale temperature gradients in the diffusive sub-range of turbulence allow a direct estimate of the dissipation rate of temperature variance χ . From this direct measurement of χ , an estimate of the Brunt-Väisälä frequency N^2 from the CTD data and several standard assumptions, indirect estimates for the diffusivity κ_T and rate of turbulent kinetic energy dissipation ϵ can also be derived. In Appendix 1 (Section 4.8) we provide a more detailed description of the measurement techniques and assumptions, and discuss the accuracy of the χ , κ_T and ϵ estimates.

Full-depth velocity profiles were calculated from data obtained using lowered acoustic Doppler current profiler (LADCP) instruments using the LDEO software developed by A. Thurnherr based on the method of *Fischer and Visbeck* (1993). The quality of the data was confirmed by comparing profiles with SADCP data and bottom tracked velocities, and by comparing profiles calculated from all odd pings and all even pings independently.

4.3 Results

The observed properties of mixing as quantified with χ , ϵ and κ_T range over several orders of magnitude (Figure 4.1). Large temperature variance dissipation $\chi > 10^{-7}\text{K}^2\text{s}^{-1}$ (Figure 4.1a,b) occurs in the upper 250m, particularly near the equator, associated with upper-ocean mixing processes such as shear instability in the Equatorial Undercurrent (*Gregg et al.*, 1985). Enhanced $\chi \sim 10^{-9}\text{K}^2\text{s}^{-1}$ occurs between 250m and 1000m and generally small $\chi < 10^{-9}\text{K}^2\text{s}^{-1}$ occurs below 1000m. However, there is a region of large χ peaking at $10^{-8}\text{K}^2\text{s}^{-1}$ at $1/2^\circ\text{S}$ between 3200m and the seafloor (Figure 4.1b). There is also evidence of enhanced χ reaching $10^{-9}\text{K}^2\text{s}^{-1}$ close to the seafloor.

Our indirect estimates of ϵ and κ_T follow the dependencies $\epsilon \sim \chi/N^2$ and $\kappa_T \sim \chi/N^4$, providing that temperature dominates stratification. Thus ϵ and κ_T are artificially enhanced with depth by small values of N^2 where χ is at noise levels (Figure 4.10). This clearly dominates over the depth range 2000 to 3200m (Figures 4.1a, 4.1c and 4.1e). However, below 3200m, χ is significantly above noise levels; here ϵ and

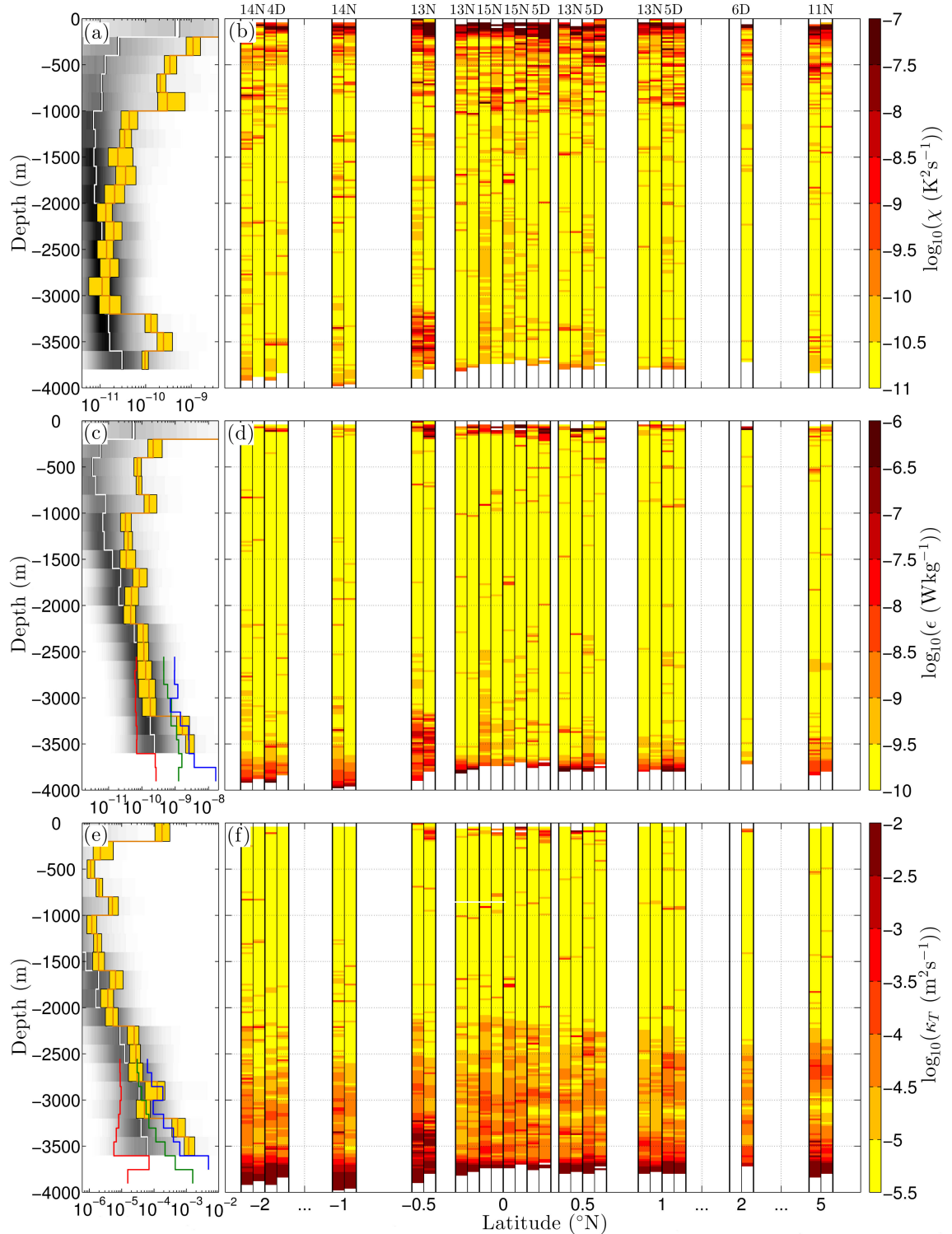


Figure 4.1: (Caption on next page)

Figure 4.1: Maps of (b) χ , (d) ϵ and (f) κ_T from the χ -pod data. Mean values of 20m vertical bins are shown for each up (left column) and down (right column) cast, with the date of the cast in November (N) or December (D) 2014 indicated above (b). Note that the x-axis is not linear. Binned estimates across all casts within $\pm 2^\circ$ of the equator for (a) χ , (c) ϵ and (e) κ_T . The bottom bin is not included for ϵ and κ_T because of very low stratification that renders the estimates unreliable. The gray shading represents the distribution of estimates in each 200m bin and the median (white) and mean with confidence intervals (orange with yellow boxes) are also shown. There are close to 6000 individual estimates in each 200m bin. The confidence intervals on the mean take into account the noise floor of the instrument (Figure 4.10). Also shown in (c) and (e) for comparison are profiles from Figure 7 of *Waterhouse et al.* (2014) (reproduced with permission) of ϵ and κ_T above smooth (red), rough (green) and mid-ocean ridge (blue) topography. These are positioned in the vertical assuming a mean seafloor depth of 3830m.

κ_T are large and significant. Averaged over all casts and in 200m bins, ϵ exceeds 10^{-9}Wkg^{-1} (Figure 4.1c) and κ_T reaches $10^{-3}\text{m}^2\text{s}^{-1}$ (Figure 4.1e).

The large temporal and spatial variability in the observations is typical of log-normally distributed turbulence data. Average values are dominated by intermittent (in both space and time) energetic events (*Baker and Gibson*, 1987; *Moum et al.*, 2002; *Alford et al.*, 2011). This is made evident by comparing 200m bin-averaged values across casts to 200m binned median values (compare orange with white lines in Figures 4.1a,c,e). The energetic event captured between 3200m and 3600m at $1/2^\circ\text{S}$ has a large influence on the bin-averaged mixing, despite only representing 9% of the data in these bins (Figure 4.2). Between 3200m and 3400m, distributions of χ and ϵ excluding the cast containing the high mixing event have means of $3.4(3.0, 4.7) \times 10^{-11}\text{K}^2\text{s}^{-1}$ and $4.7(4.4, 5.3) \times 10^{-10}\text{Wkg}^{-1}$ respectively (where the brackets refer to a 95% bootstrapped confidence interval), and are well described by log-normal distributions (dashed lines in Figure 4.2). With the cast containing the event included, the distribution means increase by almost an order of magnitude to $2.5(1.8, 3.8) \times 10^{-10}\text{K}^2\text{s}^{-1}$ and $2.7(2.2, 3.7) \times 10^{-9}\text{Wkg}^{-1}$ and the distributions acquire positive skew in log-space. The potential source of enhanced mixing in this patch is the focus of Section 4.4.

There is some evidence of enhanced turbulence in the range 250m to 1000m (see

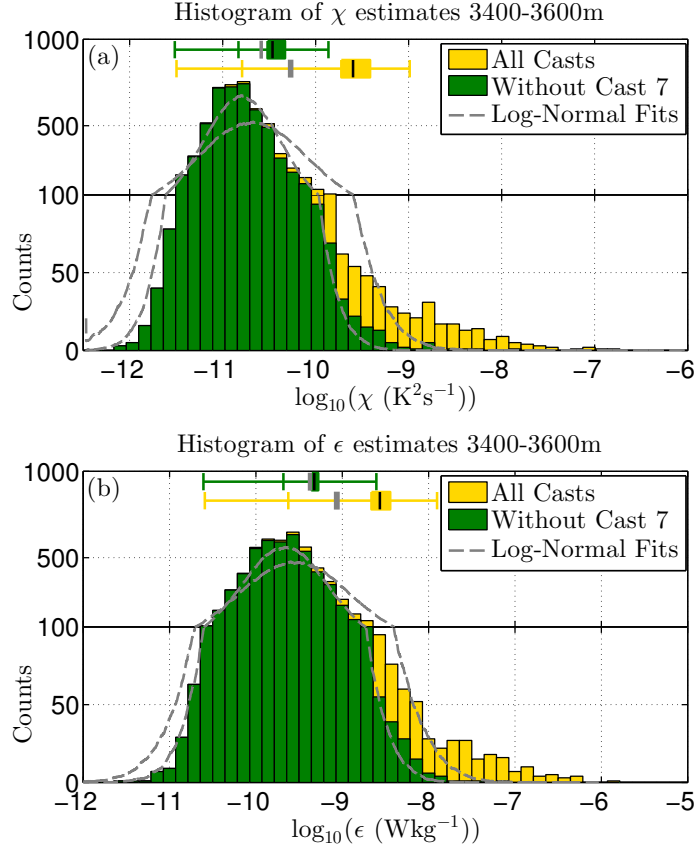


Figure 4.2: Histograms of estimates of (a) χ and (b) ϵ in the 3400-3600m bin. The yellow portion indicates values from cast 7 at $1/2^\circ\text{S}$ containing the deep mixing event, while the green portion indicates values from other casts. Note that the vertical scale has been split into two sections for emphasis. Above the histograms are the median, 0.025% and 0.975% quantiles both with and without cast 7, and the mean with 95% bootstrapped confidence intervals (black line with filled interval). In addition, the gray dashed lines indicate log-normal fits to each distribution, with their means indicated with gray boxes above the histograms.

Figure 4.1a), potentially associated with the deep equatorial jets that are prominent in this depth range (*Firing et al.*, 1998; *Dengler and Quadfasel*, 2002).

A global compilation of microstructure measurements by *Waterhouse et al.* (2014) is classified according to topographic roughness (shown as red, green and blue lines in Figures 4.1c and 4.1e) as this is recognized as a factor that influences the intensity of turbulence (*Ledwell et al.*, 2000; *St. Laurent et al.*, 2002; *Whalen et al.*, 2012;

Nikurashin and Ferrari, 2013). Above 3200m, our bin-averaged ϵ values are slightly larger than typical values found over smooth topography (Figure 4.1c). The κ_T values in this depth range are somewhat larger again, lying close to values found over rough topography (Figure 4.1e). However, below 3200m, ϵ and κ_T values are comparable to energetic turbulent mixing observed over mid-ocean ridges. This enhancement is mostly a result of the region of energetic mixing at 1/2°S.

4.4 Discussion: Possible mechanisms driving the observed mixing

At 1/2°S enhanced values of χ and ϵ reach 700m above the seafloor, collocated with a layer of enhanced vertical shear in the meridional velocity between 3600m and 3800m (Figure 4.3a) with relatively low stratification capped by a strongly-stratified layer of 40m thickness. Throughout much of this shear layer $Sh^2 > 4N^2$, where Sh^2 is the squared shear, indicating that the Richardson number ($Ri = N^2/Sh^2$) is below 1/4, potentially favorable for the generation of vertical shear instabilities (Figure 4.3b). Interestingly, the observed enhanced mixing extends roughly 400m above the region of low Ri , suggesting that vertical shear instability may not be the only process active. A second instability typically associated with strong lateral shears is inertial instability (Dunkerton, 1981), which is thought to play a role in mixing the upper equatorial oceans (Hua *et al.*, 1997; Richards and Edwards, 2003). An inertially unstable flow is characterized by a meridional gradient in absolute momentum M ,

$$M = U - \frac{1}{2}\beta y^2, \quad (4.1)$$

of the same sign as the Coriolis parameter $f = 2\Omega \sin \phi$ (ϕ is latitude and Ω is the Earth's rotation rate), and is common at the equator when the maximum in M is displaced away from the equator. In Eq. (4.1), U , y and z are the zonal velocity, meridional, and vertical positions of a fluid parcel and β is the meridional gradient in f . Evaluated using LADCP zonal velocity profiles obtained less than a day apart, the absolute momentum M below 3200m at 1/2°S is larger than that at the equator

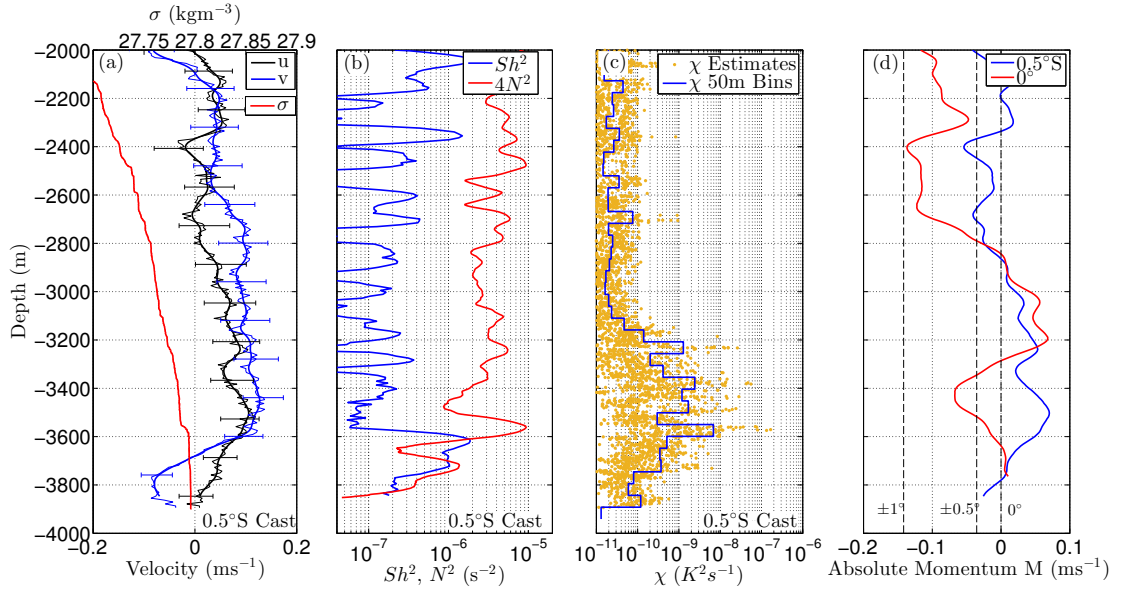


Figure 4.3: Profiles of (a) zonal and meridional velocity (bottom axis) and potential density (top axis), (b) Sh^2 and $4N^2$ and (c) χ from cast 7 at $1/2^\circ\text{S}$. In (a), both raw LADCP velocities with error bars (thin lines) and 100m triangle filtered velocities (thick lines) are shown. The curves in (b) are calculated from velocity and density data binned at 1m and filtered with a 100m triangle filter. (d) Absolute momentum $M = U - \frac{1}{2}\beta y^2$ from the LADCP data for cast 7 at $1/2^\circ\text{S}$ (blue) and cast 6 at the equator (red). The dashed lines show unperturbed ($U = 0$) absolute momentum at 0° , $\pm 0.5^\circ$ and $\pm 1^\circ$.

(Figure 4.3d), suggesting that the flow at $1/2^\circ\text{S}$ is unstable to inertial instability. Thus the region of enhanced turbulence below 3200m at $1/2^\circ\text{S}$ is associated with flow unstable to both vertical shear instability and inertial instability.

What process/processes are responsible for the unstable flow and enhanced mixing in this region? A common cause of enhanced near-bottom mixing is local internal wave breaking associated with tidal interactions with rough topography. Following *Whalen et al. (2012)* and using the *Smith and Sandwell (1997)* ship-sounding bathymetry version 18.1, we find that the average topographic roughness (variance of $1'$ topographic height averaged in 30km bins) in the study region is $1.34(1.04, 1.84) \times 10^3\text{m}^2$, which is in the smooth topography regime of *Whalen et al. (2012)* and *Waterhouse et al.*

(2014). Furthermore, the nearby East Pacific Rise while rougher than our study region is relatively smooth by global standards (*St. Laurent et al.*, 2002; *Whalen et al.*, 2012) and *St. Laurent and Garrett* (2002) conclude that the generation of internal tides through tidal-topographic interactions there should be relatively weak.

In addition to internal tides, other possibilities excluded here are double diffusive instabilities and hydrothermal activity. With these processes excluded, we first explore the possibility that the mixing patch was associated with the breaking of an internal wave generated in the upper ocean. There exists extensive observational evidence of downward propagating equatorially trapped waves below the thermocline in the equatorial Pacific (*Harvey and Patzert*, 1976; *Eriksen and Richman*, 1988), Atlantic (*Weisberg and Horigan*, 1981; *Brandt and Eden*, 2005) and Indian (*Smyth et al.*, 2015) oceans. Downward propagating Yanai waves in the Pacific with a strong signature in meridional velocity, periods near 30 days and zonal wavelengths near 1000km have been observed and modeled by *Cox* (1980); *Eriksen and Richman* (1988) and *Ascani et al.* (2010). Yanai waves are believed to be generated by wind events (*Sen-gupta et al.*, 2004; *Guiavarc'h et al.*, 2008; *Sriver et al.*, 2013) and tropical instabilities (*Cox*, 1980) in the upper ocean. In addition, higher frequency downward propagating gravity waves have also been observed (*Horigan and Weisberg*, 1981).

It is difficult to directly investigate the existence of waves in the LADCP and CTD data because of the lack of temporal information. However, using velocity profiles obtained every minute using the SADCP and a similar analysis to that of *Smyth et al.* (2015) reveals evidence of a downward propagating Yanai wave in the depth range 500m to 650m with 16.75(13.14, 20.90) day period and a downward energy flux of 2.0(0.4, 5.5)mWm⁻² (Figures 4.4,4.5). This is comparable to the value of 1.50(0.69, 2.88) mWm⁻² estimated by *Smyth et al.* (2015) for a Yanai wave in the Indian ocean. Taking into account the seasonal variations as discussed by *Smyth et al.* (2015), these are comparable to the observations of *Eriksen and Richman* (1988) of Yanai waves in the intermediate depth range 1000m-3000m around 140°W in the Pacific. As these wave signals were identified well below the thermocline and strong mean flows of the upper equatorial ocean, it is conceivable that they propagate to the seafloor with little attenuation. Performing a meridional average (between ±2°) and

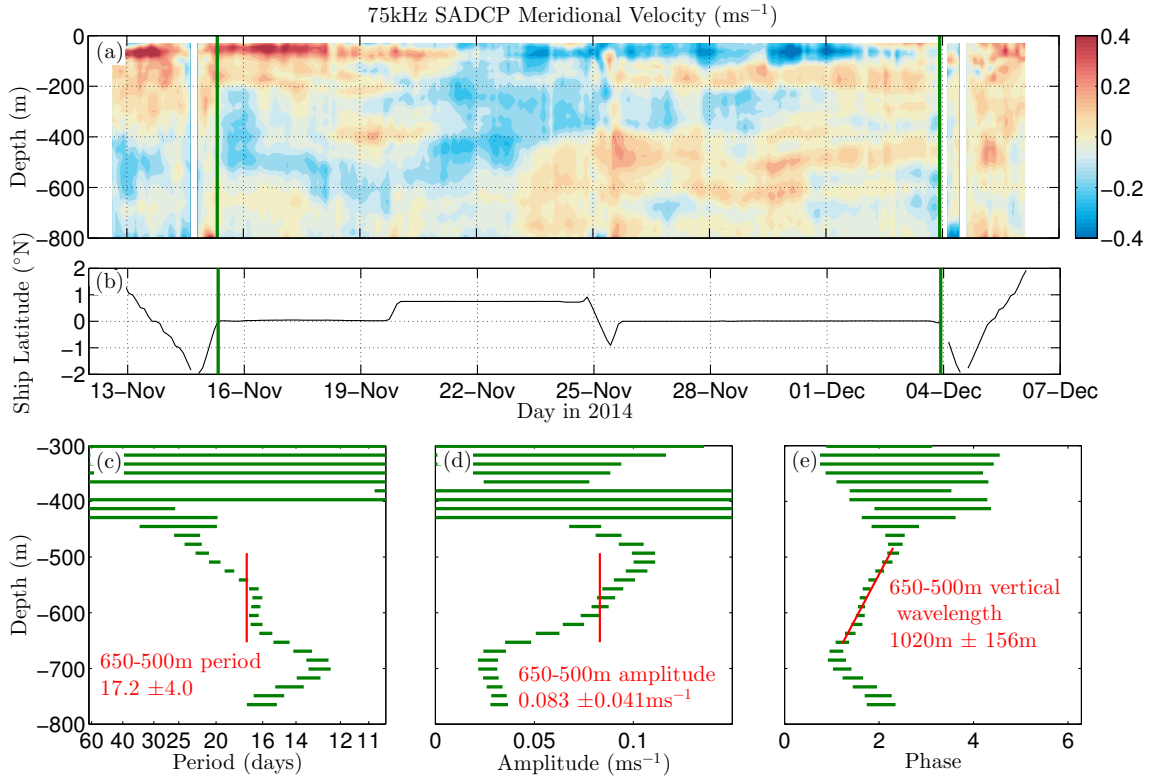


Figure 4.4: (a) Time-depth series of meridional velocity from the shipboard 75kHz ADCP. (b) Latitude location of the measurements in (a). Green bars indicate the portion used for harmonic fitting. Bootstrapped 95% confidence intervals for harmonic fits of wave (c) period, (d) amplitude and (e) phase to sets of five depth bins in (a). 250 bootstrapped samples were used. Averaging the fitted frequency between the depths 500m and 650m, where the amplitude is high and robust, gives a period of 17.2 ± 4.0 days. A linear fit to the phase in depth gives a vertical wavelength of 1020 ± 156 m.

depth integral of the observed dissipation ϵ between 3200m and 3600m (estimates of ϵ below 3600m are unreliable because of weak stratification) gives an average dissipation rate of $0.93(0.69, 1.20)$ mWm^{-2} , close in value to our estimates of downward wave energy fluxes and with the *Smyth et al. (2015)* and *Eriksen and Richman (1988)* estimates. This suggests that there is at least enough energy from the downward propagating low-frequency equatorial waves to account for the observed energy dissipation.

Both the downward 2mWm^{-2} energy flux of the Yanai wave and the average

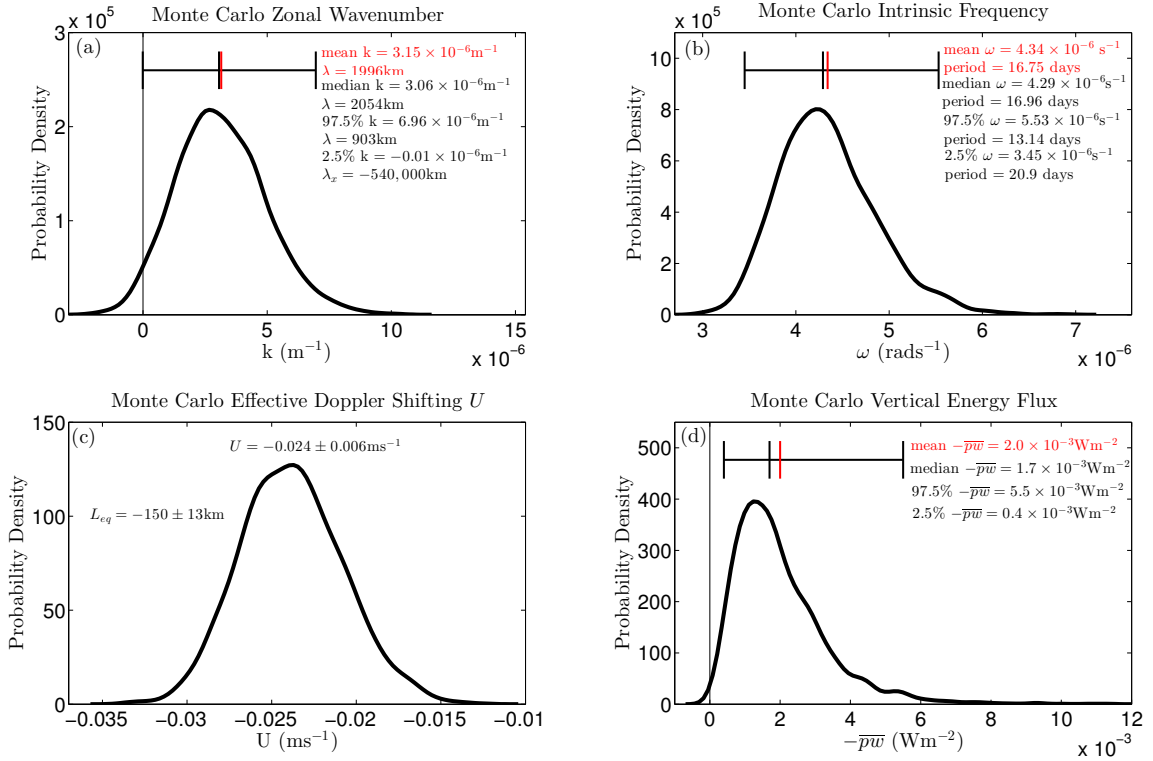


Figure 4.5: Estimate of the (a) zonal wavenumber k , (b) intrinsic frequency ω , (c) Doppler shifting effective velocity U and (d) vertical energy flux $-\bar{p}w$ obtained from the vertically propagating Yanai wave dispersion relation using the frequency and vertical wavenumbers estimated from the 75kHz SADCP (Figure 4.4). See Section 4.7 and *Smyth et al. (2015)* for details of the calculation. The distributions are generated through a Monte Carlo simulation with 2000 draws and the iterative process described in *Smyth et al. (2015)*.

dissipation rate of 1 mWm^{-2} are comparable to the $\sim 1 \text{ mWm}^{-2}$ energy flux into topographic lee waves estimated by *Nikurashin and Ferrari (2013)* for this location (see their Fig. 1b). Thus lee waves are another potential source of energy for the mixing. The generation of lee waves over smooth topography here is a consequence of the enhanced bottom kinetic energy in the equatorial band used in their calculation (see Fig. 2c of *Nikurashin and Ferrari (2011)*). It is not clear what the source of this bottom kinetic energy is. Since it is confined to the equatorial band, one possibility is downward propagating equatorial waves. A persistent near-bottom current driven by a zonal pressure gradient is another possibility, but our observations are not sufficient

to establish this. More research is required to disentangle the relationships between equatorial waves, enhanced bottom kinetic energy and lee wave generation.

For the downward propagating equatorial wave hypothesis, the remaining question is why the wave energy flux might converge where the mixing was observed. Typical wave breaking can occur at critical layers in a background mean flow. However, there is no evidence for any deep zonal flows in the LADCP observations of comparable magnitude to the zonal phase speed of the Yanai wave found in the SADCP data. In addition, the stratification generally reduces towards the seafloor, implying that the vertical wavelength of the wave should increase and shear decrease with time as it descends in the water column. In the next two subsections we describe two mechanisms through which a low-frequency wave at this location could lead to unstable flow and mixing.

4.4.1 Near-bottom wave trapping associated with the horizontal component of the Earth's rotation

Gerkema and Shrira (2005) and *Winters et al.* (2011) describe a mechanism through which the horizontal component of Earth's rotation, $\tilde{f}/2 = \Omega \cos \phi$, can drive trapping of internal waves in the deep ocean where N^2 is small. With the inclusion of the Coriolis force associated with \tilde{f} , the following simplified dispersion relation for linear, zonally-uniform waves can be derived (see Appendix 3, Section 4.8),

$$\omega^2 = f^2 + 2f\tilde{f}\alpha + (N^2 + \tilde{f}^2)\alpha^2, \quad (4.2)$$

where $\alpha = l/m$, l is the meridional wavenumber, m is the vertical wavenumber and ω is the frequency. The aspect ratio of the wave and the slope of wave characteristics, α , in general can have two solutions α_+ and α_- . This dispersion relation is similar to that for classical internal waves with the additional terms containing the horizontal Coriolis parameter \tilde{f} . These terms are most important near the equator where \tilde{f} is a maximum and f a minimum (*Gerkema et al.*, 2008).

The inclusion of \tilde{f} in the dispersion relation Eq. (4.2) allows waves to exist with subinertial frequencies ($\omega < f$; as noted by *Cushman-Roisin* (1996)) in regions of low

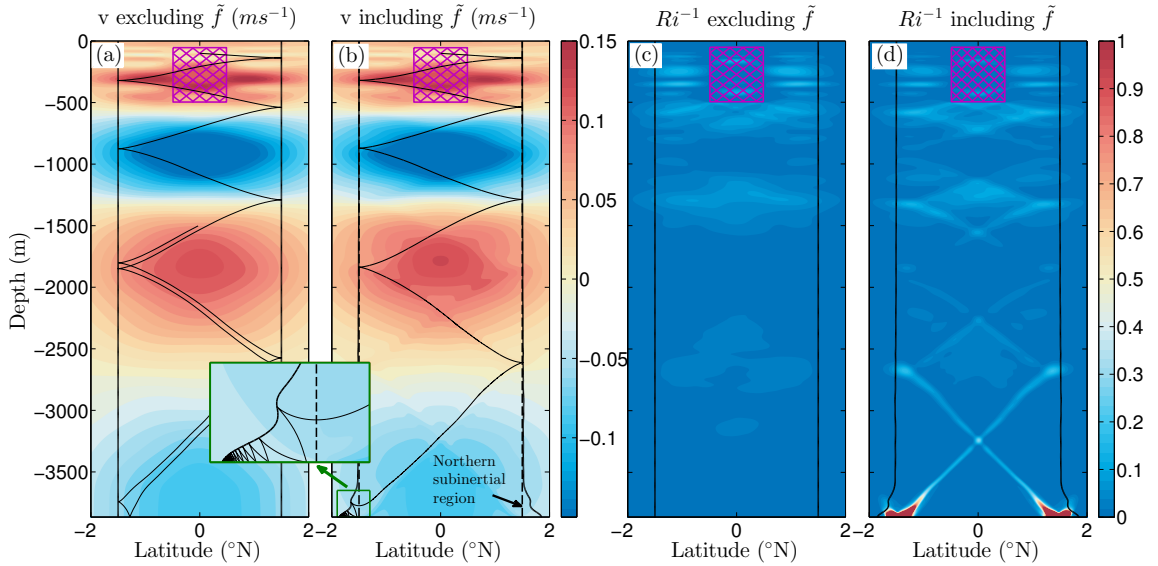


Figure 4.6: Comparison of solutions to the two-dimensional wave equation excluding (a,c) and including (b,d) the horizontal component of the Earth’s rotation for waves with frequency equal to the inertial frequency at 1.5° latitude. See Appendix 3 (Section 4.8) for a description of the numerical solution method. The region where propagating waves are permitted is equatorward of the thick lines, with the dashed lines in (b) indicating the inertial latitude. Forcing is applied within the purple hatched box. (a) and (b) show meridional velocity while (c) and (d) show Ri^{-1} . Fields are plotted at phase 0. Also shown in (a) and (b) are wave rays originating at 150m depth at the equator. The inset shows a magnification of a ray entering the trapping region. This trapping behavior is responsible for the near-bottom enhancement in Ri^{-1} when including \tilde{f} in (d).

stratification, typically near the seafloor (the region between the dashed and solid lines in Figure 4.6b). At subinertial frequencies, both characteristics have slopes with sign opposite to f . Consequently, a wave ray reflecting off the seafloor here propagates polewards into a region of decreasing volume where the wave energy density amplifies, potentially leading to breaking (see inset in Figure 4.6). In addition, the inclusion of \tilde{f} allows waves to undergo critical reflection off a flat bottom at their inertial latitude (that is the latitude where their frequency equals f , dashed lines in Figure 4.6b) (*Winters et al., 2011*), also potentially leading to amplification, breaking and mixing.

To establish whether the dynamics associated with \tilde{f} could be responsible for the

observed patch of enhanced mixing, we numerically investigated the properties of time-periodic, zonally-uniform linear waves on an equatorial β plane both with and without \tilde{f} (see Appendix 3 (Section 4.8) for a description of the numerical solution method). With forcing distributed over the upper ocean, the numerical solutions produce clear modal patterns in meridional velocity both with and without \tilde{f} (Figure 4.6a,b). However, with \tilde{f} included there is an enhancement in Ri^{-1} along wave beams entering the trapping regions (Figure 4.6d). Evidently these regions act to focus wave energy resulting in enhanced shears and lower Ri . Similar dynamics have been explored in the mid-latitudes by *Shrira and Townsend* (2010, 2013) who discuss the potential for enhanced deep mixing driven by internal waves when their physics is modified by \tilde{f} .

While the energy flux required to balance the total observed dissipation was $\sim 1\text{mWm}^{-2}$, the observations suggest that much of this energy flux converges at $1/2^\circ\text{S}$. Analysis of the SADCP data (Figure 4.4) and previous studies (*Eriksen and Richman*, 1988; *Smyth et al.*, 2015; *Ascani et al.*, 2010) indicate Yanai waves in the equatorial oceans have dominant periods of 15-30 days, corresponding to inertial latitudes of 0.95° - 1.90° . This is poleward of the observed mixing event. However, the numerical solutions (Figure 4.6d) show enhanced Ri^{-1} not only at the seafloor near the inertial latitude, but also along wave beams stretching back towards the equator, potentially explaining why the observed patch of mixing extends well above the seafloor (Figure 4.3c,d). Along the wave beams in the numerical solutions Ri does not reach values $< 1/4$, although it should be noted that these are linear, time-periodic solutions that assume a laterally-uniform stratification. The introduction of the non-linear terms, which are largest along the wave rays, time dependence and meridionally-inhomogeneous stratification will enhance mixing in some regions and suppress it in others. Finally, numerical solutions forced only over the Northern Hemisphere produce much lower Ri to the South of the equator than to the North (Figure 4.7), potentially explaining why enhanced mixing was only observed to the South of the equator.

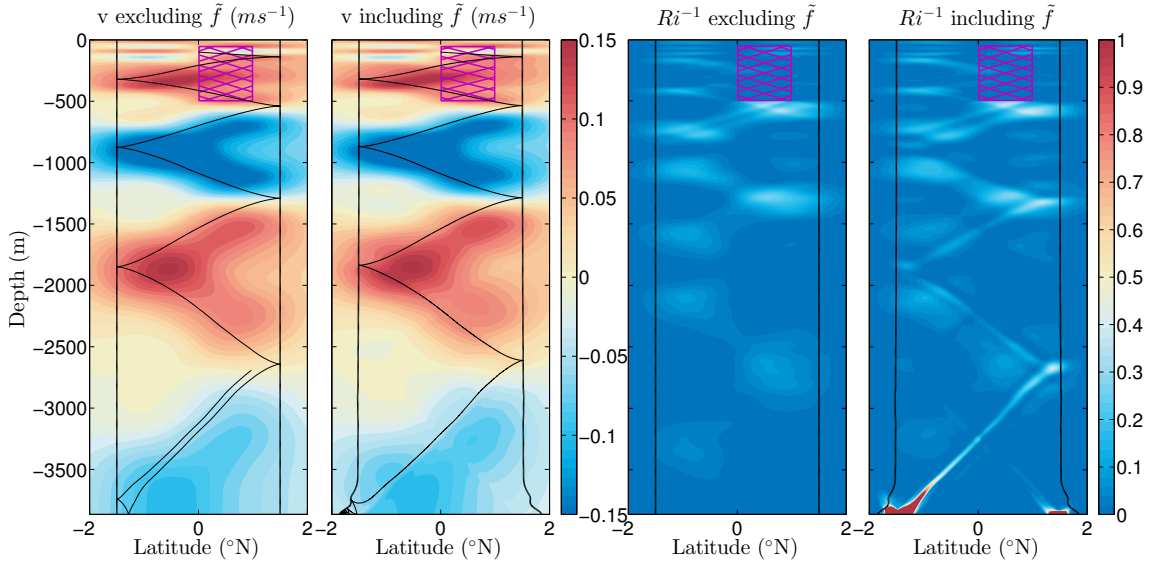


Figure 4.7: As in Figure 4.6 except with forcing restricted to the Northern Hemisphere between 0° and 1°N . The meridional asymmetry in forcing results in lower near-bottom Ri to the South of the equator than the North for the simulation including \tilde{f} .

4.4.2 Inertial instability

As noted above, the flow at $1/2^\circ\text{S}$ was found to be inertially unstable as the absolute momentum M was higher there than at the equator (Figure 4.3d). The region of instability below 3200m corresponds closely to the region of observed mixing suggesting a link between the two. Inertial instability has been linked to small-scale turbulent mixing in the coastal environment (Dewar *et al.*, 2015). However, this link must be treated with caution, as the flow was also unstable above 2800m where mixing was not observed (compare Figures 4.3c and 4.3d above 2800m). The ultimate source of energy for the inertial instability and any subsequent mixing is the source of the displacement of the maximum in absolute momentum away from the equator. The equatorial wave motions considered above drive periodic particle displacements away from the equator (for example, Figure 4.6), where inertial instability can then act most efficiently at the limit of the displacement. Analysis of T-S properties below 3000m (not shown) suggests that fluid parcels were displaced southwards on the 13th and 14th of November when the mixing patch was observed, lending support to this

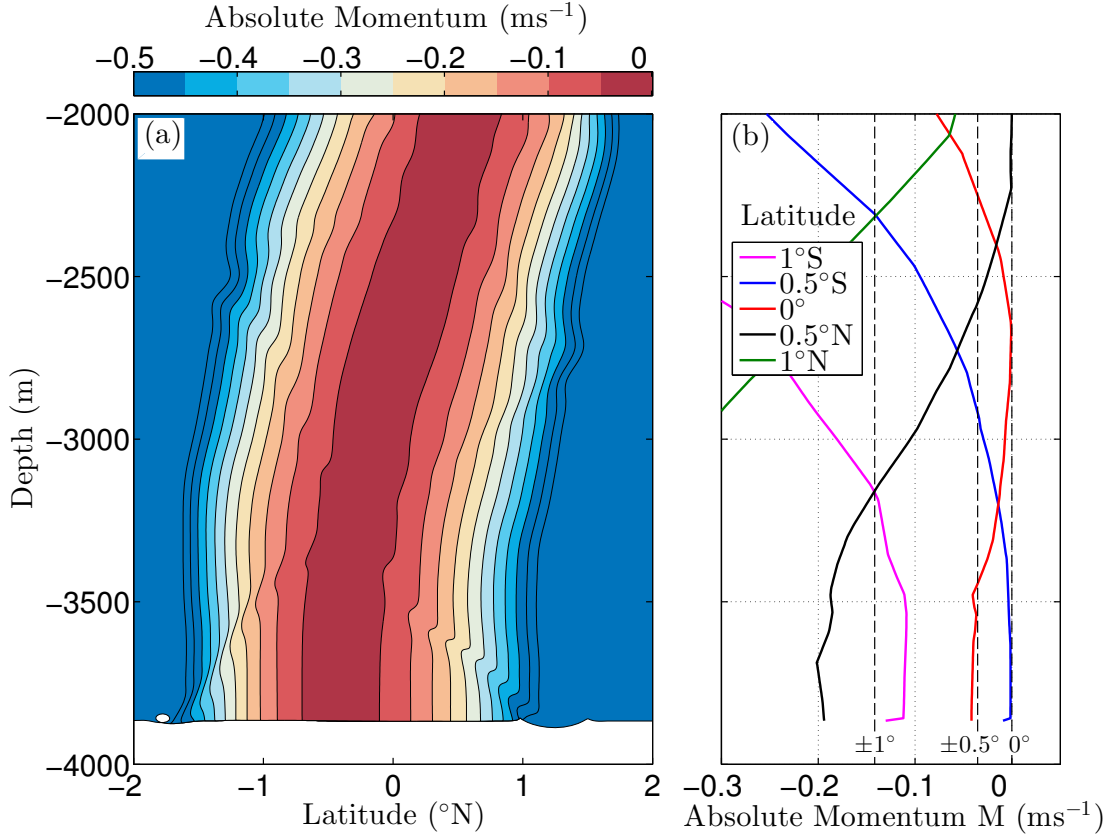


Figure 4.8: (a) Eulerian absolute momentum $M = U - \beta y^2$ (the linear equivalent of the absolute momentum considered in Eq. (4.1)) at 1/4 phase from the numerical solution with the amplitude increased by a factor of 2 for emphasis. The modal meridional velocity (Figure 4.6b) displaces fluid parcels and the maximum in absolute momentum away from the equator, creating a flow unstable to inertial instability. (b) Vertical profiles through (a) at different latitudes for comparison with Figure 4.3d. The dashed lines indicate the unperturbed ($U = 0$) absolute momentum at 0° , $\pm 1^{\circ}$ and $\pm 2^{\circ}$. Below 3300m, the absolute momentum is greater at $1/2^{\circ}\text{S}$ than at the equator, indicating the flow is unstable to inertial instability, similar to the observations.

hypothesis. Examination of the absolute momentum from the numerical solutions considered in the previous section shows that a southern maximum in absolute momentum can occur, however positive values of M cannot be generated (Figure 4.8). The growth rate of inertial instability is half the cross-equatorial shear (*Dunkerton*,

1981; *Griffiths*, 2003). Using the shear in zonal velocity between $1/2^{\circ}\text{S}$ and the equator yields a maximum growth rate of $7 - 14$ days between the depths of 3400m and 3600m, which is less than the estimated $15 - 30$ day wave period. While the cross-equatorial shear is not well resolved with our sparse measurements, this suggests that inertial instability may have enough time to act while fluid parcels are displaced southwards, and thus it cannot be ruled out as a mechanism potentially responsible for the patch of observed mixing.

4.5 Conclusion

Turbulence observations obtained in the eastern equatorial Pacific over topographically smooth seafloor show seafloor-intensified mixing with diffusivities reaching $10^{-3}\text{m}^2\text{s}^{-1}$, comparable in intensity and structure to energetic mixing associated with tidal flow over rough topography (Figure 4.1e). The generation and breaking of lee waves over relatively smooth topography is possible at equatorial latitudes and is one possible explanation for the observed mixing. However, our observations suggest that the turbulence could also have been energized by a low-frequency equatorial wave generated at the surface. We propose two mechanisms through which such a wave could create instabilities immediately above the seafloor 1) near-bottom wave trapping driven by the horizontal component of the Earth's rotation and 2) inertial instability generated through wave-driven displacement of fluid away from the equator. All three possible mechanisms discussed here constitute a unique energy pathway through which wind energy ultimately mixes the deep equatorial ocean away from regions of rough topography. Unfortunately, present observations are insufficient to conclusively establish the source of the turbulence, highlighting the need for more observations. Future theoretical and numerical work will focus on quantifying the potential contribution of these mechanisms to mixing the deep equatorial oceans.

We thank the crew, engineers and scientists aboard the R/V Oceanus for assistance in obtaining data. Pavan Vutukur and Craig Van Appledorn constructed the CTD χ -pods. Jonathan Nash contributed a version of the χ -pod software tailored to CTD profiling. R. Holmes was supported by a Stanford Graduate Fellowship while

undertaking this study. We thank A. Waterhouse for providing the comparison ϵ and κ_T profiles in Figures 4.1c and 4.1e. Data used to produce the figures and analyses in this article can be obtained upon request to the authors. This work was funded by NSF grants 1256620 (J.N.M.) and 1260312 (L.N.T.).

4.6 Appendix 1: CTD χ -pod microstructure measurements

Here we describe the measurement techniques and assumptions involved in estimating the turbulent parameters χ , ϵ and κ_T using the CTD χ -pod instrument. The spatial gradient of temperature dT/dx is calculated using thermistor measurements of the temporal derivative of temperature at 100Hz and the fall speed of the CTD package (measured using a pressure sensor and an accelerometer). With measurements of dT/dx in the diffusive sub-range of turbulence, the dissipation rate of temperature variance can then be computed as,

$$\chi = 6D_T \langle \frac{dT}{dx} \frac{dT}{dx} \rangle, \quad (4.3)$$

where we have assumed isotropy, D_T is the molecular diffusivity of heat and the angle brackets indicate an ensemble average, in this case a time average. As our measurements do not fully resolve the diffusive sub-range, we fit the resolved portion of the temperature gradient spectra to an accepted universal form to reconstruct the unresolved portion (see *Moum and Nash* (2009) for details). Given an estimate of χ , we can then make the assumption that isotropic turbulence is acting on a background vertical temperature gradient dT/dz (*Osborn and Cox*, 1972) to estimate the eddy diffusivity of heat,

$$\kappa_T = \frac{1}{2}\chi / \langle \frac{dT}{dz} \rangle^2 \quad (4.4)$$

Furthermore, assuming that $\kappa_\rho = \kappa_T$ (*Oakey*, 1982), and a steady-state balance between shear production, dissipation and buoyancy production of turbulent kinetic energy characterized by a constant mixing efficiency $\Gamma = 0.2$ (*Osborn*, 1980), we can

estimate the dissipation rate of turbulent kinetic energy,

$$\epsilon = \frac{N^2 \chi}{2\Gamma \langle dT/dz \rangle^2}, \quad (4.5)$$

where N^2 is the Brunt-Väisälä frequency. Each of these quantities is estimated from a sample size of 128 measurements, corresponding to roughly 1 second of data. Quantities are calculated both for the downcast and upcast (using the thermistors below and above the CTD package respectively), provided that the fall or rise speed of the CTD package is greater than 0.4ms^{-1} .

Following *Moum et al.* (2002), we tested the robustness of average values of χ , ϵ and κ_T to the noise level of the instrument by setting all χ , ϵ and κ_T values to zero for χ less than some threshold value χ_{th} . The results change minimally even for threshold values that zero 90% of the data (Figure 4.9). The results of this test were used to determine the uncertainty ranges on the mixing parameters used in Fig. 4.1 by using the outermost 95% confidence limits of data calculated using $\chi_{th} = 1 \times 10^{-11}\text{K}^2\text{s}^{-1}$ and $\chi_{th} = 4 \times 10^{-11}\text{K}^2\text{s}^{-1}$. Profiles using these values individually show significant differences only between 2000 and 3200m (c.f. brown profiles with yellow confidence intervals and black profiles with gray confidence intervals in Figure 4.10). This depth range is characterized by weak turbulence where mean values of χ , ϵ and κ_T are at or below the detection limit of the method (dotted lines in Figure 4.10). A sensitivity study to the filtering used to calculate N^2 and $\frac{dT}{dz}$ also shows consistent results for all three mixing quantities (red profiles in Figure 4.10).

4.7 Appendix 2: Yanai waves in the shipboard ADCP

Following *Smyth et al.* (2015), we look for evidence of equatorial waves in the 75kHz shipboard ADCP data throughout the time period for which the ship was close to the equator. In the meridional velocity there is evidence of upward phase propagation with one complete phase resolved within the depth range 400m-800m (Figure 4.4a).

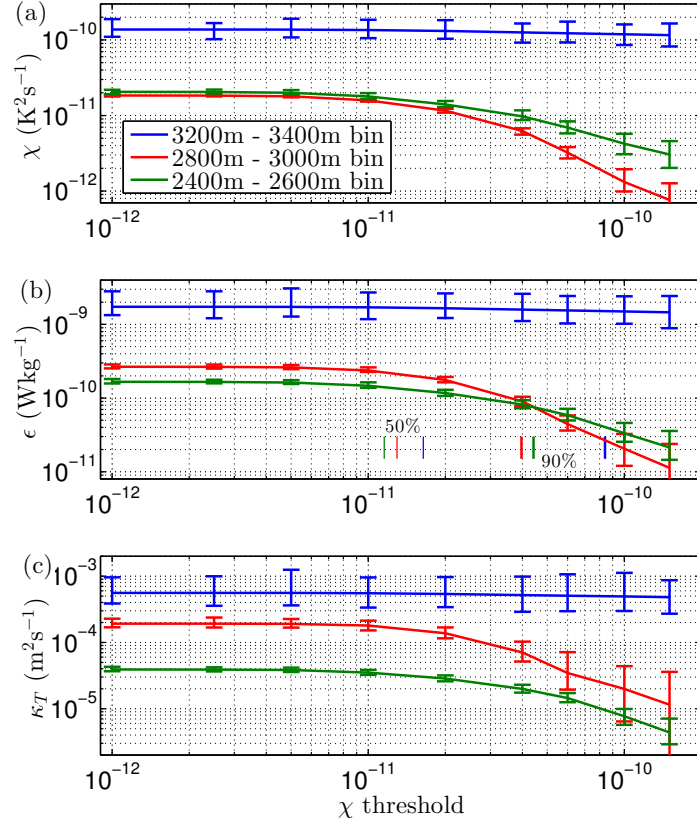


Figure 4.9: Sensitivity of (a) χ , (b) ϵ and (c) κ_T to the noise level of the χ -pod instrument. Shown are the bin mean in three different depth bins as function of χ_{th} , where all χ , ϵ and κ_T values are set to zero if $\chi < \chi_{th}$. Error bars are 95% bootstrapped confidence intervals. Vertical bars in the middle panel indicate where 50% and 90% of the data set has been set to zero for each bin.

To estimate the dominant frequency, amplitude and phase we perform a harmonic fit of groups of time series taken from five depth bins for data from the time period when the ship was within $\pm 1^\circ$ of the equator (indicated by the green bars in Figure 4.4a and 4.4b). The uncertainties in these fits are estimated by bootstrapping with 250 bootstrap samples from each five depth bin group. We find evidence for an oscillation in meridional velocity with an extrinsic period of 17.2 ± 4.0 days and a vertical wavelength of 1020 ± 156 m between the depths of 650 and 500m (Figures 4.4c, 4.4d and 4.4e). These results are qualitatively similar to the results of *Smyth*

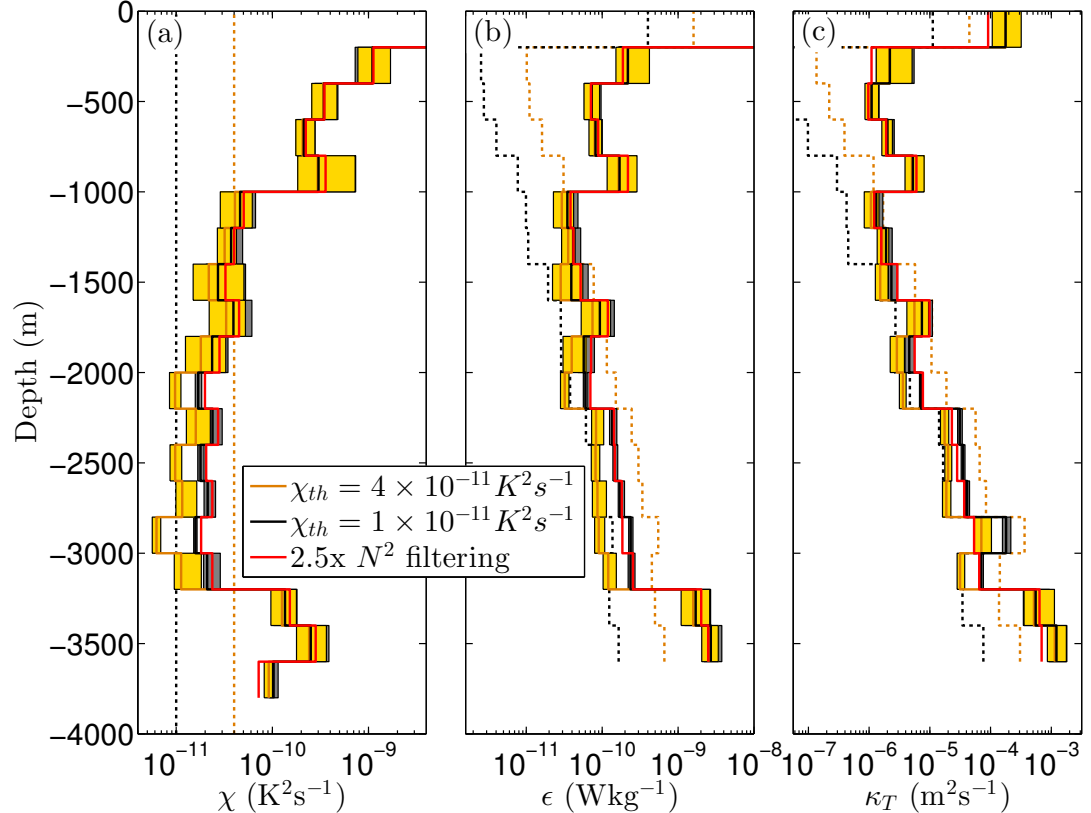


Figure 4.10: Comparison of 200m binned mean profiles of (a) χ , (b) ϵ and (c) κ_T . Profiles of χ -pod data are shown using a noise threshold (as described in Section 4.6) of $\chi_{th} = 4 \times 10^{-11} K^2 s^{-1}$ (orange with yellow 95% bootstrapped confidence limits), using a noise threshold of $\chi_{th} = 1 \times 10^{-11} K^2 s^{-1}$ (black with gray confidence limits) and with a 2.5 increase in the N^2 filtering length (red). The dotted lines show the χ_{th} values (a), and the corresponding ϵ and κ_T thresholds (b,c) using the observed N^2 and dT/dz and equations (4.4) and (4.5). The confidence intervals used in Figures 4.1a,c,e are the low limit of the $\chi_{th} = 4 \times 10^{-11} K^2 s^{-1}$ curve (yellow) to the high limit of the $\chi_{th} = 4 \times 10^{-11} K^2 s^{-1}$ curve (gray).

et al. (2015), suggesting that we have identified a downward propagating Yanai wave.

Following Appendix B of *Smyth et al.* (2015), we use the dispersion relation for downward propagating Yanai waves and the meridional structure of the zonal velocity from the 75kHz ADCP results to correct for the Doppler shift. From this process we obtain a corrected intrinsic frequency in the 650 to 500m range of $\omega =$

$4.34(3.45, 5.53) \times 10^{-6} \text{rads}^{-1}$, where the brackets refer to a 95% confidence interval obtained through Monte Carlo simulation (Figure 4.5b). This corresponds to a period of $16.75(13.14, 20.9)$ days, or an inertial latitude of $1.71^\circ(1.37^\circ, 2.17^\circ)$. We find a zonal wavenumber of $3.15(-0.01, 6.96) \times 10^{-6} \text{radm}^{-1}$, or zonal wavelength of $1996(903, -504000) \text{km}$. There is only a 2.5% chance that the phase propagation is westward (Figure 4.5a). We also obtain an estimate for the meridional trapping scale of the Yanai wave,

$$L_{eq} = \sqrt{\frac{N}{\beta|m|}} \quad (4.6)$$

of $L_{eq} = 150(138, 162) \text{km}$, or $1.35^\circ(1.24^\circ, 1.45^\circ)$. This result justifies our use of the SADCP data for latitudes off the equator but closer than $\pm 1^\circ$. The small wave steepness of $v_0/c = 0.06$, where $c = \omega/k$ is the zonal phase speed and v_0 is the amplitude estimated from the harmonic fit, justifies the use of linear equatorial wave theory.

Finally, we also estimate a downward vertical energy flux of $-\overline{pw} = 2.0(0.4, 5.5) \text{mWm}^{-2}$ (Figure 4.5d) following Eq. 7 of *Smyth et al. (2015)*. This is comparable to the values found in *Smyth et al. (2015)* and references contained therein.

4.8 Appendix 3: Linear wave theory including the horizontal component of the Earth's rotation

In this section we briefly describe the linear wave theory considered by *Gerkema and Shrira (2005)* and *Winters et al. (2011)*. We start with the inviscid zonally uniform equations of motion that account for the Coriolis force associated with the horizontal component of the Earth's rotation, linearized about a state of rest with a background

stratification profile $N^2(z)$,

$$\frac{\partial u}{\partial t} - fv + \tilde{f}w = 0 \quad (4.7)$$

$$\frac{\partial v}{\partial t} + fu = -\frac{\partial \phi}{\partial y} \quad (4.8)$$

$$\frac{\partial w}{\partial t} - b - \tilde{f}u = -\frac{\partial \phi}{\partial z} \quad (4.9)$$

$$\frac{\partial v}{\partial y} + \frac{\partial w}{\partial z} = 0 \quad (4.10)$$

$$\frac{\partial b}{\partial t} + N^2w = 0, \quad (4.11)$$

We now introduce a stream-function in the meridional plane,

$$v = \frac{\partial \psi}{\partial z}, \quad w = -\frac{\partial \psi}{\partial y}, \quad (4.12)$$

and assume that the time dependence of ψ can be represented by simple harmonic motion, $\psi(y, z, t) = \psi_0(y, z)e^{-i\omega t}$, where ω is the frequency. Equations (4.7)-(4.11) can then be combined into a single equation for ψ_0 :

$$(f^2 - \omega^2) \frac{\partial \psi_0^2}{\partial z^2} + 2f\tilde{f} \frac{\partial^2 \psi_0}{\partial z \partial y} + (\tilde{f}^2 + N^2 - \omega^2) \frac{\partial^2 \psi_0}{\partial y^2} + \tilde{f} \frac{\partial f}{\partial y} \frac{\partial \psi_0}{\partial z} = 0. \quad (4.13)$$

Defining $A = N^2 - \omega^2 + \tilde{f}^2$, $B = f\tilde{f}$ and $C = f^2 - \omega^2$, this partial differential equation admits waves where it is hyperbolic, i.e. where $B^2 - AC > 0$. Within this region, the slope of wave characteristics is given by

$$\frac{dz}{dy} = \alpha_{\pm} = \frac{B}{A} \pm \frac{\sqrt{B^2 - AC}}{A}. \quad (4.14)$$

Note that at the inertial latitude $\omega = f$, $C = 0$ and thus the shallow characteristic has zero slope.

Finally, under the WKB approximation assuming plane wave solutions $\psi_0(y, z) =$

$\hat{\psi}e^{i(ly+mz)}$, Eq. (4.13) yields a dispersion relation

$$\omega^2 = (1 + \alpha^2)^{-1} \left(f^2 + 2f\tilde{f}\alpha + (N^2 + \tilde{f}^2)\alpha^2 \right). \quad (4.15)$$

Making the quasi-hydrostatic approximation of *White and Bromley* (1995) that $\alpha^2 \ll 1$ yields the simplified dispersion relation included as Eq. (4.2).

Numerical solution:

The numerical solution in Figure 4.6 is obtained by solving the forced-dissipative version of Eq. (4.13),

$$\mathcal{L}\psi_0 = (\omega + i\mathcal{F})^2(\partial_z^2 + \partial_y^2)\psi_0 + \hat{G} \quad (4.16)$$

where $\mathcal{L} = f^2\partial_z^2 + 2f\tilde{f}\partial_z\partial_y + (\tilde{f}^2 + N^2)\partial_y^2 + \tilde{f}\frac{\partial f}{\partial y}\partial_z$, $\mathcal{F} = \nu_H \frac{\partial^2}{\partial y^2} + \nu_V \frac{\partial^2}{\partial z^2}$ represents a Laplacian friction and $G(y, z, t) = \hat{G}(y, z)e^{-i\omega t}$ is the forcing. We solve this equation using second order finite differences on a 500×500 point grid with $\Delta z = 7.75\text{m}$, $\Delta y = 2.23\text{km}$ given a frequency ω with forcing $\hat{G} = 1$ distributed over the upper water column. The $N^2(z)$ profile represents the average stratification over all CTD casts within $\pm 2^\circ$ of the equator. The viscosities for the case shown in Figure 4.6 are $\nu_h = 1.9\text{m}^2\text{s}^{-1}$ and $\nu_v = 2.3 \times 10^{-5}\text{m}^2\text{s}^{-1}$. The results of these linear simulations are scaled to produce a similar magnitude velocity as in the LADCP observations. The results are not sensitive to a halving of the resolution.

Chapter 5

Summary and Future Work

5.1 Summary of the contributions of this thesis

This thesis makes a number of contributions that address important open questions relating to the dynamics of the equatorial oceans. The results have implications for the role of upper-ocean processes in the ENSO cycle, and for the underlying physical mechanisms that drive the global meridional overturning circulation. The main contributions are:

1. a) Tropical instability waves (TIWs) and vortices (TIVs) in the equatorial Pacific share a number of important characteristics with submesoscale flows in the mid-latitudes. They are characterized by order one Rossby and Richardson numbers and contain significant ageostrophic flows, strong fronts and high vertical shear. The mechanisms driving the formation of TIVs with $\sim 500\text{km}$ lateral scales share similarities with those driving the formation of submesoscale coherent vortices with $\sim 10\text{km}$ lateral scales at mid-latitude fronts. For TIVs, these mechanisms involve the extraction of energy from the vertical shear of the Equatorial Undercurrent (EUC) through the action of an ageostrophic secondary circulation driven by frontogenesis. Thus the vertical shear of the EUC may serve as a significant energy source for TIWs, and must be resolved sufficiently well in ocean models for a satisfactory representation of TIWs and their associated lateral mixing.

- b) TIW fronts can evolve into very sharp gravity currents as they approach the equator through the combined action of frontogenesis and the reduction in the Coriolis parameter f . The gravity currents are subsequently dissipated by vertical frictional processes and constitute a small energy sink for the TIWs.
- 2. TIWs modulate turbulence in the eastern equatorial Pacific by altering the meridional and zonal vertical shears, stratification and thus the Richardson number in the upper EUC. TIW modification of the zonal shear of the EUC plays a larger role in modulating mixing than the addition of TIW meridional shear, contrary to previous hypotheses. TIW strain modifies the EUC shear through periodic horizontal vortex stretching and squashing of the meridionally oriented EUC horizontal vorticity. Numerical simulations performed using a simple one-dimensional mixing model of the EUC suggest that periodic TIW strain can result in a rectified increase in the vertical turbulent heat flux averaged over a TIW period. Thus the influence of TIWs on vertical mixing may drive a net cooling of the SST that can partially offset the warming influence of the TIW lateral heat flux on the mixed-layer heat budget. However, the degree to which TIWs modify the turbulent heat flux depends on the Richardson-number based vertical mixing parameterization included in the mixing model, with potential implications for the role of TIWs in the mixed-layer heat budget in different ocean models.
- 3. Equatorial Kelvin waves propagating across the equatorial Pacific can induce large changes in the amplitude of the TIW field. A typical downwelling Kelvin wave weakens the background circulation and can drive a decay in TIW kinetic energy of up to 40%, while upwelling Kelvin waves strengthen the background circulation and can drive a similar 40% intensification of the TIWs. However, the manner in which the TIW kinetic energy budget adjusts to the Kelvin wave-induced changes in the background flow is complex. A number of small terms initiate changes that are amplified by the shear production term associated with the meridional shear in zonal velocity, $-\rho_0 \overline{u'v'} \frac{\partial U}{\partial y}$, that depends itself on the TIW kinetic energy through the TIW momentum flux $\overline{u'v'}$. One of the

main energy sink terms, the radiation of energy downwards out of the surface ocean via waves, also undergoes large changes that act as a negative feedback on the TIW kinetic energy budget. These results have implications for the momentum and heat budgets of the equatorial circulation, in particular the temporal evolution of SST anomalies in the eastern equatorial Pacific in response to variations in atmospheric forcing.

4. Mixing in the abyssal eastern equatorial Pacific, as measured for the first time directly by a microstructure turbulence instrument, can exhibit a seafloor-intensified vertical structure over smooth topography with intensity similar to that driven by tidal flow over rough topography. The generation of lee waves over smooth topography at low latitudes and their subsequent breaking is one possible mechanism that could contribute to this mixing, but current observations are not sufficient to establish their presence. However, a downward-propagating equatorial wave with sufficient energy flux to drive the mixing was observed in the upper ocean over the same time period. There are several possible mechanisms through which such a wave could drive seafloor-intensified equatorial mixing that have not been explored in detail in the literature. The horizontal component of Earth's rotation can result in wave trapping and amplification near the seafloor near the wave's inertial latitude. Inertial instability initiated through wave-driven displacement of fluid away from the equator may also contribute. These observations suggest that more attention should be devoted to measuring and understanding mixing in the abyssal equatorial oceans over smooth topography because of its potential implications for the global overturning circulation.

5.2 Future work

The work in this dissertation has opened a number of new research questions that deserve further exploration. These are questions that I am currently working on or hope to work on in the near future.

In Chapter 1 we showed how important fronts and frontogenesis were to the dynamics of TIWs. Frontogenesis acting on TIW trailing edge fronts drives a thermally-direct secondary circulation that results in negative vortex tilting and the formation of anticyclonic vorticity that feeds the TIVs. Such a secondary circulation is predicted by the classical frontogenesis theories of *Hoskins and Bretherton* (1972) and *Hoskins* (1982), which assume that the frontal shear is in thermal-wind balance. However, as we showed in Section 1.3.2 the TIW flow is in gradient-wind balance not thermal-wind balance, with the shear in the centrifugal force resulting from the curvature of the front playing an important role. Thus one open question is; *How does frontogenesis and the properties of the secondary circulation in a curved, gradient-wind-balanced front differ from that in a straight, thermal-wind-balanced front?* Progress on this question could also help to inform the gravity currents material in Section 1.10, where we saw that the advective force associated with flow curvature still played an important role in the force balance after the formation of the gravity current (*VADV* in Fig. 1.18h).

In Chapter 2 we showed how TIWs modulate shear and stratification in the upper EUC, thus modulating the vertical heat flux. While this shed insight on the fundamental mechanisms acting, one drawback was that the mixing in the numerical model was parameterized. Several followup studies could potentially address this drawback. Firstly, an observational study on the relationship between shear and stratification (measured using the TAO buoys and ADCPs), turbulence (measured using moored CTD χ -pod instruments that are already in place on some TAO buoys) and the TIW strain $\frac{\partial v}{\partial y}$ (measured using off-equatorial moorings, shipboard ADCPs, surface drifters, satellite altimetry and/or other satellite data) would be useful to confirm whether the mechanism presented in Chapter 2 is indeed important in the real system. Secondly, a sensitivity study to the mixing parameterization included in the numerical model would be useful. In particular, results from the simple 1D mixing model in Section 2.5 suggested that a parameterization with the KPP boundary layer model and the interior scheme of *Pacanowski and Philander* (1981) may perform better than the original KPP model. This should be investigated in a full ocean model.

In Chapter 3 we showed that Kelvin waves and TIWs do indeed interact, but focused on the influence of the Kelvin waves on the TIWs. Additional modeling

and theoretical work performed using a shallow water system suggest that TIWs can influence the propagation of Kelvin waves, potentially scattering a significant proportion of their energy into other equatorial waves (unpublished work). This possibility deserves further study because of its potential influence on the initiation of El Niño events and the variability of ENSO.

Finally, the observational results presented in Chapter 4 suggest a number of new research directions. Firstly, it is clear that more microstructure turbulence observations are needed in this region, with larger temporal and spatial coverage. Secondly, the mechanisms proposed to explain the seafloor-intensified mixing require additional theoretical and numerical studies to establish their potential importance. In particular, a fully time-dependent numerical study of the properties of 2D and 3D downward propagating equatorial waves with the horizontal component of the Earth's rotation included needs to be performed. Finally, the generation mechanism for the downward propagating equatorial waves also deserves more study as suggested by not only these mixing observations, but also the importance of downward propagating waves as an energy sink in the TIWKE budget in Chapter 3 (e.g. Section 3.4) and the study of *Tanaka et al.* (2015) on the generation of downward-propagating waves by TIW fronts.

Bibliography

- Alford, M. H., R. Lukas, B. Howe, A. Pickering, and F. Santiago-Mandujano (2011), Moored observations of episodic abyssal flow and mixing at station ALOHA, *Geophys. Res. Lett.*, 38(15), L15,606, doi:10.1029/2011GL048075.
- Allen, M. R., S. P. Lawrence, M. J. Murray, C. T. Mutlow, T. N. Stockdale, D. T. Llewellyn-Jones, and D. L. T. Anderson (1995), Control of tropical instability waves in the Pacific, *Geophys. Res. Lett.*, 22(19), 2581–2584, doi:10.1029/95GL02653.
- Alley, R. B., J. Marotzke, W. D. Nordhaus, J. T. Overpeck, D. M. Peteet, R. A. Pielke, R. T. Pierrehumbert, P. B. Rhines, T. F. Stocker, L. D. Talley, and J. M. Wallace (2003), Abrupt climate change, *Science*, 299(5615), 2005–2010, doi:10.1126/science.1081056.
- An, S. (2008), Interannual variations of the tropical ocean instability wave and ENSO, *J. Climate*, 21(15), 3680–3686, doi:10.1175/2008JCLI1701.1.
- An, S., and F. Jin (2004), Nonlinearity and asymmetry of ENSO, *J. Climate*, 17(12), 2399–2412.
- Ascani, F., E. Firing, P. Dutrieux, J. P. McCreary, and A. Ishida (2010), Deep equatorial ocean circulation induced by a forced-dissipated Yanai beam, *J. Phys. Oceanogr.*, 40(5), 1118–1142, doi:10.1175/2010JPO4356.1.
- Baker, M. A., and Gibson (1987), Sampling turbulence in the stratified ocean: Statistical consequences of strong intermittency, *J. Phys. Oceanogr.*, 17(10), 1817–1836, doi:10.1175/1520-0485(1987)017<1817:STITSO>2.0.CO;2.

- Banholzer, S., and S. Donner (2014), The influence of different El Nino types on global average temperature, *Geophys. Res. Lett.*, 41(6), 2093–2099, doi:10.1002/2014GL059520.
- Benestad, R. E., R. T. Sutton, M. R. Allen, and D. L. T. Anderson (2001), The influence of subseasonal wind variability on tropical instability waves in the Pacific, *Geophys. Res. Lett.*, 28(10), 2041–2044, doi:10.1029/2000GL012563.
- Bergman, J. W., H. H. Hendon, and K. M. Weickmann (2001), Intraseasonal air-sea interactions at the onset of El Nino, *J. Climate*, 14(8), 1702–1719, doi:10.1175/1520-0442(2001)014<1702:IASIAT>2.0.CO;2.
- Bernie, D., S. Woolnough, J. Slingo, and E. Guilyardi (2005), Modeling diurnal and intraseasonal variability of the ocean mixed layer, *J. Climate*, 18(8), 1190–1202.
- Bernie, D., E. Guilyardi, G. Madec, J. Slingo, and S. Woolnough (2007), Impact of resolving the diurnal cycle in an ocean-atmosphere GCM. part 1: a diurnally forced OGCM, *Climate Dynamics*, 29(6), 575–590, doi:10.1007/s00382-007-0249-6.
- Blanke, B., and P. Delecluse (1993), Variability of the tropical Atlantic ocean simulated by a general circulation model with two different mixed-layer physics, *J. Phys. Oceanogr.*, 23(7), 1363–1388, doi:10.1175/1520-0485(1993)023<1363:VOTTAO>2.0.CO;2.
- Brandt, P., and C. Eden (2005), Annual cycle and interannual variability of the mid-depth tropical Atlantic Ocean, *Deep-Sea Res. I*, 52(2), 199–219, doi:10.1016/j.dsr.2004.03.011.
- Cai, W., G. Wang, A. Santoso, M. J. McPhaden, L. Wu, F.-F. Jin, A. Timmermann, M. Collins, G. Vecchi, M. Lengaigne, M. H. England, D. Dommenget, K. Takahashi, and E. Guilyardi (2015), Increased frequency of extreme La Nina events under greenhouse warming, *Nature Clim. Change*, 5(2), 132–137.
- Capet, X., P. Klein, B. L. Hua, G. Lapeyre, and J. C. Mcwilliams (2008), Surface kinetic energy transfer in surface quasi-geostrophic flows, *J. Fluid Mech.*, 604, 165–174.

- Chelton, D. B., M. G. Schlax, and R. M. Samelson (2011), Global observations of nonlinear mesoscale eddies, *Progress in Oceanography*, 91(2), 167 – 216, doi:10.1016/j.pocean.2011.01.002.
- Chen, D., L. M. Rothstein, and A. J. Busalacchi (1994), A hybrid vertical mixing scheme and its application to tropical ocean models, *J. Phys. Oceanogr.*, 24(10), 2156–2179, doi:10.1175/1520-0485(1994)024<2156:AHVMSA>2.0.CO;2.
- Chi, N.-H., R.-C. Lien, E. A. D'Asaro, and B. B. Ma (2014), The surface mixed layer heat budget from mooring observations in the central Indian ocean during Madden-Julian Oscillation events, *J. Geophys. Res.*, 119(7), 4638–4652, doi:10.1002/2014JC010192.
- Contreras, R. F. (2002), Long-term observations of tropical instability waves, *J. Phys. Oceanogr.*, 32(9), 2715–2722.
- Cox, M. D. (1980), Generation and propagation of 30-day waves in a numerical model of the Pacific, *J. Phys. Oceanogr.*, 10(8), 1168–1186, doi:10.1175/1520-0485(1980)010<1168:GAPODW>2.0.CO;2.
- Cravatte, S., J. Picaut, and G. Eldin (2003), Second and first baroclinic Kelvin modes in the equatorial Pacific at intraseasonal timescales, *J. Geophys. Res.*, 108(C8), doi:10.1029/2002JC001511.
- Cronin, M. F., and W. S. Kessler (2009), Near-surface shear flow in the tropical Pacific cold tongue front, *J. Phys. Oceanogr.*, 39(5), 1200–1215.
- Cushman-Roisin, B. (1996), Lower and upper bounds on internal-wave frequencies in stratified rotating fluids, *Phys. Rev. Lett.*, 77, 4903–4905, doi:10.1103/PhysRevLett.77.4903.
- Danabasoglu, G., W. G. Large, J. J. Tribbia, P. R. Gent, B. P. Briegleb, and J. C. McWilliams (2006), Diurnal coupling in the tropical oceans of CCSM3, *J. Climate*, 19(11), 2347–2365.

- De Szoeke, S., S.-P. Xie, T. Miyama, K. Richards, and R. Small (2007), What maintains the SST front north of the eastern Pacific equatorial cold tongue?, *J. Climate*, 20(11), 2500–2514, doi:10.1175/JCLI4173.1.
- Dengler, M., and D. Quadfasel (2002), Equatorial deep jets and abyssal mixing in the Indian Ocean, *J. Phys. Oceanogr.*, 32(4), 1165–1180, doi:10.1175/1520-0485(2002)032<1165:EDJAAM>2.0.CO;2.
- Dewar, W. K., J. C. McWilliams, and M. J. Molemaker (2015), Centrifugal instability and mixing in the California Undercurrent, *J. Phys. Oceanogr.*, 45(5), 1224–1241, doi:10.1175/JPO-D-13-0269.1.
- Dugan, J. P., R. P. Mied, P. C. Mignerey, and A. F. Schuetz (1982), Compact, intrathermocline eddies in the Sargasso Sea, *J. Geophys. Res.*, 87(C1), 385–393, doi:10.1029/JC087iC01p00385.
- Dunkerton, T. J. (1981), On the inertial stability of the equatorial middle atmosphere, *J. Atmos. Sci.*, 38(11), 2354–2364, doi:10.1175/1520-0469(1981)038<2354:OTISFT>2.0.CO;2.
- Dutrieux, P., C. Menkes, J. Vialard, P. Flament, and B. Blanke (2008), Lagrangian study of tropical instability vortices in the Atlantic, *J. Phys. Oceanogr.*, 38(2), 400–417, doi:10.1175/2007JPO3763.1.
- Efron, B., and C. Stein (1981), The jackknife estimate of variance, *The Annals of Statistics*, 9(3), 586–596.
- England, M. H., S. McGregor, P. Spence, G. A. Meehl, A. Timmermann, W. Cai, A. S. Gupta, M. J. McPhaden, A. Purich, and A. Santoso (2014), Recent intensification of wind-driven circulation in the Pacific and the ongoing warming hiatus, *Nature Clim. Change*, 4(3), 222–227.
- Eriksen, C. C., and J. G. Richman (1988), An estimate of equatorial wave energy flux at 9-to 90-day periods in the central Pacific, *J. Geophys. Res.*, 93(C12), 15,455–15,466, doi:10.1029/JC093iC12p15455.

- Evans, W., P. G. Strutton, and F. P. Chavez (2009), Impact of tropical instability waves on nutrient and chlorophyll distributions in the equatorial Pacific, *Deep-Sea Res. I*, 56(2), 178 – 188, doi:10.1016/j.dsr.2008.08.008.
- Farrar, J. T. (2011), Barotropic Rossby waves radiating from tropical instability waves in the Pacific ocean, *J. Phys. Oceanogr.*, 41(6), 1160–1181, doi:10.1175/2011JPO4547.1.
- Fedorov, A. V., and J. N. Brown (2009), *Ocean Currents: A Derivative of the Encyclopedia of Ocean Sciences*, chap. Equatorial Waves, pp. 486–505, Elsevier.
- Ferrari, R. (2014), Oceanography: What goes down must come up, *Nature*, 513(7517), 179–180, doi:10.1038/513179a.
- Firing, E., S. E. Wijffels, and P. Hacker (1998), Equatorial subthermocline currents across the Pacific, *J. Geophys. Res.*, 103(C10), 21,413–21,423, doi:10.1029/98JC01944.
- Fischer, J., and M. Visbeck (1993), Deep velocity profiling with self-contained ADCPs, *J. Atmos. Oceanic Tech.*, 10(5), 764–773, doi:10.1175/1520-0426(1993)010<0764:DVPWSC>2.0.CO;2.
- Flament, P., S. Kennan, R. Knox, P. Niiler, and R. Bernstein (1996), The three-dimensional structure of an upper ocean vortex in the tropical Pacific ocean, *Nature*, 383(6601), 610–613, doi:10.1038/383610a0.
- Foltz, G., J. Carton, and E. Chassignet (2004), Tropical instability vortices in the Atlantic ocean, *J. Geophys. Res.*, 109, C03,029.
- Garabato, A. C. N., K. L. Polzin, B. A. King, K. J. Heywood, and M. Visbeck (2004), Widespread intense turbulent mixing in the Southern Ocean, *Science*, 303(5655), 210–213, doi:10.1126/science.1090929.
- Garrett, C., and E. Kunze (2007), Internal tide generation in the deep ocean, *Annu. Rev. Fluid Mech.*, 39, 57–87, doi:10.1146/annurev.fluid.39.050905.110227.

- Gerkema, T., and V. Shrira (2005), Near-inertial waves on the nontraditional β plane, *J. Geophys. Res.*, 110(C1), doi:10.1029/2004JC002519.
- Gerkema, T., J. Zimmerman, L. Maas, and H. Haren (2008), Geophysical and astrophysical fluid dynamics beyond the traditional approximation, *Rev. Geophys.*, 46(2), doi:10.1029/2006RG000220.
- Giese, B. S., and D. E. Harrison (1990), Aspects of the Kelvin wave response to episodic wind forcing, *J. Geophys. Res.*, 95(C5), 7289–7312, doi:10.1029/JC095iC05p07289.
- Giese, B. S., and D. E. Harrison (1991), Eastern equatorial Pacific response to three composite westerly wind types, *J. Geophys. Res.*, 96(S01), 3239–3248, doi:10.1029/90JC01861.
- Gill, A. (1982), *Atmosphere-Ocean Dynamics, International Geophysics Series*, vol. 30, Academic Press, Inc.
- Gill, A., and B. King (1985), *The Effect of a Shoaling Thermocline on Equatorially-trapped Kelvin Waves*, Dynamical climatology technical note, Met O 20 (Dynamical Climatology Branch), Meteorological Office.
- Gordon, C., C. Cooper, C. A. Senior, H. Banks, J. M. Gregory, T. C. Johns, J. F. Mitchell, and R. A. Wood (2000), The simulation of SST, sea ice extents and ocean heat transports in a version of the Hadley Centre coupled model without flux adjustments, *Climate Dynamics*, 16(2-3), 147–168.
- Graham, T. (2014), The importance of eddy permitting model resolution for simulation of the heat budget of tropical instability waves, *Ocean Model.*, 79(0), 21 – 32, doi:10.1016/j.ocemod.2014.04.005.
- Gregg, M., H. Peters, J. Wesson, N. Oakey, and T. Shay (1985), Intensive measurements of turbulence and shear in the equatorial undercurrent, *Nature*, 318(6042), 140–144, doi:10.1038/318140a0.

- Gregg, M. C. (1989), Scaling turbulent dissipation in the thermocline, *J. Geophys. Res.*, 94(C7), 9686–9698, doi:10.1029/JC094iC07p09686.
- Gregg, M. C., T. B. Sanford, and D. P. Winkel (2003), Reduced mixing from the breaking of internal waves in equatorial waters, *Nature*, 422(6931), 513–515.
- Griffiths, S. D. (2003), The nonlinear evolution of zonally symmetric equatorial inertial instability, *J. Fluid Mech.*, 474, 245–273, doi:10.1017/S0022112002002586.
- Grodsky, S. A., J. A. Carton, C. Provost, J. Servain, J. A. Lorenzzetti, and M. J. McPhaden (2005), Tropical instability waves at 0N, 23W in the Atlantic: A case study using Pilot Research Moored Array in the Tropical Atlantic (PIRATA) mooring data, *J. Geophys. Res.*, 110(C8), C08,010, doi:10.1029/2005JC002941.
- Guiavarc'h, C., A. M. Treguier, and A. Vangriesheim (2008), Remotely forced bi-weekly deep oscillations on the continental slope of the Gulf of Guinea, *J. Geophys. Res.*, 113(C6), doi:10.1029/2007JC004471.
- Hansen, D. V., and C. A. Paul (1984), Genesis and effects of long waves in the equatorial Pacific, *J. Geophys. Res.*, 89(C6), 10,431–10,440.
- Harrison, D. E., and B. S. Giese (1988), Remote westerly wind forcing of the eastern equatorial Pacific; some model results, *Geophys. Res. Lett.*, 15(8), 804–807, doi:10.1029/GL015i008p00804.
- Harvey, R., and W. C. Patzert (1976), Deep current measurements suggest long waves in the Eastern Equatorial Pacific, *Science*, 193(4256), 883–885, doi:10.1126/science.193.4256.883.
- Hendon, H. H., B. Liebmann, and J. D. Glick (1998), Oceanic Kelvin waves and the Madden-Julian Oscillation, *J. Atmos. Sci.*, 55(1), 88–101, doi:10.1175/1520-0469(1998)055<0088:OKWATM>2.0.CO;2.
- Holmes, R. M., and L. N. Thomas (2015), The modulation of equatorial turbulence by tropical instability waves in a regional ocean model, *J. Phys. Oceanogr.*, 45(4), 1155–1173, doi:10.1175/JPO-D-14-0209.1.

- Holmes, R. M., L. N. Thomas, L. Thompson, and D. Darr (2014), Potential vorticity dynamics of tropical instability vortices, *J. Phys. Oceanogr.*, *44*(3), 995–1011, doi: 10.1175/JPO-D-13-0157.1.
- Holmes, R. M., J. N. Moum, and L. N. Thomas (2016), Evidence for seafloor-intensified mixing by surface-generated equatorial waves, *Geophysical Research Letters*, *43*(3), 1202–1210, doi:10.1002/2015GL066472.
- Holzer, M., and E. D. Siggia (1994), Turbulent mixing of a passive scalar, *Physics of Fluids*, *6*(5), 1820–1837, doi:10.1063/1.868243.
- Horigan, A. M., and R. H. Weisberg (1981), A systematic search for trapped equatorial waves in the GATE velocity data, *J. Phys. Oceanogr.*, *11*(4), 497–509, doi: 10.1175/1520-0485(1981)011<0497:ASSFTE>2.0.CO;2.
- Hoskins, B. (1982), The mathematical theory of frontogenesis., *Annu. Rev. Fluid Mech.*, *14*, 131–151.
- Hoskins, B., and F. Bretherton (1972), Atmospheric frontogenesis models: Mathematical formulation and solution, *J. Atmos. Sci.*, *29*(1), 11–37.
- Hua, B., D. Moore, and S. Le Gentil (1997), Inertial nonlinear equilibration of equatorial flows, *J. Fluid Mech.*, *331*, 345–371.
- Huang, C. J., F. Qiao, and D. Dai (2014), Evaluating CMIP5 simulations of mixed layer depth during summer, *J. Geophys. Res.*, *119*(4), 2568–2582, doi:10.1002/2013JC009535.
- Imada, Y., and M. Kimoto (2012), Parameterization of tropical instability waves and examination of their impact on ENSO characteristics, *J. Climate*, *25*(13), 4568–4581.
- Inoue, R., R. Lien, and J. Moum (2012), Modulation of equatorial turbulence by a tropical instability wave, *J. Geophys. Res.*, *117*(C10), C10,009.

- Ito, T., and J. Marshall (2008), Control of lower-limb overturning circulation in the Southern Ocean by diapycnal mixing and mesoscale eddy transfer, *J. Phys. Oceanogr.*, 38(12), 2832–2845, doi:10.1175/2008JPO3878.1.
- Ivey, G., K. Winters, and J. Koseff (2008), Density stratification, turbulence, but how much mixing?, *Annu. Rev. Fluid Mech.*, 40(1), 169–184, doi:10.1146/annurev.fluid.39.050905.110314.
- Jiang, C. L., L. A. Thompson, K. A. Kelly, and M. F. Cronin (2009), The roles of intraseasonal Kelvin waves and tropical instability waves in SST variability along the equatorial pacific in an isopycnal ocean model, *J. Climate*, 22(12), 3470–3487, doi:10.1175/2009JCLI2767.1.
- Jin, F.-F. (1997), An equatorial ocean recharge paradigm for ENSO. Part I: conceptual model, *J. Atmos. Sci.*, 54(7), 811–829.
- Jing, Z., L. Wu, D. Wu, and B. Qiu (2014), Enhanced 2-hr-8-day oscillations associated with tropical instability waves, *J. Phys. Oceanogr.*, 44(7), 1908–1918, doi:10.1175/JPO-D-13-0189.1.
- Jochum, M., and P. Malanotte-Rizzoli (2004), A new theory for the generation of the equatorial subsurface countercurrents, *J. Phys. Oceanogr.*, 34(4), 755–771.
- Jochum, M., and R. Murtugudde (2006), Temperature advection by tropical instability waves, *J. Phys. Oceanogr.*, 36(4), 592–605, doi:10.1175/JPO2870.1.
- Jochum, M., M. Cronin, W. Kessler, and D. Shea (2007), Observed horizontal temperature advection by tropical instability waves, *Geophys. Res. Lett.*, 34(9), doi:10.1029/2007GL029416.
- Johnson, E. (1996), A convergent instability wave front in the central tropical Pacific, *Deep-Sea Res. II*, 43(4-6), 753–778, doi:10.1016/0967-0645(96)00034-3.
- Johnson, E. S., and D. S. Luther (1994), Mean zonal momentum balance in the upper and central equatorial Pacific ocean, *J. Geophys. Res.*, 99(C4), 7689–7705, doi:10.1029/94JC00033.

- Johnson, E. S., and M. J. McPhaden (1993a), Effects of a three-dimensional mean flow on intraseasonal Kelvin waves in the equatorial Pacific ocean, *J. Geophys. Res.*, 98(C6), 10,185–10,194, doi:10.1029/93JC00759.
- Johnson, E. S., and M. J. McPhaden (1993b), Structure of intraseasonal Kelvin waves in the equatorial Pacific ocean, *J. Phys. Oceanogr.*, 23(4), 608–625, doi:10.1175/1520-0485(1993)023<0608:SOIKWI>2.0.CO;2.
- Johnson, E. S., and J. A. Proehl (2004), Tropical instability wave variability in the Pacific and its relation to large-scale currents, *J. Phys. Oceanogr.*, 34(10), 2121–2147.
- Johnson, G. C., M. J. McPhaden, and E. Firing (2001), Equatorial pacific ocean horizontal velocity, divergence, and upwelling*, *J. Phys. Oceanogr.*, 31(3), 839–849, doi:10.1175/1520-0485(2001)031<0839:EPOHVD>2.0.CO;2.
- Kang, D., and E. N. Curchitser (2013), Gulf stream eddy characteristics in a high-resolution ocean model, *Journal of Geophysical Research: Oceans*, 118(9), 4474–4487.
- Kawai, Y., and A. Wada (2007), Diurnal sea surface temperature variation and its impact on the atmosphere and ocean: A review, *Journal of Oceanography*, 63(5), 721–744, doi:10.1007/s10872-007-0063-0.
- Kennan, S., and P. Flament (2000), Observations of a tropical instability vortex, *J. Phys. Oceanogr.*, 30(9), 2277–2301.
- Kessler, W. S., and J. P. McCreary (1993), The annual wind-driven rossby wave in the subthermocline equatorial pacific, *J. Phys. Oceanogr.*, 23(6), 1192–1207, doi:10.1175/1520-0485(1993)023<1192:TAWDRW>2.0.CO;2.
- Kessler, W. S., M. J. McPhaden, and K. M. Weickmann (1995), Forcing of intraseasonal Kelvin waves in the equatorial Pacific, *J. Geophys. Res.*, 100(C6), 10,613–10,631, doi:10.1029/95JC00382.

- Kessler, W. S., G. C. Johnson, and D. W. Moore (2003), Sverdrup and nonlinear dynamics of the Pacific equatorial currents, *J. Phys. Oceanogr.*, 33(5), 994–1008.
- Kleeman, R., J. P. McCreary, and B. A. Klinger (1999), A mechanism for generating ENSO decadal variability, *Geophys. Res. Lett.*, 26(12), 1743–1746, doi:10.1029/1999GL900352.
- Kosaka, Y., and S.-P. Xie (2013), Recent global-warming hiatus tied to equatorial Pacific surface cooling, *Nature*, 501(7467), 403–407.
- Kostianoy, A., and I. Belkin (1989), A survey of observations on entrathermocline eddies in the world ocean, in *Mesoscale/Synoptic Coherent structures in Geophysical Turbulence*, Elsevier Oceanography Series, vol. 50, edited by J. Nihoul and B. Jamart, pp. 821 – 841, Elsevier, doi:10.1016/S0422-9894(08)70223-X.
- Kunze, E., E. Firing, J. M. Hummon, T. K. Chereskin, and A. M. Thurnherr (2006), Global abyssal mixing inferred from lowered ADCP shear and CTD strain profiles, *J. Phys. Oceanogr.*, 36(8), 1553–1576, doi:10.1175/JPO2926.1.
- Landschtzer, P., N. Gruber, F. A. Haumann, C. Rdenbeck, D. C. E. Bakker, S. van Heuven, M. Hoppema, N. Metzl, C. Sweeney, T. Takahashi, B. Tilbrook, and R. Wanninkhof (2015), The reinvigoration of the Southern Ocean carbon sink, *Science*, 349(6253), 1221–1224, doi:10.1126/science.aab2620.
- Large, W., and S. Yeager (2004), *Diurnal to decadal global forcing for ocean and sea-ice models: the data sets and flux climatologies*, National Center for Atmospheric Research.
- Large, W. G., and P. R. Gent (1999), Validation of vertical mixing in an equatorial ocean model using large eddy simulations and observations, *J. Phys. Oceanogr.*, 29(3), 449–464.
- Large, W. G., J. C. McWilliams, and S. C. Doney (1994), Oceanic vertical mixing: A review and a model with a nonlocal boundary layer parameterization, *Rev. Geophys.*, 32(4), 363–403, doi:10.1029/94RG01872.

- Lawrence, S., and J. Angell (2000), Evidence for Rossby wave control of tropical instability waves in the Pacific ocean, *Geophys. Res. Lett.*, 27(15), 2257–2260, doi: 10.1029/1999GL002363.
- Lawrence, S. P., M. R. Allen, D. L. T. Anderson, and D. T. Llewellyn-Jones (1998), Effects of subsurface ocean dynamics on instability waves in the tropical Pacific, *J. Geophys. Res.*, 103(C9), 18,649–18,663, doi:10.1029/98JC01684.
- Ledwell, J. R., E. T. Montgomery, K. L. Polzin, L. C. St. Laurent, R. W. Schmitt, and J. M. Toole (2000), Evidence for enhanced mixing over rough topography in the abyssal ocean, *Nature*, 403(6766), 179–182, doi:10.1038/35003164.
- Legeckis, R. (1977), Long waves in the eastern equatorial Pacific ocean: A view from a geostationary satellite, *Science*, 197(4309), 1179–1181.
- Lengaigne, M., J.-P. Boulanger, C. Menkes, P. Delecluse, and J. Slingo (2013), *Westerly Wind Events in the Tropical Pacific and their Influence on the Coupled Ocean-Atmosphere System: A Review*, pp. 49–69, American Geophysical Union, doi:10.1029/147GM03.
- Li, X., Y. Chao, J. C. McWilliams, and L.-L. Fu (2001), A comparison of two vertical-mixing schemes in a Pacific ocean general circulation model, *J. Climate*, 14(7), 1377–1398, doi:10.1175/1520-0442(2001)014<1377:ACOTVM>2.0.CO;2.
- Lien, R.-C., D. R. Caldwell, M. C. Gregg, and J. N. Moum (1995), Turbulence variability at the equator in the central Pacific at the beginning of the 1991-1993 El Niño, *J. Geophys. Res.*, 100(C4), 6881–6898, doi:10.1029/94JC03312.
- Lien, R.-C., E. A. D'Asaro, and C. E. Menkes (2008), Modulation of equatorial turbulence by tropical instability waves, *Geophys. Res. Lett.*, 35, L24,607, doi: 10.1029/2008GL035860.
- Lumpkin, R., and K. Speer (2007), Global ocean meridional overturning, *J. Phys. Oceanogr.*, 37(10), 2550–2562, doi:10.1175/JPO3130.1.

- Luther, D. S., and E. S. Johnson (1990), Eddy energetics in the upper equatorial Pacific during the Hawaii-to-Tahiti shuttle experiment, *J. Phys. Oceanogr.*, *20*(7), 913–944, doi:10.1175/1520-0485(1990)020<0913:EEITUE>2.0.CO;2.
- Lyman, J. b., G. Johnson, and W. Kessler (2007), Distinct 17- and 33-day tropical instability waves in subsurface observations, *J. Phys. Oceanogr.*, *37*(4), 855–872, doi:10.1175/JPO3023.1.
- Lyman, J. M., D. B. Chelton, R. A. deSzoeke, and R. M. Samelson (2005), Tropical instability waves as a resonance between equatorial Rossby waves, *J. Phys. Oceanogr.*, *35*(2), 232–254.
- Ma, C.-C., C. R. Mechoso, A. Arakawa, and J. D. Farrara (1994), Sensitivity of a coupled oceanatmosphere model to physical parameterizations, *J. Climate*, *7*(12), 1883–1896, doi:10.1175/1520-0442(1994)007<1883:SOACOM>2.0.CO;2.
- Maas, L. R. M., and U. Harlander (2007), Equatorial wave attractors and inertial oscillations, *J. Fluid Mech.*, *570*, 47–67, doi:10.1017/S0022112006002904.
- MacDonald, D. G., and F. Chen (2012), Enhancement of turbulence through lateral spreading in a stratified-shear flow: Development and assessment of a conceptual model, *J. Geophys. Res.*, *117*(C5), doi:10.1029/2011JC007484.
- Malard, J.-P., C. Perigaud, P. De Mey, and J.-F. Minster (1987), Observation of long equatorial waves in the pacific ocean by seasat altimetry, *J. Phys. Oceanogr.*, *17*(12), 2273–2279, doi:10.1175/1520-0485(1987)017<2273:OOLEWI>2.0.CO;2.
- Mantua, N., and S. Hare (2002), The Pacific decadal oscillation, *Journal of Oceanography*, *58*(1), 35–44, doi:10.1023/A:1015820616384.
- Marchesiello, P., X. Capet, C. Menkes, and S. Kennan (2011), Submesoscale dynamics in tropical instability waves, *Ocean Model.*, *39*(1-2), 31–46, doi:10.1016/j.ocemod.2011.04.011.
- Marinov, I., A. Gnanadesikan, J. L. Sarmiento, J. R. Toggweiler, M. Follows, and B. K. Mignone (2008), Impact of oceanic circulation on biological carbon storage

- in the ocean and atmospheric pCO₂, *Global Biogeochemical Cycles*, 22(3), GB3007, doi:10.1029/2007GB002958.
- Marshall, J., and K. Speer (2012), Closure of the meridional overturning circulation through Southern Ocean upwelling, *Nature Geosci.*, 5(3), 171–180, doi:10.1038/ngeo1391.
- Masina, S., S. Philander, and A. Bush (1999), An analysis of tropical instability waves in a numerical model of the Pacific ocean 2. Generation and energetics of the waves, *J. Geophys. Res.*, 104(29), 637–29, doi:10.1029/1999JC900226.
- McCreary, J. P., K. E. Kohler, R. R. Hood, S. Smith, J. Kindle, A. S. Fischer, and R. A. Weller (2001), Influences of diurnal and intraseasonal forcing on mixed-layer and biological variability in the central Arabian Sea, *Journal of Geophysical Research: Oceans*, 106(C4), 7139–7155, doi:10.1029/2000JC900156.
- McCreary, J. P., Jr. (1984), Equatorial beams, *Journal of Marine Research*, 42(2), 395–430, doi:doi:10.1357/002224084788502792.
- McHugh (2013), Tropical instability wave fronts: interpretation as a gravity current, Ph.D. thesis, Oregon State University.
- McManus, J. F., R. Francois, J.-M. Gherardi, L. D. Keigwin, and S. Brown-Leger (2004), Collapse and rapid resumption of Atlantic meridional circulation linked to deglacial climate changes, *Nature*, 428(6985), 834–837.
- McPhaden, M. J. (2002), Mixed layer temperature balance on intraseasonal timescales in the equatorial Pacific ocean, *J. Climate*, 15(18), 2632–2647, doi:10.1175/1520-0442(2002)015<2632:MLTBOI>2.0.CO;2.
- McPhaden, M. J. (2015), Playing hide and seek with El Nino, *Nature Clim. Change*, 5(9), 791–795.
- McPhaden, M. J., and B. A. Taft (1988), Dynamics of seasonal and intraseasonal variability in the eastern equatorial Pacific, *J. Phys. Oceanogr.*, 18(11), 1713–1732, doi:10.1175/1520-0485(1988)018<1713:DOSAIV>2.0.CO;2.

- McPhaden, M. J., J. A. Proehl, and L. M. Rothstein (1986), The interaction of equatorial Kelvin waves with realistically sheared zonal currents, *J. Phys. Oceanogr.*, 16(9), 1499–1515, doi:10.1175/1520-0485(1986)016<1499:TIOEKW>2.0.CO;2.
- McPhaden, M. J., A. J. Busalacchi, R. Cheney, J.-R. Donguy, K. S. Gage, D. Halpern, M. Ji, P. Julian, G. Meyers, G. T. Mitchum, P. P. Niiler, J. Picaut, R. W. Reynolds, N. Smith, and K. Takeuchi (1998), The tropical ocean-global atmosphere observing system: A decade of progress, *Journal of Geophysical Research: Oceans*, 103(C7), 14,169–14,240, doi:10.1029/97JC02906.
- McPhaden, M. J., S. E. Zebiak, and M. H. Glantz (2006), ENSO as an integrating concept in earth science, *Science*, 314(5806), 1740–1745, doi:10.1126/science.1132588.
- McWilliams, J., E. Huckle, and A. Shchepetkin (2009), Buoyancy effects in a stratified Ekman layer, *J. Phys. Oceanogr.*, 39(10), 2581–2599.
- McWilliams, J. C. (1985), Submesoscale, coherent vortices in the ocean, *Rev. Geophys.*, 23(2), 165–182.
- Menkes, C., J. Vialard, S. Kennan, J. Boulanger, and G. Madec (2006), A modeling study of the impact of tropical instability waves on the heat budget of the eastern equatorial Pacific, *J. Phys. Oceanogr.*, 36(5), 847–865, doi:10.1175/JPO2904.1.
- Menkes, C. E., S. C. Kennan, P. Flament, Y. Dandonneau, S. Masson, B. Biessy, E. Marchal, G. Eldin, J. Grelet, Y. Montel, A. Morlire, A. Lebourges-Dhaussy, C. Moulin, G. Champalbert, and A. Herblant (2002), A whirling ecosystem in the equatorial Atlantic, *Geophys. Res. Lett.*, 29(11), 1553–.
- Menkes, C. E., M. Lengaigne, J. Vialard, M. Puy, P. Marchesiello, S. Cravatte, and G. Cambon (2014), About the role of westerly wind events in the possible development of an El Niño in 2014, *Geophys. Res. Lett.*, doi:10.1002/2014GL061186.
- Molemaker, M., J. McWilliams, and I. Yavneh (2005), Baroclinic instability and loss of balance, *J. Phys. Oceanogr.*, 35(9), 1505–1517, doi:10.1175/JPO2770.1.

- Moore, A. M., and R. Kleeman (1999), Stochastic forcing of ENSO by the in-traseasonal oscillation, *J. Climate*, 12(5), 1199–1220, doi:10.1175/1520-0442(1999)012<1199:SFOEBT>2.0.CO;2.
- Moum, J., D. Caldwell, J. Nash, and G. Gunderson (2002), Observations of boundary mixing over the continental slope, *J. Phys. Oceanogr.*, 32(7), 2113–2130, doi:10.1175/1520-0485(2002)032<2113:OOBMOT>2.0.CO;2.
- Moum, J., R.-C. Lien, A. Perlin, J. Nash, M. Gregg, and P. Wiles (2009), Sea surface cooling at the equator by subsurface mixing in tropical instability waves, *Nature Geosci.*, 2(11), 761–765, doi:10.1038/ngeo657.
- Moum, J. N., and J. D. Nash (2009), Mixing measurements on an equatorial ocean mooring, *J. Atmos. Oceanic Tech.*, 26(2), 317–336, doi:10.1175/2008JTECHO617.1.
- Moum, J. N., A. Perlin, J. D. Nash, and M. J. McPhaden (2013), Seasonal sea surface cooling in the equatorial Pacific cold tongue controlled by ocean mixing, *Nature*, 500, 64–67.
- Munk, W., and C. Wunsch (1998), Abyssal recipes II: energetics of tidal and wind mixing, *Deep-Sea Res. I*, 45(12), 1977 – 2010, doi:10.1016/S0967-0637(98)00070-3.
- Munk, W. H. (1966), Abyssal recipes, *Deep Sea Research and Oceanographic Abstracts*, 13(4), 707 – 730, doi:[http://dx.doi.org/10.1016/0011-7471\(66\)90602-4](http://dx.doi.org/10.1016/0011-7471(66)90602-4).
- Nikurashin, M., and R. Ferrari (2010), Radiation and dissipation of internal waves generated by geostrophic motions impinging on small-scale topography: Application to the Southern Ocean, *J. Phys. Oceanogr.*, 40(9), 2025–2042, doi:10.1175/2010JPO4315.1.
- Nikurashin, M., and R. Ferrari (2011), Global energy conversion rate from geostrophic flows into internal lee waves in the deep ocean, *Geophysical Research Letters*, 38(8), doi:10.1029/2011GL046576, l08610.

- Nikurashin, M., and R. Ferrari (2013), Overturning circulation driven by breaking internal waves in the deep ocean, *Geophys. Res. Lett.*, *40*(12), 3133–3137, doi: 10.1002/grl.50542.
- Nikurashin, M., and G. Vallis (2012), A theory of the interhemispheric meridional overturning circulation and associated stratification, *J. Phys. Oceanogr.*, *42*(10), 1652–1667, doi:10.1175/JPO-D-11-0189.1.
- Nikurashin, M., G. K. Vallis, and A. Adcroft (2013), Routes to energy dissipation for geostrophic flows in the Southern Ocean, *Nature Geosci.*, *6*(1), 48–51.
- NOAA/NESDIS (2003), Goes level 3 6km near real time sst 24 hour. ver. 1. po.daac, ca, usa, doi:<http://dx.doi.org/10.5067/GOES3-24HOR>, dataset accessed 2014-12-15.
- Oakey, N. S. (1982), Determination of the rate of dissipation of turbulent energy from simultaneous temperature and velocity shear microstructure measurements, *J. Phys. Oceanogr.*, *12*(3), 256–271, doi:10.1175/1520-0485(1982)012<0256:DOTROD>2.0.CO;2.
- Osborn, T. R. (1980), Estimates of the local rate of vertical diffusion from dissipation measurements, *J. Phys. Oceanogr.*, *10*(1), 83–89, doi:10.1175/1520-0485(1980)010<0083:EOTLRO>2.0.CO;2.
- Osborn, T. R., and C. S. Cox (1972), Oceanic fine structure, *Geophysical Fluid Dynamics*, *3*(1), 321–345, doi:10.1080/03091927208236085.
- Pacanowski, R. C., and S. G. H. Philander (1981), Parameterization of vertical mixing in numerical models of tropical oceans, *J. Phys. Oceanogr.*, *11*(11), 1443–1451.
- Perez, R. C., and W. S. Kessler (2009), Three-dimensional structure of tropical cells in the central equatorial Pacific ocean, *J. Phys. Oceanogr.*, *39*(1), 27–49.
- Perez, R. C., M. F. Cronin, and W. S. Kessler (2010), Tropical cells and a secondary circulation near the northern front of the equatorial Pacific cold tongue, *J. Phys. Oceanogr.*, *40*(9), 2091–2106.

- Peters, H., M. C. Gregg, and J. M. Toole (1988), On the parameterization of equatorial turbulence, *J. Geophys. Res.*, 93(C2), 1199–1218, doi:10.1029/JC093iC02p01199.
- Pezzi, L. P., and K. J. Richards (2003), Effects of lateral mixing on the mean state and eddy activity of an equatorial ocean, *J. Geophys. Res.*, 108(C12), doi:10.1029/2003JC001834.
- Philander, S. (1976), Instabilities of zonal equatorial currents, *J. Geophys. Res.*, 81(21), 3725–3735.
- Philander, S. G. H. (1978), Instabilities of zonal equatorial currents, 2, *J. Geophys. Res.*, 83(C7), 3679–3682.
- Picaut, J., F. Masia, and Y. du Penhoat (1997), An advective-reflective conceptual model for the oscillatory nature of the ENSO, *Science*, 277(5326), 663–666, doi: 10.1126/science.277.5326.663.
- Ponte, R. M. (1988), Equatorial Kelvin waves embedded in mean flow, with application to the deep jets, *Journal of Geophysical Research: Oceans (1978–2012)*, 93(C11), 13,941–13,946.
- Price, J. F., R. A. Weller, and R. Pinkel (1986), Diurnal cycling: Observations and models of the upper ocean response to diurnal heating, cooling, and wind mixing, *J. Geophys. Res.*, 91(C7), 8411–8427, doi:10.1029/JC091iC07p08411.
- Proehl, J. A. (1996), Linear stability of equatorial zonal flows, *J. Phys. Oceanogr.*, 26(4), 601–621.
- Qiao, L., and R. H. Weisberg (1995), Tropical instability wave kinematics: Observations from the tropical instability wave experiment, *J. Geophys. Res.*, 100(C5), 8677–8693, doi:10.1029/95JC00305.
- Qiao, L., and R. H. Weisberg (1997), The zonal momentum balance of the equatorial undercurrent in the central Pacific, *J. Phys. Oceanogr.*, 27(6), 1094–1119, doi: 10.1175/1520-0485(1997)027<1094:TZMBOT>2.0.CO;2.

- Qiao, L., and R. H. Weisberg (1998), Tropical instability wave energetics: Observations from the tropical instability wave experiment, *J. Phys. Oceanogr.*, *28*(2), 345–360, doi:10.1175/1520-0485(1998)028<0345:TIWEOF>2.0.CO;2.
- Rahmstorf, S. (2007), A semi-empirical approach to projecting future sea-level rise, *Science*, *315*(5810), 368–370, doi:10.1126/science.1135456.
- Richards, K. J., and N. R. Edwards (2003), Lateral mixing in the equatorial Pacific: The importance of inertial instability, *Geophys. Res. Lett.*, *30*(17), doi:10.1029/2003GL017768, 1888.
- Riebesell, U., A. Krtzinger, and A. Oschlies (2009), Sensitivities of marine carbon fluxes to ocean change, *Proceedings of the National Academy of Sciences*, *106*(49), 20,602–20,609, doi:10.1073/pnas.0813291106.
- Roundy, P. E., and G. N. Kiladis (2006), Observed relationships between oceanic Kelvin waves and atmospheric forcing, *J. Climate*, *19*(20), 5253–5272, doi:10.1175/JCLI3893.1.
- Sabine, C. L., R. A. Feely, N. Gruber, R. M. Key, K. Lee, J. L. Bullister, R. Wanninkhof, C. S. Wong, D. W. R. Wallace, B. Tilbrook, F. J. Millero, T.-H. Peng, A. Kozyr, T. Ono, and A. F. Rios (2004), The oceanic sink for anthropogenic CO₂, *Science*, *305*(5682), 367–371, doi:10.1126/science.1097403.
- Sengupta, D., R. Senan, V. Murty, and V. Fernando (2004), A biweekly mode in the equatorial Indian Ocean, *J. Geophys. Res.*, *109*(C10), doi:10.1029/2004JC002329.
- Seo, H., M. Jochum, R. Murtugudde, A. J. Miller, and J. O. Roads (2007), Feedback of tropical instability-wave-induced atmospheric variability onto the ocean, *J. Climate*, *20*(23), 5842–5855, doi:10.1175/JCLI4330.1.
- Shchepetkin, A., and J. McWilliams (2005), The Regional Oceanic Modeling System (ROMS): A split-explicit, free-surface, topography-following-coordinate oceanic model, *Ocean Model.*, *9*(4), 347–404, doi:10.1016/j.ocemod.2004.08.002.

- Shcherbina, A. Y., E. A. D'Asaro, C. M. Lee, J. M. Klymak, M. J. Molemaker, and J. C. McWilliams (2013), Statistics of vertical vorticity, divergence, and strain in a developed submesoscale turbulence field, *Geophys. Res. Lett.*, doi:10.1002/grl.50919.
- Sheen, K. L., A. C. Naveira Garabato, J. A. Brearley, M. P. Meredith, K. L. Polzin, D. A. Smeed, A. Forryan, B. A. King, J.-B. Sallee, L. St. Laurent, A. M. Thurnherr, J. M. Toole, S. N. Waterman, and A. J. Watson (2014), Eddy-induced variability in Southern Ocean abyssal mixing on climatic timescales, *Nature Geosci.*, 7(8), 577–582, doi:10.1038/ngeo2200.
- Shinoda, T., P. E. Roundy, and G. N. Kiladis (2008), Variability of intraseasonal Kelvin waves in the equatorial Pacific ocean, *J. Phys. Oceanogr.*, 38(5), 921–944, doi:10.1175/2007JPO3815.1.
- Shrira, V. I., and W. A. Townsend (2010), Inertia-gravity waves beyond the inertial latitude. Part 1. Inviscid singular focusing, *Journal of Fluid Mechanics*, 664, 478–509, doi:10.1017/S0022112010003812.
- Shrira, V. I., and W. A. Townsend (2013), Near-inertial waves and deep ocean mixing, *Physica Scripta*, 2013(T155), 014,036, doi:10.1088/0031-8949/2013/t155/014036.
- Skyllingstad, E. D., and R. M. Samelson (2012), Baroclinic frontal instabilities and turbulent mixing in the surface boundary layer. Part I: Unforced simulations, *J. Phys. Oceanogr.*, 42(10), 1701–1716, doi:10.1175/JPO-D-10-05016.1.
- Small, R. J., K. J. Richards, S.-P. Xie, P. Dutrieux, and T. Miyama (2009), Damping of tropical instability waves caused by the action of surface currents on stress, *J. Geophys. Res.*, 114(C4), doi:10.1029/2008JC005147.
- Smith, W. H., and D. T. Sandwell (1997), Global sea floor topography from satellite altimetry and ship depth soundings, *Science*, 277(5334), 1956–1962, doi:10.1126/science.277.5334.1956.

- Smyth, W. D., and J. N. Moum (2013), Marginal instability and deep cycle turbulence in the eastern equatorial Pacific ocean, *Geophys. Res. Lett.*, doi:10.1002/2013GL058403.
- Smyth, W. D., T. S. Durland, and J. N. Moum (2015), Energy and heat fluxes due to vertically propagating Yanai waves observed in the equatorial Indian Ocean, *J. Geophys. Res.*, 120(1), 1–15, doi:10.1002/2014JC010152.
- Spall, M. (1995), Frontogenesis, subduction, and cross-front exchange at upper ocean fronts, *J. Geophys. Res.*, 100(C2), 2543–2557.
- Sriver, R. L., M. Huber, and L. Chafik (2013), Excitation of equatorial Kelvin and Yanai waves by tropical cyclones in an ocean general circulation model, *Earth System Dynamics*, 4(1), 1–10, doi:10.5194/esd-4-1-2013.
- Srokosz, M., M. Baringer, H. Bryden, S. Cunningham, T. Delworth, S. Lozier, J. Marotzke, and R. Sutton (2012), Past, present, and future changes in the Atlantic meridional overturning circulation, *Bull. Amer. Meteor. Soc.*, 93(11), 1663–1676, doi:10.1175/BAMS-D-11-00151.1.
- St. Laurent, L., and C. Garrett (2002), The role of internal tides in mixing the deep ocean, *J. Phys. Oceanogr.*, 32(10), 2882–2899, doi:10.1175/1520-0485(2002)032<2882:TROITI>2.0.CO;2.
- St. Laurent, L. C., H. L. Simmons, and S. R. Jayne (2002), Estimating tidally driven mixing in the deep ocean, *Geophys. Res. Lett.*, 29(23), 21–1–21–4, doi:10.1029/2002GL015633, 2106.
- Stewart, A., and P. Dellar (2011), The rôle of the complete Coriolis force in cross-equatorial flow of abyssal ocean currents, *Ocean Model.*, 38(3), 187–202.
- Suarez, M. J., and P. S. Schopf (1988), A delayed action oscillator for ENSO, *J. Atmos. Sci.*, 45(21), 3283–3287, doi:10.1175/1520-0469(1988)045<3283:ADAOFE>2.0.CO;2.

- Sun, H., and E. Kunze (1999), Internal wave-wave interactions. Part II: Spectral energy transfer and turbulence production, *J. Phys. Oceanogr.*, 29(11), 2905–2919, doi:10.1175/1520-0485(1999)029<2905:IWWIPI>2.0.CO;2.
- Tanaka, Y., T. Hibiya, and H. Sasaki (2015), Downward lee wave radiation from tropical instability waves in the central equatorial Pacific ocean: A possible energy pathway to turbulent mixing, *J. Geophys. Res.*, 120(11), 7137–7149, doi:10.1002/2015JC011017.
- Thomas, L. (2005), Destruction of potential vorticity by winds, *J. Phys. Oceanogr.*, 35(12), 2457–2466, doi:10.1175/JPO2830.1.
- Thomas, L. (2008), Formation of intrathermocline eddies at ocean fronts by wind-driven destruction of potential vorticity, *Dynam. Atmos. Ocean*, 45(3-4), 252–273, doi:10.1016/j.dynatmoce.2008.02.002.
- Thomas, L. N., A. Tandon, and A. Mahadevan (2008), Submesoscale processes and dynamics, *Ocean Modeling in an Eddying Regime*, *Geophys. Monogr. Ser.*, 177, 17–38.
- Thompson, D. W. J., J. J. Kennedy, J. M. Wallace, and P. D. Jones (2008), A large discontinuity in the mid-twentieth century in observed global-mean surface temperature, *Nature*, 453(7195), 646–649.
- Thompson, L. (2000), Ekman layers and two-dimensional frontogenesis in the upper ocean, *J. Geophys. Res.*, 105(C3), 6437–6451, doi:10.1029/1999JC900336.
- Thum, N., S. K. Esbensen, D. B. Chelton, and M. J. McPhaden (2002), Air-sea heat exchange along the northern sea surface temperature front in the eastern tropical Pacific, *J. Climate*, 15(23), 3361–3378.
- Trenberth, K. E., and J. M. Caron (2001), Estimates of meridional atmosphere and ocean heat transports, *J. Climate*, 14(16), 3433–3443, doi:10.1175/1520-0442(2001)014<3433:EOMAAO>2.0.CO;2.

- Trenberth, K. E., and J. T. Fasullo (2013), An apparent hiatus in global warming?, *Earth's Future*, 1(1), 19–32, doi:10.1002/2013EF000165.
- Turk, D., M. J. McPhaden, A. J. Busalacchi, and M. R. Lewis (2001), Remotely sensed biological production in the equatorial Pacific, *Science*, 293(5529), 471–474, doi:10.1126/science.1056449.
- Ubelmann, C., and L.-L. Fu (2011), Cyclonic eddies formed at the Pacific tropical instability wave fronts, *J. Geophys. Res.*, 116(12), C12,021, doi:10.1029/2011JC007204.
- Vialard, J., C. Menkes, J.-P. Boulanger, P. Delecluse, E. Guilyardi, M. J. McPhaden, and G. Madec (2001), A model study of oceanic mechanisms affecting equatorial Pacific sea surface temperature during the 1997-98 El Niño, *J. Phys. Oceanogr.*, 31(7), 1649–1675.
- Wang, C. (2001), A unified oscillator model for the El Niño - Southern Oscillation, *J. Climate*, 14(1), 98–115, doi:10.1175/1520-0442(2001)014<0098:AUOMFT>2.0.CO; 2.
- Wang, C., and P. C. Fiedler (2006), ENSO variability and the eastern tropical Pacific: A review, *Prog. Oceanogr.*, 69(24), 239–266, doi:10.1016/j.pocean.2006.03.004.
- Wang, C., C. Deser, J.-Y. Yu, P. DiNezio, and A. Clement (2012), El Niño - Southern Oscillation (ENSO): A review.
- Waterhouse, A. F., J. A. MacKinnon, J. D. Nash, M. H. Alford, E. Kunze, H. L. Simmons, K. L. Polzin, L. C. St. Laurent, O. M. Sun, R. Pinkel, L. D. Talley, C. B. Whalen, T. N. Huussen, G. S. Carter, I. Fer, S. Waterman, A. C. Naveira Garabato, T. B. Sanford, and C. M. Lee (2014), Global patterns of diapycnal mixing from measurements of the turbulent dissipation rate, *J. Phys. Oceanogr.*, 44(7), 1854–1872, doi:10.1175/JPO-D-13-0104.1.
- Waterman, S., and B. J. Hoskins (2013), Eddy shape, orientation, propagation, and mean flow feedback in western boundary current jets, *J. Phys. Oceanogr.*, 43(8), 1666–1690, doi:10.1175/JPO-D-12-0152.1.

- Weisberg, R. H., and A. M. Horigan (1981), Low-frequency variability in the Equatorial Atlantic, *J. Phys. Oceanogr.*, 11(7), 913–920, doi:10.1175/1520-0485(1981)011<0913:LFVITE>2.0.CO;2.
- Weisberg, R. H., and T. J. Weingartner (1988), Instability waves in the equatorial Atlantic ocean, *J. Phys. Oceanogr.*, 18(11), 1641–1657.
- Wenegrat, J. O., and M. J. McPhaden (2015), Wind, waves, and fronts: Frictional effects in a generalized ekman model, *J. Phys. Oceanogr.*, pp. –, doi: 10.1175/JPO-D-15-0162.1.
- Wentz, F., C. Gentemann, and K. Hilburn (2015), Remote sensing systems TRMM TMI 3-day environmental suite on 0.25 deg grid, version 7.1, remote Sensing Systems, Santa Rosa, CA. Available online at www.remss.com/missions/tmi. [Accessed 01-12-2015].
- Whalen, C. B., L. D. Talley, and J. A. MacKinnon (2012), Spatial and temporal variability of global ocean mixing inferred from Argo profiles, *Geophys. Res. Lett.*, 39(18), L18,612–, doi:10.1029/2012GL053196.
- White, A. A., and R. Bromley (1995), Dynamically consistent, quasi-hydrostatic equations for global models with a complete representation of the Coriolis force, *Q. J. Roy. Meteorol. Soc.*, 121(522), 399–418, doi:10.1002/qj.49712152208.
- Willett, C. S., R. R. Leben, and M. F. Lavn (2006), Eddies and tropical instability waves in the eastern tropical Pacific: A review, *Prog. Oceanogr.*, 69, 218 – 238, doi:10.1016/j.pocean.2006.03.010.
- Winters, K. B., P. Bouruet-Aubertot, and T. Gerkema (2011), Critical reflection and abyssal trapping of near-inertial waves on a β -plane, *J. Fluid Mech.*, 684, 111–136, doi:10.1017/jfm.2011.280.
- Wittenberg, A. T., A. Rosati, T. L. Delworth, G. A. Vecchi, and F. Zeng (2014), ENSO modulation: Is it decadally predictable?, *J. Climate*, 27(7), 2667–2681.

- Wunsch, C., and R. Ferrari (2004), Vertical mixing, energy, and the general circulation of the oceans, *Annu. Rev. Fluid Mech.*, 36, 281–314, doi:10.1146/annurev.fluid.36.050802.122121.
- Yoder, J., S. Ackleson, R. Barber, P. Flament, and W. Balch (1994), A line in the sea, *Nature*, 371(6499), 689–692.
- Yu, J., and W. Liu (2003), A linear relationship between ENSO intensity and tropical instability wave activity in the eastern Pacific ocean, *Geophys. Res. Lett.*, 30(14), 1735.
- Yu, Z., J. P. McCreary, and J. A. Proehl (1995), Meridional asymmetry and energetics of tropical instability waves, *J. Phys. Oceanogr.*, 25(12), 2997–3007, doi:10.1175/1520-0485(1995)025<2997:MAAEOT>2.0.CO;2.
- Zaron, E. D., and J. N. Moum (2009), A new look at Richardson number mixing schemes for equatorial ocean modeling, *J. Phys. Oceanogr.*, 39(10), 2652–2664.
- Zhang, C. (2001), Intraseasonal perturbations in sea surface temperatures of the equatorial eastern Pacific and their association with the Madden-Julian Oscillation, *J. Climate*, 14(6), 1309–1322, doi:10.1175/1520-0442(2001)014<1309:IPISST>2.0.CO;2.